

**Numerical studies of bypass transition
in the Blasius boundary layer.**

by

Luca Brandt

April 2003
Technical Reports from
Royal Institute of Technology
Department of Mechanics
SE-100 44 Stockholm, Sweden

Typsatt i $\mathcal{A}\mathcal{M}\mathcal{S}$ - $\mathcal{L}\mathcal{A}\mathcal{T}\mathcal{E}\mathcal{X}$.

Akademisk avhandling som med tillstånd av Kungliga Tekniska Högskolan i Stockholm framlägges till offentlig granskning för avläggande av teknologie doktorsexamen tisdagen den 20:e maj 2003 kl 10.15 i Kollegiesalen, Administrationsbyggnaden, Kungliga Tekniska Högskolan, Valhallavägen 79, Stockholm.

©Luca Brandt 2003

Universitetsservice AB, Stockholm 2003

Numerical studies of bypass transition in the Blasius boundary layer.

Luca Brandt 2003

Department of Mechanics, Royal Institute of Technology
SE-100 44 Stockholm, Sweden.

Abstract

Experimental findings show that transition from laminar to turbulent flow may occur also if the exponentially growing perturbations, eigensolutions to the linearised disturbance equations, are damped. An alternative non-modal growth mechanism has been recently identified, also based on the linear approximation. This consists of the transient growth of streamwise elongated disturbances, with regions of positive and negative streamwise velocity alternating in the spanwise direction, called streaks. These perturbations are seen to appear in boundary layers exposed to significant levels of free-stream turbulence. The effect of the streaks on the stability and transition of the Blasius boundary layer is investigated in this thesis. The analysis considers the steady spanwise-periodic streaks arising from the nonlinear evolution of the initial disturbances leading to the maximum transient energy growth. In the absence of streaks, the Blasius profile supports the viscous exponential growth of the Tollmien-Schlichting waves. It is found that increasing the streak amplitude these two-dimensional unstable waves evolve into three-dimensional spanwise-periodic waves which are less unstable. The latter can be completely stabilised above a threshold amplitude. Further increasing the streak amplitude, the boundary layer is again unstable. The new instability is of different character, being driven by the inflectional profiles associated with the spanwise modulated flow. In particular, it is shown that, for the particular class of steady streaks considered, the most amplified modes are antisymmetric and lead to spanwise oscillations of the low-speed streak (sinuous scenario). The transition of the streak is then characterised by the appearance of quasi-streamwise vortices following the meandering of the streak.

Simulations of a boundary layer subjected to high levels of free-stream turbulence have been performed. The receptivity of the boundary layer to the external perturbation is studied in detail. It is shown that two mechanisms are active, a linear and a nonlinear one, and their relative importance is discussed. The breakdown of the unsteady asymmetric streaks forming in the boundary layer under free-stream turbulence is shown to be characterised by structures similar to those observed both in the sinuous breakdown of steady streaks and in the varicose scenario, with the former being the most frequently observed.

Descriptors: Fluid mechanics, laminar-turbulent transition, boundary layer flow, transient growth, streamwise streaks, *lift-up* effect, receptivity, free-stream turbulence, secondary instability, Direct Numerical Simulation.

Preface

This thesis considers the study of bypass transition in a zero-pressure-gradient boundary layer. The first part is a summary of the research presented in the papers included in the second part. The summary includes an introduction to the basic concept, a review of previous works and a presentation and discussion of the main results obtained.

The thesis is based on and contains the following papers.

Paper 1. ANDERSSON, P., BRANDT, L., BOTTARO, A. & HENNINGSON, D. S. 2001 On the breakdown of boundary layer streaks. *Journal of Fluid Mechanics*, **428**, pp. 29-60.

Paper 2. BRANDT, L., COSSU, C., CHOMAZ, J.-M., HUERRE, P. & HENNINGSON, D. S. 2003 On the convectively unstable nature of optimal streaks in boundary layers. *Journal of Fluid Mechanics*, In press.

Paper 3. BRANDT, L. & HENNINGSON, D. S. 2002 Transition of streamwise streaks in zero-pressure-gradient boundary layers. *Journal of Fluid Mechanics*, **472**, pp. 229-262.

Paper 4. COSSU, C. & BRANDT, L. 2002 Stabilization of Tollmien-Schlichting waves by finite amplitude optimal streaks in the Blasius boundary layer. *Physics of Fluids*, **14**, pp. L57-L60.

Paper 5. COSSU, C. & BRANDT, L. 2003 On the stabilizing role of boundary layer streaks on Tollmien-Schlichting waves.

Paper 6. BRANDT, L., HENNINGSON, D. S., & PONZIANI D. 2002 Weakly non-linear analysis of boundary layer receptivity to free-stream disturbances. *Physics of Fluids*, **14**, pp. 1426-1441.

Paper 7. BRANDT, L., SCHLATTER, P. & HENNINGSON, D. S. 2003 Boundary-layer transition under free-stream turbulence.

Division of work between authors

The Direct Numerical Simulations (DNS) were performed with a numerical code already in use mainly for transitional research, developed originally by Anders Lundbladh, Dan Henningson (DH) and Arne Johansson. It is based on a pseudo-spectral technique and has been further developed by several users, including Luca Brandt (LB) for generating new inflow conditions and extracting flow quantities needed during the work.

The DNS data and secondary instability calculations presented in Paper 1 were done by LB, who also collaborated in the writing process. The theory and the writing was done by Paul Andersson, Alessandro Bottaro and DH. The simulations presented in Paper 2 were performed by LB with help from Carlo Cossu (CC). The writing was done by LB and Patrick Huerre, with feedback from J.-M. Chomaz and DH. The DNS in Paper 3 were performed by LB. The writing was done by LB with help from DH.

The simulations presented in Paper 4 were performed by CC and LB. The paper was written by CC with help from LB. The numerical code for the stability calculations in Paper 5 was implemented by CC, who also carried out the computations. The paper was written by CC with help from LB.

The numerical implementation of the perturbation model presented in Paper 6 was done in collaboration between LB and Donatella Ponziani (DP). The writing was done by LB and DP with help from DH.

The turbulent inflow generation used in Paper 7 was implemented by Philipp Schlatter (PS) with help from LB and DH. The simulation were carried out by PS and LB. The paper was written by LB with help from PS and DH.

Contents

Preface	iv
Chapter 1. Introduction	1
Chapter 2. Transition in Blasius boundary layers	4
2.1. Natural transition	4
2.2. Bypass transition	5
Chapter 3. Direct numerical simulations	8
3.1. Numerical method	8
3.2. Disturbance generation	10
Chapter 4. Instability and breakdown of steady optimal streaks	12
4.1. Steady saturated streaks	12
4.2. Streak instability	14
4.2.1. Viscous instabilities in low-amplitude streaks	18
4.2.2. Inviscid instability	21
4.2.3. Spatio-temporal behaviour	22
4.3. Streak breakdown	26
Chapter 5. Transition in boundary layers subjected to free-stream turbulence	30
5.1. Receptivity	30
5.2. Effect of the integral length scales of the free-stream turbulence	33
5.3. Turbulent spot generation	34
Chapter 6. Conclusions and outlook	38
Acknowledgment	41
Bibliography	42
Part 2. Papers	47

Paper 1.	On the breakdown of boundary layer streaks	51
Paper 2.	On the convectively unstable nature of optimal streaks in boundary layers	93
Paper 3.	Transition of streamwise streaks in zero-pressure-gradient boundary layers	123
Paper 4.	Stabilization of Tollmien-Schlichting waves by finite amplitude optimal streaks in the Blasius boundary layer	167
Paper 5.	On the stabilizing role of boundary layer streaks on Tollmien-Schlichting waves	177
Paper 6.	Weakly nonlinear analysis of boundary layer receptivity to free-stream disturbances	211
Paper 7.	Boundary-layer transition under free-stream turbulence	245

CHAPTER 1

Introduction

The motion of a fluid is usually defined as *laminar* or *turbulent*. A laminar flow is an ordered, predictable and layered flow (from Latin “lamina”: layer, sheet, leaf) as opposed to the chaotic, swirly and fluctuating turbulent flow. In a laminar flow the velocity gradients and the shear stresses are smaller; consequently the drag force over the surface of a vehicle is much lower than in a turbulent flow. One of the major challenges in aircraft design is in fact to obtain a laminar flow over the wings to reduce the friction in order to save fuel. On the other hand a turbulent flow provides an excellent mixing in the flow because of the chaotic motion of the fluid particles, and it is therefore required in chemical reactors or combustion engines.

In real applications, as the velocity of the fluid or the physical dimension limiting the flow increase, a laminar motion cannot be sustained; the perturbations inevitably present within the flow are amplified and the flow evolves into a turbulent state. This phenomenon is called *transition*.

Transition and its triggering mechanisms are today not fully understood, even though the first studies on this field dates back to the end of the nineteenth century. The very first piece of work is traditionally considered the classical experiment of Osborne Reynolds in 1883 performed at the hydraulics laboratory of the Engineering Department at Manchester University. Reynolds studied the flow inside a glass tube injecting ink at the centreline of the pipe inlet. If the flow stayed laminar, he could observe a straight coloured line inside the tube. When transition occurred, the straight line became irregular and the ink diffused all over the pipe section. He found that the value of a non dimensional parameter, later called Reynolds number, $Re = \frac{Ur}{\nu}$, where U is the bulk velocity, r the pipe radius and ν the kinematic viscosity, governed the passage from the laminar to the turbulent state. This non dimensional parameter relates the inertial effects to the viscous forces acting on the moving fluid particles. The two latter forces are therefore the only involved in the phenomenon under consideration. Reynolds stated quite clearly, however, that there is no a single *critical* value of the parameter Re , above which the flow becomes unstable and transition may occur; the whole matter is much more complicated. He noted the sensitivity of the transition to disturbances in the flow before entering the tube. For large disturbances at the pipe inlet, in fact, the flow became unstable at lower critical velocities and the chaotic motion appeared intermittently for short distances, like *flashes*, along the pipe.

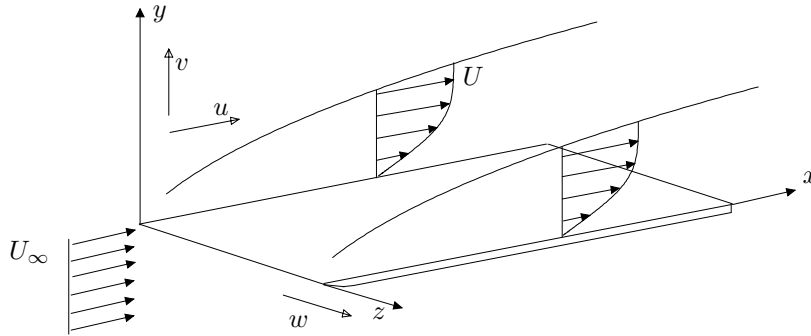


FIGURE 1.1. Boundary layer flow with free-stream velocity U_∞ . The velocity has components u , v and w in the coordinate system x , y and z .

The knowledge of why, where and how a flow becomes turbulent is of great practical importance in almost all the application involving flows either internal or external; therefore there is a need to improve the models able to predict the transition onset currently available. In gas turbines, where a turbulent free stream is present, the flow inside the boundary layer over the surface of a blade is transitional for 50 – 80% of the chord length. Wall shear stresses and heat transfer rates are increased during transition and a correct design of the thermal and shear loads on the turbine blades must take into account the features of the transitional process.

The present thesis deals with transition in the simplified case of the boundary layer over a flat plate subject to a uniform oncoming flow. The friction at the wall will slow down the fluid particles; due to viscosity the velocity of the flow will vary from the free-stream value a distance above the wall (boundary layer thickness) to zero at the plate surface, with the thickness growing as the flow evolves downstream, see figure 1.1. This flow is also referred to as *Blasius boundary layer* after the scientist who, under certain assumptions, solved the governing fluid dynamics equations (Navier–Stokes equations) for this particular configuration. This is one of the simplest configurations, but still helps us to gain some physical insight in the transition process. It has been in fact observed that independently of the background disturbances and environment the flow eventually becomes turbulent further downstream. The background environment determines, however, the route the transition process will follow and the location of its onset. Other effects present in real applications such as curvature of the surface or pressure gradients, which give an accelerating or decelerating flow outside the boundary layer, will not be considered.

The transition process may be divided into three stages: receptivity, disturbance growth and breakdown. In the *receptivity* stage the disturbance is initiated inside the boundary layer. This is the most difficult phase of the full transition process to predict because it requires the knowledge of the ambient

disturbance environment, which is difficult to determine in real applications. The main sources of perturbations are free-stream turbulence, free-stream vortical disturbances, acoustic waves and surface roughness. Once a small disturbance is introduced, it may *grow* or decay according to the stability characteristics of the flow. Examining the equation for the evolution of the kinetic energy of the perturbation (Reynolds–Orr equation), a strong statement can be made regarding the nonlinear effects: the nonlinear terms redistribute energy among different frequencies and scales of the flow but have no net effect on the instantaneous growth rate of the energy. This implies that linear growth mechanisms are responsible for the energy of a disturbance of any amplitude to increase. After the perturbation has reached a finite amplitude, it often saturates and a new, more complicated, flow is established. This new steady or quasi-steady state is usually unstable; this instability is referred to as “secondary”, to differentiate it from the “primary” growth mechanism responsible for the formation of the new unstable flow pattern. It is at this stage that the final nonlinear *breakdown* begins. It is followed by other symmetry breaking instabilities and nonlinear generation of the multitude of scales and frequencies typical of a turbulent flow. The breakdown stage is usually more rapid and characterised by larger growth rates of the perturbation compared to the initial primary growth.

Transition in Blasius boundary layers

2.1. Natural transition

Historically, the first approach to transition was the analysis of the stability of a flow. Equations for the evolution of a disturbance, linearised around a mean velocity profile were first derived by Lord Rayleigh (1880) for an inviscid flow. He considered a two-dimensional basic flow consisting only of the streamwise velocity component assumed to vary only in one cross-stream direction (*parallel flow assumption*). Assuming a wave-like form of the velocity perturbation and Fourier transforming the equation, it reduces to an eigenvalue problem for exponentially growing or decaying disturbances. From this equation, Rayleigh proved his inflection point theorem which states that a necessary condition for inviscid instability is the presence of an inflection point in the basic velocity profile. Later Orr (1907) and Sommerfeld (1908) included the effects of viscosity, deriving independently what we today call the Orr–Sommerfeld equation. The latter is an equation for the wall-normal component of the perturbation velocity and it suffices to describe the evolution of two-dimensional disturbances. To describe three-dimensional perturbation one more equation is needed; for this, an equation for the wall-normal vorticity is commonly used (Squire equation). The first solutions for two-dimensional unstable waves in the Blasius boundary layer were presented by Tollmien (1929) and Schlichting (1933). The existence of such solutions (TS-waves) was experimentally shown to exist by Schubauer & Skramstad (1947).

About at the same time, Squire’s theorem (1933), stating that two dimensional waves are the first to become unstable, directed the early studies on stability towards two-dimensional perturbations. The stability of such eigenmodes of the Orr–Sommerfeld problem depends on their wavelength, frequency, and on the Reynolds number, defined for a boundary layer flow as $Re = \frac{U_\infty \delta}{\nu}$, with $\delta = \sqrt{(x\nu/U_\infty)}$ the boundary layer thickness. Since δ is increasing in the downstream direction, see figure 1.1, the Reynolds number varies and the TS-waves growth rate is also function of the downstream position along the plate. The classical stability theory assumes that the boundary layer has a constant thickness, the so called *parallel flow* assumption. The stability of a disturbance is evaluated for different Reynolds numbers, mimicking the downstream evolution of the Blasius flow. This proved to be a reasonable approximation (Fasel & Konzelman 1990; Klingmann *et al.* 1993), even if different models

have been now developed to include the boundary layer growth in the stability calculations (see for example the Parabolized Stability Equations introduced by Herbert & Bertolotti 1987).

If an amplified Tollmien–Schlichting wave grows above an amplitude in u_{rms} of 1% of the free-stream velocity, the flow become susceptible to secondary instability. Klebanoff, Tidstrom & Sargent (1962) observed that three-dimensional perturbations, which are present in any natural flow, were strongly amplified. The three-dimensional structure of the flow was characterised by regions alternating in the spanwise direction of enhanced and diminished perturbation velocity amplitudes, denoted by them “peaks and valleys”. The spanwise scale of the new pattern was of the same order of the streamwise wavelength of the TS-waves and the velocity time signal showed the appearance of high frequency disturbance spikes at the peak position. This transition scenario was later denoted as K-type after Klebanoff but also fundamental since the frequency of the secondary, spanwise periodic, fluctuations is the same as the one of the TS-waves. In the non-linear stages of the K-type scenario, rows of “ Λ -shaped” vortices, aligned in the streamwise directions, have been observed. An other scenario was also observed, first by Kachanov, Kozlov & Levchenko (1977). This is denoted N-type after Novosibirsk, where the experiments were carried out or H-type after Herbert, who performed a theoretical analysis of the secondary instability of TS-waves (Herbert 1983). In this scenario, the frequency of the secondary instability mode is half the one of the TS-waves and, thus, this is also known as subharmonic breakdown. “ Λ -shaped” vortices are present also in this case, but they are arranged in a staggered pattern. Experiments and computations reveals that the N-type scenario is the first to be induced, when small three-dimensional perturbations are forced in the flow.

Transition originating from exponentially growing eigenfunctions is usually called *classical* or *natural* transition. This is observed in natural flows only if the background turbulence is very small; as a rule of thumb it is usually assumed that natural transition occurs for free-stream turbulence levels less than 1%. For higher values, the disturbances inside the boundary layer are large enough that other mechanisms play an important role and the natural scenario is bypassed.

2.2. Bypass transition

In 1969 Morkovin coined the expression “bypass transition”, noting that “we can bypass the TS-mechanism altogether”. In fact, experiments reveal that many flows, including channel and boundary layer flows, may undergo transition for Reynolds numbers well below the critical ones from linear stability theory. The first convincing explanation for this was proposed by Ellingsen & Palm (1975). They considered, in the inviscid case, an initial disturbance independent of the streamwise coordinate in a shear layer and showed that the streamwise velocity component may grow linearly in time, producing alternating low- and high-velocity *streaks*. Hultgren & Gustavsson (1981) considered

the temporal evolution of a three-dimensional disturbance in a boundary layer and found that in a viscous flow the initial growth is followed by a viscous decay (*transient growth*).

Landahl (1975) proposed a physical explanation for this growth. A wall-normal displacement of a fluid element in a shear layer will cause a perturbation in the streamwise velocity, since the fluid particle will initially retain its horizontal momentum. As a consequence, since weak pairs of quasi streamwise counter rotating vortices are able to lift up fluid with low velocity from the wall and bring high speed fluid towards the wall, they are the most effective in forcing streamwise oriented *streaks* of high and low streamwise velocity, alternating in the spanwise direction. This mechanism is denoted *lift-up effect* and it is inherently a three-dimensional phenomenon. Some insight in it may also be gained from the equation for the wall-normal vorticity of the perturbation (Squire equation), which is proportional to the streamwise velocity for streamwise independent disturbances. The equation is, in fact, forced by a term due to the interaction between the spanwise variation of the wall-normal velocity perturbation and the mean shear of the base flow.

From a mathematical point of view, it is now clear that since the linearised Navier–Stokes operator is non-normal for many flow cases (e.g. shear flows), a significant transient growth may occur before the subsequent exponential behaviour (see Schmid & Henningson 2001). Such growth is larger for disturbances mainly periodic in the spanwise direction, that is with low frequency or streamwise wave numbers; it can exist for sub-critical values of the Reynolds number and it is the underlying mechanism in bypass transition phenomena. In particular, for the Blasius boundary layer, Andersson, Berggren & Henningson (1999) and Luchini (2000) used an optimisation technique to determine which disturbance present at the leading edge gives the largest disturbance in the boundary layer. This *optimal perturbation* was found to consist of a pair of steady streamwise counter-rotating vortices, which induce strong streamwise streaks.

For real applications, the most interesting case in which disturbances originating from non-modal growth are responsible for transition, is probably in the presence of free-stream turbulence. Inside the boundary layer in fact, the turbulence is highly damped, but low frequency oscillations, associated with long streaky structures, appear. The first experimental study of such disturbances is due to Klebanoff (1971). Arnal & Juillen (1978) also showed that for free-stream turbulence levels higher than 0.5–1%, the dominant disturbances inside the boundary layer are characterised by low frequencies and they are not TS-waves. Kendall (1985) denoted these disturbances as Klebanoff modes. As the streaks grow downstream, they breakdown into regions of intense randomised flow, turbulent *spots*. The leading edge of these spots travels at nearly the free-stream velocity, while the trailing edge at about half of the speed; thus a spot grows in size and merges with other spots until the flow is completely turbulent. Westin *et al.* (1994) presented detailed measurements

of a laminar boundary layer subjected to free-stream turbulence and showed how different experiments with apparently similar conditions can disagree on the location and extent of transition. A recent review on the experimental studies of boundary-layer transition induced by free-stream turbulence can be found in Matsubara & Alfredsson (2001), while the first numerical simulations are presented in Jacobs & Durbin (2001). This scenario is usually observed for high levels of free-stream turbulence and transition occurs at Reynolds numbers lower than in the case of natural transition.

An other case where transient growth plays an important role is in the so called *oblique transition*. In this scenario, streamwise aligned vortices are generated by non-linear interaction between a pair of oblique waves with equal angle but opposite sign in the flow direction. These vortices, in turn, induce streamwise streaks, which may grow over a certain amplitude and become unstable, initiating the breakdown to a turbulent flow. Oblique transition has been studied in detail both numerically and experimentally by Berlin, Wiegel & Henningson (1999).

Transition to turbulence may, thus, follow different routes, according to the disturbance environment. In general, as soon as streamwise vortices are present in the flow, strong streamwise streaks are created, and the breakdown to turbulence occurs through their growth and breakdown. In this thesis, bypass transition is analysed; first, the instability and breakdown of steady, spanwise periodic streaks is studied as a model problem to understand the mechanisms involved in the scenario under consideration. The results are then applied to the case of a boundary layer subject to high levels of free-stream turbulence. The different approaches used and the main results obtained are shortly summarised in the next chapters.

Direct numerical simulations

3.1. Numerical method

Most of the results presented in this thesis have been obtained by means of direct numerical simulations (DNS). That is, the temporal and spatial evolution of the flow is obtained by numerical solution of the governing Navier-Stokes equations without any simplifying assumptions. This requires larger computational efforts, both in term of memory and effective time of the calculations, since all the relevant scales characterising the flow configuration under examination must be resolved.

The rapid development of fast parallel computers in recent years has provided the scientific community with the possibility of simulating fully turbulent flows. A clear advantage is that, once a flow is simulated, it is completely accessible to observation including three-dimensional views and derived quantities which are usually impossible to obtain in an experiment. Also important is the possibility of simulating 'unphysical' flows, obtained by equations and boundary conditions which differ from the real ones, so as to allow us to study partial processes, to verify hypothetical mechanisms or to test possible control strategies. The numerical simulation has lead to important improvements of our physical understanding of transitional and turbulent flows, especially on the dynamics of flow structures. However, in the case of turbulent flows the simulations are limited to Reynolds number lower than those of typical applications. The available computational resources may also limit the physical dimension of the computational domain, leading to crucial choices of the boundary conditions. On the other hand, experiments allow to study larger Reynolds number and more complicated geometries. In a experiment, it is also simpler to perform a parametric study; once the set-up is validated, it is relatively cheaper to perform a new experiment than a completely new simulation.

The direct numerical simulations presented in this thesis have all been performed with the pseudo-spectral algorithm described in Lundbladh *et al.* (1999). In spectral methods the solution is approximated by an expansion in smooth functions, trigonometric functions and Chebyshev polynomials in our case. The earliest applications to partial differential equations were developed by Kreiss & Olinger (1972) and Orszag (1972), who also introduced the pseudo-spectral approach. In this, the multiplications of the nonlinear terms are calculated in physical space to avoid the evaluation of convolution sums.

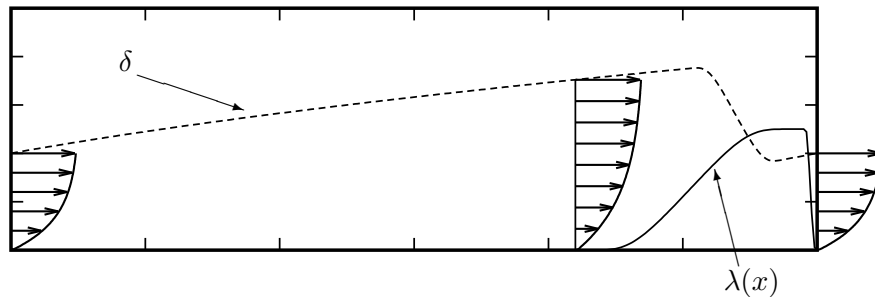


FIGURE 3.1. The boundary layer thickness δ (dashed) of a laminar mean flow that grows downstream in the physical domain and is reduced in the fringe region by the forcing. The flow profile is returned to the desired inflow profile in the fringe region, where the fringe function $\lambda(x)$ is non-zero.

As a consequence, transformations between physical and spectral space are required during the numerical integration of the equations and therefore efficient implementations of pseudo-spectral methods must rely on low-cost transform algorithms. These are the Fast Fourier Transform (FFT) algorithms, that became generally known in the 1960's.

The fast convergence rate of spectral approximations of a function and its derivatives results in very high accuracy as compared to finite-element or finite-difference discretizations. Further, the data structure makes the algorithms suitable for both parallelisation and vectorisation. The high density of points close to the physical boundaries naturally obtained by Chebyshev series can also be profitable for wall-bounded flows. However, the spectral approximation and the associated boundary conditions (as example, periodic in the case of trigonometric functions) limit the applications to simple geometries. Pseudo-spectral methods became widely used for a variety of flows during the 1980's. Early simulations of a transitional boundary layer were performed by Orszag & Patera (1983) in a temporal framework (i.e. parallel boundary layer) and by Bertolotti, Herbert & Spalart (1988) for a spatially evolving Blasius boundary layer.

The numerical code used solves the three-dimensional, time-dependent, incompressible Navier-Stokes equations. The algorithm is similar to that of Kim, Moin & Moser (1987), using Fourier representation in the streamwise and spanwise directions and Chebyshev polynomials in the wall-normal direction, together with a pseudo-spectral treatment of the nonlinear terms. The time advancement used is a four-step low-storage third-order Runge-Kutta method for the nonlinear terms and a second-order Crank-Nicolson method for the linear terms. Aliasing errors from the evaluation of the nonlinear terms

are removed by the $\frac{3}{2}$ -rule when the FFTs are calculated in the wall parallel plane. In order to set the free-stream boundary condition closer to the wall, a generalisation of the boundary condition used by Malik, Zang & Hussaini (1985) is employed. It is an asymptotic condition applied in Fourier space with different coefficients for each wavenumber that exactly represents a potential flow solution decaying away from the wall.

To correctly account for the downstream boundary layer growth a spatial technique is necessary. This requirement is combined with the periodic boundary condition in the streamwise direction by the implementation of a “fringe region”, similar to that described by Bertolotti, Herbert & Spalart (1992). In this region, at the downstream end of the computational box, the function $\lambda(x)$ in equation (3.1) is smoothly raised from zero and the flow is forced to a desired solution \mathbf{v} in the following manner,

$$\frac{\partial \mathbf{u}}{\partial t} = NS(\mathbf{u}) + \lambda(x)(\mathbf{v} - \mathbf{u}) + \mathbf{g}, \quad (3.1)$$

$$\nabla \cdot \mathbf{u} = 0, \quad (3.2)$$

where \mathbf{u} is the solution vector and $NS(\mathbf{u})$ the right hand side of the (unforced) momentum equations. Both \mathbf{g} , which is a disturbance forcing, and \mathbf{v} may depend on the three spatial coordinates and time. The forcing vector \mathbf{v} is smoothly changed from the laminar boundary layer profile at the beginning of the fringe region to the prescribed inflow velocity vector. This is normally a boundary layer profile \mathbf{v}_0 , but can also contain a disturbance. This method damps disturbances flowing out of the physical region and smoothly transforms the flow to the desired inflow state, with a minimal upstream influence (see Nordström *et al.* 1999, for an investigation of the fringe region technique). Figure 3.1 illustrates the variation of the boundary layer thickness in the computational box for a laminar case together with a typical fringe function $\lambda(x)$.

3.2. Disturbance generation

Using this numerical code, disturbances can be introduced in the laminar flow by including them in the flow field \mathbf{v} , thereby forcing them in the fringe region; by a body force \mathbf{g} , and by blowing and suction at the wall through non homogeneous boundary conditions. The first of these three methods is the most used in the simulations presented in the thesis. In fact, to study the instability and breakdown of steady, spanwise periodic streaks, the velocity fields \mathbf{v}_s and \mathbf{v}_d are added to the Blasius solution \mathbf{v}_0 to give a forcing vector of the form $\mathbf{v} = \mathbf{v}_0 + \mathbf{v}_s + \mathbf{v}_d e^{i\omega t}$. \mathbf{v}_s represents the steady streaks: those linear optimal computed by Andersson *et al.* (1999) are forced at the inflow in Paper 1 and the nonlinearly saturated streaks obtained are then used as inlet conditions in some of the following studies. The time periodic disturbance \mathbf{v}_d is an instability mode riding on the streak which is used to simulate the full transition process of a steady streak in Paper 3.

To simulate a boundary layer under free-stream turbulence (Paper 7) a more involved methodology has been implemented. Following Jacobs & Durbin

(2001), a turbulent inflow is described as a superposition of modes of the continuous spectrum of the linearised Orr-Sommerfeld and Squire operators. These modes have also been added to the forcing vector \mathbf{v} and thus introduced in the fringe region. Isotropic grid turbulence can be reproduced by a sum of Fourier modes with random amplitudes (see Rogallo 1981); however in the presence of an inhomogeneous direction an alternative complete basis is required; in particular, in the present case, the new basis functions need to accommodate the wall. A natural choice is therefore the use of the modes of the continuous spectrum. It is useful to recall, in fact, that the Orr-Sommerfeld and Squire eigenvalue problem for a parallel flow in a semi-bounded domain is characterised by a continuous and a discrete spectrum (Grosch & Salwen 1978). The discrete modes decay exponentially with the distance from the wall, while modes of the continuous spectrum are nearly sinusoidal in the free stream. As a consequence, a three-dimensional wave-vector $\kappa = (\alpha, \gamma, \beta)$ can be associated to each eigenfunction of the continuous spectrum: The streamwise and spanwise wave numbers α and β are defined by the normal mode expansion in the homogeneous directions of the underlying linear problem while the wall-normal wavelength is determined by the eigenvalue along the continuous spectrum. Invoking Taylor's hypothesis, the streamwise wavenumber α can be replaced by a frequency $\omega = \alpha U_\infty$ and the expansion may be written

$$u = \sum A_N \hat{u}_N(y) e^{(i\beta z + i\alpha x - i\omega t)},$$

where the real values of β and ω and the complex wavenumber α are selected according to the procedure described below. Note that the desired wall-normal wavenumber γ enters through the eigenfunction shape $\hat{u}_N(y)$ and it is defined by the eigenvalue α . In particular, the wave numbers pertaining to the modes used in the expansion are selected by defining in the wavenumber space (ω, γ, β) a number of spherical shells of radius $|\kappa|$. 40 points are then placed randomly but at equal intervals on the surface of these spheres. The coordinates of these points define the wave numbers of the modes used in the expansion above. The complex coefficients A_N provide random phase but a given amplitude. The amplitude $|A_N|$ is in fact the same for all modes on each shell and reproduces the following analytical expression for a typical energy spectrum of homogeneous isotropic turbulence

$$E(\kappa) = \frac{2}{3} \frac{a (\kappa L)^4}{(b + (\kappa L)^2)^{17/6}} L T u. \quad (3.3)$$

In the expression above, Tu is the turbulence intensity, L a characteristic integral length scale and a, b two normalisation constants. The methodology briefly introduced here is able to satisfactorily reproduce a boundary layer subject to free-stream turbulence as documented in Paper 7.

Instability and breakdown of steady optimal streaks

4.1. Steady saturated streaks

The two linear disturbance-growth mechanisms usually encountered in flat-plate boundary layers have been introduced in chapter 2. These are the exponential growth of Tollmien-Schlichting waves and the transient growth of streamwise elongated streaks. If the amplification of either of the two is large enough, the disturbances eventually reach an amplitude where nonlinear effects become relevant. These *primary* perturbations saturate and take the flow into a new more complicated steady or quasi-steady laminar state. The linear stability of this new flow configuration is the object of *secondary stability* investigations.

The analysis performed here concerns the linear secondary stability of the streaks resulting from the nonlinear evolution of the spatial optimal perturbation in a Blasius boundary layer. The investigation is motivated by the need to understand in a simpler configuration the physics of bypass transition in boundary layers with high levels of free-stream turbulence, where low frequency streaks are the type of perturbations induced inside the boundary layer. The base flows under consideration are computed by solving the full Navier-Stokes equations (see Paper 1). In particular, the complete velocity field representing the initial evolution of the steady, spanwise periodic, linear optimal perturbations calculated by Andersson *et al.* (1999), is forced in the fringe region as described in the previous chapter. The downstream nonlinear development of the streaks is monitored for different upstream amplitudes of the input disturbance. To quantify the size of this primary disturbance at each streamwise position, an amplitude A is defined as

$$A(X) = \frac{1}{2} \left[\max_{y,z} \left(U(X, y, z) - U_B(X, y) \right) - \min_{y,z} \left(U(X, y, z) - U_B(X, y) \right) \right],$$

where $U_B(x, y)$ is the Blasius profile and $U(X, y, z)$ is the total streamwise velocity in the presence of streaks and they are made non dimensional with respect to the free-stream velocity U_∞ .

The downstream amplitude development is displayed in figure 4.1(a) for the set of upstream amplitudes considered. The abscissa X in the figure indicates the distance from the leading edge and it is divided by the reference length L , where $L = 1$ is the station at which the linear growth of the upstream

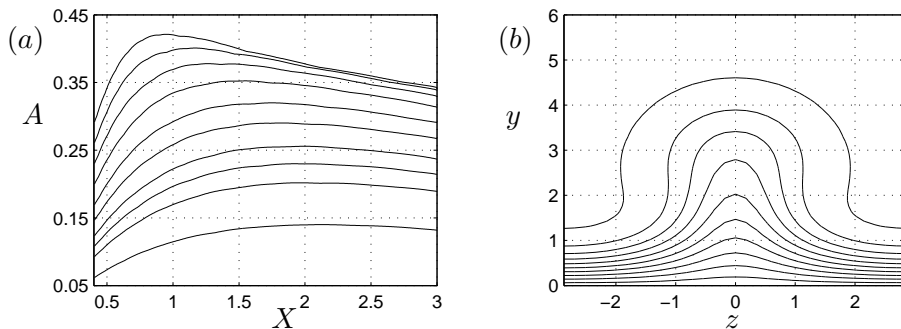


FIGURE 4.1. (a) Downstream development of the streak amplitude A versus streamwise coordinate X for different upstream amplitudes A_0 . (b) Streamwise velocity contour plot of the nonlinear base flow in a (y, z) cross-stream plane at $X = 2$, $A = 0.36$. The coordinates have been made non-dimensional using the local Blasius length scale δ . Maximum contour level 0.98, contour spacing 0.1.

streamwise vortices has been optimised (see Andersson *et al.* 1999). The spanwise wavenumber $\beta = 0.45$ is the optimal one and it is scaled with respect to the local Blasius length $\delta = \sqrt{x\nu/U_\infty}$ at position $x = L$. In figure 4.1(b), a typical nonlinearly saturated streak is illustrated by its streamwise velocity contour plot in the cross-stream (y, z) plane. Regions of strong spanwise shear are formed on the sides of the low-speed region, which is also displaced further away from the wall during the saturation process.

It is worth introducing a scaling property of the considered nonlinear streaks which will be used to extend the validity of the results obtained, to a wide range of Reynolds numbers and spanwise wave numbers. In fact, it is shown in Paper 1 that a streak family $U(x, y, z)$, defined by the upstream amplitude A_0 and by the spanwise wavenumber β_0 at the inlet X_0 , obeys the boundary layer equations and it is therefore independent of the Reynolds number if scaled by the boundary layer scalings. This results in a scaling property that couples the streamwise and spanwise scales, implying that the same solution is valid for every combination of $x = x^*/L$ and $\beta = \beta^*\delta$ such that the product $x\beta^2$ stays constant (the star denotes dimensional quantities). Alternatively, one could consider the product between the local Reynolds number based on the distance from the leading edge $Re_x = U_\infty x^*/\nu$ and the wavenumber $\bar{\beta} = \beta^*\nu/U_\infty$ and keep $Re_x\bar{\beta}^2 = const$. In other words, it is possible to freely choose the local Reynolds number pertaining to a given streak profile $U(y, z)$. This amounts to moving along the plate and varying the spanwise wavenumber β_0 so that the local spanwise wavenumber $\beta_0\delta/\delta_0$, where δ_0 indicates the local Blasius thickness at the upstream position X_0 , remains constant. Note also that in the non dimensional form of the boundary layer equations

the cross-stream velocities v and w are multiplied by the Reynolds number $Re = \sqrt{Re_x}$. As a consequence, the amplitude of the initial vortex needed to produce a fixed amplitude of the streak along the curve $Re_x \bar{\beta}^2 = const$ decreases in a manner inversely proportional to the square root of Re_x . Using the coupling between the streamwise and spanwise scales, this corresponds to say that the amplitude of the initial vortex is proportional to the spanwise wavenumber $\bar{\beta}$.

4.2. Streak instability

If the amplitude of the streak grows to a sufficiently high value, instabilities can develop which may provoke early breakdown and transition to turbulence despite the predicted modal decay of the primary disturbance. A possible secondary instability is caused by inflectional profiles of the base flow velocity, a mechanism which does not rely on the presence of viscosity.

In flows over concave walls or in rotating channels, the primary exponential instability results in streamwise vortices, which, in turn, create streaks. It is therefore not surprising that the first studies on the secondary instability of streaky structures refer to these types of flows and it can be expected that the secondary instability mechanisms of the flat-plate boundary-layer streaks considered here will show similarities with the instabilities observed in the flows mentioned above (see Schmid & Henningson 2001 among others). The experiments of Swearingen & Blackwelder (1987) were the first to document the emergence of streaks with inflectional profiles due to the formation of streamwise vortices (called Görtler vortices) in the boundary layer over a concave wall. This investigation demonstrated that time-dependent fluctuations appear in the flow either in a spanwise symmetric (*varicose*) or antisymmetric (*sinuous*) pattern with respect to the underlying streak. The varicose perturbations are more closely related with the wall-normal inflection points while the sinuous oscillations are related with the spanwise inflectional profile and they were found to be the fastest growing. These findings were successively confirmed by theoretical analysis of the instability of Görtler vortices, both assuming inviscid flow and including the effect of viscosity (e.g. Park & Huerre 1995; Bottaro & Klingmann 1996). The instability of streaks arising from the transient growth of streamwise vortices in channel flows has been studied theoretically by Waleffe (1995, 1997) and Reddy *et al.* (1998) and experimentally by Elofsson, Kawakami & Alfredsson (1999). These studies confirmed that the instability is of inflectional type and that the dominating instability appears as spanwise (sinuous) oscillations of the streaks.

The secondary instability of the steady, spanwise periodic streaks introduced in the previous section is studied under two basic assumptions. Since the streaks satisfy the boundary layer approximation, the downstream variation of the streamwise velocity is slow and the wall-normal and spanwise velocities are very small, of the order $O(1/Re_x^{1/2})$, as compared to the streamwise component. Therefore the basic flow will consist only of the streamwise velocity

U . Further, the secondary instability is observed in flow visualisations to vary rapidly in the streamwise direction. Hence, we will assume a parallel mean flow $U(y, z)$, dependent only on the cross-stream coordinates. This basic parallel flow is extracted at different streamwise stations X from the spatial numerical simulations presented in figure 4.1.

The equations governing the linear evolution of a perturbation velocity $\mathbf{u}(x, y, z, t) = (u, v, w)$, of corresponding pressure p , on the streak profile $U(y, z)$ are obtained by substituting $U + \mathbf{u}$ into the Navier-Stokes equations and neglecting the quadratic terms in the perturbation. This yields

$$u_t + Uu_x + U_yv + U_zw = -p_x + \frac{1}{Re}\Delta u, \quad (4.1)$$

$$v_t + Uv_x = -p_y + \frac{1}{Re}\Delta v, \quad (4.2)$$

$$w_t + Uw_x = -p_z + \frac{1}{Re}\Delta w, \quad (4.3)$$

$$u_x + v_y + w_z = 0. \quad (4.4)$$

Following a procedure similar to that used in the derivation of the Orr-Sommerfeld and Squire system, the above equations can be reduced to two equations in terms of the normal velocity v and the normal vorticity $\eta = v_z - w_x$

$$\begin{aligned} \Delta v_t + U\Delta v_x + U_{zz}v_x + 2U_zv_{xz} - U_{yy}v_x - 2U_zw_{xy} - 2U_{yz}w_x &= \frac{1}{Re}\Delta\Delta v, \\ \eta_t + U\eta_x - U_zv_y + U_{yz}v + U_yv_z + U_{zz}w &= \frac{1}{Re}\Delta\eta. \end{aligned} \quad (4.5)$$

In the above, the spanwise velocity w can be eliminated by using the identity

$$w_{xx} + w_{zz} = -\eta_x - v_{yz}.$$

Since the flow is assumed parallel, solution can be sought in the form of streamwise waves. Further, due to the spanwise periodicity of the flow, Floquet theory can be applied (e.g. Nayfeh & Mook 1979). As a consequence, for any flow quantity q , the instability modes of the basic flow U of spanwise wavelength $\lambda_z = 2\pi/\beta$ may be expressed in the form

$$q(x, y, z, t) = \tilde{q}(y, z) e^{i[\alpha x + \theta z - \omega t]}, \quad (4.6)$$

where \tilde{q} is spanwise periodic and it has the same periodicity λ_z of the basic flow. α , the streamwise wavenumber, and ω , the circular frequency, can assume complex values; θ is a real detuning parameter or Floquet exponent. Due to the spanwise symmetry of the basic streak profile $U(y, z)$ (see figure 4.1b), the modes can be divided into separate classes according to their odd or even symmetry. Further, it is sufficient to study values of the parameter θ between zero and π/λ_z , with $\theta = 0$ corresponding to a *fundamental* instability mode of spanwise wavelength λ_z and $\theta = \pi/\lambda_z$ corresponding to a *subharmonic* mode of wavelength twice that of the underlying streak. Symmetric and antisymmetric modes are called varicose and sinuous respectively, with reference to the visual appearance of the motion of the low-speed streak.

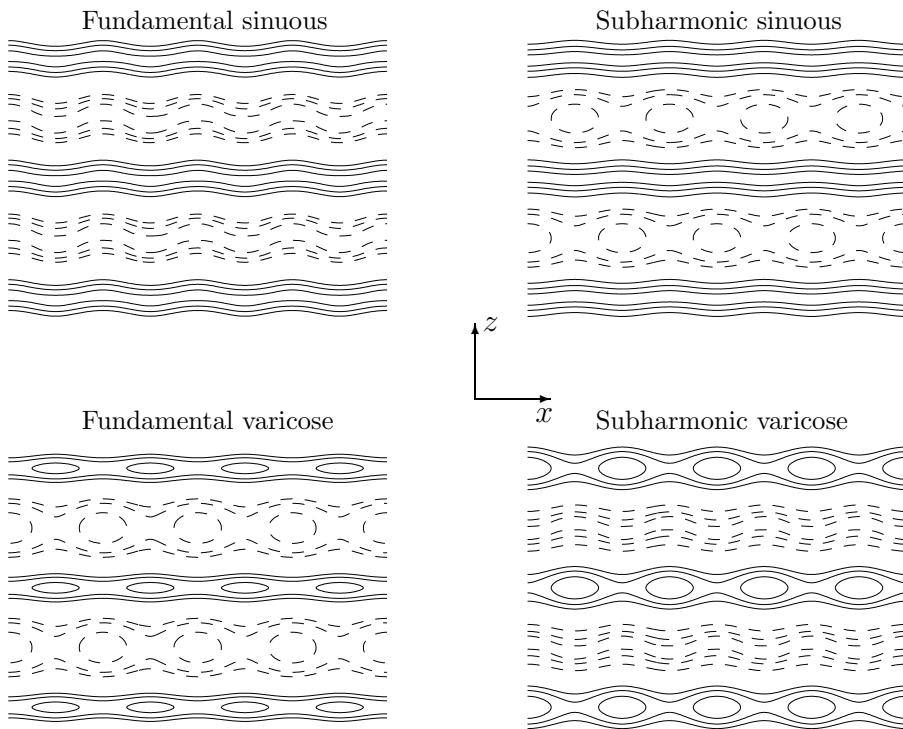


FIGURE 4.2. Sketch of streak instability modes in the $(x - z)$ -plane over four streamwise and two spanwise periods, by contours of the streamwise velocity. The low-speed streaks are drawn with solid lines while dashed lines are used for the high-speed streaks.

A sketch of the sinuous and varicose fundamental and subharmonic modes is provided in figure 4.2: it is shown how the symmetries of the subharmonic sinuous/varicose fluctuations of the low speed streaks are associated to staggered varicose/sinuous oscillations of the high speed streak.

To gain physical understanding of the mechanisms responsible for the instabilities, the production of perturbation kinetic energy is analysed. The basic idea is to derive the evolution equation for the kinetic energy density $e = (u^2 + v^2 + w^2)/2$, from the Navier-Stokes equations (4.1-4.4) linearised around the basic profile $U(y, z)$. A normal mode expansion as in equation (4.6) is assumed for the perturbation variables. If the wavenumber α is assumed real, non-trivial solutions $\tilde{q}(y, z)$ of system (4.5) will generally require a complex value for the frequency ω , thus eigenvalue of the problem. These solutions are called *temporal* modes and represent spatially periodic waves of infinite extent,

travelling with phase velocity $c_r = w_r/\alpha$ and being damped or amplified at temporal growth rate ω_i (the suffix r and i indicate the real and imaginary part respectively). This type of modes is considered in the analysis of the perturbation kinetic energy production. Upon integration over a wavelength of the secondary mode in the streamwise and spanwise directions and from the wall to infinity in the wall-normal direction, the divergence terms in the evolution equation give a zero global contribution to the energy balance and one is left with

$$\frac{\partial \tilde{E}}{\partial t} = \tilde{T}_y + \tilde{T}_z - \tilde{D}, \quad (4.7)$$

where

$$\tilde{E} = \frac{1}{\lambda_z} \int_0^{\lambda_z} \int_0^\infty \tilde{e} \, dy \, dz, \quad \tilde{D} = \frac{1}{\lambda_z} \int_0^{\lambda_z} \int_0^\infty \tilde{d} \, dy \, dz, \quad (4.8)$$

$$\tilde{T}_y = \frac{1}{\lambda_z} \int_0^{\lambda_z} \int_0^\infty \tilde{\tau}_{uv} \frac{\partial U}{\partial y} \, dy \, dz, \quad \tilde{T}_z = \frac{1}{\lambda_z} \int_0^{\lambda_z} \int_0^\infty \tilde{\tau}_{uw} \frac{\partial U}{\partial z} \, dy \, dz, \quad (4.9)$$

and

$$\tilde{e} = (\tilde{u}\tilde{u}^* + \tilde{v}\tilde{v}^* + \tilde{w}\tilde{w}^*), \quad \tilde{d} = 2 \left(\tilde{\xi}\tilde{\xi}^* + \tilde{\eta}\tilde{\eta}^* + \tilde{\zeta}\tilde{\zeta}^* \right) / Re,$$

$$\tilde{\tau}_{uv} = -(\tilde{u}\tilde{v}^* + \tilde{u}^*\tilde{v}), \quad \tilde{\tau}_{uw} = -(\tilde{u}\tilde{w}^* + \tilde{u}^*\tilde{w}).$$

The quantity \tilde{E} is the total perturbation kinetic energy and \tilde{D} is the viscous dissipation term given by the square of the perturbation vorticity vector (ξ, η, ζ) . \tilde{T}_y and \tilde{T}_z are the perturbation kinetic energy production terms associated with the work of the Reynolds stresses $\tilde{\tau}_{uv}$ and $\tilde{\tau}_{uw}$ against, respectively, the wall-normal shear $\partial U/\partial y$ and spanwise shear $\partial U/\partial z$ of the basic flow. The following identity is immediately derived from equation (4.7) by noting that the quadratic quantities $(\tilde{E}, \tilde{D}, \tilde{T}_y, \tilde{T}_z)$ have an exponential time behaviour $e^{2\omega_i t}$:

$$\omega_i = \frac{\tilde{T}_y}{2\tilde{E}} + \frac{\tilde{T}_z}{2\tilde{E}} - \frac{\tilde{D}}{2\tilde{E}}. \quad (4.10)$$

In order to evaluate the different terms entering equation (4.10) one has to solve the system (4.5) for the eigenmode and eigenvalue corresponding to the selected velocity profile $U(y, z)$, Reynolds number and streamwise wavenumber α . In the absence of errors in the computation, the left-hand side, coming from the eigenvalue computation, and the right-hand side derived from the corresponding mode shape, should match. Equation (4.10) provides an insight into the instability mechanisms by separating the three terms which contribute to the temporal growth rate ω_i . An instability is seen to appear when the work of the Reynolds stresses against the basic shears is positive and able to overcome viscous dissipation.

4.2.1. *Viscous instabilities in low-amplitude streaks*

According to Rayleigh's criterion, velocity profiles without inflection points, typical of wall-bounded shear flows such as the Blasius boundary layer of interest here, are linearly stable in the inviscid approximation. However, it is demonstrated that viscous effects may, paradoxically, be destabilising for a range of finite Reynolds number thus leading to the growth of the Tollmien-Schlichting waves. Inviscid instabilities develop on a convective time scale $\tau_i \approx L/v$, with L and v characteristic length and velocity. For flows destabilised by viscosity instead, the growth rates are smaller and the perturbation evolves on a diffusive time scale $\tau_v \approx L^2/\nu$.

As discussed earlier, small amounts of streamwise vorticity in a laminar boundary layer are very effective in moving low-momentum particles away from the wall and high-momentum particles toward the wall, thus forming elongated spanwise modulations of the streamwise velocity. Since streamwise streaks can be expected to arise whenever a boundary layer is subject to weak perturbations with streamwise vorticity, it is interesting to study the behaviour of the viscous instability in a streaky boundary layer. This analysis is the first step in the study of the effect of streamwise vortices and streaks on the transition in the Blasius boundary layer and it can be considered more relevant in the case of low-amplitude stable streaks.

Previous experimental work on the subject have given somewhat surprising results. Kachanov & Tararykin (1987) generated streamwise steady streaks by blowing and suction at the wall and used a vibrating ribbon to generate TS-waves. They found three-dimensional waves, modulated by the underlying streaks, having essentially the same phase speed as the TS-waves developing in an undisturbed Blasius boundary layer, but with lower growth rates. Boiko *et al.* (1994) also forced TS-waves with a vibrating ribbon but in a boundary layer subject to free-stream turbulence, therefore with randomly appearing low-frequency streaks. They also found waves less amplified than in a two-dimensional Blasius flow.

Before considering the different energy production terms in equation (4.10), the viscous temporal stability of the steady optimal streaks presented in figure 4.1(a) is studied. The eigenvalues having largest imaginary part ω_i are computed over a range of wave numbers α for the Blasius boundary layer and three streak profiles extracted at position $X = 2$. The local Reynolds number is selected to be $Re = 1224$. Note that all the streaks under consideration are stable in the inviscid approximation, as shown in the next section. The temporal growth rate curves $\omega_i(\alpha)$ and the corresponding phase speeds $c_r = \omega_r/\alpha$ of varicose perturbations of respectively fundamental and subharmonic type are displayed in figure 4.3. Sinuous perturbations resulted stable. Increasing the amplitude of the streak reduces the growth rates of fundamental modes up to their complete stabilisation for the largest amplitude considered. The phase speeds of the fundamental modes are roughly unchanged with respect to the Blasius-TS waves; they are only slightly reduced as the amplitude

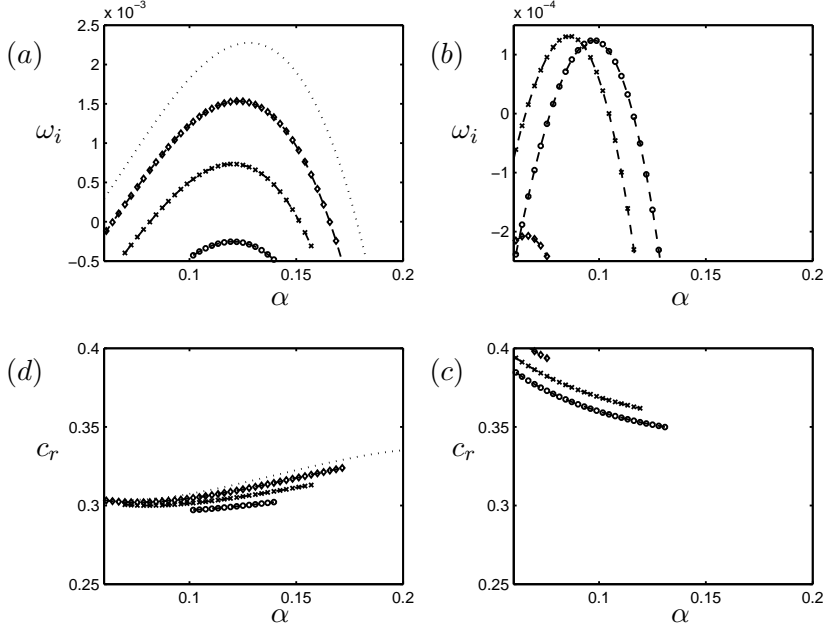


FIGURE 4.3. Growth rate ω_i and corresponding real phase speed c_r versus streamwise wavenumber α of fundamental, plot (a) and (c), and subharmonic modes, plot (b) and (d), for the Blasius boundary layer (dotted line) and streaky flows of amplitude $A = 0.13$ (\diamond), $A = 0.2$ (\times) and $A = 0.25$ (\circ) at $X = 2$ for $Re_\delta = 1224$.

and/or wavenumber is increased. The fundamental varicose mode therefore appears to be a sort of ‘continuation’ of the two-dimensional Blasius-TS waves into three-dimensional streaky-TS waves. Subharmonic modes exhibit growth rates which are an order of magnitude smaller than their fundamental counterparts except for the streak with largest amplitude which is stable to fundamental perturbations but is slightly unstable to subharmonic perturbations. The subharmonic-mode phase speeds may differ up to 25% from the Blasius-TS phase speeds and they follow an opposite trend since they decrease with increasing wave numbers.

The different terms entering equation (4.10) are reported in table 4.1 for the wave numbers giving the maximum temporal growth, i.e. at the peak of the $\omega_i(\alpha)$ curves in figure 4.3(a). The instability of the Blasius boundary layer must be ascribed to the excess of kinetic energy production \tilde{T}_y , over the viscous dissipation \tilde{D} . The subtle role of viscosity as cause of the instability can be briefly explained as follows. In the case of the Blasius profile, $\partial U/\partial z = 0$ and therefore $\tilde{T}_z = 0$. In the inviscid case, moreover, also $\tilde{D} = 0$ since $Re = \infty$ and $\omega_i = 0$ since the equation governing the evolution of inviscid perturbations

Case	$\omega_{i,max} * 10^3$	$\tilde{T}_y/2\tilde{E} * 10^3$	$\tilde{T}_z/2\tilde{E} * 10^3$	$\tilde{D}/2\tilde{E} * 10^3$
A	3.91668463	6.3942359	0.	2.47534592
B	2.63927744	9.7013363	-2.82568584	4.23475597
C	1.26350209	12.0851384	-4.88611863	5.94099013
D	-0.498663542	13.6826327	-6.28768442	7.89361186

TABLE 4.1. Maximum growth rates and normalised kinetic energy production and dissipation pertaining to the most unstable varicose fundamental mode for the streaks considered in figure 4.3. Case A indicates the undisturbed Blasius profile, while Cases B, C and D streaks of amplitude $A = 0.13$, $A = 0.2$ and $A = 0.25$.

admits either neutral waves or unstable waves (but the latter is not possible according to Rayleigh's criterion). As a consequence, $\tilde{\tau}_{uv}$ is also identically zero. From the expression above one can see that the Reynolds stress

$$\tilde{\tau}_{uv} = -(\tilde{u}\tilde{v}^* + \tilde{u}^*\tilde{v}) = |\tilde{u}||\tilde{v}|\cos(\phi_u - \phi_v)$$

is controlled by the phase difference between the streamwise and wall-normal velocities. The fact that $\tilde{\tau}_{uv} = 0$ in the inviscid case implies that u and v are in quadrature. However, for finite Reynolds numbers, viscosity may affect this phase difference so as to generate a Reynolds stress large enough to more than balance the stabilising effect of dissipation. If the Reynolds number is too small, however, the flow is again stable due to the large amount of dissipation. It is possible to show (Drazin & Reid 1981) that in the large Reynolds number limit a finite Reynolds stress is created in the layer close to the wall as a result of the phase difference between \tilde{u} and \tilde{v} induced by viscosity. In order to satisfy the zero condition in the free stream, the value of the Reynolds stress returns then to zero at a distance y_c from the wall (*the critical layer*), such that $U_B(y_c) = c$, where c is the phase speed of the wave.

In the case of the three-dimensional streaky base flow $U(y, z)$, a third production term enters the scene, namely \tilde{T}_z . This is shown to give a stabilising contribution in the case of varicose modes. The absolute value of the normalised production and dissipation terms is seen to increase with streak amplitude but the stabilising contribution $(\tilde{T}_z - \tilde{D})/2\tilde{E}$ grows more than the destabilising contribution $\tilde{T}_y/2\tilde{E}$, thereby ultimately leading to stability. The negative production term $\tilde{T}_z/2\tilde{E}$ is of the same order of magnitude as the dissipation term $\tilde{D}/2\tilde{E}$ and therefore it plays an essential role in the stabilisation process.

Thus one may conclude that the viscous instability is, in the presence of the streaks, fed by the work of the uv -Reynolds stress against the wall normal shear $\partial U/\partial y$, just as in the two-dimensional boundary layer. However, the work of the uv -Reynolds stresses against the spanwise shear $\partial U/\partial z$ is stabilising. This stabilising contribution and the viscous dissipation increase with the streak

amplitude, thereby reducing the growth rate and eventually leading to stability. These results enable to envision a possible control strategy for applications in boundary-layer transition delay in low-noise environment where the classical transition scenario is the most likely to occur. Further investigation is needed on possible streak-generation schemes and on the computation of total spatial growth-rate reductions in the presence of streaks.

4.2.2. Inviscid instability

As discussed earlier, high-amplitude streak develop inflectional profiles which can lead to strong inviscid secondary instabilities. Therefore, the marginal condition for streak instability is investigated here under the assumption of inviscid flow. If viscosity is neglected it is possible to find an uncoupled equation for the perturbation pressure (Henningson 1987; Hall & Horseman 1991)

$$\left(\frac{\partial}{\partial t} + U\frac{\partial}{\partial x}\right)\Delta p - 2U_y p_{xy} - 2U_z p_{xz} = 0. \quad (4.11)$$

This equation governs the linear stability of a parallel streak. Such basic flow is said to be stable in the inviscid approximation, if all possible perturbations superposed on the streak are damped. On the contrary, if some perturbations grow in amplitude the flow is said to be unstable. In the control parameter space, two domains corresponding to either stability or instability may be identified. These are separated by the so called *neutral surface*.

The inviscid instability is analysed in the temporal framework so that a complex value for the frequency ω is obtained as eigenvalue of the system (4.11). The flow is thus unstable if it is possible to find a value of α for which $\omega_i > 0$. Further it is possible to show that when all temporal modes are damped, the flow is linearly stable (e.g. Huerre & Rossi 1998). Thus, a temporal analysis completely determines the stability or instability of a given flow.

Since the flow has been assumed inviscid, a single control parameter, the streak amplitude A , is allowed to vary and the neutral surface reduces to a *neutral curve* in the (α, A) plane. The curves obtained are displayed in figure 4.4 for the fundamental and subharmonic sinuous symmetries. The dashed lines in the plots represent contour levels of positive growth rates. These results are obtained with the streak profiles extracted at $x = 2$ in figure 4.1(a), where the primary disturbance has saturated and, for the cases with lower initial energy, the streak amplitude achieves its maximum value. It is immediately observed that a streak amplitude of about 26% of the free-stream velocity is needed for an instability to occur. This critical value is much larger than the threshold amplitude for the secondary instability of Tollmien-Schlichting waves (1 – 2%) and roughly around the value of about 20% reported from the experimental study of Bakchinov *et al.* (1995). Similarly, in the case of plane Poiseuille flow, Elofsson *et al.* (1999) have shown that the threshold amplitude for streak breakdown is 35% of the centre line velocity. It can also be noticed from the figure that the subharmonic mode is unstable for lower amplitudes than the fundamental mode. When increasing the amplitude, not only do the growth

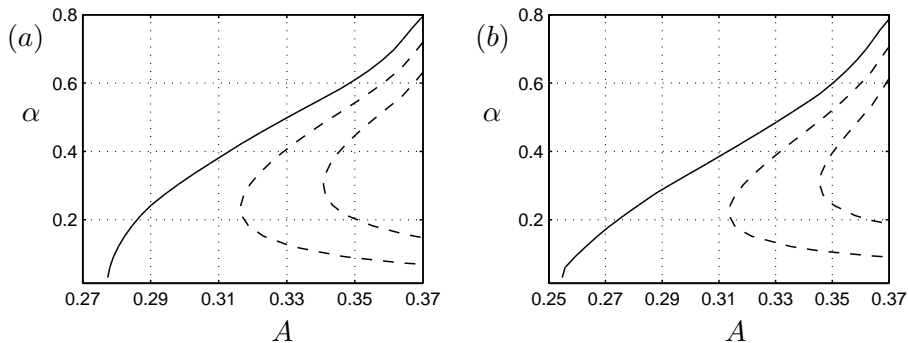


FIGURE 4.4. Neutral curves for streak instability in the (α, A) plane (solid line). The dashed lines represent contour levels of positive growth rates $\omega_i = 0.008$ and $\omega_i = 0.016$. The data have been made non-dimensional using the local Blasius length scale δ .

rates increase but their maxima are also shifted towards larger values of the wavenumber α . For values of A larger than 0.3 the fundamental symmetry has slightly larger growth rates. It is also found that in the case of the sinuous instability, the production of kinetic energy of the perturbation is entirely due to the work of the Reynolds stress $\tilde{\tau}_{uw}$ against the spanwise shear of the streak. The contribution from the term \tilde{T}_y , related to the wall-normal shear of the basic flow, is negative and about one order of magnitude smaller than its counterpart \tilde{T}_z .

No results are presented here on the varicose instabilities. In fact, the varicose modes result unstable only for amplitudes larger than $A = 0.37$, with growth rates smaller than one fifth of the corresponding sinuous growth rates. From the results presented, it seems more likely that the transition of the considered steady optimal streaks is triggered by a sinuous instability, either of fundamental or subharmonic type. The common feature of the two scenarios is the spanwise oscillation of the low-speed streak.

4.2.3. Spatio-temporal behaviour

The boundary layer flow is an *open flow*, i.e. the fluid particles are not recycled within the physical domain of interest but leave it in a finite time (see Huerre & Monkewitz 1990). Linearly unstable open flows can be classified according to the evolution of amplified perturbations in space and time into two distinct classes. To introduce this distinction, we consider the response of the system to an impulse in space and time $\delta(t)\delta(x)$. The flow is initially perturbed at $t = 0$ and $x = 0$ and left free to evolve. The solution to this problem represents the Green function $G(x, t)$ of the particular linear system under considerations and contains the information concerning the evolution of any disturbances. In

fact, the response to any forcing functions may be obtained by convolution of such forcing with the Green function.

In linearly unstable flows, two distinct asymptotic behaviours of the impulse response can be observed. The flow is said to be *linearly convectively* unstable if the amplified perturbations are convected away, downstream or upstream of the source, so that the perturbation ultimately decreases at any location and the flow returns to its basic state as $t \rightarrow \infty$. Conversely, a flow is said to be *linearly absolutely* unstable if the disturbance generated by the impulse spreads both upstream and downstream of the source and gradually contaminates the entire medium.

Formally, a given flow is convectively unstable if

$$\lim_{t \rightarrow \infty} G(x, t) = 0, \quad \text{along the ray } x/t = 0$$

and absolutely unstable if

$$\lim_{t \rightarrow \infty} G(x, t) = \infty, \quad \text{along the ray } x/t = 0.$$

In the case of parallel flows, that are invariant under Galileian transformations, this distinction seems to be related to the selected frame of reference: a simple change of reference frame may transform an absolutely unstable flow into a convectively unstable. However, in flows forced at a specific streamwise station x the Galileian invariance is broken and a 'laboratory frame' can be unambiguously defined. In these cases, the distinction between convective and absolute instability becomes of interest. Convectively unstable flows essentially behave as *noise amplifiers*: they are very sensitive to external perturbations. The characteristics of the latter determine, in fact, the type of waves amplifying in the flow. Absolutely unstable flows, on the contrary, display an intrinsic dynamics. They behave as *hydrodynamic oscillators*. The features of the perturbations amplifying in the flow are determined by the control parameters and do not depend on the external noise. The flow beats at a well-defined frequency independently on the frequency at which it is forced (see Huerre & Rossi 1998).

From the definitions above, it follows that the spatio-temporal analysis of a linearly unstable flow aims at computing the asymptotic temporal growth rates σ attained along rays $x/t = v$, that is the temporal growth rate perceived by an observer moving at velocity v . This is equivalent to the study in Fourier-Laplace space of modes of real *group velocity* v , as reviewed, for instance, in Huerre (2000). This analysis shows that the impulse response takes the form of a wave packet, the long time behaviour along each spatio-temporal ray being (Bers 1983)

$$q(x, t) \propto t^{-1/2} e^{i[\alpha^*(v)x - \omega^*(v)t]}, \quad t \rightarrow \infty$$

where α^* and ω^* represent the complex wavenumber and frequency observed moving at the velocity v . The temporal growth rate σ is defined by the real part of the exponential $\sigma = \omega_i^* - v \alpha_i^*$. In unstable flows, $\sigma > 0$ for some values of v and the curve $\sigma(v)$ completely defines the growth of the wave packet generated by the impulse. The wave packet extent is determined by the rays along which

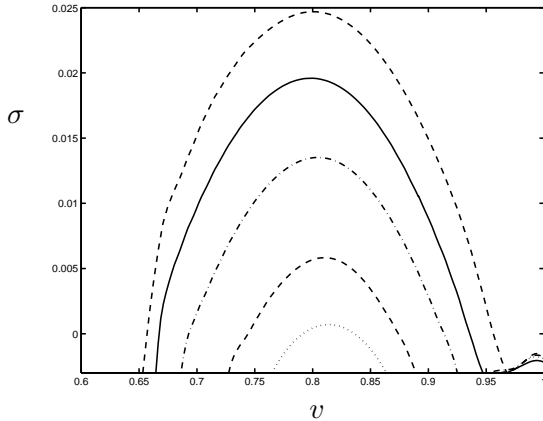


FIGURE 4.5. Temporal growth rate versus ray velocity $x/t = v$ for different increasing saturated streak amplitudes $A = 0.28, 0.31, 0.34, 0.36, 0.38$ at $X = 2$ computed for $Re = 610$. The solid line corresponds to the base flow at $A = 0.36$ depicted in figure 4.1 (b). The other curves correspond to scanning the vertical line $X = 2$ of unstable streaks in figure 4.1 (a).

neutral waves are observed, i.e. $\sigma(v) = 0$. These velocities are denoted v^- , the trailing edge velocity of the wave packet, and $v^+ > v^-$, the leading edge velocity of the wave packet. If $v^- > 0$, the wave packet is advected downstream and the base flow is convectively unstable. Conversely, if $v^- < 0$, the trailing edge moves upstream and the flow is absolutely unstable.

The study of the spatio-temporal instability of the steady saturated streaks introduced above, is presented in Paper 2. The analysis is performed in physical space and the instability characteristics are retrieved from the direct numerical simulations of the response of the flow to a localised disturbance. Note that, as a consequence of the numerical code used, the spatio-temporal instability is studied without the assumption of inviscid flow. As in the temporal stability analysis discussed in the previous section, the basic flow consists only of the streamwise velocity $U(y, z)$ and it is assumed parallel. Since such a basic flow is solution of the Euler equations, a body force $-Re^{-1}\Delta U(y, z)$ is implemented into the Navier-Stokes solver to compensate for diffusion and keep the flow steady and parallel. The procedure used to evaluate the temporal growth rates $\sigma(v)$ from the evolution of the wave packet riding on the streaks is described in detail in Paper 2 and references therein. In particular, the analysis performed here extends to the case of a three-dimensional periodic unidirectional flow the technique developed by Delbende, Chomaz & Huerre (1998) and Delbende & Chomaz (1998). The temporal growth rate curve of the fundamental sinuous mode versus group velocity is displayed in figure 4.5 for the unstable streak amplitudes at position $X = 2$ in figure 4.1(a). This diagram represents the

spatio-temporal analogue of the inviscid temporal growth rates reported in figure 4.4(a). It can be seen in figure 4.5 that the trailing edge velocity v^- is always positive and therefore it may be concluded that the instability is convective. The growth rates and the spreading rates $\Delta v = v^+ - v^-$ of the wave packet increase with the streak amplitude and the maximum growth σ occurs approximately at the group velocity $v = 0.8$ for all amplitudes.

It is interesting to note that the secondary streak instability is travelling at velocities higher than those of the Tollmien-Schlichting waves in the undisturbed Blasius boundary layer. In the latter case, in fact, the leading and trailing edge velocities of the wave packet are respectively $v^+ = 0.5$ and $v^- = 0.36$ at $Re = 580$ (see Gaster 1975; Gaster & Grant 1975), while sinuous instability waves have a trailing edge velocity of about 70% of the free-stream velocity. This difference is due to the fact that the two instabilities are driven by distinct physical mechanisms. The Tollmien-Schlichting instability is viscous in nature and its production is located in a low-velocity region close to the wall. The streak instability, instead, is inviscid in character and it is induced by the spanwise shear of the basic flow. It can be seen in figure 4.1(b) that the regions of largest spanwise shear are located further up in the boundary layer where the local streamwise velocities are large. Thus, the instability is produced in high-velocity regions and this can explain the values of the group velocities pertaining to the sinuous instability modes.

The sinuous streak instability is induced by the mean spanwise shear on the sides of the low-velocity region as in two-dimensional wakes past a bluff body. This similarity has been further confirmed by comparing the absolute/convective instability properties of the streak under consideration with the family of wake profiles introduced by Monkewitz (1988). It is shown in Paper 2 that the streak profile $U(y, z)$ may be approximately modelled by a two-dimensional wake profile $U(z)$, which is independent of the wall-normal coordinate, provided one selects the plane parallel to the wall corresponding to the maximum production of kinetic energy of the instability modes. As said before, this roughly corresponds to the location of maximum spanwise shear.

The convective nature of the secondary streak instability implies that the by-pass transition scenario considered here is noise-driven, i.e. the streaks behave as noise amplifiers in terms of the classification introduced above. As a consequence, transition prediction criteria cannot be only related to the control parameters but they need to depend on the level of external noise. From a theoretical point of view, the convective nature of the instability implies that a *spatial instability analysis* of the flow has a physical significance. The spatial analysis denotes the study of unstable modes of real frequency ω and complex wavenumber α . These represent time-periodic waves of amplitude amplified exponentially in the streamwise direction but constant in time at a fixed location. The study of the nonlinear stages following the spatial amplification of the fundamental sinuous instability mode are presented in the next section.

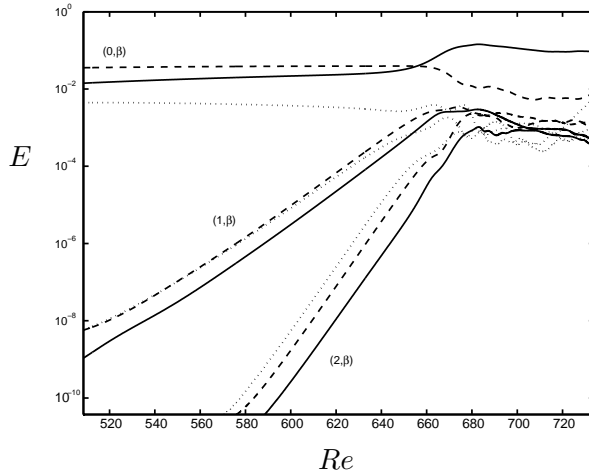


FIGURE 4.6. Energy in different Fourier modes (ω, β) versus the Reynolds number. Frequencies: zero (streaks), one (secondary instability), two (higher harmonic). —, $\beta = 0$; - - -, $\beta = 1$; \cdots , $\beta = 2$.

4.3. Streak breakdown

The full transition scenario resulting from the fundamental sinuous instability of the steady saturated streaks is presented in Paper 3. The saturated streaks and one of the instability modes of highest spatial growth rate are forced as inflow perturbation in the fringe region of the numerical code. The direct numerical simulation of the streak transition requires extensive computer resources since a turbulent flow is induced at the end of the computational domain and this needs to be fully resolved.

First, the perturbation velocity fields obtained at each streamwise station are transformed in time and in the spanwise direction to Fourier space. To present the results, the notation (ω, β) is used, where ω and β are the frequency and spanwise wavenumber each normalised with the fundamental frequency and wavenumber of the secondary instability mode. In the present analysis we therefore consider the amplitude of the spanwise Fourier components of the periodic eigenfunction $\tilde{q}(y, z)$ and of its harmonics in time. The downstream energy growth in some selected time and spanwise Fourier modes is displayed in figure 4.6. The zero-frequency mode, i.e. the streak, and the secondary instability ($\omega = 1$) are present at the beginning of the computation, while the higher harmonics ($\omega > 1$) are excited as the flow evolves downstream. Initially the growth is exponential with the growth rate of the first harmonic ($\omega = 2$) twice that of the fundamental mode and similarly, for higher frequencies, the growth rate is proportional to the harmonic order (not shown here, see Paper 3). This can be explained by the fact that the nonlinear interaction of

the fundamental mode $\tilde{q} \approx e^{i(\alpha x - \omega t)}$, the only time-dependent mode initially in the flow, with itself gives a forcing term of the type $\approx e^{i(2\alpha x - 2\omega t)}$. This introduces in the flow the frequency 2ω with associated spatial growth rate $2\alpha_i$, where α_i is the spatial growth rate of the fundamental instability. Thus, in general, the exponential behaviour at a frequency is given by the sum of the exponential of the modes whose interaction gives a contribution at the specific frequency considered. Hence, in the same way, the mode $\omega = 3$ is induced by the interaction of the modes $\omega = 1$ and $\omega = 2$ and it has a spatial growth rate that is about $3\alpha_i$. Thus, at these early stages in the transition process, nonlinear interactions become appreciable. However, one can note that the behaviour of the most energetic modes (the streak and the secondary instability) is hardly affected by the generation of the higher harmonics. The behaviours of these, in turn, can be explained simply by the interaction of modes of higher energy. This type of behaviour is usually referred to as *weakly nonlinear* and it accounts for the simplest type of nonlinear effects; the interaction between high energy modes induce new harmonics in the flow without affecting the interacting modes.

It can also be seen in figure 4.6 that the energy content is of the same order for modes of different spanwise wave numbers but same frequency. This is due to the fact that the streak develops to a highly nonlinear stage before it becomes unstable to time-dependent disturbances. Therefore the harmonics in β are generated during the streak growth and they are responsible for the large spanwise shear of the flow. The instability of the streaks is characterised by modes localised in the spanwise direction so that a number of spanwise wave numbers is needed to correctly capture it.

The growth in the different modes starts to saturate around position $Re = 650$ and soon the energy become of the same order for the different frequencies. From this point, the weakly nonlinear approximation is no longer valid. In fact, it can be noted in the figure how the energy in the $(0, 1)$ and $(0, 2)$ modes, representing the spanwise modulation of the flow, decreases by a factor of ten, which implies that the streak is disrupted. Conversely, the $(0, 0)$ perturbation mode is growing since the mean laminar velocity profile is approaching its turbulent counterpart. The late stages of the transition process, before the flow reaches a fully turbulent state, are then analysed in terms of large-scale flow structures.

Vortical structures can be identified in the flow by plotting regions of low pressure, or, alternatively, regions where the second largest eigenvalue λ_2 of the Hessian of the pressure assumes negative values (Jeong *et al.* 1997). Both quantities enable to locate regions of strong rotational fluid motion. A top and side view of the flow structures characteristic of the late stages of the sinuous streak breakdown are shown in figure 4.7. The dark gray isosurfaces represent low-pressure regions while the low-speed streak is depicted with lighter grey. The main structures observed consist of quasi streamwise vortices located on the flanks of the low-speed streak, which is oscillating in the spanwise direction.

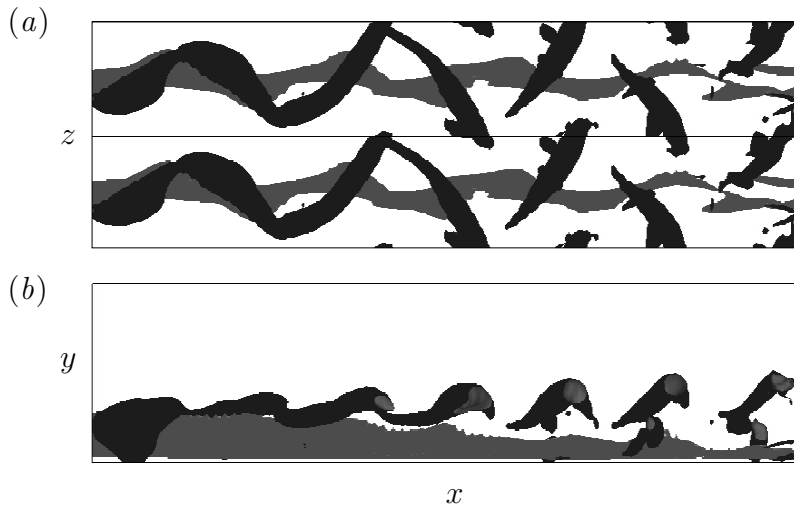


FIGURE 4.7. (a) Top and (b) side view of the structures at the late stages of transition. Lighter grey represents negative streamwise velocity perturbation and dark grey regions of low pressure. In (a) two spanwise streaks are displayed.

Vortices of alternating sign are overlapping in the streamwise direction in a staggered pattern and they are symmetric counterparts, both inclined away from the wall and tilted in the downstream direction toward the middle of the undisturbed low-speed region. The strength and extent of these vortices and the spanwise motion of the low-speed streak increase downstream. It is also evident from the top view that the downstream end of the streamwise vortices, located in the outer part of the boundary layer, is tilted in the spanwise direction to form arch vortices.

It is interesting to note that the single streamwise vortex observed in figure 4.7 show similarities to the leg of the Λ -structures seen in transition initiated by TS-waves (e.g. Rist & Fasel 1995; Bake, Meyer & Rist 2002) and in oblique transition (Berlin *et al.* 1999). In fact, in the latter scenarios, positive and negative streamwise vortices are also present on the side of the low-speed region but they are not staggered in the streamwise direction. Instead the left and right streamwise vortices join at the centre of the streak and form the typical Λ -structures. The different relative position of the streamwise vortices is found to depend on the symmetry of the streamwise vorticity of the secondary instability mode. In the present case, the vorticity disturbance is symmetric, while in oblique transition and TS-wave induced transition the streamwise vorticity is antisymmetric.

Note finally that the streamwise vortices and streaks are fundamental structures also in the near-wall region of turbulent boundary layers and the vortices seem to be related to streak instability. In fact, the structures identified as

typical of the transition of a laminar streak show important similarities with the streak instability observed in turbulent flows (Jeong *et al.* 1997; Schoppa & Hussain 2002; Jiménez & Pinelli 1999). On the other hand, the experiments of Acarlar & Smith (1987) and the related simulations of Skote *et al.* (2002) among others, show that the appearance of an unstable inflectional wall-normal velocity profile is a precursor to the formation of horseshoe vortices, thus associated to the varicose instability of near-wall streaks.

Transition in boundary layers subjected to free-stream turbulence

Flow visualisations and analogies with transition in vortex-dominated flows led to believe that transition in boundary layers subjected to free-stream turbulence proceeds via the breakdown of the streaks induced inside the boundary layer. This motivated the studies presented in the first part of the thesis, where the streak transition is analysed in the simpler case of a steady spanwise-periodic configuration. In this chapter, simulations of a boundary layer subjected to free-stream turbulence are presented, where a synthetic turbulent inflow is generated by the procedure outlined in chapter 3. The hypothesised scenario resulting from the previous studies will find partial confirmation and new relevant elements will arise. In particular, the present study is focused upon the receptivity stage and the final breakdown into turbulent spots.

5.1. Receptivity

The occurrence of streamwise elongated structures in boundary layers subject to free-stream turbulence was first identified by Klebanoff (1971) in terms of low-frequency oscillations in hot wire signals caused by slow spanwise motions of the streaks. However, the first theoretical explanations of this phenomenon were proposed about 25 years later. Bertolotti (1997) has assumed as initial disturbances vortical modes, solutions of the linearised Navier-Stokes equations in the free stream, which are waves periodic in the spanwise direction and decaying in the streamwise. He has found receptivity to modes with zero streamwise wavenumber and has shown that the streak growth is connected to the theories of non-modal growth. Essentially the same linear mechanism for streak generation caused by the diffusion of a free-stream streamwise vortex into the boundary layer has been studied by Andersson *et al.* (1999) and Luchini (2000) using the boundary layer approximation and by Wundrow & Goldstein (2001) by means of asymptotic expansions. These studies assume the presence of the vortex at the leading edge show that the growth of the streak amplitude is proportional to the Reynolds number Re .

Besides these linear models, Berlin & Henningson (1999) have proposed a nonlinear mechanism. Numerical simulations have in fact shown that oblique waves in the free stream can interact to generate streamwise vortices, which, in turn, induce streaks inside the boundary layer. The latter process is further

investigated in this thesis by means of a weakly nonlinear model based on a perturbation expansion of the disturbance truncated at second order. The perturbation equations are derived directly from the Navier-Stokes equations, superimposing a perturbation field to the base flow, the Blasius profile which is assumed parallel in the streamwise direction. A single equation is then obtained for each wavenumber pair (α, β) of the perturbation velocity field. The problem for the first order disturbance velocity and for the second order correction are both governed by the Orr-Sommerfeld and Squire operators. The solution for the first order perturbation velocity is induced by an external forcing of small amplitude ϵ . At second order, $O(\epsilon^2)$, the problem is forced by the nonlinear interaction of first order solutions with wavenumber pairs such that their combination is equal to the wavenumber of the mode under consideration. In particular, the long time response of the boundary layer to a couple of oblique modes of given frequency ω travelling in the free stream is studied. Oblique modes are associated to $(\alpha, \pm\beta)$ modes and their quadratic interactions produce perturbations of wavenumber $(0, \pm 2\beta)$, which correspond to streamwise elongated structures.

The results of this analysis are presented in Paper 6, where two types of free-stream perturbations are considered: the first case amounts to the receptivity to oblique waves generated by a wave-like external forcing term oscillating in the free-stream, the second the receptivity to free-stream turbulence-like disturbances, represented as superposition of modes of the continuous spectrum of the Orr-Sommerfeld and Squire operators. In both cases, the generation of a strong streamwise component of the disturbance in streamwise-independent modes is the dominant feature. The underlying mechanism can be reduced to a two-step process, first the nonlinear generation of streamwise vorticity forced by the interactions between disturbances in the free stream and then the formation of streaks by the linear lift-up effect. An interesting result is that the importance of the two steps in the receptivity process is comparable. In fact, the analysis of the equations derived applying the weakly nonlinear approach shows that an amplification of $O(Re)$ occurs both for the generation of the streamwise vortices and, afterwards, for the formation of streaks. Thus, the streak growth is of order $O(Re^2)$. Recall, however, that the nonlinear mechanism assumes a forcing of amplitude ϵ^2 , i.e. quadratic in the amplitude of the free-stream disturbances, in comparison with the stronger direct forcing of amplitude ϵ of the linear receptivity models cited above.

The two mechanisms are compared by means of DNS to try to identify which of the two can be considered as the most relevant in cases with known free-stream perturbations. In order to do so different levels of free-stream turbulence intensity are considered and, moreover, the free-stream turbulence generation is manipulated in order to involve few or many modes with very low values of the frequency ω . In this way, we are able to control the amount of low-frequency perturbation part of the inflow turbulence. As shown by Hultgren & Gustavsson (1981) among others, modes of the continuous spectra with very

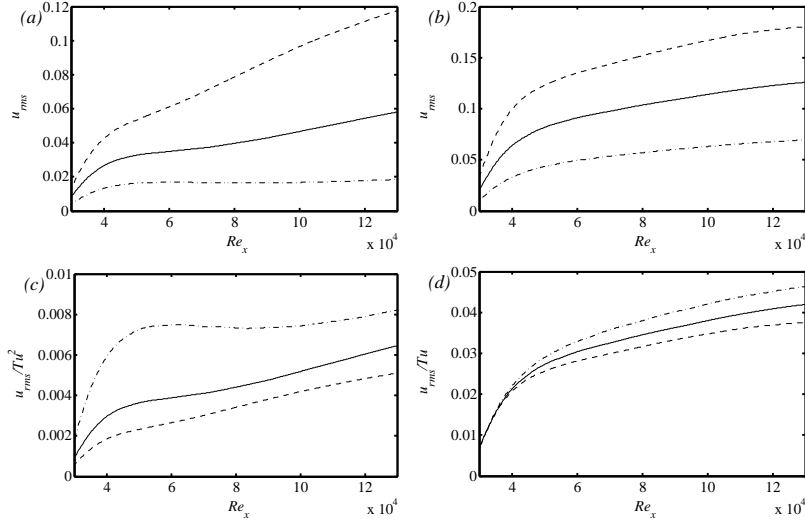


FIGURE 5.1. Streamwise evolution of the wall-normal maximum of u_{rms} for three levels of free-stream turbulence intensity: ---, $Tu = 4.7\%$; —, $Tu = 3\%$ and - · -, $Tu = 1.5\%$. The results in (a) pertain to the case of few low-frequency modes as part of the inflow perturbation spectrum, while the data in (b) to a free-stream turbulence spectrum rich with low-frequency modes. (c): The same rms -values as in (a) are scaled with the square of the free-stream turbulence intensity Tu . (d): The same rms -values as in (b) are scaled with the free-stream turbulence intensity Tu .

low values of α and ω do not feel the shear layer and they are therefore not zero inside the boundary layer.

The wall-normal maximum of the streamwise velocity perturbation induced inside the boundary layer is displayed in figure 5.1 versus the local Reynolds number for six cases considered. The results in figure 5.1(a) pertain to three different free-stream turbulence levels, $Tu = 4.7\%$, $Tu = 3\%$ and $Tu = 1.5\%$, with integral length scale $L = 7.5\delta_0^*$, where δ_0^* is the boundary-layer displacement thickness at the inlet of the computational domain ($Re_{\delta_0^*} = 300$). For all cases only few modes characterised by low frequency are introduced as part of the inflow perturbation spectrum. It is shown in figure 5.1(c) that by dividing the u_{rms} values in figure 5.1(a) with the square of the turbulence intensity Tu , the growth of the perturbation follows, after an initial phase, almost parallel lines. This is more evident in the case of largest intensities. Therefore the dominating receptivity mechanism is the nonlinear one (see Paper 7 for more details). The results in figure 5.1(b) pertain to cases with the same free-stream turbulence levels and integral length scale, but this time the perturbation spectrum is

characterised by many low-frequency modes, as shown by the high u_{rms} -values already at the inlet of the computational domain. In this case, the streaks formed in the boundary layer further downstream are stronger than before; the u_{rms} scales linearly with the perturbation intensity Tu (see figure 5.1d) and the receptivity mechanism responsible for the streak growth is the linear one. From the results in the figure it is possible to conclude that the linear mechanism is the most relevant if the free-stream turbulence contains significant low-frequency modes.

5.2. Effect of the integral length scales of the free-stream turbulence

Simulations have then been performed to follow the subsequent breakdown and transition to turbulence. Results are presented for three cases. In all of them the inlet of the computational box is at $Re_{\delta_0^*} = 300$ ($Re_{x_0} = 30000$) and the free-stream turbulence intensity is 4.7%. Different integral length scales of the inflow turbulence have been used, that is $L = 2.5\delta_0^*$, $L = 5\delta_0^*$ and $L = 7.5\delta_0^*$ where L is related to the longitudinal two-point correlation as $L_{11} = 0.643L$.

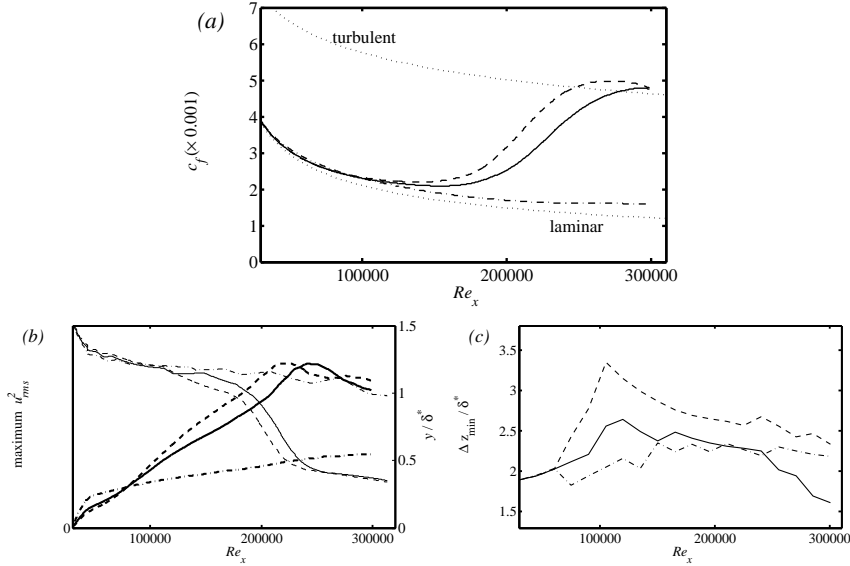


FIGURE 5.2. (a) Skin friction coefficient, (b) maximum u_{rms}^2 (thick lines) and its wall-normal position (thin lines), and (c) first minimum of the spanwise correlation of the streamwise velocity fluctuations scaled with the local displacement thickness δ^* ; plotted for $L = 7.5\delta_0^*$ (dashed line), $L = 5\delta_0^*$ (solid line) and $L = 2.5\delta_0^*$ (dash-dotted line).

Some of the data obtained by averaging in time and in the spanwise direction are displayed in figure 5.2. The friction coefficient is shown in figure 5.2(a); also the values for a laminar and a turbulent boundary layer are displayed for comparison. For the case with the smallest integral length scale transition does not occur within the computational domain, while the transition location is at lower Re_x for $L = 7.5\delta_0^*$, in agreement with the experimental findings in Jonáš *et al.* (2000). In figure 5.2(b) the maximum u_{rms}^2 at each downstream position is depicted to show the evolution of the streaks. In all cases the energy of the streaks is proportional to the distance from the leading edge, as observed in the experiments, and the growth is initially largest in the case of $L = 2.5\delta_0^*$, indicating that the smallest scales penetrate easier into the boundary layer. However, this growth can not be sustained as in the other cases. In fact, the free-stream turbulence decays faster for smaller L and therefore it is less effective in continuously forcing the streaks along the plate. In figure 5.2(a) the wall-normal position of maximum u_{rms} is also shown. This is reported in units of δ^* , the local boundary-layer displacement thickness. The laminar streaks have a maximum at about $y = 1.3\delta^*$, while their turbulent counterparts are located much closer to the wall. In figure 5.2(c) one can see the evolution of the first minimum of the spanwise correlation of the streamwise velocity fluctuations at the wall normal position of maximum u_{rms} ; this is a measure of half the spanwise wavelength of the streaks. It can be seen from the figure that the length scale of the perturbation inside the boundary layer is only slightly dependent on the free-stream turbulence characteristic scale. The spanwise scales observed are in agreement with the prediction of optimal amplification (Andersson *et al.* 1999).

5.3. Turbulent spot generation

A snapshot of the flow is shown in figure 5.3 where the instantaneous streamwise and spanwise velocities are plotted in a plane parallel to the wall. The overall picture of the transition scenario can be deduced from the figure. Starting from the inlet position, the perturbation in the boundary layer appears mainly in the streamwise velocity component, in the form of elongated structures. Patches of irregular motion are seen to appear further downstream; these are more evident in the spanwise component, otherwise very weak in the streaky boundary layer. As they travel downstream, the spots become wider and longer. Note also that laminar streaks can be observed downstream of the spots. The turbulent region at the end of the domain is created by the enlargement and merging of the various spots and therefore the streamwise position at which the flow is turbulent varies with time; the turbulent flow is convected downstream and it would not be seen if new spots were not formed all the time.

The breakdown is analysed in detail by looking at the instantaneous three-dimensional flow configurations for a number of spots, tracing back in time the location of their formation. An important feature of the spot precursors, observed in all cases considered, is the presence of regions of positive and negative wall-normal and spanwise velocity arranged in a quasi-periodic array. Such

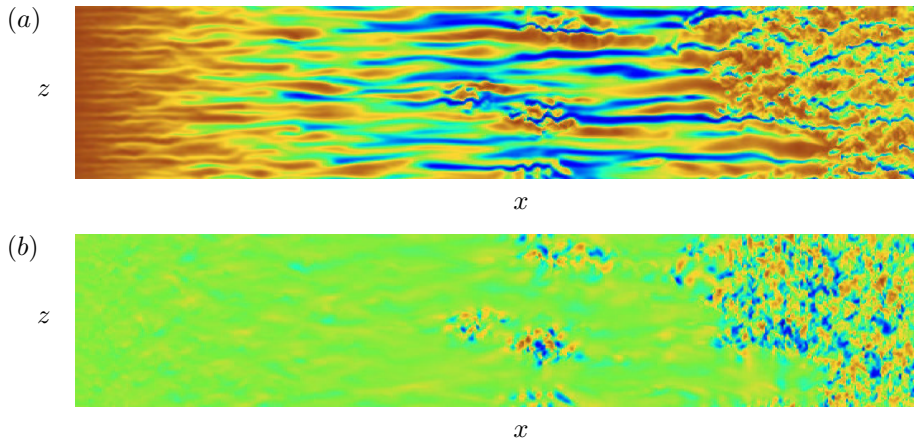


FIGURE 5.3. (a) Instantaneous streamwise velocity and (b) spanwise velocity (bottom figure) in a plane parallel to the wall at $y/\delta_0^* = 2$. The plots are not at the actual scale since the domain depicted is 900 units long and 90 units wide in terms of δ_0^* . The fringe region is not shown.

quasi regular distribution of the cross-stream velocity components is responsible for the observed wavy motions of the streaks preceding the breakdown. Visual inspection of many velocity fields enabled to classify the type of breakdown occurring on the streaks by considering the spanwise symmetry of the wall-normal and spanwise velocities and their position relative to the underlying streak.

The flow structures at the incipient spot stage resemble very much those observed in previous study on the breakdown of steady symmetric streaks, both in the case of the scenario following a sinuous instability (see Paper 3 in this thesis) and in the case of a varicose scenario (see the experiments by Asai *et al.* 2002). The similarity with either of the two cases is observed in all spots under consideration.

In the case of the sinuous breakdown, a single low-speed streak undergoes spanwise antisymmetric oscillations, with strong high-frequency perturbation velocity located in the region of largest spanwise shear between the low- and high-speed streaks. An instantaneous flow configuration for this type of scenario is displayed in figure 5.4. The characteristic vortical structures, represented in green by negative values of the eigenvalue λ_2 , consist of quasi-streamwise vortices located on the flanks of the low-speed streak (depicted here in blue colour). Vortices of alternating sign are overlapping in the streamwise direction in a staggered pattern, exactly as observed in figure 4.7 for the breakdown of a periodic array of steady streaks.

In the case of varicose or symmetric breakdown the oscillations of the streaks are driven by the wall-normal shear and the transition scenario is characterised by the appearance of horse-shoe or hairpin structures. An example of such vortical structures is displayed in figure 5.5. One can note the formation of hairpin vortices, with pairs of counter-rotating quasi-streamwise vortices joining in the middle of the streak, pointing alternatively upstream and downstream. The streaks generated by free-stream turbulence are obviously not symmetric and the perturbations riding on them are not symmetric either; however the velocity components of the high-frequency oscillations show almost the same pattern with respect to the mean shear of the streaks as in the model studies mentioned above. In particular, for the 'quasi-sinusoidal' breakdown, it is observed that, for a significant number of spots considered, only streamwise vortices of same sign are clearly identified on one flank of the low-speed region. In these cases, in fact, the spanwise shear is sufficiently high only on one side of the low-speed streak.

From the analysis of flow visualisations and animations, it is further noticed how the interaction between low- and high-speed streaks plays an important role for the formation of incipient spots. It can be seen in figure 5.5, for example, how the interaction of the low-speed streak with a fast-moving incoming region of high streamwise velocity is the triggering cause of the instability leading to the formation of the hairpin vortices. It is observed in experiments (Lundell & Alfredsson 2003) that the streaks are tilted downstream so as the front part is located in the upper part of the boundary layer whereas the rear part is located closer to the wall. Such a structure is growing in the streamwise direction while convected downstream. As a consequence, highly inflectional wall-normal velocity profiles are induced by the high-speed region when reaching the tail of the low-speed region ahead, which thus becomes the site of a local instability. Similarly, the antisymmetric type of breakdown is induced whenever high-speed fluid is approaching a low-speed region on a side. In this case, an inflectional profile is forming in the spanwise direction (see figure 5.4). Note also that the streaks are not perfectly aligned in the streamwise direction but they slowly oscillates in the boundary layer.

It is finally important to note that the antisymmetric sinusoidal breakdown is found to be the most likely to occur; it is observed in 16 of the 28 spots considered. From the results presented one may conclude that the breakdown is related to local instabilities associated to the strong shear of the streaks; the fact that almost identical structures are observed in the case of transition induced by free-stream turbulence and in the previous model studies on streaks leads to believe that the relevant physics has correctly been captured by these studies on the breakdown of steady symmetric streaks.

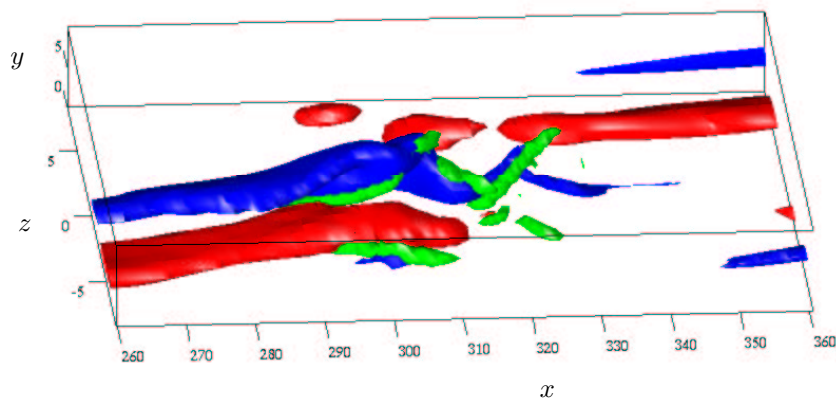


FIGURE 5.4. Instantaneous flow configuration at the breakdown of a streamwise streak. Red represents positive perturbation streamwise velocity, while blue indicates the low-speed streak. The green structures are regions of negative λ_2 , used to identify vortical structures.

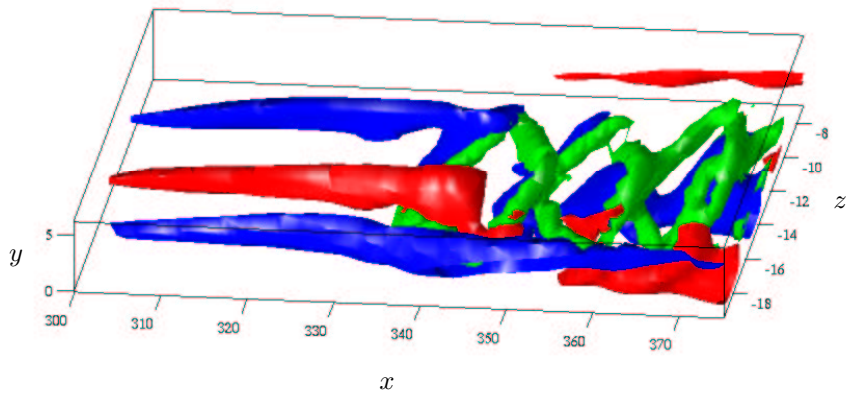


FIGURE 5.5. Instantaneous flow configuration at the breakdown of a streamwise streak. Red represents positive perturbation streamwise velocity, while blue indicates the low-speed streak. The green structures are regions of negative λ_2 , used to identify vortical structures.

Conclusions and outlook

The investigations presented in this thesis are motivated by the need to understand bypass transition in boundary layers with high levels of free-stream turbulence. The overall picture of the transition scenario has been elucidated by flow visualisations and velocity measurements in previous experimental studies (see the review articles by Kendall 1998; Matsubara & Alfredsson 2001; Saric *et al.* 2002). However, some important issues still remain unclear and have been the object of the present work. These concern the receptivity stage, during which perturbations enter the boundary layer, and the mechanisms of the breakdown into turbulent spots occurring on isolated streaks.

The phenomena under consideration occur randomly in a boundary layer subject to free-stream turbulence and are characterised by a high degree of intermittency. Therefore, they have first been analysed in detail using simpler flow configurations and known repeatable disturbances. In particular, a weakly nonlinear model for the receptivity of a parallel boundary layer to free-stream disturbances has been developed. This model provided an efficient tool to disentangle the sequence of events in the receptivity process. This amounts to be a two-step process: the generation of streamwise vortices due to the nonlinear interactions of oblique waves in the free stream, and the formation of streaks by the linear lift-up effect.

The streak instability and breakdown have been studied by considering spanwise-periodic perturbations resulting from the nonlinear saturation of the optimal upstream perturbations computed by Andersson *et al.* (1999) for a non parallel zero-pressure-gradient boundary layer. The perturbations considered are steady and optimal only in the linear sense and therefore they represent one of several plausible approximations of the streaks observed in boundary layers subject to relatively high free-stream turbulence levels. However, the wall-normal shape of the linearly optimal disturbance theoretically determined by Andersson *et al.* (1999) and Luchini (2000) is found to be remarkably similar to the measured u_{rms} values (Matsubara & Alfredsson 2001). The streak can be regarded, in fact, as a 'pseudo-mode' triggered in a boundary layer subject to significant outside disturbances.

The instability of the boundary layer flow perturbed by such streaks has been studied both in the inviscid approximation and considering the effect of viscosity. A viscous analysis is required to assess the effect of low-amplitude streaks on the viscous exponential instability of the undisturbed Blasius profile.

It is found that the two-dimensional TS-waves evolve into three-dimensional spanwise-periodic viscous instability modes which are damped by increasing the streak amplitude. Above a certain threshold these waves are quenched and the boundary layer is thus stable at intermediate streak amplitudes (of the order of 20% of the free-stream velocity). However, sinuous antisymmetric perturbations are found to become unstable when further increasing the streak amplitude. This instability is of completely different nature, it is in fact of inflectional type and is driven by the spanwise shear of the basic flow. Moreover, this instability is convective with the most unstable waves travelling downstream at relatively high velocities (of about 80% of the free-stream velocity). It is also shown that the sinuous instability can lead the flow directly into the turbulent state, the transition scenario being characterised by the appearance of quasi-streamwise vortices alternating in the streamwise direction in a staggered pattern.

Extensive numerical simulations of a boundary layer subjected to free-stream turbulence have then been performed also to confirm the mechanisms predicted by the previous studies. The simulation of a fully transitional boundary layer is a formidable task also for the modern supercomputers and therefore one cannot hope to reproduce as rich parametric studies as in experimental works. However, it is possible to correctly reproduce the main features of the transition scenario under consideration (see Jacobs & Durbin 2001) and, as a consequence, simulations can be designed to investigate specific problems, thus exploiting the advantages of a numerical study. An obvious advantage of numerical simulations is that, once the flow has been simulated, all variables, including those difficult to obtain experimentally, are accessible to observation at the same instant. This enabled us to identify the relevant flow structures at the breakdown, which is not possible in an experiment due to the random nature of the spot appearance.

The structures at the breakdown are found to be very similar to those observed in previous model studies on the breakdown of steady streaks, both for the sinuous symmetry, which resulted the most likely to occur, and for the varicose symmetry (see Asai *et al.* 2002, for a recent experimental investigation). Hence, one can assume that the relevant physics has correctly been captured by these studies on the breakdown of steady symmetric streaks.

Further, the numerical methodology used allows to determine and manipulate the energy content of the turbulent inflow. In this way, it has been possible to investigate the receptivity mechanism and the effect of the characteristic length scale of the free-stream turbulence. The relevance of the nonlinear receptivity mechanism proposed could be verified and compared with the linear receptivity process presented in previous studies (Bertolotti 1997; Andersson *et al.* 1999; Luchini 2000).

The direct numerical simulations have also shown the importance of elements not considered in the model studies. Probably the most important concerns the interaction between the low- and high-speed streaks, which is

seen to be the main triggering mechanism of the streak instability. The relevance of such interactions was first suggested by Johansson, Alfredsson & Kim (1991) and Landahl (1990) for the case of near-wall turbulent streaks. This could be the object of future investigations, for example assuming simpler and repeatable initial conditions.

The physical understanding of transition in boundary layers under free-stream turbulence can be used to implement future control strategies. The first experimental studies show that it is possible to reduce the streak growth (Lundell 2003); however, the design of a control system, which is able to detect the presence of dangerous situation and decide when to act, needs to be improved. In the light of the observation above, a successful control strategy may aim at reducing the streak interaction and can be based on the detection of the relative position between streaks (through the gradients of the streamwise velocity), rather than on their presence or amplitude.

It is also important to note that the similarity between the wall-layer streaks in turbulent boundary and their instability (Jiménez & Pinelli 1999; Schoppa & Hussain 2002) and the structure observed in transitional boundary layers. One can speculate that the near-wall streamwise vortices and streaks are driven by the turbulence in the outer part of the boundary layer in the same way laminar streaks are induced by the free-stream turbulence. As a consequence, the receptivity stage becomes an important ingredient of the regeneration cycle of near-wall turbulence, together with the streak formation by the linear lift-up effect and the streak breakdown.

Acknowledgment

First of all I would like to thank Prof. Dan Henningson which made this not only possible but also enjoyable. Freedom, support, encouragement, guidance and optimism are indispensable ingredients for any scientific endeavour and he has spared none of them.

I want to acknowledge all the people at LadHyX for the warm hospitality during the six months I had the possibility to spend in Paris. Special thanks to Patrick Huerre and Jean-Marc Chomaz who greatly assisted me when learning about the absolute instability and to Carlo Cossu.

I also want to thank all the people I worked with during these years: Paul Andersson, Alessandro Bottaro, Donatella Ponziani and Philipp Schlatter; I surely learned from all of them.

People at the Department provided a nice and friendly atmosphere and I learn to enjoy innebandy and other swedish specialties very much. I would like to thank all the teachers I had during my years at KTH: Arne Johansson, Henrik Alfredsson, Gustav Amberg, Tony Burden, Anders Dahlkild and Lars Söderholm. I also want to name some of my friends and colleagues in Stockholm: Janne Pralits, my swedish room-mates Markus Högberg and Martin Skote, Astrid Herbst, Ori Levin, Jerome Hoepffner, Arnim Brüger, Björn Lindgren, Gustaf Mårtensson, Jens Fransson, Kristian Granne Angele, June Shiomi, Fredrik Lundell, Davide Medici, Roland Wyberg, Luca Facciolo.

Several friends have contributed to make these Swedish years even more enjoyable: Marco, Claudio, Gianantonio, Francois, Alessandro, Karin, Barbara, Cecilia, Roberto, Dick, Francesca and Torkel, Alessandra and Alessandro, Davide and Lena, Rosanna and Flavio, Matteo Luca, the Rissne Slow Motion football team, the volleyball team and Hemsparkat innebandy lag.

Grazie ai miei familiari per esserci stati vicini in questi anni.

Tack Giulia, för all din kärlek, ditt stöd, tålmod och hjälp.

Bibliography

- ACARLAR, M. S. & SMITH, C. R. 1987 A study of hairpin vortices in a laminar boundary layer. Part 2. Hairpin vortices generated by fluid injection. *J. Fluid Mech.* **175**, 43–68.
- ANDERSSON, P., BERGGREN, M. & HENNINGSON, D. S. 1999 Optimal disturbances and bypass transition in boundary layers. *Phys. Fluids* **11**, 134–150.
- ARNAL, D. & JUILLEN, J. C. 1978 Contribution expérimentale à l'étude de la reptivité d'une couche limite laminaire à la turbulence de l'écoulement général. Rapport Technique 1/5018. ONERA.
- ASAI, M., MINAGAWA, M. & NISHIOKA, M. 2002 The instability and breakdown of a near-wall low-speed streak. *J. Fluid Mech.* **455**, 289–314.
- BAKCHINOV, A. A., GREK, G. R., KLINGMANN, B. G. B. & KOZLOV, V. V. 1995 Transition experiments in a boundary layer with embedded streamwise vortices. *Phys. Fluids* **7**, 820–832.
- BAKE, S., MEYER, D. G. W. & RIST, U. 2002 Turbulence mechanism in Klebanoff-transition: a quantitative comparison of experiment and direct numerical simulation. *J. Fluid Mech.* (459), 217–243.
- BERLIN, S. & HENNINGSON, D. S. 1999 A nonlinear mechanism for receptivity of free-stream disturbances. *Phys. Fluids* **11** (12), 3749–3760.
- BERLIN, S., WIEGEL, M. & HENNINGSON, D. S. 1999 Numerical and experimental investigations of oblique boundary layer transition. *J. Fluid Mech.* **393**, 23–57.
- BERS, A. 1983 Space-time evolution of plasma instabilities – absolute and convective. In *Handbook of Plasma Physics* (ed. M. N. Rosenbluth & R. Z. Sagdeev), , vol. 1, pp. 451–517. North-Holland.
- BERTOLOTTI, F. P. 1997 Response of the blasius boundary layer to free-stream vorticity. *Phys. Fluids* **9** (8), 2286–2299.
- BERTOLOTTI, F. P., HERBERT, T. & SPALART, P. R. 1992 Linear and nonlinear stability of the Blasius boundary layer. *J. Fluid Mech.* **242**, 441–474.
- BOIKO, A. V., WESTIN, K. J. A., KLINGMANN, B. G. B., KOZLOV, V. V. & ALFREDSSON, P. H. 1994 Experiments in a boundary layer subjected to free stream turbulence. part 2. the role of TS-waves in the transition process. *J. Fluid Mech.* **281**, 219–245.
- BOTTARO, A. & KLINGMANN, B. G. B. 1996 On the linear breakdown of Görtler vortices. *Eur. J. Mech. B/Fluids* **15**, 301–330.

- DELBENDE, I. & CHOMAZ, J.-M. 1998 Nonlinear convective/absolute instabilities of parallel two-dimensional wakes. *Physics of Fluids* **10**, 2724–2736.
- DELBENDE, I., CHOMAZ, J.-M. & HUERRE, P. 1998 Absolute and convective instabilities in the Batchelor vortex: a numerical study of the linear impulse response. *Journal of Fluid Mech.* **355**, 229–254.
- DRAZIN, P. & REID, W. 1981 *Hydrodynamic Stability*. Cambridge Univ. Press.
- ELLINGSEN, T. & PALM, E. 1975 Stability of linear flow. *Phys. Fluids* **18**, 487–488.
- ELOFSSON, P. A., KAWAKAMI, M. & ALFREDSSON, P. H. 1999 Experiments on the stability of streamwise streaks in plane Poiseuille flow. *Phys. Fluids* **11**, 915–930.
- FASEL, H. & KONZELMAN, U. 1990 Non-parallel stability of flat-plate boundary layer using the complete Navier-Stokes equations. *J. Fluid Mech.* **221**, 311–347.
- GASTER, M. 1975 A theoretical model of a wave packet in a boundary layer over a flat plate. *Proc. R. Soc. London, Ser. A* **347**, 271–289.
- GASTER, M. & GRANT, I. 1975 An experimental investigation of the formation and development of a wave packet in a laminar boundary layer. *Proc. R. Soc. London, Ser. A* **347**, 253–269.
- GROSCHE, C. E. & SALWEN, H. 1978 The continuous spectrum of the Orr-Sommerfeld equation. Part 1. The spectrum and the eigenfunctions. *J. Fluid Mech.* **87**, 33–54.
- HALL, P. & HORSEMAN, N. J. 1991 The linear inviscid secondary instability of longitudinal vortex structures in boundary-layers. *J. Fluid Mech.* **232**, 357–375.
- HENNINGSON, D. S. 1987 Stability of parallel inviscid shear flow with mean spanwise variation. Tech. Report FFA-TN 1987-57. Aeronautical Research Institute of Sweden, Bromma.
- HERBERT, T. 1983 Secondary instability of plane channel flow to subharmonic three-dimensional disturbances. *Phys. Fluids* **26**, 871–874.
- HERBERT, T. & BERTOLOTTI, F. P. 1987 Stability analysis of non parallel boundary layers. *Bull. Am. Phys. Soc.* **32**, 2079.
- HUERRE, P. 2000 Open shear flow instabilities. In *Perspectives in Fluid Dynamics* (ed. G. K. Batchelor, H. K. Moffatt & M. G. Worster), pp. 159–229. Cambridge University Press.
- HUERRE, P. & MONKEWITZ, P. A. 1990 Local and global instabilities in spatially developing flows. *Annu. Rev. Fluid Mech.* **22**, 473–537.
- HUERRE, P. & ROSSI, M. 1998 Hydrodynamic instabilities in open flows. In *Hydrodynamic and Nonlinear Instabilities* (ed. C. Godrèche & P. Manneville), pp. 81–294. Cambridge University Press.
- HULTGREN, L. S. & GUSTAVSSON, L. H. 1981 Algebraic growth of disturbances in a laminar boundary layer. *Phys. Fluids* **24** (6), 1000–1004.
- JACOBS, R. J. & DURBIN, P. A. 2001 Simulations of bypass transition. *J. Fluid Mech.* **428**, 185–212.
- JEONG, J., HUSSAIN, F., SCHOPPA, W. & KIM, J. 1997 Coherent structures near the wall in a turbulent channel flow. *J. Fluid Mech.* **332**, 185–214.
- JIMÉNEZ, J. & PINELLI, A. 1999 The autonomous cycle of near wall turbulence. *J. Fluid Mech.* **389**, 335–359.
- JOHANSSON, A. V., ALFREDSSON, P. H. & KIM, J. 1991 Evolution and dynamics of shear-layer structures in near-wall turbulence. *J. Fluid Mech.* **224**, 579–599.
- JONÁŠ, P., MAZUR, O. & URUBA, V. 2000 On the receptivity of the by-pass transition

- to the length scale of the outer stream turbulence. *Eur. J. Mech. B/Fluids* **19**, 707–722.
- KACHANOV, Y. S., KOZLOV, V. V. & LEVCHENKO, V. Y. 1977 Nonlinear development of a wave in a boundary layer. *Izv. Akad. Nauk SSSR Mekh. Zhid. Gaza* **3**, 49–58, in Russian.
- KACHANOV, Y. S. & TARARYKIN, O. I. 1987 Experimental investigation of a relaxing boundary layer. *Izv. SO AN SSSR, Ser. Tech. Nauk* **18**.
- KENDALL, J. M. 1985 Experimental study of disturbances produced in a pre-transitional laminar boundary layer by weak free-stream turbulence. *AIAA Paper* **85**, 1695.
- KENDALL, J. M. 1998 Experiments on boundary layer receptivity to free-stream turbulence. *AIAA Paper* (98-0530).
- KIM, J., MOIN, P. & MOSER, R. 1987 Turbulence statistics in fully developed channel flow. *J. Fluid Mech.* **177**, 133–166.
- KLEBANOFF, P. S. 1971 Effect of free-stream turbulence on the laminar boundary layer. *Bull. Am. Phys. Soc.* **10**, 1323.
- KLEBANOFF, P. S., TIDSTROM, K. D. & SARGENT, L. M. 1962 The three-dimensional nature of boundary layer instability. *J. Fluid Mech.* **12**, 1–34.
- KLINGMANN, B. G. B., BOIKO, A., WESTIN, K. J. A., KOZLOV, V. V. & ALFREDSSON, P. H. 1993 Experiments on the stability of Tollmien-Schlichting waves. *Eur. J. Mech. B/Fluids* **12**, 493–514.
- KREISS, H.-O. & OLIGER, J. 1972 Comparison of accurate methods for the integration of hyperbolic equations. *Tellus* **XXIV**, 199–215.
- LANDAHL, M. T. 1975 Wave breakdown and turbulence. *SIAM J. Appl. Maths* **28**, 735–756.
- LANDAHL, M. T. 1990 On sublayer streaks. *J. Fluid Mech.* **212**, 593–614.
- LUCHINI, P. 2000 Reynolds-number independent instability of the boundary layer over a flat surface. Part 2: Optimal perturbations. *J. Fluid Mech.* **404**, 289–309.
- LUNDBLADH, A., BERLIN, S., SKOTE, M., HILDINGS, C., CHOI, J., KIM, J. & HENNINGSON, D. S. 1999 An efficient spectral method for simulation of incompressible flow over a flat plate. Technical Report KTH/MEK/TR-99/11-SE. KTH, Department of Mechanics, Stockholm.
- LUNDELL, F. 2003 Experimental studies of bypass transition and its control. PhD thesis, Royal Institute of Technology, Stockholm, Sweden.
- LUNDELL, F. & ALFREDSSON, P. H. 2003 Streamwise scaling of streaks in laminar boundary layers subjected to free-stream turbulence. *J. Fluid. Mech.* Submitted for publication.
- MALIK, M. R., ZANG, T. A. & HUSSAINI, M. Y. 1985 A spectral collocation method for the Navier-Stokes equations. *J. Comp. Phys.* **61**, 64–88.
- MATSUBARA, M. & ALFREDSSON, P. H. 2001 Disturbance growth in boundary layers subjected to free stream turbulence. *J. Fluid. Mech.* **430**, 149–168.
- MONKEWITZ, P. 1988 The absolute and convective nature of instability in two-dimensional wakes at low Reynolds numbers. *Phys. Fluids* **31** (5), 999–1006.
- MORKOVIN, M. V. 1969 The many faces of transition. In *Viscous Drag Reduction* (ed. C. S. Wells). Plenum Press.
- NAYFEH, A. H. & MOOK, D. T. 1979 *Nonlinear oscillations*. Wiley-Interscience.
- NORDSTRÖM, J., NORDIN, N. & HENNINGSON, D. S. 1999 The fringe region technique

- and the Fourier method used in the direct numerical simulation of spatially evolving viscous flows. *SIAM J. Sci. Comp.* **20**, 1365–1393.
- ORR, W. M. F. 1907 The stability or instability of the steady motions of a perfect liquid and of a viscous liquid. Part I: A perfect liquid. Part II: A viscous liquid. *Proc. R. Irish Acad. A* **27**, 9–138.
- ORSZAG, S. A. 1972 Comparison of pseudospectral and spectral approximations. *Stud. Appl. Math.* **51**, 253–259.
- ORSZAG, S. A. & PATERA, A. T. 1983 Secondary instability of wall-bounded shear flows. *J. Fluid Mech.* **128**, 347–385.
- PARK, D. S. & HUERRE, P. 1995 Primary and secondary instabilities of the asymptotic suction boundary layer on a curved plate. *J. Fluid Mech.* **283**, 249–272.
- RAYLEIGH, L. 1880 On the stability of certain fluid motions. *Proc. Math. Soc. Lond.* **11**, 57–70.
- REDDY, S. C., SCHMID, P. J., BAGGETT, J. S. & HENNINGSON, D. S. 1998 On the stability of streamwise streaks and transition thresholds in plane channel flows. *J. Fluid Mech.* **365**, 269–303.
- RIST, U. & FASEL, H. 1995 Direct numerical simulation of controlled transition in a flat-plate boundary layer. *J. Fluid Mech.* **298**, 211–248.
- ROGALLO, R. S. 1981 Numerical experiments in homogeneous turbulence. *Tech. Rep. Tech. Memo. 81315*. NASA.
- SARIC, W. S., REED, H. L. & KERSCHEN, E. J. 2002 Boundary-layer receptivity to freestream disturbances. *Annu. Rev. Fluid Mech.* **34**, 291–319.
- SCHLICHTING, H. 1933 Berechnung der anfängung kleiner störungen bei der plattenströmung. *ZAMM* **13**, 171–174.
- SCHMID, P. J. & HENNINGSON, D. S. 2001 *Stability and Transition in Shear Flows*. New York: Springer.
- SCHOPPA, W. & HUSSAIN, F. 2002 Coherent structure generation in near-wall turbulence. *J. Fluid Mech.* **453**, 57–108.
- SCHUBAUER, G. B. & SKRAMSTAD, H. F. 1947 Laminar boundary layer oscillations and the stability of laminar flow. *J. Aero. Sci.* **14**, 69–78.
- SKOTE, M., HARITONIDIS, J. H. & HENNINGSON, D. S. 2002 Varicose instabilities in turbulent boundary layers. *Physics of Fluids* **14**, 2309–2323.
- SOMMERFELD, A. 1908 Ein beitrage zur hydrodynamischen erklärang der turbulenten flüssigkeitbewegungen. In *Atti. del 4. Congr. Internat. dei Mat. III, Roma*, pp. 116–124.
- SWEARINGEN, J. D. & BLACKWELDER, R. F. 1987 The growth and breakdown of streamwise vortices in the presence of a wall. *J. Fluid Mech.* **182**, 255–290.
- TOLLMIE, W. 1929 Über die entstehung der turbulenz. *Nachr. Ges. Wiss. Göttingen* *21-24*, English translation NACA TM 609, 1931.
- WALEFFE, F. 1995 Hydrodynamic stability and turbulence: Beyond transients to a self-sustaining process. *Stud. Appl. Math.* **95**, 319–343.
- WALEFFE, F. 1997 On a self-sustaining process in shear flows. *Phys. Fluids* **9**, 883–900.
- WESTIN, K. J. A., BOIKO, A. V., KLINGMANN, B. G. B., KOZLOV, V. V. & ALFREDSSON, P. H. 1994 Experiments in a boundary layer subject to free-stream turbulence. part i: Boundary layer structure and receptivity. *J. Fluid Mech.* **281**, 193–218.

- WUNDROW, D. W. & GOLDSTEIN, M. E. 2001 Effect on a laminar boundary layer of small-amplitude streamwise vorticity in the upstream flow. *J. Fluid Mech.* **426**, 229–262.

Part 2

Papers

Paper 1

On the breakdown of boundary layer streaks

By Paul Andersson^{†‡}, Luca Brandt[†], Alessandro Bottaro^{*} and Dan S. Henningson^{†‡}

[†]Department of Mechanics, Royal Institute of Technology (KTH), S-100 44
Stockholm, Sweden

[‡]FFA, the Aeronautical Research Institute of Sweden,
P.O. Box 11021, S-161 11 Bromma, SWEDEN

^{*}Institut de Mécanique des Fluides de Toulouse (IMFT), Université Paul Sabatier,
118 route de Narbonne, 31062 Toulouse Cedex 4, France

A scenario of transition to turbulence likely to occur during the development of natural disturbances in a flat-plate boundary layer is studied. The perturbations at the leading edge of the flat plate that show the highest potential for transient energy amplification consist of streamwise aligned vortices. Due to the lift-up mechanism these optimal disturbances lead to elongated streamwise streaks downstream, with significant spanwise modulation. Direct numerical simulations are used to follow the nonlinear evolution of these streaks and to verify secondary instability calculations. The theory is based on a linear Floquet expansion and focuses on the temporal, inviscid instability of these flow structures. The procedure requires integration in the complex plane, in the coordinate direction normal to the wall, to properly identify neutral modes belonging to the discrete spectrum. The streak critical amplitude, beyond which streamwise travelling waves are excited, is about 26% of the free-stream velocity. The sinuous instability mode (either the fundamental or the sub-harmonic, depending on the streak amplitude) represents the most dangerous disturbance. Varicose waves are more stable, and are characterized by a critical amplitude of about 37%. Stability calculations of streamwise streaks employing the shape assumption, carried out in a parallel investigation, are compared to the results obtained here using the nonlinearly modified mean fields; the need to consider a base flow which includes mean flow modification and harmonics of the fundamental streak is clearly demonstrated.

1. Introduction

1.1. “Lift-up” effect and transient growth

For quite a long time the fluid mechanics community has recognized transition to turbulence as a fundamental problem and has directed intense research efforts toward its understanding. Even so, our current picture of the physical

processes involved is far from complete. The classical starting point for theoretical investigations of transition is linear stability theory. Here, exponentially growing solutions—in time or space—to the linearised Navier–Stokes equations are sought. If such solutions are not found, the flow is predicted by the theory to be stable. However, experiments show that the route to turbulence is highly dependent on the initial conditions and on the continuous forcing that background noise can provide (see for example Morkovin & Reshotko 1990; Reshotko 1994, for reviews).

Experiments reveal that many flows, including for example Poiseuille and boundary layer flows, may undergo transition to turbulence for Reynolds numbers well below the critical ones from the linear stability theory. For the case of plane Couette flow the theory predicts stability at all Reynolds numbers (Romanov 1973) while numerical and laboratory experiments point to a finite transitional value (Lundbladh & Johansson 1991; Tillmark & Alfredsson 1992; Dauchot & Daviaud 1995).

The reason for this discrepancy between the theory and the experiments has been sought in the nonlinear terms of the Navier–Stokes equations. Examples of nonlinear theories are given by Orszag & Patera (1983), Bayly, Orszag & Herbert (1988) and Herbert (1988). However, examining the Reynolds–Orr equation (Drazin & Reid 1981) a remarkably strong statement can be made on the nonlinear effects: the nonlinear terms redistribute energy among disturbance frequencies but have no net effect on the instantaneous growth rate of the energy. This implies that there must exist a linear growth mechanism for the energy of a disturbance of any amplitude to increase (Henningson & Reddy 1994; Henningson 1996). The apparent need for an alternative growth mechanism based on the linearized equations has recently led to intense re-examination of the classical linear stability theory.

The first convincing alternative was proposed by Ellingsen & Palm (1975). By introducing an infinitesimal disturbance without streamwise variation in a shear layer, they showed that the streamwise velocity component can increase linearly with time, within the inviscid approximation, producing alternating low- and high-velocity streaks in the streamwise velocity component. Landahl (1975,1980) extended this result to the linear evolution of localized disturbances and supplied the physical insight to the linear growth mechanism with what he denoted the *lift-up* effect. He argued that vortices aligned in the streamwise direction advect the mean velocity gradient towards and away from the wall, generating spanwise inhomogeneities.

It is now clear that since the linearized Navier–Stokes operator is non-normal for many flow cases (especially in shear flows) a significant transient growth of a given perturbation might occur, before the subsequent exponential behaviour. Such an algebraic growth involves non-modal perturbations and can exist for subcritical values of the governing parameters.

Indeed, early investigators of the lift-up and transient growth mechanisms found considerable linear energy amplification before the viscous decay (Hultgren & Gustavsson 1981; Boberg & Brosa 1988; Gustavsson 1991; Butler & Farrell 1992; Reddy & Henningson 1993; Henningson, Lundbladh & Johansson 1993). An overview of recent work can be found in the review articles by Trefethen *et al.* (1993) and Henningson (1995). The initial disturbance that yields the maximum spatial transient growth in a non-parallel flat plate boundary layer flow was determined independently by Andersson *et al.* (1999) and Luchini (2000) to consist of vortices aligned in the streamwise direction. These vortices leave an almost permanent scar in the boundary layer in the form of long-lived, elongated streaks of alternating low and high streamwise speed.

1.2. "Secondary" instability of streamwise streaks

If the amplitude of the streaks grows to a sufficiently large value, instabilities can develop which may provoke early breakdown and transition, despite the theoretically predicted modal decay. In the remainder of the paper we will refer to the instability of the streak as a "secondary" instability, to differentiate it from the "primary" growth mechanism responsible for the formation of these flow structures. A (secondary) instability can be induced by the presence of inflection points in the base flow velocity profile, a mechanism which does not rely on the presence of viscosity. Controlled experiments on the breakdown of periodically arranged (along the span) streaks produced by an array of roughness elements have been conducted by Bakchinov *et al.* (1995). It was shown that the instability of the streaks causes transition in a similar manner as do the Görtler and cross-flow cases, i.e. via amplification of the secondary wave up to a stage where higher harmonics are generated, and on to a destruction of the spanwise coherence of the boundary layer. Alfredsson & Matsubara (1996) considered the case of transition induced by streaks formed by the passage of the fluid through the screens of the wind-tunnel settling chamber. They report on the presence of a high frequency "wiggle" of the streak with a subsequent breakdown into a turbulent spot.

Today, the description of the *establishment* of steady streaky structures is well captured by the theory. The work presented here aims at understanding the instability of these streaks on the path to boundary layer turbulence. Parenthetically, we note also that streamwise vortices and streaks are an essential ingredient of the near-wall turbulent boundary layer and that the instability of streaky structures is one crucial feature of the near-wall cycle which is thought to lie at the heart of the genesis and dynamics of turbulent coherent structures (Jiménez & Pinelli 1999; Schoppa & Hussain 1997; Schoppa & Hussain 1998).

Some work has recently appeared in the literature on the instability of streaks in channel flows (Waleffe 1995, 1997; Reddy *et al.* 1998) and, among the findings reported, it is interesting to note that slip and no-slip boundaries do not display significant differences in the instability scenario (Waleffe 1997).

The present study focuses on the linear, inviscid breakdown of boundary layer streaks. It is believed that the inviscid approximation captures the essential features of the breakdown. This is supported primarily by the controlled experiments of Bakchinov *et al.* (1995), who demonstrate unambiguously the role of the critical layer in the development of the instability. The measurements conducted by Boiko *et al.* (1997) on the instability of a vortex in a boundary layer and the very carefully controlled experiments on the breakdown of streaks in channel flow conducted by Elofsson *et al.* (1999) further attest to the inflectional nature of the breakdown. The latter authors generated elongated streamwise streaky structures by applying wall suction, and triggered a secondary instability by the use of earphones. The growth rate of the secondary instability modes was unaffected by a change of the Reynolds number of their flow, over a subcritical range, and the regions of (sinuous-type) oscillations of the streaks in cross-stream planes were reasonably well correlated to the spanwise shear of the main flow. The numerical/theoretical comparative viscous-inviscid investigations on the linear breakdown of longitudinal vortices in a curved channel (Randriarifara 1998) and the numerous studies on the secondary instability of Görtler vortices (Hall & Horseman 1991; Yu & Liu 1991; Bottaro & Klingmann 1996), show that the inviscid approach captures correctly the dominant features of the instability with viscosity playing mainly a damping role. These secondary instability studies bear a close resemblance to the present one.

1.3. Mean field with optimal streaks and linear stability analysis

The equations governing the streak evolution are obtained by applying the boundary layer approximations to the three-dimensional steady incompressible Navier-Stokes equations and linearizing around the Blasius base flow. After defining the disturbance energy density as the integral, in the wall-normal direction, of the square of the disturbance velocity components, techniques commonly employed when solving optimal control problems are used to determine the optimal disturbance (streamwise oriented vortices) and its downstream response (streamwise streak). The output streak predicted by the theory of Andersson *et al.* (1999a) and Luchini (2000) is remarkably similar to that measured in the laboratory (see figure 1). The measurements were performed in a pre-transitional flat plate boundary layer, where the largest amplitude of the streamwise velocity was eleven percent of the free-stream velocity. The streak is, in fact, a "pseudo-mode" triggered in a flat-plate boundary layer subject to significant outside disturbances.

The instability of these optimal streaks is studied here with different levels of approximation. Two different representations are used for the mean field: the simpler shape assumption, where the shape of the streak obtained from the linearized equations is considered unmodified even at large amplitudes, and the complete nonlinear development of the streak.

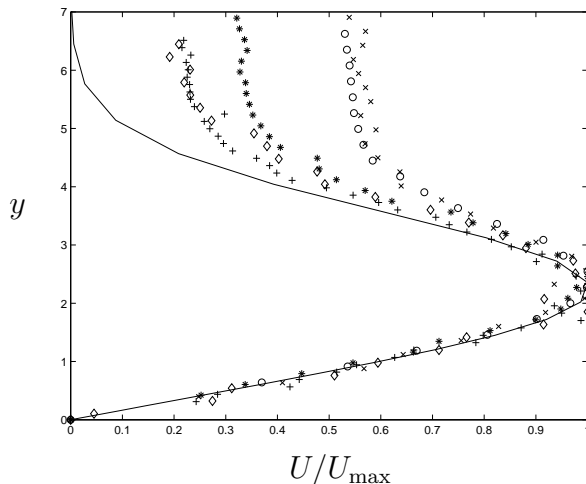


FIGURE 1. Comparison between the streamwise velocity component of the downstream response to an optimal perturbation, and the u -r.m.s. data in a flat-plate boundary layer subject to free-stream turbulence (—, Reynolds-number-independent theory). The symbols represent experiments from Westin *et al.* (1994) (\circ , $Re_\delta=203$; $+$, $Re_\delta=233$; \times , $Re_\delta=305$; \star , $Re_\delta=416$; \diamond , $Re_\delta=517$). Here y has been made non-dimensional—and the Reynolds number is defined—using the Blasius length scale $\delta = (L\nu/U_\infty)^{1/2}$.

In both formulations the linear secondary stability calculation are carried out on the basis of the boundary layer approximation, i.e. the mean field to leading order will consist only of the streamwise velocity component (here denoted U), consistent with the scaling hypothesis which led to the definition of the streak. Such a mean field varies on a slow streamwise scale, whereas the secondary instability varies rapidly in the streamwise direction x , as observed in the visualisations by Alfredsson & Matsubara (1996). Hence, our leading order stability problem is the parallel flow problem, with perturbation mode shapes dependent only on the cross-stream coordinates y (wall-normal) and z (spanwise). The same approximation was made previously for the case of the Görtler flow (Hall & Horseman 1991; Yu & Liu 1991; Bottaro & Klingmann 1996).

Due to the spanwise periodicity of the base flow—consisting of streamwise aligned streaks superimposed on a flat-plate Blasius flow—a temporal Floquet analysis is employed with the objective of determining which disturbance pattern shows the highest potential for temporal growth. In particular we are interested in determining if the maximum disturbance growth occurs for a sinusoidal or a varicose disturbance, and whether it is of fundamental or subharmonic

type. In addition, the critical threshold amplitude of the streak for the onset of the secondary instability is determined.

In § 2 the two-dimensional eigenvalue problem arising from the governing partial differential equation is formulated and the numerical methods adopted are described. In § 3 a scaling property of the mean field calculated by nonlinear simulations is introduced; this property allows a reduced number of simulations to cover a wide range of spanwise scales of the disturbance. Numerical experiments on streak instability are also carried out using DNS and the results are compared with the linear stability calculations. In § 4 a parametric study of the sinuous modes is presented and some comparisons with the shape assumption calculations are discussed. The main conclusions of the work are summarized in § 5.

2. Governing Equations and Numerical Methods

2.1. Inviscid stability equations

The dimensionless, incompressible Euler equations linearized around the mean field $(U(y, z), 0, 0)$ are

$$u_x + v_y + w_z = 0, \quad (1)$$

$$u_t + Uu_x + Uyv + Uz w = -p_x, \quad (2)$$

$$v_t + Uv_x = -p_y, \quad (3)$$

$$w_t + Uw_x = -p_z, \quad (4)$$

and the system is closed by slip boundary conditions at the solid wall and by decaying disturbances in the free stream;

$$(u, v, w) = (u(x, y, z, t), v(x, y, z, t), w(x, y, z, t))$$

are the perturbation velocities in the streamwise, wall-normal and spanwise directions, respectively, t is time and $p = p(x, y, z, t)$ is the disturbance pressure. All velocities have been scaled with the free-stream speed U_∞ and the pressure with ρU_∞^2 , where ρ is the fluid density. The length scale is $\delta = (L\nu/U_\infty)^{1/2}$, with ν kinematic viscosity and L distance from the leading edge. For later use we define two Reynolds numbers using the two different length scales, $Re_\delta = U_\infty\delta/\nu$ and $Re = U_\infty L/\nu$, which relate as $Re = Re_\delta^2$.

The presence of both wall-normal and spanwise gradients in the mean field makes it impossible to obtain an uncoupled equation for either of the velocity components. It is, however, possible to find an uncoupled equation for the pressure by taking the divergence of the momentum equations, introducing continuity and then applying equations (3) and (4) (Henningson 1987; Hall & Horseman 1991). These manipulations yield

$$\left(\frac{\partial}{\partial t} + U\frac{\partial}{\partial x}\right)\Delta p - 2U_y p_{xy} - 2U_z p_{xz} = 0. \quad (5)$$

We consider perturbation quantities consisting of a single wave component in the streamwise direction, i.e.

$$p(x, y, z, t) = \text{Real}\{\tilde{p}(y, z)e^{i\alpha(x-ct)}\},$$

where α is the (real) streamwise wavenumber and $c = c_r + ic_i$ is the phase speed. The equation governing the pressure reduces to

$$(U - c)\left(\frac{\partial^2}{\partial y^2} + \frac{\partial^2}{\partial z^2} - \alpha^2\right)\tilde{p} - 2U_y\tilde{p}_y - 2U_z\tilde{p}_z = 0; \quad (6)$$

this constitutes a generalized eigenproblem with c in the role of eigenvalue and needs to be solved for given mean field and streamwise wavenumber. Once the pressure eigenfunctions are computed, the velocity components can be obtained from the explicit expressions

$$i\alpha(U - c)\tilde{v} = -\tilde{p}_y, \quad (7)$$

$$i\alpha(U - c)\tilde{w} = -\tilde{p}_z, \quad (8)$$

$$i\alpha(U - c)\tilde{u} + U_y\tilde{v} + U_z\tilde{w} = -i\alpha\tilde{p}. \quad (9)$$

The pressure component \tilde{p} is expanded in an infinite sum of Fourier modes

$$\tilde{p}(y, z) = \sum_{k=-\infty}^{\infty} \hat{p}_k(y)e^{i(k+\gamma)\beta z}, \quad (10)$$

where β is the spanwise wavenumber of the primary disturbance field and γ is the (real) Floquet exponent. We note two symmetries: first, to within renumbering of the Fourier coefficients γ and $\gamma \pm n$ yield identical modes for any integer n , and second, equation (6) is even under the reflection $z \rightarrow -z$. These symmetries make it sufficient to study values of γ between zero and one half, with $\gamma = 0$ corresponding to a *fundamental* instability mode, and $\gamma = 0.5$ corresponding to a *subharmonic* mode (see Herbert 1988 for a thorough discussion on fundamental and detuned instability modes). The mean field is also expanded as a sum of Fourier modes

$$U(y, z) = \sum_{k=-\infty}^{\infty} U_k(y)e^{ik\beta z} \quad (11)$$

and these expansions are introduced into equation (6) to yield an equation that holds for each integer k :

$$\begin{aligned} \sum_{j=-\infty}^{\infty} \left(U_{k-j} \left[\frac{\partial^2}{\partial y^2} - \beta^2(j+\gamma)^2 - \alpha^2 \right] - 2 \frac{\partial U_{k-j}}{\partial y} \frac{\partial}{\partial y} + 2\beta^2(k-j)(j+\gamma)U_{k-j} \right) \hat{p}_j \\ = c \left[\frac{\partial^2}{\partial y^2} - \beta^2(k+\gamma)^2 - \alpha^2 \right] \hat{p}_k. \end{aligned} \quad (12)$$

The appropriate boundary conditions are:

$$\frac{\partial \hat{p}_k}{\partial y} = 0 \text{ at } y = 0 \text{ and } \frac{\partial \hat{p}_k}{\partial y} \rightarrow 0 \text{ when } y \rightarrow \infty. \quad (13)$$

This problem consists of an infinite number of coupled ordinary differential equations which must be truncated in order to find a numerical solution. The complete system must be solved numerically, when the solution is sought for an arbitrary value of the detuning parameter γ . If, however, even and odd solutions in z are sought, the system of equations can be simplified for the fundamental and subharmonic modes. In this case the numerical effort is decreased considerably because the dimension of the matrices arising from the discretisation is halved.

In the fundamental ($\gamma = 0$) case, even (odd) modes are obtained by imposing the condition $\hat{p}_{-k} = \hat{p}_k$ ($\hat{p}_{-k} = -\hat{p}_k$). This is equivalent to introducing either a cosine or a sine expansion

$$\tilde{p}(y, z) = \sum_{k=0}^{\infty} \hat{p}_k(y) \cos(k\beta z), \quad (14)$$

$$\tilde{p}(y, z) = \sum_{k=1}^{\infty} \hat{p}_k(y) \sin(k\beta z), \quad (15)$$

into equation (6), to yield two different systems of ODE's.

In the case of subharmonic disturbances ($\gamma = 0.5$) the spanwise periodicity of the fluctuations is twice that of the base flow. The subharmonic mode also contains a symmetry which renders the decoupling into even and odd modes possible. In this case the cosine and sine expansions are:

$$\tilde{p}(y, z) = \sum_{k=0}^{\infty} \hat{p}_k(y) \cos\left(\frac{2k+1}{2}\beta z\right), \quad (16)$$

$$\tilde{p}(y, z) = \sum_{k=0}^{\infty} \hat{p}_k(y) \sin\left(\frac{2k+1}{2}\beta z\right). \quad (17)$$

These two expansions produce two new systems of ODE's which clearly yield two different classes of solutions, as in the case of the fundamental modes. Notice, however, that the sinuous fluctuations of the low-speed streaks, represented in the fundamental case by the sine expansion (15) are given, in the subharmonic case, by the cosine expansion (16). This is because the subharmonic sinuous case treats two streaks, which oscillate out of phase (cf Le Cunff & Bottaro 1993). Likewise, varicose oscillations of the low-speed streaks are represented by the cosine series (14) for the fundamental mode, and by the sine expansion (17) in the case of subharmonic perturbations.

For the sake of clarity, in the remainder of the paper only the definitions of *sinuous* or *varicose* modes of instability will be employed, with reference to the visual appearance of the motion of the *low-speed streaks*. A sketch of the different fundamental and subharmonic modes is provided in figure 2: it clearly illustrates how in the subharmonic cases sinuous (varicose) fluctuations of the low-speed streaks are always associated with staggered (in x) varicose (sinuous) oscillations of the high-speed streaks.

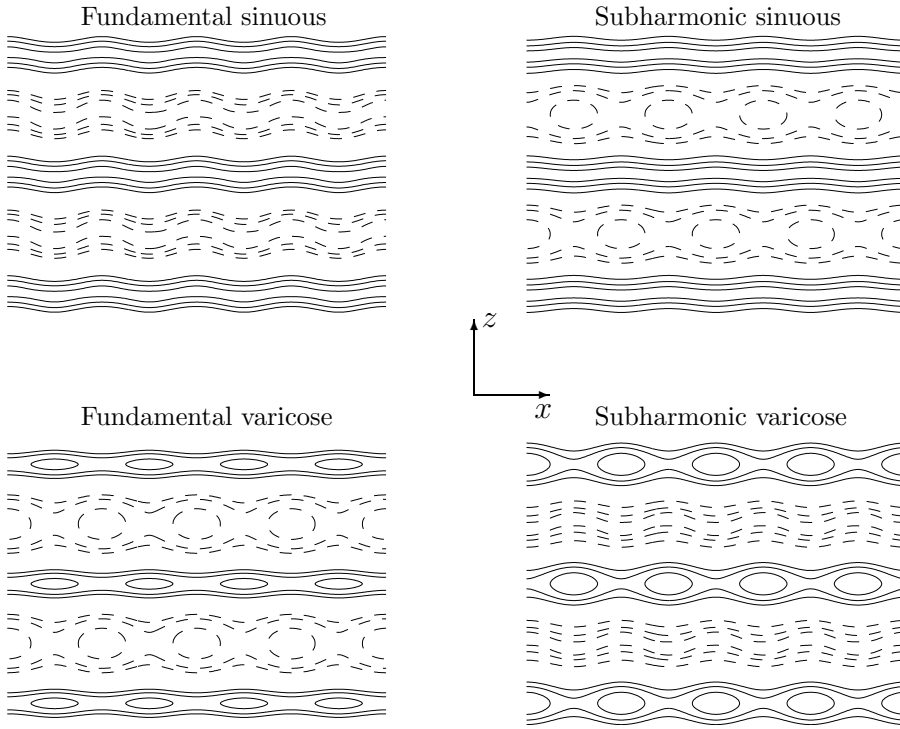


FIGURE 2. Sketch of streak instability modes in the $(x - z)$ -plane over four streamwise and two spanwise periods, by contours of the streamwise velocity. The low-speed streaks are drawn with solid lines while dashed lines are used for the high-speed streaks.

2.2. Chebyshev polynomials in real space

The temporal eigenvalue system derived in section 2 is solved numerically using a spectral collocation method based on Chebyshev polynomials. Consider the truncated Chebyshev expansion

$$\phi(\eta) = \sum_{n=0}^N \bar{\phi}^n T_n(\eta),$$

where

$$T_n(\eta) = \cos(n \cos^{-1}(\eta)) \quad (18)$$

is the Chebyshev polynomial of degree n defined in the interval $-1 \leq \eta \leq 1$. We use

$$\eta_j = \cos \frac{\pi j}{N}, \quad j = 0, 1, \dots, N,$$

as collocation points, that is, the extrema of the N th-order Chebyshev polynomial T_N plus the endpoints of the interval.

The calculations are performed using 121 ($N=120$) Chebyshev collocation points in y , and with the Fourier series in z truncated after fifteen modes. The wall-normal domain varies in the range $(0, y_{\max})$, with y_{\max} well outside the boundary layer (typically y_{\max} is taken equal to 50). The Chebyshev interval $-1 \leq \eta \leq 1$ is transformed to the computational domain $0 \leq y \leq y_{\max}$ by the use of the conformal mapping

$$y = a \frac{1 + \eta}{b - \eta}, \quad (19)$$

where

$$a = \frac{y_i y_{\max}}{y_{\max} - 2y_i} \quad \text{and} \quad b = 1 + \frac{2a}{y_{\max}}.$$

This mapping puts half the grid points in the region $0 \leq y \leq y_i$, with y_i chosen to be equal to 8.

The unknown functions $\hat{p}_k = \hat{p}_k(y)$ may now be approximated by

$$\hat{p}_k^N(y) = \sum_{n=0}^N \bar{p}_k^n \tilde{T}_n(y),$$

where $\tilde{T}_n(y) = T_n(\eta)$ with $\eta \mapsto y$ being the mapping (19). The Chebyshev coefficients \bar{p}_k^n , $n = 0, \dots, N$ are determined by requiring equation (12) to hold for \hat{p}_k^N at the collocation points y_j , $j = 1, \dots, N - 1$. The boundary conditions (13) are enforced by adding the equations

$$\sum_{n=0}^N \bar{p}_k^n \tilde{T}_{n,y}(0) = \sum_{n=0}^N \bar{p}_k^n \tilde{T}_{n,y}(y_{\max}) = 0,$$

where subscript n, y denotes the y -derivative of the n -th Chebyshev polynomial.

2.3. Chebyshev polynomials in complex space

The discretization leads to a generalized eigenproblem with the two matrices containing only real elements; hence, the solutions will consist of either real eigenvalues or complex conjugate pairs. No strictly damped solutions can be found using these equations together with an integration path running along the real y -axis from 0 to y_{\max} , since the neglect of viscosity introduces a continuous spectrum of singular neutral modes. Lin (1944) performed an asymptotic analysis on the Orr–Sommerfeld equation, requiring the inviscid eigenvalue problem (the Rayleigh equation) to be a limit of the viscous one when the Reynolds number approaches infinity. For this to apply, he found that the integration path in the inviscid case could be taken on the real axis if $c_i > 0$ and that it should be taken in the complex plane for $c_i \leq 0$, in such a way that the singularities lie on the same side of the integration path as in the $c_i > 0$ case.

Information on the singularities is contained in the system's determinant. We are satisfied here with the approximate location of the singularities and to simplify the analysis the mean field with the shape assumption is considered, i.e.

$$U(y, z) = U_B(y) + \frac{A_s}{2} u_s(y; \beta) e^{i\beta z} + \frac{A_s}{2} u_s(y; \beta) e^{-i\beta z}, \quad (20)$$

with U_B the Blasius solution, u_s the streak's mode shape provided by the analysis of Andersson *et al.* (1999a) and scaled so that $\max[u_s(y; \beta)] = 1$, A_s the amplitude of the streak and β the spanwise wavenumber. Figure 1 show the streak's mode shape u_s . Introducing expansion (20) into equation (12) yields an equation that holds for each integer k :

$$\begin{aligned} & \frac{A_s}{2} u_s \left(\frac{\partial^2}{\partial y^2} - \beta^2(k-1+\gamma)(k-3+\gamma) - \alpha^2 \right) \hat{p}_{k-1} - A_s u_{s,y} \frac{\partial}{\partial y} \hat{p}_{k-1} + \\ & (U_B - c) \left(\frac{\partial^2}{\partial y^2} - \beta^2(k+\gamma)^2 - \alpha^2 \right) \hat{p}_k - 2U_{B,y} \frac{\partial}{\partial y} \hat{p}_k + \\ & \frac{A_s}{2} u_s \left(\frac{\partial^2}{\partial y^2} - \beta^2(k+1+\gamma)(k+3+\gamma) - \alpha^2 \right) \hat{p}_{k+1} - A_s u_{s,y} \frac{\partial}{\partial y} \hat{p}_{k+1} = 0, \end{aligned} \quad (21)$$

plus boundary conditions (13).

By rewriting equations (21) and (13) as a system of first-order equations and studying the system's determinant, the singularities can be identified analytically as the roots of the equation

$$\prod_{k=1}^K \left\{ U_B - c + A_s u_s \cos \left(\frac{k\pi}{K+1} \right) \right\} = 0,$$

where K is the number of Fourier modes. For small values of c_i the approximate location of each singularity in the complex y -plane can be identified with a Taylor expansion around $y = y_r$, i.e.

$$U_B(y_r) + A_s u_s(y_r; \beta) \cos \left(\frac{k\pi}{K+1} \right) = c_r + h.o.t.$$

and to first order these locations are:

$$y_s = y_r + i \frac{c_i}{U_{B,y}(y_r) + A_s u_{s,y}(y_r) \cos(k\pi/(K+1))}. \quad (22)$$

These are, as might have been expected, the values of y for which the base flow velocity becomes equal to c at the discrete values of the z coordinate imposed by the truncated Fourier expansion in z . Clearly, y_s crosses the real y axis when c_i changes sign, so that the integration path has to go out into the complex y -plane in order for the singularities to lie on the same side of the path. Integration in the complex plane is necessary when neutral curves are sought. The mapping

$$y^c = y - iB(y_{\max} y - y^2)^{1/2} \quad (23)$$

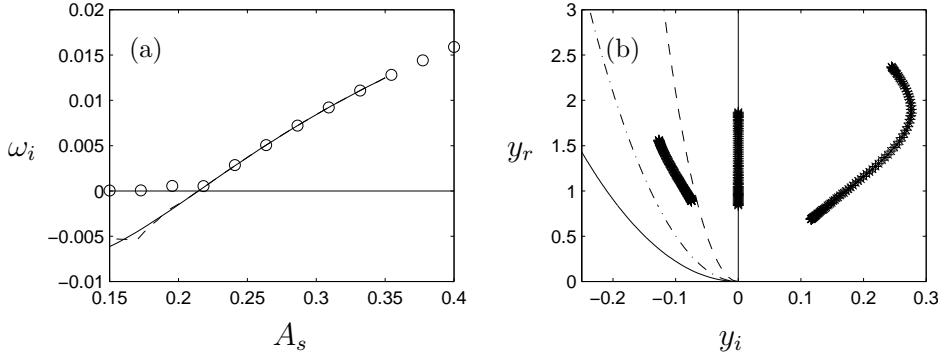


FIGURE 3. (a) Temporal growth rate of the fundamental varicose mode versus the streak's amplitude for $\alpha=0.2$ and $\beta=0.45$ (\circ real integration path, - - - complex integration path with $B=0.01$, — complex integration path with $B=0.03$). (b) The three curved lines denote different integration paths: - - - $B=0.01$, - · - · $B=0.02$, — $B=0.03$. The thick segments of stars denote the singular segments for three different streak's amplitudes. From the left: $A_s = 0.15$ (amplified modes do not exist), 0.215 (the least stable discrete mode is neutral) and 0.35 (at least one amplified mode exists). Only for the latter case the real integration path is suitable.

allows the computation of damped (and neutral) modes. It is introduced into (19), that is $y^c \mapsto \eta^c$, to deliver a curve in the complex plane with endpoints in $\eta^c = -1$ and 1. Complex Chebyshev polynomials $T_n^c(\eta^c)$ are defined by using (18), and the unknown functions are approximated using this new basis. This can be done since the analytic continuation of a polynomial is given by the same polynomial but with a complex argument.

As can be inferred from equation (22) the singularities corresponding to a given set of problem parameters are confined to a finite segment in the complex y -plane. For amplified modes this segment is found in the right half-plane in figure 3(b); for damped modes it is displaced to the left half-plane, whereas for neutral modes the singular segment is a subset of the real axis. In figure 3(a) the results of three calculations of the temporal growth rate are plotted versus the streak amplitude, employing the shape assumption for given streamwise, $\alpha=0.2$, and spanwise, $\beta=0.45$, wavenumbers. The circles are obtained by integrating over the real y -axis; as the amplitude A_s of the streak decreases, so does the largest growth rate of the instability ω_i , until the value $A_S \approx 0.215$ below which only quasi-neutral modes are found. For such modes the real integration path is located on the wrong side of the singularities. If the complex integration path denoted by a dashed line in both figures (corresponding to $B=0.01$ in the mapping 23) is employed, the integration correctly follows the damped mode down to an amplitude of about 18%. Clearly one can proceed to even

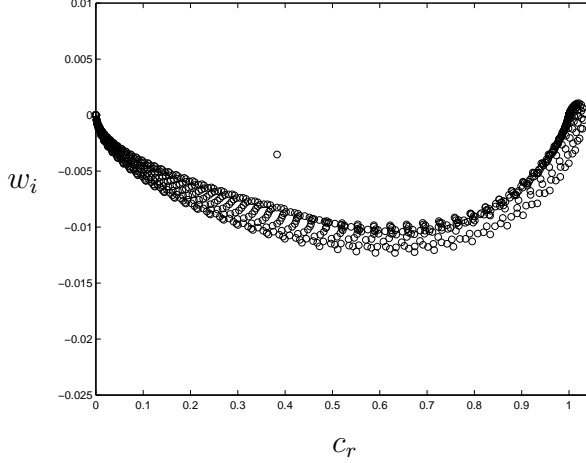


FIGURE 4. Eigenvalue spectrum of the fundamental varicose mode for $\alpha=0.2$, $\beta=0.45$ and $A_s=0.18$, displayed as temporal growth rate versus phase speed. It is obtained using a complex integration path with $B=0.03$.

smaller amplitudes simply by increasing B , i.e. by displacing the integration contour further into the negative y_i region. For example, the dotted-dashed contour in figure 3(b) can be used, or the continuous line path (corresponding to $B = 0.03$). The latter integration path has been used and the resulting full spectrum is shown in figure 4 for a streak amplitude of 0.18. The continuous spectrum of singular neutral modes is displaced downward and an isolated, damped mode can be identified at a phase speed close to 0.4. Provided that the singular segment lies on the correct side of the integration path, changes in the path do not affect this eigenvalue; the continuous spectrum is, instead, further moved towards lower values of ω_i for increasing B . Values of B between 0.01 and 0.03 have been used in most of the calculations identifying neutral modes in the present paper.

Clearly also other integration paths are possible; in fact, any complex detour that leaves the singularities to its right side in the complex y -plane will yield the correct physical eigenvalues. Since the physical solutions vanish rapidly at infinity there is no need for the integration path to return to the real axis at $y = y_{\max}$ in order to enforce the boundary conditions at the free stream (Peter Schmid, private communication). In some calculations, the mapping

$$y^c = y - iD(2y_{\max}y - y^2)^{1/2} \quad (24)$$

corresponding to a quarter of an ellipse has also been used successfully (D was taken equal to 0.006 in our calculations).

The growing and decaying solutions obtained by our procedure are the asymptotic limits of amplified and damped modes of the viscous stability equations as the Reynolds number approaches infinity (Lin 1955). We re-emphasise here that it is only by the use of this procedure that neutral (and damped) modes can be defined without ambiguities.

2.4. DNS method

2.4.1. Numerical scheme

The simulation code (see Lundbladh *et al.* 1999) employed for the present computations uses spectral methods to solve the three-dimensional, time-dependent, incompressible Navier–Stokes equations. The algorithm is similar to that of Kim *et al.* (1987), i.e. Fourier representation in the streamwise and spanwise directions and Chebyshev polynomials in the wall-normal direction, together with a pseudo-spectral treatment of the nonlinear terms. The time advancement used is a four-step low storage third-order Runge–Kutta method for the nonlinear terms and a second-order Crank–Nicolson method for the linear terms. Aliasing errors from the evaluation of the nonlinear terms are removed by the $\frac{3}{2}$ -rule when the FFTs are calculated in the wall-parallel plane. In wall-normal direction it has been found more efficient to increase resolution rather than using dealiasing.

To correctly account for the downstream boundary layer growth a spatial technique is necessary. This requirement is combined with the periodic boundary condition in the streamwise direction by the implementation of a “fringe region”, similar to that described by Bertolotti *et al.* (1992). In this region, at the downstream end of the computational box, the function $\lambda(x)$ in equation (25) is smoothly raised from zero and the flow is forced to a desired solution \mathbf{v} in the following manner,

$$\frac{\partial \mathbf{u}}{\partial t} = NS(\mathbf{u}) + \lambda(x)(\mathbf{v} - \mathbf{u}) + \mathbf{g}, \quad (25)$$

$$\nabla \cdot \mathbf{u} = 0, \quad (26)$$

where \mathbf{u} is the solution vector and $NS(\mathbf{u})$ the right hand side of the (unforced) momentum equations. Both \mathbf{g} , which is a disturbance forcing, and \mathbf{v} may depend on the three spatial coordinates and time. The forcing vector \mathbf{v} is smoothly changed from the laminar boundary layer profile at the beginning of the fringe region to the prescribed inflow velocity vector. This is normally a boundary layer profile, but can also contain a disturbance. A convenient form of the fringe function is as follows:

$$\lambda(x) = \lambda_{max} \left[S\left(\frac{x - x_{start}}{\Delta_{rise}}\right) - S\left(\frac{x - x_{end}}{\Delta_{fall}} + 1\right) \right], \quad (27)$$

where λ_{max} is the maximum strength of the damping, x_{start} to x_{end} the spatial extent of the region where the damping function is nonzero and Δ_{rise} and Δ_{fall} the “rise” and “fall” distance of the damping function. $S(a)$ is a smooth step function rising from zero for negative a to one for $a \geq 1$. We have used the

	$x_l \times y_l \times z_l$ δ_0	$n_x \times n_y \times n_z$ (resolution)	Re_{δ_0}
Box1	$1940 \times 34.4 \times 22.06$	$576 \times 65 \times 32$	272.2
Box2	$1940 \times 34.4 \times 22.06$	$576 \times 65 \times 32$	332.1
Box3	$1702 \times 34.4 \times 16.68$	$512 \times 81 \times 8$	264.6
Box4	$3096 \times 34.4 \times 16.68$	$1024 \times 81 \times 8$	591.6
Box5	$3404 \times 34.4 \times 14.71$	$1024 \times 81 \times 8$	948.7

TABLE 1. Resolution and box dimensions for the simulations presented. The box dimensions includes the fringe region, and are made dimensionless with respect to δ_0 , the Blasius length scale at the beginning of the computational box. The parameters z_l and n_z represent the full span and the total number of Fourier modes, respectively. Note that z_l corresponds in all cases to one spanwise wavelength of the primary disturbance.

following form for S , which has the advantage of having continuous derivatives of all orders:

$$S(a) = \begin{cases} 0 & a \leq 0 \\ 1/[1 + \exp(\frac{1}{a-1} + \frac{1}{a})] & 0 < a < 1 \\ 1 & a \geq 1 \end{cases} \quad (28)$$

This method damps disturbances flowing out of the physical region and smoothly transforms the flow to the desired inflow state, with a minimal upstream influence.

In order to set the free-stream boundary condition closer to the wall, a generalization of the boundary condition used by Malik *et al.* (1985) is implemented. Since it is applied in Fourier space with different coefficients for each wavenumber, it is non-local in physical space and takes the following form,

$$\frac{\partial \hat{\mathbf{u}}}{\partial y} + |k| \hat{\mathbf{u}} = \frac{\partial \hat{\mathbf{v}}_0}{\partial y} + |k| \hat{\mathbf{v}}_0, \quad (29)$$

where k is the absolute value of the horizontal wavenumber vector and $\hat{\mathbf{u}}$ is the Fourier transforms of \mathbf{u} . Here \mathbf{v}_0 denotes the local solution of the Blasius equation and $\hat{\mathbf{v}}_0$ its Fourier transform.

2.4.2. Disturbance generation and parameter settings

The presented numerical implementation provides several possibilities for disturbances generation. The complete velocity vector field from the linear results by Andersson *et al.* (1999a) is used for the primary disturbance. These optimally growing streaks, here denoted \mathbf{v}_d , are introduced in the fringe region by adding them to the Blasius solution to yield the forcing vector $\mathbf{v} = \mathbf{v}_0 + \mathbf{v}_d$.

In order to trigger a secondary instability of the streaks a harmonic localized wall-normal volume force is implemented. The harmonic forcing, $\mathbf{g} =$

$(0, F, 0)$, is constructed as an exponentially (in space) decaying function centred at $y = y_0$ and $x = x_{loc}$:

$$F = C \exp[-((x - x_{loc})/x_{scale})^2] \exp[-((y - y_0)/y_{scale})^2] g(z) f(t), \quad (30)$$

where the constant C determines the strength of the forcing and the parameters x_{scale} and y_{scale} its spatial extent. The time dependence is provided by the function

$$f(t) = S(t/t_{scale}) \cos(\omega t), \quad (31)$$

where ω is the angular frequency and the function S has been used again in $f(t)$ to ensure a smooth turn on of the forcing (of duration t_{scale}) in order to avoid problems with transients that may grow and cause transition in the flow. It is also possible to choose the spanwise symmetry of the forcing, to separately excite two classes of secondary disturbances; in

$$g(z) = \cos(\beta z + \phi), \quad (32)$$

we choose $\phi = 0$ or $\frac{\pi}{2}$ for varicose or sinuous symmetries, respectively.

The box sizes and resolutions used for the simulations presented in this paper are displayed in table 1. The dimensions of the boxes are reported in δ_0 , which here denotes the boundary layer thickness at the beginning of the computational box. Box1 is used to produce the non-linear streaks and study their secondary instability, while Box2 is employed to verify the scaling property introduced in section 3.2; Box3, Box4 and Box5 are, instead, used to test the DNS against the linear results (see figure 7(a)). The Reynolds numbers based on δ_0 are also reported in the table. For the calculations presented on the secondary instability induced by harmonic forcing, we use $x_{loc} = 300\delta_0$ from the beginning of the computational box, and $y_0 = 3\delta_0$ with x_{scale} and y_{scale} of $35\delta_0$ and $3\delta_0$, respectively.

3. DNS Results

3.1. Nonlinear development of the streaks

Nonlinear mean fields are computed solving the full Navier–Stokes equations in a spatially evolving boundary layer, using the optimal streaks as initial conditions. The complete velocity vector field from the linear results by Andersson *et al.* (1999a) is used as input close to the leading edge and the downstream non-linear development is monitored for different initial amplitudes of the perturbation. This is shown in figure 5(a), where all energies are normalized by their initial values. The dashed line corresponds to an initial energy small enough for the disturbance to obey the linearized equations. For this case the maximum of the energy is obtained at $x=2.7$; note that this location of maximum energy is weakly dependent on the initial amplitude, even for quite large values of the initial energy.

A contour plot in the (z, y) -plane of the nonlinear mean field corresponding to the circled line in figure 5(a) at $x = 2$ is shown in figure 6(b). This velocity

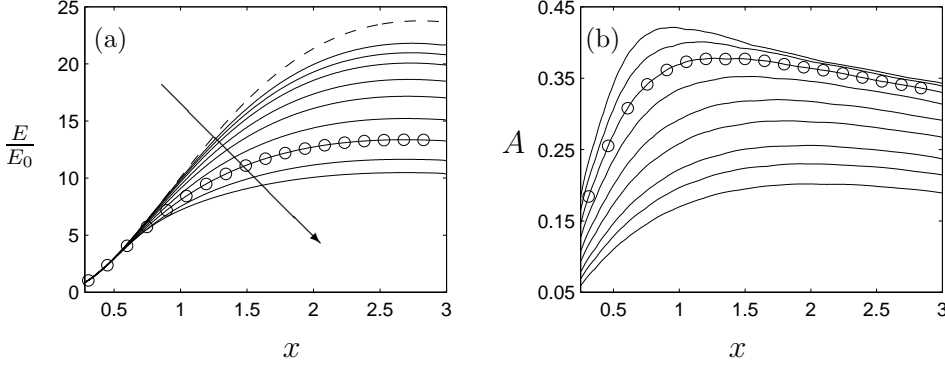


FIGURE 5. (a) The energy of the primary disturbance, E , normalized with its initial value, E_0 , versus the streamwise coordinate, x , for $\beta=0.45$ and $Re_\delta=430$. Here x has been made non-dimensional using the distance L to the leading edge. The arrow points in the direction of increasing initial energies, $E_0=2.92 \times 10^{-2}$, 3.97×10^{-2} , 5.18×10^{-2} , 7.30×10^{-2} , 9.78×10^{-2} , 1.36×10^{-1} , 1.81×10^{-1} , 2.33×10^{-1} , 2.91×10^{-1} (E_0 is computed at $x=0.3$). The dashed line represents the optimal linear growth. (b) The downstream amplitude development for the same initial conditions as in (a). The amplitude A is defined by equation (34). (The two lines have been circled for future reference).

field may be expanded in the sum of cosines

$$U(y, z) = \sum_{k=0}^{\infty} U_k(y) \cos(k\beta z) \quad (33)$$

where U_0 differs from the Blasius solution U_B by the mean flow distortion term. To be able to quantify the size of the primary disturbance field an amplitude A is defined as

$$A = \frac{1}{2} \left[\max_{y,z} (U - U_B) - \min_{y,z} (U - U_B) \right]. \quad (34)$$

When the shape assumption is adopted, A coincides with A_s . Figure 5(b) displays the downstream amplitude development for the same initial conditions as figure 5(a). One can note that the amplitude reaches its maximum value upstream of the position where the energy attains its peak, and starts to decrease at a position where the energy is still increasing. This is due to the thickening of the boundary layer.

The effect of the nonlinear interactions on the base flow are shown by the contour plots in figures 6. Figure 6(a) displays the primary disturbance obtained using the shape assumption with $A_s=0.36$, while 6(b) shows a fully nonlinear mean field, characterized by the same disturbance amplitude. In the

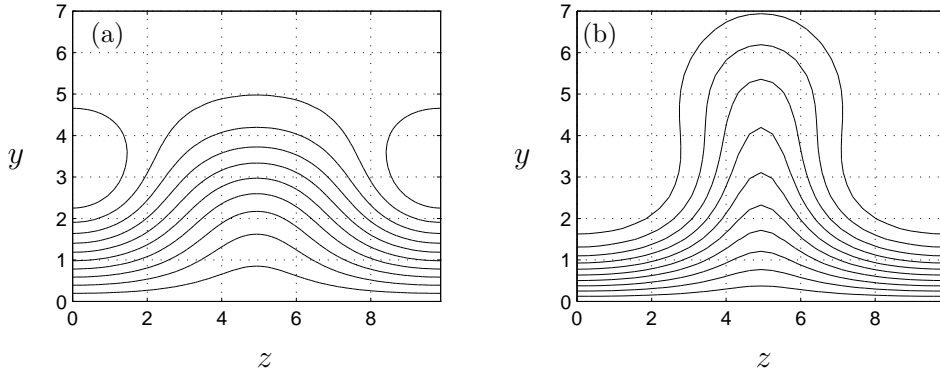


FIGURE 6. (a) Contour plot in a (z, y) -plane of the primary disturbance streamwise velocity using the shape assumption. The spanwise wavenumber is $\beta=0.45$, the streamwise position $x=2$ and the amplitude $A_s=0.36$. (b) Contour plot in a z - y plane of the nonlinear mean field corresponding to the circled line in figure 5(a) at $x=2$ (where $A=0.36$). Here $Re_\delta=430$. In both figures the coordinates y and z have been made non-dimensional using the local Blasius length scale δ , at the streamwise position $x=2$. In fact, for all y, z plots hereafter the cross-stream coordinates have been scaled using the local Blasius length scale.

latter case, the low-speed region is narrower, therefore associated with higher spanwise gradients, and displaced further away from the wall.

A base flow like the one presented in figure 6(b) is representative of flat-plate boundary layer flows dominated by streamwise streaks as encountered in experiments (Bakchinov *et al.* 1995; Westin *et al.* 1994; Kendall 1985, 1990) and simulations (Berlin *et al.* 1999).

3.2. Scaling of the mean field

In Andersson *et al.* (1999a) a scaling property of the optimal streamwise streaks in the flat-plate boundary layer was found to exist. In a linearized setting, they considered an upstream velocity perturbation at the leading edge of the flat plate, $\mathbf{u}_{\text{in}}(0)$, and its downstream response, $\mathbf{u}_{\text{out}}(x)$, a distance x from the leading edge, and maximized the output energy $E(\mathbf{u}_{\text{out}}(x)) = E(x, \beta, E_0, Re)$ over all initial disturbances with fixed energy $E(\mathbf{u}_{\text{in}}(0)) = E_0$.

The disturbance energy can be written

$$E(\mathbf{u}(x)) = \int_0^{2\pi/\beta} \int_0^\infty \left(u^2 + \frac{\bar{v}^2}{Re} + \frac{\bar{w}^2}{Re} \right) dy dz, \quad (35)$$

where $\bar{v} = v\sqrt{Re}$ and $\bar{w} = w\sqrt{Re}$ are the cross-stream velocities in boundary layer scales. The optimal disturbances, which were calculated using the linearized, steady boundary layer approximation, were found to consist of streamwise vortices developing into streamwise streaks. Since streamwise aligned vortices contain no streamwise velocity component, the energy at the leading edge E_0 can be written as

$$E_0 = \frac{\bar{E}_0}{Re}, \quad \text{where} \quad \bar{E}_0 = \int_0^{2\pi/\beta} \int_0^\infty (\bar{v}^2 + \bar{w}^2) dy dz, \quad (36)$$

with \bar{E}_0 is independent of the Reynolds number. The boundary layer equations governing $(u, \bar{v}, \bar{w}, \bar{p})$, here $\bar{p}=pRe$, contain no explicit dependence on the Reynolds number; furthermore, all velocities are $O(1)$ a distance sufficiently far downstream of the plate leading edge. Hence, the streamwise velocity component will dominate in the disturbance energy (35) and the output energy obeys the scaling law

$$\bar{E}(x, \beta, \bar{E}_0) = \lim_{Re \rightarrow \infty} E(x, \beta, \bar{E}_0, Re). \quad (37)$$

This scaling property holds also when the solutions are obtained from the Navier–Stokes equations, if $u = 0$ at $x = 0$. In figure 7 both linear and nonlinear solutions obtained from the Navier–Stokes equations are presented which verify (37).

Figure 7(a) displays \bar{E}/\bar{E}_0 versus x for the spanwise wavenumber, $\beta=0.45$. The solid line corresponds to a solution obtained using the linearized, steady boundary layer approximations. The other three lines represent results obtained from solving the Navier–Stokes equations, for three different Reynolds numbers, with initial disturbance energies small enough to yield a linear evolution. Figure 7(a) shows that the boundary layer approximation is valid and yields solutions in agreement with those obtained from the Navier–Stokes simulations.

Figure 7(b) depicts two curves representing the spatial development of \bar{E} using an initial energy, \bar{E}_0 , large enough to induce substantial nonlinear effects. The two curves, which represent solutions to the Navier–Stokes equations for the same initial energy and spanwise wavenumber, collapse onto one, although they correspond to two different Reynolds numbers. From figure 7(b) we conclude that the scaling property (37) holds also when the velocity field of the primary disturbance is fully nonlinear.

To clarify the implication of (37), consider the same dimensional problem with the dimensional energy denoted E^* scaled with two different length scales, L and L_1 . We write

$$E^*(x, \beta, \bar{E}_0, Re) = E^*(x^1, \beta^1, \bar{E}_0^1, Re^1), \quad (38)$$

where the variables are scaled as

$$x^* = xL = x^1L_1, \quad \beta^* = \beta\sqrt{\frac{U_\infty}{\nu L}} = \beta^1\sqrt{\frac{U_\infty}{\nu L_1}} \quad \text{and} \quad Re = \frac{U_\infty L}{\nu}, \quad Re_1 = \frac{U_\infty L_1}{\nu}; \quad (39)$$

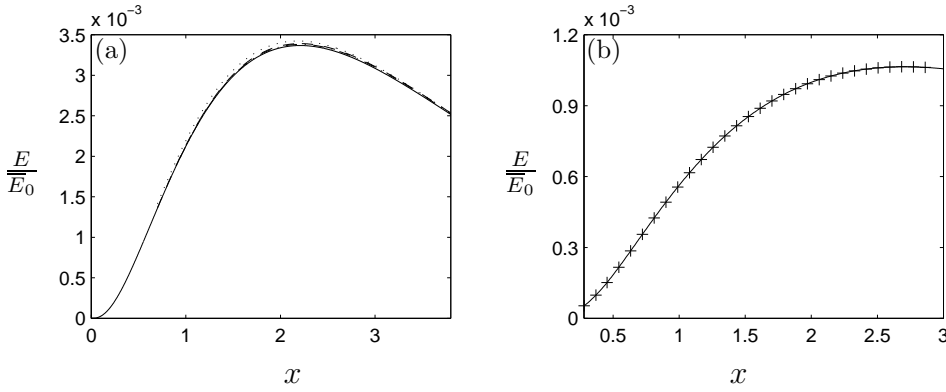


FIGURE 7. The spatial energy growth versus the streamwise coordinate, for the spanwise wavenumber, $\beta=0.45$. (a) With three small-amplitude solutions to the Navier–Stokes equations for Reynolds numbers (– – – $Re = 1 \times 10^6$, – · · – $Re = 5 \times 10^5$, · · · $Re = 1 \times 10^5$), and (—) one Reynolds number independent solution from the linearized, steady boundary layer approximations. (b) With an initial amplitude large enough to induce considerable nonlinear effects, $A=0.30$. Here the two curves represent solutions to the Navier–Stokes equations for two different Reynolds numbers (— $Re = 5 \times 10^5$, and + $Re = 7.5 \times 10^5$).

here x^* and β^* are the dimensional downstream position and spanwise wave number, respectively. The disturbance energies scale as

$$E^* = EU_\infty^2 \delta^2 = E^1 U_\infty^2 \delta_1^2 \quad \text{and} \quad \overline{E}_0 = \overline{E}_0^1. \quad (40)$$

Introducing $c^2 = L/L_1 = \delta^2/\delta_1^2$ and rewriting the right-hand expression in (38), in the variables x, β, Re we obtain

$$c^2 E(x, \beta, \overline{E}_0, Re) = E(c^2 x, \beta/c, \overline{E}_0, Re/c^2). \quad (41)$$

Now letting the Reynolds numbers tend to infinity and using (37) we get

$$c^2 \overline{E}(x, \beta, \overline{E}_0) = \overline{E}(c^2 x, \beta/c, \overline{E}_0), \quad (42)$$

for each $c > 0$.

An important physical implication of (37) can now be inferred from relation (42). Since (42) is Reynolds number independent, a non-dimensional solution $\overline{E}(x, \beta, \overline{E}_0)$ represent a continuous set of physical solutions in (x^*, β^*) -space, for a fixed \overline{E}_0 . We have seen that an initial array of streamwise aligned vortices at the leading edge will result in an array of streamwise streaks downstream. Since the streamwise and spanwise length scales are coupled, increasing the spanwise length scale at the leading edge will yield the same downstream behaviour of the solutions but on a larger streamwise length scale.

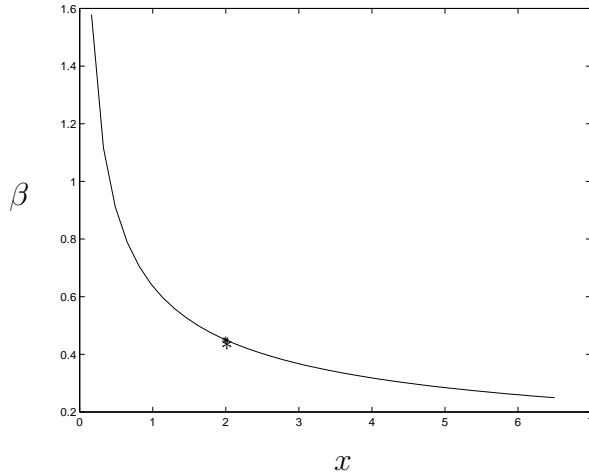


FIGURE 8. Loci of spanwise wavenumbers, β , and streamwise positions, x , representing the known solutions from the linear or nonlinear calculations at $x=2$ with $\beta=0.45$. The streamwise position and the spanwise wavenumber have been made non-dimensional using the distance from the leading edge L and the Blasius length scale $\delta = (L\nu/U_\infty)^{1/2}$, respectively.

In figure 8 the curve $(c^2x, \beta/c)$, with $x=2$ and $\beta=0.45$, is shown. From (42) the results along this curve are known and correspond to a rescaling of the solutions calculated at $x=2$ and $\beta=0.45$ (represented by the star in figure 8).

Note that (42) implies that \bar{E} increases linearly as the streamwise coordinate x increases, and the spanwise wavenumber β decreases (cf. figure 8). The increase in the energy of the streak E^* is a result of the widening of the cross-stream spatial extent of the disturbance. Since the shape of the streak velocity profile is the same, this implies that the amplitude remains constant along the curve $x\beta^2=\text{constant}$. In contrast, the energy of the corresponding initial vortex E_0^* remains the same for this parameter combination. This implies that the amplitude of the initial vortex, A_v , increases linearly with the spanwise wavenumber, i.e. $A_v \sim \beta$. Thus the amplitude of the initial vortex needed to produce a fixed amplitude of the streak along the curve $x\beta^2=\text{constant}$ decreases in a manner inversely proportional to the spanwise wavelength.

3.3. Secondary instability results from DNS

In this section direct numerical simulations of the secondary instability of streaks in a spatially growing flat-plate boundary layer are compared to the results from the inviscid secondary instability theory. This is done to ensure that the inviscid approximation is appropriate and can be used in further investigations and parametric studies of streak instabilities.

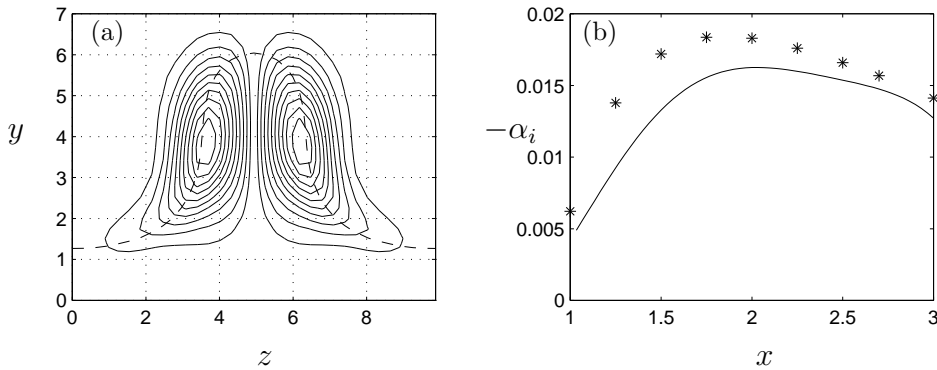


FIGURE 9. (a) Isocontours of r.m.s. values of the streamwise velocity component of the secondary disturbance ($\omega_r=0.211$) for the fundamental sinuous mode at $x=2$, obtained from the DNS. The dashed line represents the contour of the constant value of the mean field corresponding to the phase speed of the disturbance ($U = c_r = 0.80$). (b) Spatial growth rates, α_i versus x ; —, DNS data with $Re_\delta=430$ and $\beta=0.45$; *, linear temporal inviscid stability calculations using mean fields at each corresponding x -position and streamwise wavenumber $\alpha_r=0.260$.

The spatial stability problem is defined by the use of a real frequency ω and a complex wavenumber $\alpha = \alpha_r + i\alpha_i$. Here the spatial growth rate $-\alpha_i$ is obtained from the maximum of the streamwise velocity component of the secondary disturbance. The secondary disturbances are triggered using the harmonic forcing introduced in section 2.4.2, allowing for the two symmetries of fundamental type which can be excited separately. The amplitude of the volume force is selected low enough to yield linear secondary disturbances, avoiding the appearance of higher harmonics in the frequency spectra.

To choose the forcing frequency for the DNS, temporal linear secondary stability calculations for the sinuous mode are performed using the nonlinear mean field corresponding to the circled line in figure 5(a), at the local position $x=2$. The selected mean field has amplitude $A=0.36$, close to the threshold value for secondary instability in plane channel flow (Elofsson *et al.* 1999). The maximum temporal growth is found for $\alpha=0.257$, corresponding to a secondary disturbance frequency of 0.211.

The direct numerical simulations for the fundamental sinuous mode of the secondary instability are carried out using this forcing frequency, $\omega=0.211$, and the velocity fields are Fourier transformed in time to obtain the amplitude variation in the streamwise direction and the cross-stream distribution of the disturbance velocity at the frequency of the forcing.

Figure 9(a) shows the u_{rms} distribution of the fundamental sinuous mode at $x=2$. Note how the disturbance fluctuations follow quite closely the dashed line representing the contour of constant value of the mean field velocity corresponding to the phase speed of the secondary instability, $U = c_r = 0.80$. The solid line in figure 9(b) represents the spatial growth rate of the sinuous mode obtained from the direct numerical simulations. Here the secondary instability is excited at the streamwise position $x=0.85$. However, since the local forcing does not input pure eigenmodes the values of the growth rates are measured from an x -position downstream of the forcing, where the onset of an "eigenfunction" is identified.

Linear temporal stability calculations, using the real part of the streamwise wavenumber obtained from the direct numerical simulations, $\alpha_r=0.260$, are also performed, employing mean fields extracted at different streamwise positions from the DNS. In order to compare the spatial results to the growth rates obtained from the temporal inviscid stability problem (12), (13) a transformation first proposed by Gaster (1962) is employed:

$$\omega_i = -\frac{\alpha_i}{\partial\alpha/\partial\omega}. \quad (43)$$

From the temporal eigenvalues, Gaster's transformation (43) provides estimates of spatial growth rates (cf. the stars in figure 9(b)). The agreement between the stability theory and the full simulation results can be regarded as good, since the linear stability calculations are inviscid and performed under the assumptions of parallel mean flow. Note that, as one could expect, the inviscid approximation provides a slight overestimate of the amplification factors, and that closer agreement is found as the Reynolds number increases; here $Re=500\,000$ at the streamwise position $x=2.7$.

Using the same saturated mean field, direct numerical simulations are also carried out for the fundamental varicose mode of the secondary instability. Attempts to identify instabilities are made with different frequencies and for different streamwise and wall normal positions of the forcing in the direct simulations. Also, linear stability calculations at $x=2$ and for a range of different streamwise wavenumbers are performed. Both methods produce only stable solutions for this symmetry of the disturbances.

However, linear calculations using as base flow the streaks obtained with the largest initial energy tested (see figure 5), produce small positive temporal growth rates for the fundamental varicose instability. We then proceed as for the sinuous case: the largest growth rate, ω_i , is identified to correspond, at $x=2$, to a streamwise wavenumber $\alpha=0.250$ and a frequency $\omega_r=0.217$. This value is used in the DNS forcing and the spatial growth rates obtained are compared to linear stability calculations performed at different streamwise positions for $\alpha_r=0.252$. The results are shown in figure 10(b); the inviscid analysis gives small positive growth rates, while in the DNS the perturbation growth rates remain close to neutral as x exceeds 2.

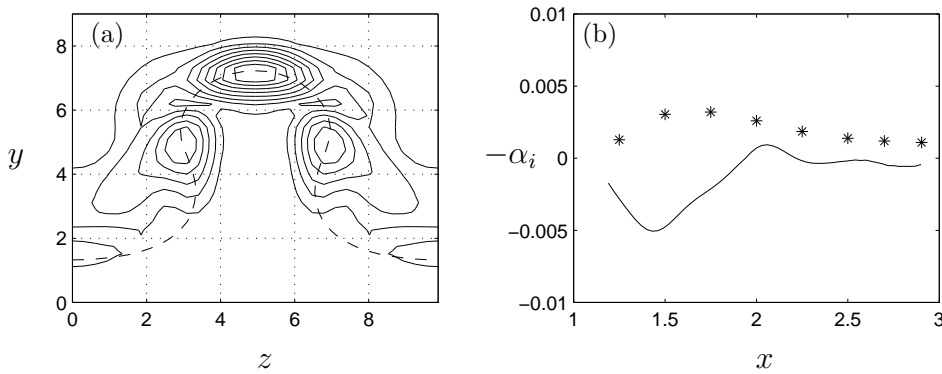


FIGURE 10. (a) Isocontours of r.m.s. values of the streamwise velocity component of the secondary disturbance ($\omega_r=0.217$) for the fundamental varicose mode at $x=2$, obtained from the DNS. The dashed line represents the contour of the constant value of the mean field corresponding to the phase speed of the disturbance ($U = c_r = 0.863$). (b) Spatial growth rates α_i versus x ; —, DNS data with $Re_\delta=430$ and $\beta=0.45$; *, linear temporal inviscid stability calculations using mean fields at each corresponding x -position and streamwise wavenumber $\alpha_r=0.252$.

Figure 10(a) shows the u_{rms} distribution of the fundamental varicose mode together with the contour of constant value of the mean field velocity corresponding to the phase speed of the secondary instability, i.e. $U = c_r = 0.863$. Note also here the close correspondence between the critical layer (displayed in the figure with a dashed line) and regions of intense u -fluctuations.

From the above calculations and comparisons we draw as first conclusion that the secondary instability of streamwise streaks is initially of sinuous type, and that the essential stability features can successfully be captured by an inviscid approach. The above statements are further confirmed by the results described below.

4. Inviscid Secondary Instability Results

4.1. The shape assumption versus the nonlinearly developed mean field

As a preliminary investigation, the secondary instability of streaks approximated by the shape assumption was parametrically studied (Andersson *et al.* 1999b). Comparison of the results with those obtained from calculations where the base flow is the nonlinearly developed streak demonstrate the inapplicability of the shape assumption for this type of studies (except for sinuous symmetries where a qualitative agreement could still be claimed).

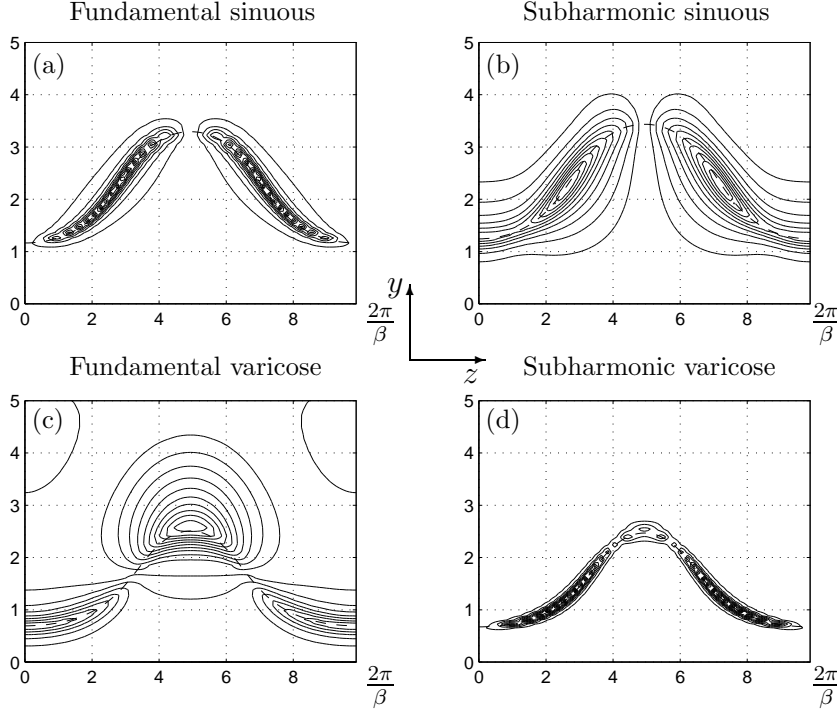


FIGURE 11. Contours of constant absolute values of the streamwise velocity component of four different kinds of modes obtained using the shape assumption. The dashed lines represent the contours of the constant value of the mean field corresponding to the phase velocities of the disturbances. The sinuous modes are calculated with parameters $\alpha=0.150$, $\beta=0.45$ and $A_s=0.36$ at $x=2$ ($c_r = 0.627$ and $\omega_i = 0.00301$ for the fundamental mode; $c_r = 0.661$ and $\omega_i = 0.0104$ for the subharmonic mode). The varicose modes are calculated with parameters $\alpha=0.150$, $\beta=0.45$ and $A_s=0.38$ at $x=2$ ($c_r = 0.379$ and $\omega_i = 0.00998$ for the fundamental mode; $c_r = 0.371$ and $\omega_i = 0.00297$ for the subharmonic mode). Note that the real and imaginary parts of the subharmonic modes have a period of $4\pi/\beta$. However, their absolute values are $2\pi/\beta$ -periodic.

In figures 11 and 12 the u -eigenfunctions, obtained with the shape approximation and the nonlinear mean field, respectively, are displayed for the parameters indicated.

Figure 11(a) shows the fundamental sinuous mode which is characterized by out-of-phase oscillations on either side of the low speed-streak, whereas the near-wall region is relatively quiescent. The subharmonic sinuous mode

(figure 11b) has real and imaginary parts of u symmetric around the $z=0$ and $z=2\pi/\beta$ axes. This eigenfunction shows a striking resemblance to that obtained by Ustinov (1998) who solved the linearized Navier–Stokes equations in time; it is also the same high frequency mode triggered in the experiments by Bakchinov *et al.* (1995). In figure 11(c) the fundamental varicose mode is displayed. In-phase fluctuations are spread in a z -range around π/β and halfway through the undisturbed boundary layer height. Some effect is also noticeable around $z = 0$ and $2\pi/\beta$, close to the wall. This mode is also very similar to that computed by Ustinov (1998). The subharmonic varicose mode (figure 11d) is characterized by almost the same phase speed as that of its fundamental counterpart, but here the real and the imaginary parts of this u -eigenfunction are anti-symmetric around the axes $z = 0$ and $z=2\pi/\beta$.

The fundamental u -eigenfunction displayed in figure 12(a) was obtained using the same mean field and streamwise wavenumber as the direct numerical simulations shown in figure 9(a). The agreement between figures 9(a) and 12(a) is very good and in fact, for this symmetry, there is also a fair agreement with the u -eigenfunction displayed in figure 11(a), which was obtained using the shape assumption. Also, the sinuous subharmonic u -eigenfunction 12(b) is in fair agreement with the one obtained using the shape assumption displayed in figure 11(b). In contrast, the fundamental and subharmonic varicose u -eigenfunctions are in poor agreement with both the u_{rms} plot of figure 10(a), obtained from direct numerical simulations, and the u -eigenfunctions of figures 11(c) and 11(d). As shown in figures 12(c) and 12(d) the u -eigenfunctions are considerably less diffuse and strongly concentrated around the isoline $U = c_r$.

The growth rates of the varicose (fundamental and subharmonic) symmetries are highly over-predicted when the shape assumption is used. The positive growth rates of the fundamental varicose case are found to be even larger than those for the fundamental sinuous case, which contradicts experiments and previous, comparable, calculations (Schoppa & Hussain 1997; 1998)

In comparing the mean fields obtained from the shape assumptions to the fully nonlinear ones, we find that the inflection point in the wall-normal direction is smoothed by the nonlinear modification, cf. figure 13(a). This figure shows the streamwise velocity profiles centred on the low-speed streak (i.e. $z = \pi/\beta$) for the two types of mean fields and for a large amplitude. This- z location has been chosen since it is where a wall-normal inflection point first appears when the streak's amplitude is increased, and also where the varicose eigenfunctions achieve their peak values. As reported in a number of experimental and numerical studies (Swearingen & Blackwelder 1987; Yu & Liu 1991; Bottaro & Klingmann 1996; Matsubara & Alfredsson 1998), the wall-normal inflection point can be related to the varicose mode, whereas sinuous instabilities correlate well to the spanwise mean shear.

The reason for the overpredicted varicose amplification factor when using the shape assumption can be deduced from inspection of figure 13: an inflection

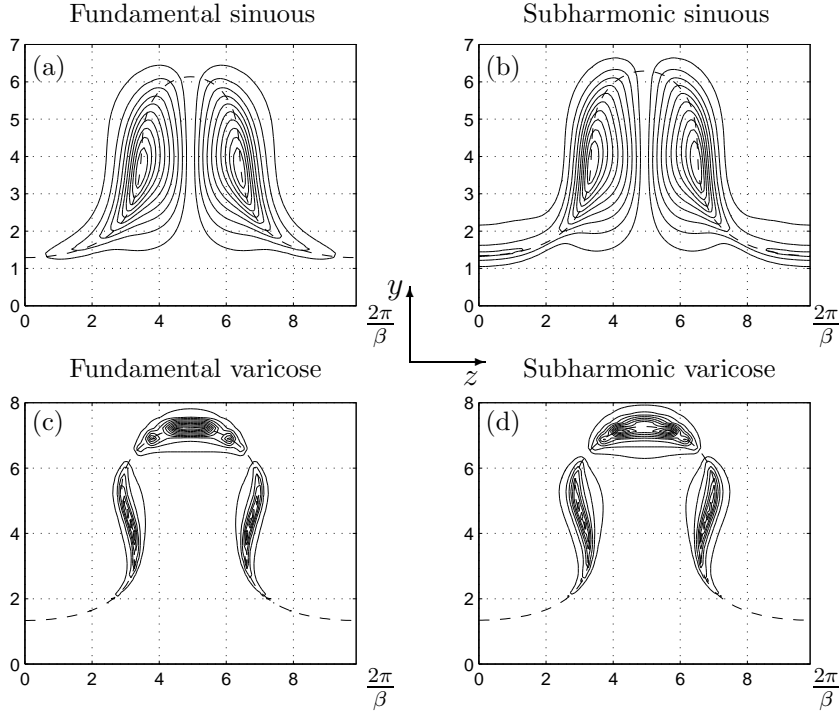


FIGURE 12. Contours of constant absolute values of the streamwise velocity component of four different kinds of modes obtained using the nonlinear mean fields. The dashed lines represent the contours of the constant value of the mean field corresponding to the phase velocities of the disturbances. The sinuous modes are calculated using the nonlinear mean field corresponding to the circled line in figure 5(a), at streamwise position $x=2$, where $A = 0.36$, for a streamwise wavenumber $\alpha = 0.280$ ($c_r = 0.821$ and $\omega_i = 0.0144$ for the fundamental mode; $c_r = 0.839$ and $\omega_i = 0.0125$ for the subharmonic mode). The varicose modes are calculated using the mean field with largest streak's amplitude (see figure 5(b)) at position $x = 2$, where $A = 0.378$, for a streamwise wavenumber $\alpha = 0.275$ ($c_r = 0.866$ and $\omega_i = 0.00218$ for the fundamental mode; $c_r = 0.876$ and $\omega_i = 0.00243$ for the subharmonic mode). In all calculations $Re_\delta=430$ and $\beta=0.45$.

point appears for y close to 3 in this case, but it disappears when the base flow contains all harmonics of the streak. Both the direct numerical simulations and the linear stability calculations using the nonlinearly distorted mean fields produce stable varicose modes for $A=0.33$. In fact, only for the largest streak

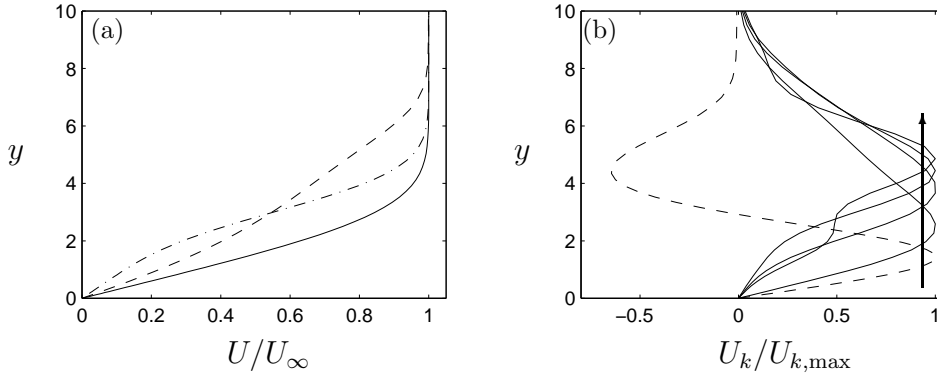


FIGURE 13. (a) The total streamwise velocity versus the wall-normal coordinate at $z = \pi/\beta$ for: - - -, the nonlinear mean field, and - · - · -, the shape-assumption-approximated mean field. Here both amplitudes are $A=A_s=0.33$, the streamwise position is $x=2$ and the spanwise wavenumber is $\beta=0.45$; the Blasius profile is drawn, for reference, with a solid line. (b) The different Fourier modes $U_k(y)$ representing the streamwise velocity of the nonlinear mean field in (a) versus the wall-normal coordinate. The dashed line corresponds to the mean flow distortion, $(U_0 - U_B)$, and the arrow points in the direction of higher-order modes. Every mode is normalized with its maximum ($(U_0 - U_B)_{\max}=0.11$, $U_{1,\max}=0.26$, $U_{2,\max}=6.6 \times 10^{-2}$, $U_{3,\max}=1.1 \times 10^{-2}$, $U_{4,\max}=9.2 \times 10^{-4}$). Here $Re_\delta=430$.

studied in this paper, corresponding to an amplitude $A=0.373$, a slightly unstable varicose mode is found. The discrepancy in the secondary stability results between the two cases can be traced to the mean flow distortion $(U_0 - U_B)$ (see the dashed line in figure 13b). Calculations employing a “nonlinear” mean field constructed without the mean flow distortion (where U_0 is replaced by U_B) result in varicose perturbations with positive growth rates for $A = 0.33$.

Furthermore, the phase speed of the secondary instability is considerably increased when using the nonlinear mean fields. This can be explained by observing that nonlinearities “move” the primary instability outwards from the wall. In figure 13(b) the individual Fourier modes from the cosine expansion of the nonlinear mean field from figure 13(a) are shown, normalized to unit value. Note that higher-order modes are displaced away from the wall. The phase speed of the secondary instability equals the mean field velocity at the critical layer, cf. figure 11. Therefore, as the critical layer is moved outwards, where the mean flow velocity is higher, the phase speed of the secondary instability is also increased.

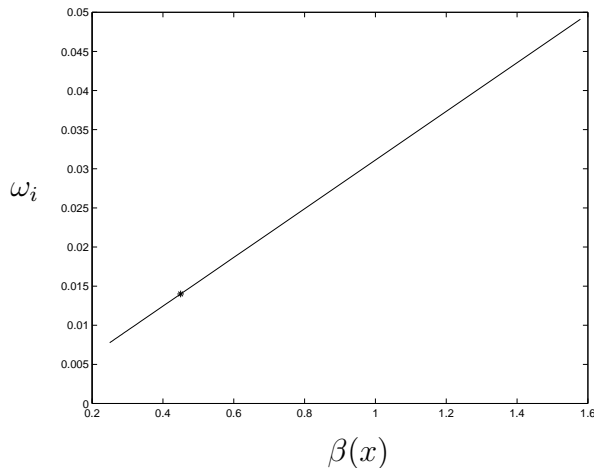


FIGURE 14. Results for the fundamental sinuous growth rates, ω_i , versus the spanwise wavenumbers along the curve in figure 8. The star gives the value of the amplification factor obtained when $A=0.36$, $\alpha=0.30$, $\beta=0.45$ and $x=2$, i.e. $\omega_i=0.014$.

4.2. Parametric study

In figure 5(b) the downstream amplitude development of streamwise streaks for a spanwise wavenumber $\beta=0.45$ and for different initial amplitudes is shown. Most of the linear stability calculations are performed using the velocity fields with the amplitudes found at $x=2$. This position was chosen since it is close to the point where the primary disturbance energy attains its maximum value.

According to the scaling property of the mean fields derived in section 3.2, the results obtained for the parameters used in this section, $x=2$ and $\beta=0.45$, can be rescaled to apply for all values of β (see figure 8). This implies that a result from a secondary instability calculation obtained using a mean field corresponding to a point on the curve in figure 8 can be rescaled to yield the amplification value for all points on this curve. Since $\omega_i/\beta=\text{constant}$, the value of the constant can be determined from a secondary instability result for a specific parameter combination. The line representing the growth rates of the fundamental sinuous symmetry is displayed in figure 14. In practice, however, the scaling property relating ω_i and β is limited to an intermediate range of β . Since their distance of amplification is so short, large values of β will need a very large initial disturbance amplitude at the leading edge, while disturbances represented by low values of β will saturate far downstream, where Tollmien–Schlichting instabilities may become important and change the transition scenario. For larger values of β , the corresponding x -position is closer to the leading edge and viscous effects may have a damping influence on the amplification of unstable waves.

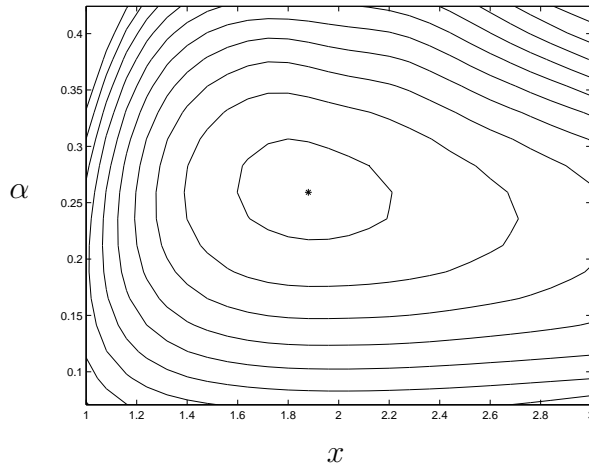


FIGURE 15. Isocontours of the growth rate ω_i , in the (x, α) -plane, for the sinuous fundamental mode, employing the mean field corresponding to the circled line in figure 5. The maximum contour level is 0.014 and the spacing is 0.0014. The * represents the maximum growth rate, $\omega_i=0.0147$, obtained at position $x=1.88$ and for a streamwise wavenumber $\alpha=0.259$.

Primary disturbances with β in the range $[0.3, 0.6]$ (here considered with respect to a fixed streamwise position, $x=1$), have the largest transient amplification (Andersson *et al.* 1999a; Luchini 2000). The spanwise distance selected in the controlled experiments by Bakchinov *et al.* (1995) corresponds to a value of β equal to 0.45 (at the location of their roughness elements), and this is also the scale of boundary layer fluctuations in the presence of free-stream turbulence (Westin *et al.* 1994). It could be speculated that this particular range of β is particularly appropriate when dealing with boundary layer streaks, since it corresponds to a spanwise spacing of about 100 wall units once viscous length scales are introduced. The spacing of 100 viscous wall units is not only obeyed by quasi-regular streaks in turbulent but also in laminar and transitional boundary layers (see Blackwelder 1983; Kendall 1985, 1990; Westin *et al.* 1994). It is also the typical transverse 'box' dimension for turbulence to survive in the minimal channel simulations of Jimenez & Moin (1991) and Hamilton, Kim & Waleffe (1995). In the present case, if a simple measure of the friction velocity is adopted by the use of the Blasius wall shear, it is easy to see that streaks spaced 100 wall units apart are present in a subcritical (with respect to TS waves) boundary layer if β is in the range $(0.3, 0.63)$.

Figure 15 shows the isocontours of the growth rate ω_i , for the fundamental sinuous instability in the (x, α) -plane for the mean field corresponding to the circled line in figure 5. The growth rates do not vary significantly for the range

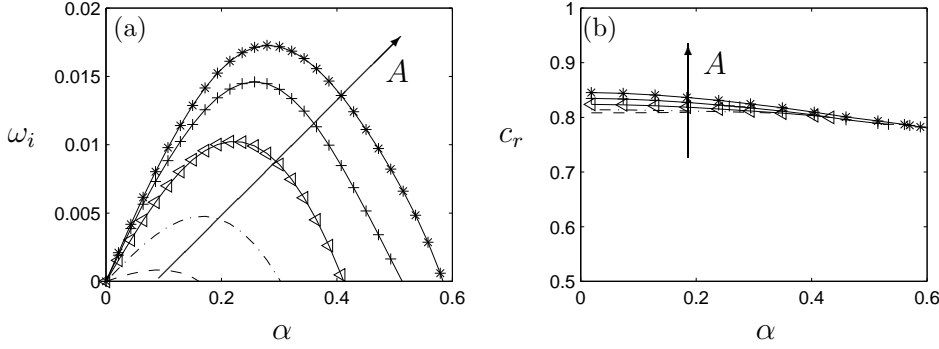


FIGURE 16. Temporal growth rate (a) and phase speed (b) versus streamwise wavenumber for the fundamental sinuous modes for different amplitudes of the primary disturbance (- - $A=0.288$, - · - · - $A=0.317$, —◁— $A=0.345$, —+— $A=0.364$, —*— $A=0.373$). The arrows point in the direction of increasing A .

of x between $1.6 < x < 2.2$, and in this interval, the maximum growth rate is obtained for nearly the same value of the streamwise wavenumber ($\alpha=0.259$). Stability calculations are, therefore, performed on the mean field at $x=2$, where the primary disturbance has saturated and, for the cases with lower initial energy, the streak amplitude achieve its maximum value (cf. figures 5).

An extensive parametric study is carried out for the sinuous fundamental ($\gamma = 0$), arbitrarily detuned ($0 < \gamma < 0.5$) and subharmonic ($\gamma = 0.5$) symmetries, which were the only ones found to be significantly unstable. At first the Floquet parameter is set to zero, i.e. fundamental modes are focused upon. In figure 16(a) the growth rate of the instability $\omega_i = \alpha c_i$ is plotted against the streamwise wavenumber, for the different amplitudes of the streaks, obtained with the DNS. One can note that on increasing the amplitude, not only do the growth rates increase but their maxima are also shifted towards larger values of the streamwise wavenumber α . As shown in figure 16(b) the phase speeds of the fundamental sinuous modes are but weakly dispersive.

Next, we examine the effect of changes in the spanwise wavelength of the secondary disturbance, i.e. we study the effect of the detuning parameter γ . It is often assumed that the preferentially triggered secondary instability modes have the same transverse periodicity as the base flow; this is not at all evident here. The full system of equations (12)-(13) has been solved without resorting to symmetry considerations to yield the results displayed in figures 17, corresponding to a streamwise wavenumber α equal to 0.255 and for mean fields with amplitudes large enough to lead to instabilities for the chosen α . A monotonic behaviour is observed in the γ range of $[0, 0.5]$ except for the case of lower amplitude A .

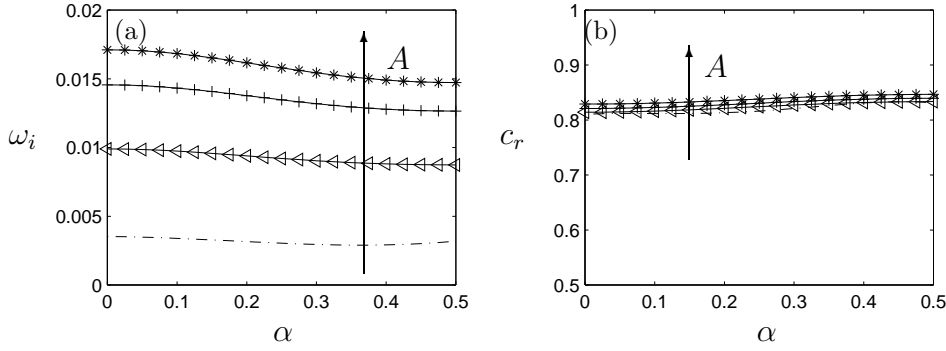


FIGURE 17. Temporal growth rate (a) and phase speed (b) versus the Floquet parameter for sinuous modes, for four different amplitudes of the primary disturbance (symbols as in figure 16).

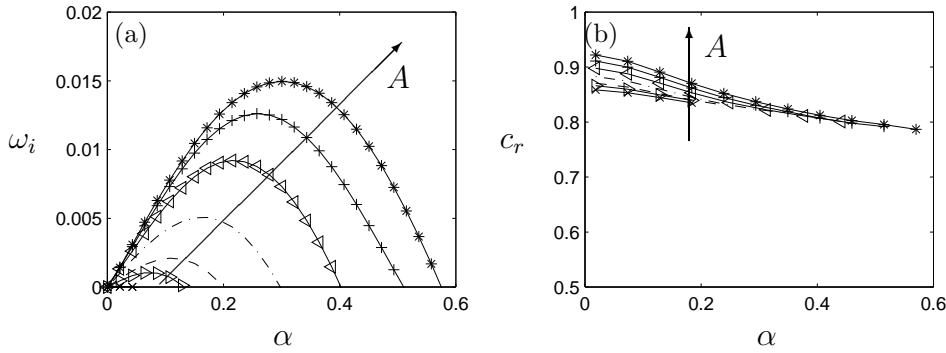


FIGURE 18. Temporal growth rate (a) and phase speed (b) versus streamwise wavenumber for the subharmonic sinuous modes for different amplitudes of the primary disturbance (— \times — $A=0.256$, — \triangleright — $A=0.272$, - - - $A=0.288$, - - - - $A=0.317$, — \triangleleft — $A=0.345$, —+— $A=0.364$, —*— $A=0.373$).

The behaviour of the amplification factor of the subharmonic modes for different streamwise wavenumbers and different amplitudes of the primary disturbance is shown in figure 18(a). For amplitudes larger than about 0.30, the subharmonic symmetry produces lower maximum growth rates than the fundamental symmetry. Note, however, that for lower amplitudes the sinuous subharmonic symmetry represents the most unstable mode. The phase speed for the subharmonic symmetry, displayed in figure 18(b), is larger than in the fundamental case and the waves are slightly more dispersive.

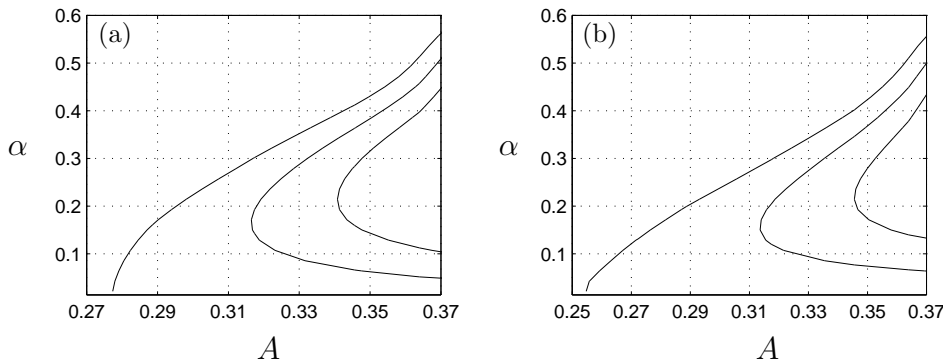


FIGURE 19. Neutral curves for streak instability in the (A, α) -plane for (a) fundamental sinuous mode, (b) subharmonic sinuous mode (contour levels: $\omega_i=0, 0.0046, 0.0092$).

4.3. The neutral conditions of streak's breakdown

A study has been conducted to identify the marginal conditions of breakdown, with each neutral point $\omega_i = 0$ calculated for a range of α by means of the complex integration technique discussed in section 2.3. The steady base velocity profiles obtained with the DNS at $x=2$ are used here. The results are displayed in figures 19(a-b) for the two sinuous symmetries, together with contour levels of constant growth rates.

It is immediately observed that a streaks amplitude of about 26% of the free-stream speed is needed for breakdown to occur. Although this critical value is achieved for small values of α (where the parallel flow assumption becomes questionable) we are roughly around the values reported by P. H. Alfredsson (private communication, 1998), who stated that "amplitudes of at least 20%" are needed for an instability of the streaks to emerge, and by Bakchinov *et al.* (1995) who in their experiments produced streaks with $A \approx 20\%$ and generated their controlled excitation with a vibrating ribbon. In the case of plane Poiseuille flow, the experiments of Elofsson *et al.* (1999) show that the threshold amplitude for streaks' breakdown is 35%, irrespective of the Reynolds number. This Reynolds-number independence was also observed in direct numerical simulations of Couette flow by Kreiss, Lundbladh & Henningson (1994) who reported that "the disturbances in the calculations are found to reach an amplitude of order one for all Reynolds numbers before the rapid secondary instability sets in".

One can notice that the subharmonic mode is unstable for lower amplitudes than the fundamental mode and that the growth rates for larger amplitudes are quite close for the two symmetries. The direct numerical simulations and experiments of oblique transition in a boundary layer conducted by Berlin, Lundbladh & Henningson (1994) and Berlin, Wiegel & Henningson (1999)

show that a subharmonic breakdown of the streaks precedes transition to turbulence.

We do not present any results for the varicose instabilities here. In fact, both the fundamental and the subharmonic symmetries resulted in weak instabilities for amplitudes larger than $A=0.37$ with growth rates smaller than one fifth of the corresponding sinuous growth rates. Therefore a breakdown scenario triggered by a varicose instability seems unlikely.

It appears then that there is not a dominating mode but rather that fundamental and detuned sinuous instabilities have the same probability of being observed. Hence, the knowledge provided by these results must be combined with that of the inflow disturbance spectrum, i.e. the prevailing receptivity conditions. The present study furnishes possible scenarios which should be confirmed by careful experiments, i.e. with controlled harmonic disturbances to try and trigger specific modes.

5. Conclusions

We have investigated one of the mechanisms which is a possible precursor of transition to turbulence in a boundary layer, namely the linear instability of streaks produced by the non-modal streamwise evolution of free-stream disturbances. Such a breakdown has been observed in experiments carried out by the Swedish (Westin *et al.* 1994; Alfredsson & Matsubara 1996) and the Russian groups (Gulyaev *et al.* 1989; Bakchinov *et al.* 1995): they generated streaky structures and visualized their development, breakdown and the formation of turbulent spots, via smoke injection.

There is starting to be a good correspondence between experiments and theory, and most of the segments of transition induced by the breakdown of streaks are now elucidated (at least qualitatively). Our study aims at the modelling of only one part of this process. More complete pictures are starting to emerge, often based on simple model systems, particularly for the description of the self-sustained process that makes near-wall turbulence viable (for a recent account refer to the book by Panton 1997). Although similarities exist between the wall turbulence process and the breakdown of laminar streaks, it is best not to draw definite parallels because of the widely different space and time scales involved in the two cases.

Clearly, other steps can be envisioned to lead to early transition to turbulence (i.e. strong nonlinearities, resonant interactions, etc.) and the present work represents but one brick in the building of a comprehensive picture. One has to further appreciate the fact that in an actual experiment irregular streaky structures are often observed, i.e. with non-uniform spacing and with neighbouring streaks in different stages of development, see Bottin, Dauchot & Daviaud (1998) for an example in plane Couette flow. Thus, these structures do not necessarily become unstable together at a given x -position, but their breakdown will likely occur in an irregular manner. These aspects are linked to the flow receptivity, the understanding of which is, hence, crucial. For recent progress

in this direction the reader is referred to Luchini & Bottaro (1998) and Airiau & Bottaro (1998).

The local, large Reynolds number limit has been considered here, with the implication that this simplified approach captures the essential features of the instability. The inviscid assumption means that one has to be careful in choosing the integration path for the eigenvalue calculation, and a simple procedure for identifying the singularities in the complex y -plane and for integrating around them has been outlined. With our approach, inspired by Lin (1944), neutral and damped inviscid modes can be computed, and a quasi-linear behaviour of the growth rate of the instability with the streak's amplitude is found, in agreement with the careful channel flow measurements by Elofsson *et al.* (1999).

We have shown here that both the linear and nonlinear spatial development of optimal streamwise streaks are well described by the boundary layer approximation and, as a consequence, Reynolds number independent for large enough Reynolds numbers. This results in a boundary layer scaling property that couples the streamwise and spanwise scales, implying that the same solution is valid for every combination of x and β such that the product $x\beta^2$ stays constant. The parameter study of streak instability is therefore representative of a wide range of intermediate values of β for which saturation occurs at a reasonable x : large enough so that the boundary layer approximation may still be valid and small enough so that Tollmien–Schlichting waves may not play a significant role.

The different modes of instability have been catalogued and studied. At a preliminary stage secondary instability calculations of the shape-assumption-approximated mean fields were carried out; however, most results presented here are performed employing the fully nonlinear mean fields. In comparing the two levels of approximations we conclude that the shape assumption must be abandoned in secondary instability studies of streamwise streaks in flat-plate boundary layers. The secondary instability results are very sensitive to a slight change in the shape of the mean field velocity profile and, even if the sinuous modes are reasonably well captured by the shape assumption, the growth rates of varicose modes are widely over-predicted.

When considering the nonlinear mean field we find that the sinuous modes are by far the dominating instabilities. The varicose modes become unstable only for very large amplitudes (around 37% of the free-stream speed) and should, therefore, be rarely observed in natural transition. This is in agreement with DNS and experiments, where the sinuous modes of instability are most often reported for the streak breakdown.

Noticeable is the fact that the sinuous, detuned instability waves can be more amplified than the fundamental modes. The subharmonic modes are in fact found to first become unstable with a critical streak amplitude of about 26% of the free-stream velocity. Plots of the eigenfunctions for fundamental and subharmonic modes demonstrate clearly that the instability is concentrated

around the critical layer, and both types of sinuous modes of breakdown are found to be almost non-dispersive. When the streak amplitude is large enough (around 30% of the free-stream velocity) both the fundamental and detuned modes have positive growth rates; thus, they might both be observed and to decide on their downstream fate is a matter of environmental bias. It is noteworthy that both experiments (Bakchinov *et al.* 1995) and DNS (Berlin *et al.* 1994) did show subharmonic breakdown of the streaks, although neither paper stated so explicitly.

Neutral curves have been obtained here in the amplitude–streamwise wave-number plane; their identification should prove useful for controlling transition and near-wall turbulence.

Future experiments under controlled conditions may attempt to trigger some of the modes described here. Also, an interesting direction of future research concerns the search for a possible absolute instability of the streaks. Finding a self-sustaining instability mechanism could provide a firmer connection with the birth of turbulent spots.

Acknowledgments

We thank Theo Randriarifara for making his stability code available for some of the validation tests, Paolo Luchini and Peter Schmid for interesting and fruitful discussions, and the referees for valuable comments that helped us produce a more physically relevant account of the breakdown of boundary layer streaks. Part of the work was performed during the first author’s stay in Toulouse, supported by “Internationaliseringsmedel för Doktorander” dnr 930-766-95, dossier 71, at the Royal Institute of Technology.

References

- AIRIAU, C. & BOTTARO, A. 1998 Receptivity of Tollmien-Schlichting waves via adjoint PSE. Presented at the EUROMECH colloquium 380: *Laminar-Turbulent Transition Mechanisms and Prediction*, Göttingen, Germany, September 14-17, 1998.
- ALFREDSSON, P. H. & MATSUBARA, M. 1996 Streaky structures in transition In *Proc. Transitional Boundary Layers in Aeronautics*. (ed. R. A. W. M. Henkes & J. L. van Ingen), pp. 373-386, Royal Netherlands Academy of Arts and Sciences. Elsevier Science Publishers.
- ANDERSSON, P., BERGGREN, M. & HENNINGSON, D. S. 1999a Optimal disturbances and bypass transition in boundary layers. *Phys. Fluids* **11**, 134.
- ANDERSSON, P., BOTTARO, A., HENNINGSON, D. S. & LUCHINI, P. 1999b Secondary instability of boundary layer streaks based on a shape assumption. *TRITA-MEK Rep.* 199:13. Department of Mechanics, The Royal Institute of Technology, Stockholm, Sweden.

- BAKCHINOV, A. A., GREK, G. R., KLINGMANN, B. G. B. & KOZLOV, V. V. 1995 Transition experiments in a boundary layer with embedded streamwise vortices. *Phys. Fluids* **7**, 820.
- BAYLY, B. J., ORSZAG, S. A. & HERBERT, T. 1988 Instability mechanisms in shear flow transition. *Ann. Rev. Fluid Mech.* **20**, 359.
- BERLIN, S. & HENNINGSON, D. S. 1999 A new nonlinear mechanism for receptivity of free-stream disturbances. *Phys. Fluids* **11**, 3749.
- BERLIN, S., LUNDBLADH, A. & HENNINGSON, D. S. 1994 Spatial simulations of oblique transition in a boundary layer. *Phys. Fluids* **6**, 1949.
- BERLIN, S., WIEGEL, M. & HENNINGSON, D. S. 1999 Numerical and experimental investigations of oblique boundary layer transition. *J. Fluid Mech.* **393**, 23.
- BERTOLOTI, F. P., HERBERT, T. & SPALART, P. R. 1992 Linear and nonlinear stability of the Blasius boundary layer. *J. Fluid Mech.* **242**, 441.
- BLACKWELDER, R. F. 1983 Analogies between transitional and turbulent boundary layers. *Phys. Fluids* **26**, 2807.
- BOBERG, L. & BROSA, U. 1988 Onset of turbulence in a pipe. *Z. Naturforschung* **43a**, 697.
- BOIKO, A. V., KOZLOV, V. V., SYZRANTSEV, V. V. & SHCHERBAKOV, V. A. 1997 A study of the influence of internal structure of a streamwise vortex on the development of travelling disturbances inside it. *Thermoph. and Aeromech.* **4**, 343.
- BOTTARO, A. & KLINGMANN, B. G. B. 1996 On the linear breakdown of Görtler vortices. *Eur. J. Mech., B/Fluids.* **15**, 301.
- BOTTIN, S., DAUCHOT, O. & DAVIAUD, F. 1998 Experimental evidence of streamwise vortices as finite amplitude solutions in transitional plane Couette flow. *Phys. Fluids* **10**, 2597.
- BUTLER, K. M. & FARRELL, B. F. 1992 Three-dimensional optimal perturbations in viscous shear flow. *Phys. Fluids A* **4**, 1637.
- DAUCHOT, O. & DAVIAUD, F. 1995 Finite amplitude perturbation and spots growth mechanism in plane Couette flow. *Phys. Fluids* **7**, 335.
- DRAZIN, P. G. & REID, W. H. 1981 *Hydrodynamic Stability*. Cambridge University Press.
- ELLINGSEN, T. & PALM, E. 1975 Stability of linear flow. *Phys. Fluids* **18**, 487.
- ELOFSSON, P. A., KAWAKAMI, M. & ALFREDSSON, P. H. 1999 Experiments on the stability of streamwise streaks in plane Poiseuille flow. *Phys. Fluids* **11**, 915.
- GASTER, M. 1962 A note on the relation between temporally-increasing and spatially-increasing disturbances in hydrodynamic stability. *J. Fluid Mech.* **14**, 222.
- GULYAEV, A. N., KOZLOV, V. E., KUZNETSOV, V. R., MINEEV, B. I., & SEKUNDOV, A. N. 1989 Interaction of a laminar boundary layer with external turbulence. *Izv. Akad. Nauk SSSR, Mekh. Zhid. Gaza.* **5**, 55. (in Russian, English transl. 1990 in *Fluid Dyn.* **24**:5, 700)
- GUSTAVSSON, L. H. 1991 Energy growth of three-dimensional disturbances in plane Poiseuille flow. *J. Fluid Mech.* **224**, 241.
- HALL, P. & HORSEMAN, N. J. 1991 The linear inviscid secondary instability of longitudinal vortex structures in boundary-layers. *J. Fluid Mech.* **232**, 357.
- HAMILTON, J. M., KIM, J. & WALEFFE, F. 1995 Regeneration mechanisms of near-wall turbulence structures. *J. Fluid Mech.* **287**, 317.

- HENNINGSON, D. S. 1987 Stability of parallel inviscid shear flow with mean spanwise variation. *Tech. Rep.* FFA-TN 1987-57. Aeronautical Research Institute of Sweden, Bromma.
- HENNINGSON, D. S. 1995 Bypass transition and linear growth mechanisms. In *Advances in Turbulence V* (ed. R. Benzi). Kluwer.
- HENNINGSON, D. S. 1996 Comment on "Transition in shear flows. Nonlinear normality versus non-normal linearity" [Phys. Fluids 7 3060 (1995)] *Phys. Fluids* **8**, 2257.
- HENNINGSON, D. S., LUNDBLADH, A. & JOHANSSON, A. V. 1993 A mechanism for bypass transition from localized disturbances in wall bounded shear flows. *J. Fluid Mech.* **250**, 169.
- HENNINGSON, D. S. & REDDY, S. C. 1994 On the role of linear mechanisms in transition to turbulence. *Phys. Fluids* **6**, 2862.
- HERBERT, T. 1988 Secondary instability of boundary layers. *Ann. Rev. Fluid Mech.* **20**, 487.
- HULTGREN, L. S. & GUSTAVSSON, L. H. 1981 Algebraic growth of disturbances in a laminar boundary layer. *Phys. Fluids* **24**, 1000.
- JIMENEZ, J. & MOIN, P. 1991 The minimal flow unit in near wall turbulence. *J. Fluid Mech.* **225**, 221.
- JIMENEZ, J. & PINELLI, A. 1999 The autonomous cycle of near wall turbulence. *J. Fluid Mech.* **389**, 335.
- KENDALL, J. M. 1985 Experimental study of disturbances produced in a pre-transitional laminar boundary layer by weak free-stream turbulence. AIAA Paper 85-1695.
- KENDALL, J. M. 1990 Boundary layer receptivity to free-stream turbulence. AIAA Paper 90-1504.
- KIM, J., MOIN, P. & MOSER, R. 1987 Turbulence statistics in fully developed channel flow *J. Fluid Mech.* **177**, 133.
- KREISS, G., LUNDBLADH, A. & HENNINGSON, D. S. 1994 Bounds for threshold amplitudes in subcritical shear flows. *J. Fluid Mech.* **270**, 175.
- LANDAHL, M. T. 1975 Wave breakdown and turbulence. *SIAM J. Appl. Math* **28**, 735.
- LANDAHL, M. T. 1980 A note on an algebraic instability of inviscid parallel shear flows. *J. Fluid Mech.* **98**, 243.
- LE CUNFF, C. & BOTTARO, A. 1993 Linear stability of shear profiles and relation to the secondary instability of the Dean flow. *Phys. Fluids A* **5**, 2161.
- LI, F. & MALIK, M. R. 1995 Fundamental and subharmonic secondary instabilities of Görtler vortices. *J. Fluid Mech.* **297**, 77.
- LIN, C. C. 1944 On the stability of two-dimensional parallel flows. *Proc. Nat. Acad. Sci.* **30**, 316.
- LIN, C. C. 1955 *The Theory of Hydrodynamic Stability*. Cambridge University Press.
- LUCHINI, P. 2000 Reynolds-number-independent instability of the boundary layer over a flat surface: optimal perturbations. Accepted *J. Fluid Mech.* **404**, 289.
- LUCHINI, P. & BOTTARO, A. 1998 Görtler vortices: a backward-in-time approach to the receptivity problem. *J. Fluid Mech.* **363**, 1.

- LUNDBLADH, A., BERLIN, S., SKOTE, M., HILDINGS, C., CHOI, J., KIM, J. & HENNINGSON, D. S. 1999 An efficient spectral method for simulation of incompressible flow over a flat plate. *TRITA-MEK Technical Report* 1999:11, Royal Institute of Technology, Stockholm, Sweden
- LUNDBLADH, A. & JOHANSSON, A. V. 1991 Direct simulation of turbulent spots in plane Couette flow. *J. Fluid Mech.* **229**, 499.
- MALIK, M. R., ZANG, T. A. & HUSSAINI, M. Y. 1985 A spectral collocation method for the Navier-Stokes equations *J. Comp. Phys.* **61**, 64.
- MATSUBARA, M & ALFREDSSON, P. H. 1998 Secondary instability in rotating channel flow. *J. Fluid Mech.* **368**, 27.
- MORKOVIN, M. V. & RESHOTKO, E. 1990 Dialogue on progress and issues in stability and transition research. In *Laminar-Turbulent Transition* (ed. D. Arnal & R. Michel). Springer.
- ORSZAG, S. A. & PATERA, A. T. 1983 Secondary instability of wall-bounded shear flows. *J. Fluid Mech.* **128**, 347.
- PANTON, R. L. 1997 (Ed.) *Self-sustaining mechanisms of wall turbulence*. Computational Mechanics Publications, Southampton.
- PARK, D. S. & HUERRE, P. 1995 Primary and secondary instabilities of the asymptotic suction boundary layer on a curved plate. *J. Fluid Mech.* **283**, 249.
- RANDRIARIFARA, T. 1998 The instability of streamwise vortices in a curved, rotating channel. *submitted to Phys. Fluids*.
- REDDY, S. C. & HENNINGSON, D. S. 1993 Energy growth in viscous channel flows. *J. Fluid Mech.* **252**, 209.
- REDDY, S. C., SCHMID, P. J., BAGGETT, J. S. & HENNINGSON, D. S. 1998 On the stability of streamwise streaks and transition thresholds in plane channel flows. *J. Fluid Mech.* **365**, 269.
- RESHOTKO, E. 1994 Boundary layer instability, transition and control. AIAA Paper 94-0001.
- ROMANOV, V. A. 1973 Stability of plane-parallel Couette flow. Translated in *Functional Anal. & Its Applics* **7**, 137.
- SCHOPPA, W. & HUSSAIN, F. 1997 Genesis and dynamics of coherent structures in near-wall turbulence: a new look. In *Self-Sustaining Mechanisms of Wall Turbulence*. (ed. R. L. Panton), pp. 385-422. Computational Mechanics Publications, Southampton.
- SCHOPPA, W. & HUSSAIN, F. 1998 Formation of near-wall streamwise vortices by streak instability. AIAA Paper 98-3000.
- SWEARINGEN, J. D. & BLACKWELDER, R. F. 1987 The growth and breakdown of streamwise vortices in the presence of a wall. *J. Fluid Mech.* **182**, 255.
- TILLMARK, N. & ALFREDSSON, P. H. 1992 Experiments on transition in plane Couette flow. *J. Fluid Mech.* **235**, 89.
- TREFETHEN, L. N., TREFETHEN, A. E., REDDY, S. C. & DRISCOLL, T. A. 1993 Hydrodynamic stability without eigenvalues. *Science* **261**, 578.
- USTINOV, M. V. 1998 Stability of streaky structures in boundary layer. Presented at the EUROMECH colloquium 380: *Laminar-Turbulent Transition Mechanisms and Prediction*, Göttingen, Germany, September 14-17 1998.
- WALEFFE, F. 1995 Hydrodynamic stability and turbulence: Beyond transients to a self-sustaining process. *Stud. Appl. Math.* **95**, 319.

- WALEFFE, F. 1997 On a self-sustaining process in shear flows. *Phys. Fluids A* **9**, 883.
- WESTIN, K. J. A., BOIKO, A. V., KLINGMANN, B. G. B., KOZLOV, V. V. & ALFREDSSON, P. H. 1994 Experiments in a boundary layer subject to free-stream turbulence. Part I. Boundary layer structure and receptivity. *J. Fluid Mech.* **281**, 193.
- YU, X. & LIU, J. T. C. 1991 The secondary instability in Goertler flow. *Phys. Fluids A* **3**, 1845.

Paper 2

2

On the convectively unstable nature of optimal streaks in boundary layers

By Luca Brandt[†], Carlo Cossu^{*}, Jean-Marc Chomaz^{*}, Patrick Huerre^{*} and Dan S. Henningson^{†‡}

[†]Department of Mechanics, Royal Institute of Technology (KTH), S-100 44 Stockholm, Sweden

^{*}Laboratoire d'Hydrodynamique (LadHyX), CNRS-École Polytechnique, F-91128 Palaiseau, France

[‡] FOI, The Swedish Defense Research Agency, Aeronautics Division, SE-172 90 Stockholm, SWEDEN

The objective of the study is to determine the absolute/convective nature of the secondary instability experienced by finite-amplitude streaks in the flat-plate boundary layer. A family of parallel streaky base flows is defined by extracting velocity profiles from the direct numerical simulations of nonlinearly saturated optimal streaks performed by Andersson, Brandt, Bottaro & Henningson (2001). The computed impulse response of the streaky base flows is then determined as a function of streak amplitude and streamwise station. Both the temporal and spatio-temporal instability properties are directly retrieved from the impulse response wave packet, without solving the dispersion relation or applying the pinching point criterion in the complex wavenumber plane. The instability of optimal streaks is found to be unambiguously convective for all streak amplitudes and streamwise stations. It is more convective than the Blasius boundary layer in the absence of streaks: the trailing edge-velocity of a Tollmien-Schlichting wave packet in the Blasius boundary layer is around 35% of the free-stream velocity, while that of the wave packet riding on the streaky base flow is around 70%. This feature is due to the fact that the streak instability is primarily induced by the spanwise shear and the associated Reynolds stress production term is located further away from the wall, in a larger velocity region, than for the Tollmien-Schlichting instability. The streak impulse response consists of the sinuous mode of instability triggered by the spanwise wake-like profile, as confirmed by comparing the numerical results with the absolute/convective instability properties of the family of two-dimensional wakes introduced by Monkewitz (1988). The convective nature of the secondary streak instability implies that the type of bypass transition studied here involves streaks that behave as amplifiers of external noise.

1. Introduction

It is now well established that the existence of a pocket of absolute instability plays a crucial role in accounting for the occurrence of synchronized self-sustained oscillations, or global modes, in a variety of spatially developing shear flows such as wakes, hot jets, counter-flow mixing layers, etc. For a review of these concepts, the reader is referred to Huerre (2000). The theoretical and experimental studies of Lingwood (1995, 1996) have more recently demonstrated that in the case of the rotating disk boundary layer, a local change in the nature of the primary instability from convective to absolute surprisingly coincides with the transition from laminar flow to turbulence. In the same spirit as the latter transition studies, we would like to investigate the possibility that a related scenario might occur for the secondary instability of the nonlinearly saturated streaks which emerge from the spatial evolution of optimal perturbations in the flat plate boundary layer. In other words, are the non linearly saturated streaks determined by Andersson, Brandt, Bottaro & Henningson (2001) convectively unstable or absolutely unstable ?

According to the theoretical and experimental studies of Gaster (1975) and Gaster & Grant (1975), the primary Tollmien-Schlichting instability is unambiguously convective in nature: the impulse response of the Blasius boundary layer takes the form of a wave packet that is convected in the downstream direction. It is known, however, since the work of Butler & Farrell (1992) among others, that the class of perturbations which sustain maximum temporal growth in the linear regime takes the shape of spanwise periodic streamwise vortices. Such *optimal* perturbations give rise at maximum growth to a spanwise periodic distribution of low and high-speed streaks. A similar conclusion holds if one considers instead optimal perturbations of maximum spatial growth, as demonstrated by Andersson, Berggren & Henningson (1999) and Luchini (2000). A comprehensive presentation of hydrodynamic instability and transient growth phenomena in shear flows is given in the book by Schmid & Henningson (2001).

Spatial optimal perturbations (from a linear point of view) may be fed as upstream forcing into a direct numerical simulation of the flow along a flat plate, as carried out by Andersson *et al.* (2001). Optimal disturbances give rise to nonlinearly saturated streamwise streaks, which are spanwise periodic and therefore amenable to a secondary Floquet instability formulation, if the flow is assumed to be locally parallel. The main findings of this local inviscid secondary instability analysis are as follows: there exists a critical streak amplitude around 26% of the free-stream velocity, above which the streaky base flow becomes unstable to sinuous streamwise travelling waves. The most amplified perturbation is either a fundamental mode (with the same spanwise wavelength as the streaks) or a subharmonic mode (with twice the spanwise wavelength of the streaks), depending on the streak amplitude. The fundamental and subharmonic modes display quantitatively similar temporal instability characteristics in term of both maximum growth rate and band of unstable streamwise wavenumbers. Streaks only become unstable to varicose streamwise

travelling waves when their amplitude exceeds 37% of the free-stream velocity. The objective of our study is precisely to extend the temporal instability analysis of Andersson *et al.* (2001) by examining the spatio-temporal features of the impulse response. If a local absolute instability were found, one could relax the parallel flow assumption and look for self-sustained global modes in the spatially evolving boundary layer, as done by Pier & Huerre (2001) for a two-dimensional wake. In fact, it is possible to show that for flows slowly varying in the streamwise direction the existence of a pocket of absolute instability is a necessary condition for a global instability to occur (Chomaz, Huerre & Redekopp 1991).

The investigations discussed above as well as the present work are motivated by the need to understand the physics of bypass transition in boundary layers with high levels of free-stream turbulence (Morkovin & Reshokto 1990; Saric, Reed & Kerschen 2002; Wu & Choudari 2001). In this context, Matsubara & Alfredsson (2001) have recently demonstrated experimentally that in boundary layers subject to free-stream turbulence the appearance of streaks leads to unsteady oscillations and breakdown into turbulent spots. The reader is referred to this paper for a review of the recent literature on this topic. In order to identify the physical mechanisms responsible for breakdown, it appears essential to determine if the observed oscillations of streaks grow *in situ*, as in an absolute instability. If this were the case, one could pin down the onset of the oscillations and possibly of transition to the particular downstream station where the secondary instability shifts from convective to absolute. *A contrario*, if the instability were to be convective, i.e. advected downstream, the development of the oscillations would strongly depend on the ambient upstream noise level. The perturbations considered here are steady and optimal only in the linear sense and therefore they represent one of several plausible approximations of the streaks observed in boundary layers subject to relatively high free-stream turbulence. However, it is important to note that in Matsubara & Alfredsson (2001) the wall-normal shape of the linearly optimal disturbance theoretically determined by Andersson *et al.* (1999) and Luchini (2000) is found to be remarkably similar to the measured u_{rms} values. The streak can be regarded as a 'pseudo-mode' triggered in a boundary layer subject to significant outside disturbances.

The experiments of Swearingen & Blackwelder (1987) were crucial in documenting the emergence of streaks with inflectional velocity profiles due to the formation of Görtler vortices in the boundary layer on a concave wall. This investigation demonstrated that the time-dependent fluctuations appearing in the flow are more closely correlated with the spanwise shear than with the wall-normal shear. The secondary linear instability of Görtler vortices was first analyzed theoretically by Hall & Horseman (1991). A generalized Rayleigh equation was derived for a class of three-dimensional base states consisting of the streak profiles generated by Görtler vortices. The fastest growing secondary mode was then found to be sinuous in character. Similar features prevailed

for the secondary instability of temporally-evolving nonlinear Görtler vortices, as demonstrated theoretically by Park & Huerre (1995). These authors confirmed that the dominant sinuous mode is primarily induced by the spanwise shear while the varicose mode is triggered by the wall-normal shear. The corresponding analysis of the secondary instability of streamwise-developing Görtler vortices was performed by Bottaro & Klingmann (1996). This study led to a satisfactory prediction of the dominant frequency and sinuous perturbation velocity field observed by Swearingen & Blackwelder (1987).

The widespread occurrence of streaks in various flow configurations has very recently led Asai, Minagawa & Nishioka (2002) to examine experimentally the spatial response of a single low-speed streak in a laminar boundary layer submitted to a time-harmonic excitation of sinuous or varicose type. The growth of the sinuous mode was observed to evolve into a train of quasi-streamwise vortices with vorticity of alternate sign. By contrast, the varicose mode led to the formation of hairpin structures made up of a pair of counter-rotating vortices. Wu & Luo (2001) proposed a new mechanism to explain the appearance of the varicose instability for low amplitudes of the streaks.

The possibility that in a given flow configuration, primary and secondary instabilities might display a distinct absolute/convective character was recognized by Huerre (1988) in the framework of a simple Ginzburg-Landau model equation. In many situations, the primary instability gives rise to spatially periodic saturated states. The secondary instability of such basic flows then typically requires the implementation of Floquet theory. The generalization of the classical absolute/convective instability analysis of Bers (1983) to the case of spatially periodic flows has been comprehensively carried out by Brevdo & Bridges (1996). Their mathematical formulation provides in particular a precise convective/absolute instability criterion applicable to general spatially periodic flows. The implementation of such a pinching point criterion is however non-trivial and it has only been applied to model evolution equations, as in Brevdo & Bridges (1996) and Chomaz, Couairon & Julien (1999). For “real” flows, the task which consists in verifying the proper pinching of spatial branches appears formidable. Our approach will here be radically different: we deliberately remain in physical space and retrieve the spatio-temporal instability characteristics *a posteriori* from direct numerical simulations of the linear impulse response. This strategy has been well proven by Delbende, Chomaz & Huerre (1998) in the context of the primary instability in swirling jets and wakes. The procedure yields results which compare extremely favorably with the more orthodox pinching point criterion, as applied in swirling jets and wakes by Olendraru, Sellier, Rossi & Huerre (1999). The impulse response method has also been successfully applied by Brancher & Chomaz (1997) to examine secondary absolute/convective instabilities in a streamwise periodic array of Stuart vortices.

The present investigation is most closely related to the recent analysis of Koch (2002) on the absolute/convective nature of the secondary instability sustained by cross-flow vortices in three-dimensional boundary layers. The latter author determined the spatio-temporal characteristics of secondary fundamental instability modes, i.e. of the same wavelength as the cross-flow vortices, in a direction perpendicular to the vortex axis. The implementation of a saddle-point continuation method in the complex wavenumber plane leads to the conclusion that the secondary instability is convective.

The paper is organized as follows. In section 2, we summarize the main characteristics of the nonlinearly saturated streamwise-developing streaks determined in the numerical simulations of Andersson *et al.* (2001). Parallel streaks are then extracted from the simulations in order to define an appropriate family of base flows for the linear impulse calculations. The diagnostic tools which are essential in retrieving the temporal and spatio-temporal features of the secondary instability are presented, as well as the numerical methods necessary in the implementation of the impulse response simulations. The nature of the impulse response wave packet is analyzed in section 3. The temporal instability properties are first retrieved and compared with available inviscid dispersion relation calculations. The bulk of the section concentrates on the determination of the characteristic propagation velocities and growth rates of the wave packet as a function of streak amplitude and streamwise station. In the discussion of section 4, we propose a physical explanation for the results in terms of the distribution of the Reynolds stress production term in a cross-stream plane. Finally the crucial role of the spanwise shear in determining the propagation velocities of the wave packet is ascertained by comparison of our results with those pertaining to the family of two-dimensional wakes defined in Monkewitz (1988). The paper ends with a summary of the main conclusions.

2. Flow configuration and spatio-temporal diagnostic tools

2.1. Base flow and physical configuration

We consider the boundary layer over a flat plate and define the local Reynolds number, $Re = (U_\infty \delta_*)/\nu$, by means of the free-stream velocity U_∞ and the local Blasius boundary layer displacement thickness δ_* . The analysis concerns the linear secondary instability of the streaks resulting from the nonlinear evolution of the spatial optimal perturbation in a zero pressure gradient boundary layer. This base flow was computed in Andersson *et al.* (2001) by solving the full Navier–Stokes equations. In that work, the complete velocity field representing the steady linear optimal perturbation calculated by Andersson *et al.* (1999) was used as input close to the leading edge and its downstream nonlinear development was monitored for different upstream amplitudes of the input disturbance. The flow was assumed periodic in the spanwise direction and only one spanwise wavelength of the optimal perturbation considered. To quantify the size of this primary disturbance field at each streamwise position, an

amplitude A was defined in Andersson *et al.* (2001) as

$$A(X) = \frac{1}{2} \left[\max_{y,z} \left(U(X, y, z) - U_B(X, y) \right) - \min_{y,z} \left(U(X, y, z) - U_B(X, y) \right) \right], \quad (1)$$

where $U_B(X, y)$ is the Blasius profile and $U(X, y, z)$ is the total streamwise velocity in the presence of streaks. The streamwise velocity U is made non dimensional with respect to the free-stream velocity U_∞ . The streamwise distance X is scaled with the inlet displacement thickness δ_{*0} at the Reynolds number $Re = 468.4$, i.e. at the inflow station $X = 0$ in the spatial simulations of Andersson *et al.* (2001). The wall-normal and spanwise variables y and z are made non dimensional with respect to the local Blasius boundary layer displacement thickness $\delta_*(X)$. The spanwise wavenumber is taken to be $\beta_0 = 0.48$ at $X = 0$, which corresponds to linearly optimally growing streaks at $X = 246$. The downstream nonlinear amplitude development for different upstream amplitudes is displayed in figure 1 (a), which reproduces figure 5 (b) of Andersson *et al.* (2001). In figure 1 (b), a typical nonlinearly saturated streak is illustrated by its streamwise velocity contour plot in the cross-stream (y, z) plane. The selected streamwise station is $X = 632$, which corresponds to $x/L = 2$ in the scaling adopted in Andersson *et al.* (2001) where $L = 1$ is the station of linear optimal growth, and the corresponding amplitude at this location is $A = 0.36$. This condition, indicated by a star in figure 1 (a), has been chosen because it is associated with the highest secondary instability temporal growth rate over all X stations along that amplitude curve. As observed in Andersson *et al.* (2001), regions of strong spanwise shear are formed on the sides of the low-speed region, which is also displaced further away from the wall during the saturation process.

We are interested in determining the local spatio-temporal instability properties of the streaks in the parallel flow approximation. In other words, one wishes to study the local instability characteristics of a basic flow which evolves slowly in the streamwise direction, as required in the boundary layer approximation. This assumption is justified since the instability is inviscid in nature and therefore leads to fast streamwise growth. A similar approach was followed in the case of Görtler vortices by Hall & Horseman (1991) and Bottaro & Klingmann (1996). The parallel flow assumption was further validated in the direct numerical simulations of Andersson *et al.* (2001): time harmonic disturbances introduced upstream on the streaks were found to evolve with the spatial growth rate of the underlying parallel base flow, within a good degree of approximation.

In the present study, we therefore choose to perform numerical simulations of the linear impulse response for a basic parallel flow which consists only of the total streamwise velocity $U(y, z)$, the wall-normal and spanwise velocities of $O(1/Re)$ being negligible. This basic parallel flow is extracted at different streamwise stations X from the spatial numerical simulations of Andersson *et al.* (2001). In order to compensate for viscous diffusion, a body

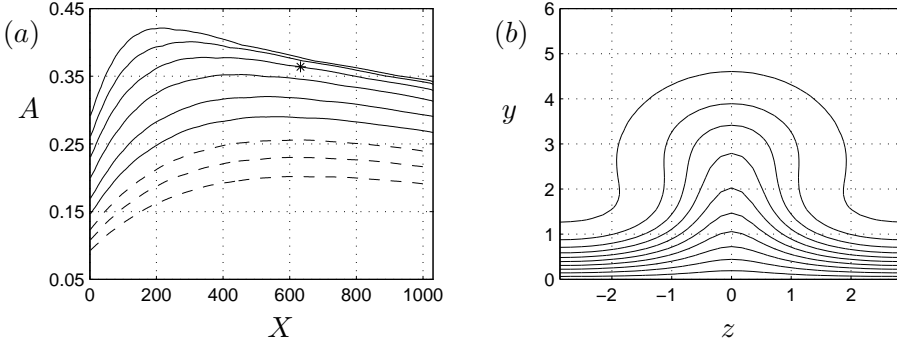


FIGURE 1. Base flow spatial simulations at $Re_0 = 468.4$, $\beta_0 = 0.48$. (a) Streak amplitude versus streamwise coordinate X for different upstream amplitudes $A = 0.09, 0.1, 0.12, 0.14, 0.16, 0.19, 0.22, 0.25, 0.28$ at $X = 0$. The three lower dashed curves correspond to stable streaks and the solid curves correspond to unstable streaks in some streamwise range. This plot reproduces figure 5(b) in Andersson *et al.* (2001). (b) Streamwise velocity contour plot of the nonlinear base flow in a (y, z) cross-stream plane at $X = 632$, $A = 0.36$, $Re = 1047$ for the condition indicated by a star in a). Maximum contour level 0.98, contour spacing 0.1.

force $-Re^{-1}\Delta U(y, z)$ is introduced in the numerical code so that the basic flow stays parallel and steady. The results of the local instability analysis are presented in terms of spatial and temporal variables x , y , z and t made non dimensional with respect to the local boundary layer displacement thickness δ_* and the free-stream velocity U_∞ .

According to classical Floquet theory (e.g. Nayfeh & Mook 1979), for any flow variable q , instability modes of the spanwise periodic basic flow $U(y, z)$ of spanwise wavelength λ_z may be sought in the form

$$q(x, y, z, t) = \tilde{q}(y, z) e^{i[k_x x + \delta k_z z - \omega t]}, \quad (2)$$

where $\tilde{q}(y, z)$ is spanwise periodic and has the same wavelength λ_z as $U(y, z)$, k_x is the streamwise wavenumber, ω is the circular frequency and δk_z is the detuning parameter defined in the range $|\delta k_z| \leq \pi/\lambda_z$. In the present investigation, we restrict our attention to perturbations q which have the same spanwise periodicity as the base flow, i.e. the detuning parameter is taken to be $\delta k_z = 0$. This reduction to the fundamental mode is numerically implemented by considering a total flow (basic flow plus perturbation) which is spanwise periodic of fundamental wavelength λ_z . In this framework, the eigenfunctions of the system depend both on the spanwise z -variable and on the wall-normal

y -variable. In the wall-normal direction, no-slip boundary conditions are imposed at the wall $y = 0$ and zero velocity perturbation at $y = y_{max}$, sufficiently high above the boundary layer.

To mimic forcing by a delta-function in time and space, the initial condition is defined in terms of a stream function as

$$\psi(x, y, z; 0) = A_\epsilon \bar{x} \bar{y}^3 \bar{z} \exp(-\bar{x}^2 - \bar{y}^2 - \bar{z}^2), \quad (3)$$

where $\bar{x} = (x - x_0)/l_x$, $\bar{y} = y/l_y$ and $\bar{z} = (z - z_0)/l_z$. The corresponding streamwise, wall-normal and spanwise velocity components are given by $(u, v, w) = (0, \psi_z, -\psi_y)$ and the amplitude A_ϵ is set to sufficiently low values in order to ensure a linear development of the perturbations over a numerical integration run. This was checked by comparing the evolutions obtained for two different values of A_ϵ . Typical values of the initial amplitude lie in the range $10^{-10} < A_\epsilon < 10^{-6}$. The length scales, $l_x = 5$, $l_y = 2$ and $l_z = 1.5$ have been chosen small enough to reproduce a localized impulse within the limits of a good resolution in the truncated spectral space of the numerical simulations. As an *a posteriori* test, it was verified that the initial condition contained all the physically relevant wavenumbers, typically twice the range of unstable streamwise wavenumbers. Note also that since the eigenfunctions depend on both y and z , a strong localization is not needed in these directions. Moreover, the disturbance is centered around $z = z_0$, which is chosen to lie off axis in one of the two regions of strongest spanwise shear (figure 1 *b*) so that no particular symmetry is enforced on the solution. The initial condition (3) consists of two counter-rotating streamwise vortex pairs. It has been used previously by Henningson, Lundbladh & Johansson (1993); Bech *et al.* (1998) and almost in the same form by Breuer & Haritonidis (1990). Not only is the parallel flow spanwise periodic, which implies the Floquet decomposition (2), but also it is symmetric with respect to the (x, y) plane. As a consequence, it admits two classes of normal modes: a sinuous mode with u, v antisymmetric and w symmetric in z , a varicose mode with u, v symmetric and w antisymmetric in z . As previously stated, the initial condition potentially excites these two types of disturbances.

2.2. Diagnostics

The technique developed by Delbende *et al.* (1998) and Delbende & Chomaz (1998) is now extended to the case of a three-dimensional unidirectional base flow. This method allows to retrieve the linear temporal and spatio-temporal instability features directly from the analysis of the simulated impulse response arising from the initial disturbance (3) described in the previous section. The analysis is thus performed in physical space according to the original definitions, without resorting to the spectral theory of absolute and convective instability. The procedure is only briefly outlined; for more details, the reader is referred to Delbende *et al.* (1998) and Delbende & Chomaz (1998).

Within a temporal framework the wavenumber k_x is given real and the frequency $\omega(k_x)$ is complex and unknown. Let us define the amplitude spectrum

of the perturbations

$$\tilde{e}(k_x, t) = \left(\int_0^{y_{max}} \int_0^{\lambda_z} |\tilde{q}(k_x, y, z, t)|^2 dy dz \right)^{1/2}, \quad (4)$$

where $q(x, y, z, t)$ may be any flow perturbation variable, e.g. a single velocity component or the square root of the total kinetic energy, and $\tilde{q}(k_x, y, z, t)$ its Fourier transform in the streamwise direction. For large times the asymptotic exponential behavior is attained and, if a well separated temporal branch is present, the temporal growth rate ω_i of each k_x -component is given by

$$\omega_i(k_x) \sim \frac{\partial}{\partial t} \ln \tilde{e}(k_x, t), \quad t \rightarrow \infty, \quad (5)$$

where ω_i is the imaginary part of ω . Recall here that, according to the temporal inviscid instability analysis presented in Andersson *et al.* (2001), only one unstable sinuous branch is expected to arise.

In the *spatio-temporal* formulation the development of the wave packet along rays of specific given velocity $x/t = v$ is considered. This is equivalent to the investigation of modes of real group velocity v , as reviewed, for instance, in Huerre & Rossi (1998) and Huerre (2000). In order to demodulate the wave packet and define its amplitude unambiguously, it is convenient, as in Delbende *et al.* (1998), to introduce the analytical complex field variable $\bar{q}(x, y, z, t)$ associated with $q(x, y, z, t)$ through the convolution

$$\bar{q}(x, y, z, t) = \left[\delta(x) + \frac{i}{\pi x} \right] * q(x, y, z, t), \quad (6)$$

where the symbol $*$ designates the convolution operator with respect to x . The complex field $\bar{q}(x, y, z, t)$ in effect generalizes the complex exponential representation of a sine wave to an arbitrary real function $q(x, y, z, t)$ (Roddier 1971). In wavenumber space, equation (6) reduces to

$$\bar{q}(k_x, y, z, t) = 2H(k_x)\tilde{q}(k_x, y, z, t), \quad (7)$$

where $H(k_x)$ is the Heavyside unit-step function. In other words, the Fourier transform of the analytical field is obtained by setting to zero all the Fourier modes of negative streamwise wavenumber. As in the temporal analysis, the integration of the analytical field \bar{q} in the cross-stream (y, z) plane then yields the amplitude Q defined by

$$Q(x, t) = \left(\int_0^{y_{max}} \int_0^{\lambda_z} |\bar{q}(x, y, z, t)|^2 dy dz \right)^{1/2}. \quad (8)$$

According to steepest-descent arguments (Bers 1983), the long-time behavior of the wave packet along each spatio-temporal ray $x/t = v$ is

$$Q(x, t) \propto t^{-1/2} e^{i[k_x(v)x - \omega(v)t]}, \quad t \rightarrow \infty, \quad (9)$$

where $k_x(v)$ and $\omega(v)$ represent the complex wavenumber and frequency travelling at the real group velocity $v = x/t$. For a detailed discussion of the meaning

of group velocity for unstable systems, the reader is referred to Huerre & Rossi (1998) among others. In (9), the real part of the exponential

$$\sigma(v) = \omega_i(v) - k_{x,i}(v)v \quad (10)$$

denotes the temporal growth rate observed while travelling at the group velocity v and it can be evaluated for large t directly from the amplitude Q in (9) as

$$\sigma(v) \sim \frac{\partial}{\partial t} \ln[t^{1/2} Q(vt, t)]. \quad (11)$$

In unstable flows, $\sigma > 0$ for some range of v . The curves $\sigma(v)$ contain all the information characterizing the spatio-temporal growth of the wave packet. Its extent, in fact, is delineated by the rays along which neutral waves are observed. These velocities are denoted v^- , the trailing edge velocity of the wave packet, and v^+ , the leading edge velocity of the wave packet, and they are formally defined by the conditions $\sigma(v^-) = \sigma(v^+) = 0$ and $v^- < v^+$. In the present case only one connected region of unstable group velocities is observed and the velocities v^- and v^+ are unambiguously defined. If $v^- > 0$, the wave packet is advected downstream and the base flow is convectively unstable. Conversely, if $v^- < 0$, the trailing edge moves upstream and the wave packet grows *in situ*. The base flow is then absolutely unstable. Finally, let v^{max} denote the spatio-temporal ray along which the largest temporal growth rate σ^{max} is observed. This quantity provides a measure of the propagation velocity of the center of the wave packet. According to Delbende *et al.* (1998) $\sigma^{max} = \omega_i(k_x^{max})$, i.e. the maximum temporal amplification rate coincides with its maximum spatio-temporal counterpart, which is attained for a real wavenumber k_x^{max} . This relation provides a further cross-check on the accuracy of the temporal and spatio-temporal analysis.

2.3. Numerical methods

The direct numerical simulations are performed with the code described in Lundbladh *et al.* (1999). Spectral methods are used to solve the three-dimensional, time-dependent, incompressible Navier–Stokes equations with the body force needed to remove the viscous diffusion of the base flow, as discussed in section 2.1. As in Delbende *et al.* (1998), we find it convenient to immerse the streamwise development of the wave packet in a streamwise periodic box which is sufficiently large so as to avoid “recirculation effects”. Consequently the computational domain is effectively periodic in both z - and x -directions. For the results presented here, streamwise lengths $L_x = 600$ and $L_x = 1200$ have been selected. A typical value of the box height is $y_{max} = 10$. The algorithm is similar to that of Kim, Moin & Moser (1987), i.e. Fourier representation in the streamwise and spanwise directions and Chebyshev polynomials in the wall-normal direction, together with a pseudo-spectral treatment of the non-linear terms. The time advancement used is a four-step low storage third-order Runge–Kutta scheme for the nonlinear terms and a second-order Crank–Nicholson method for the linear terms. Aliasing errors from the evaluation of

the nonlinear terms are removed by the $\frac{3}{2}$ -rule when the FFTs are calculated in the wall-parallel plane. In the wall-normal direction it has been found more convenient to increase resolution rather than to use dealiasing. In all the results presented below, $n_y = 97$ and $n_z = 32$ modes have been chosen in the wall-normal and spanwise direction respectively; in the streamwise direction $n_x = 512$ or $n_x = 1024$ modes have been deemed sufficient according to the length $L_x = 600$ or $L_x = 1200$ of the domain.

In order to evaluate the usual temporal growth rates and the temporal growth rates “at the velocity v ”, equations (5) and (11) are numerically discretized (Delbende *et al.* 1998; Delbende & Chomaz 1998) according to the expressions

$$\tilde{\omega}_i(k_x) \approx \frac{\ln[\tilde{e}(k_x, t_2)/\tilde{e}(k_x, t_1)]}{t_2 - t_1}, \quad (12)$$

$$\sigma(v) \approx \frac{\ln[Q(vt_2, t_2)/Q(vt_1, t_1)]}{t_2 - t_1} + \frac{\ln(t_2/t_1)}{2(t_2 - t_1)}. \quad (13)$$

In the above, t_1 and t_2 need to be large enough so that transient effects are negligible. For each streak amplitude under consideration different pairs t_1, t_2 , are selected in the evaluation of (12) and (13) until results have satisfactorily converged. The values of t_1, t_2 change from case to case, with the least unstable modes requiring longer integration times and therefore longer streamwise distances. For the maximum temporal growth rates, a typical integration time is $t_2 = 300$ with $t_2 - t_1 = 100$. For the lowest temporal growth rates, a typical integration time is $t_2 = 700$ with $t_2 - t_1 = 200$. The analytical signal $\bar{q}(x, y, z, t)$ of $q(x, y, z, t)$ defined in (6) is computed in spectral space $\bar{q}(k_x, y, z, t)$, where it reduces to setting to zero all the Fourier modes with negative wavenumber k_x . The uncertainty on all the results presented is at most 2%.

3. Streak linear impulse response

The streak impulse response is displayed in physical space in figure 2 for the particular base flow of figure 1 (*b*). The evolution in a plane parallel to the wall at a distance $y = 1.8$ is illustrated. The background color indicates the parallel base flow $U(y, z)$, with the low-speed region located at the center of the computational domain. The blue contour lines represent the wall-normal velocity of the impulse response wave packet at three different times $t = 0, t = 200$ and $t = 400$, so that the initial condition, defined by equation (3), can be readily seen. The emerging wave packet is sinuous with respect to the background streak, since its wall-normal velocity is antisymmetric in z . According to the temporal analysis of Andersson *et al.* (2001), the sinuous mode was indeed the only one found to be unstable for this particular streak. Note furthermore that the v -structures of the packet are bent in the downstream direction in the outer parts where the basic advection is larger. The downstream propagation of the wave packet appears to indicate that the streak instability is convective. This conclusion, however, is premature: the trailing edge velocity v^- of the wave

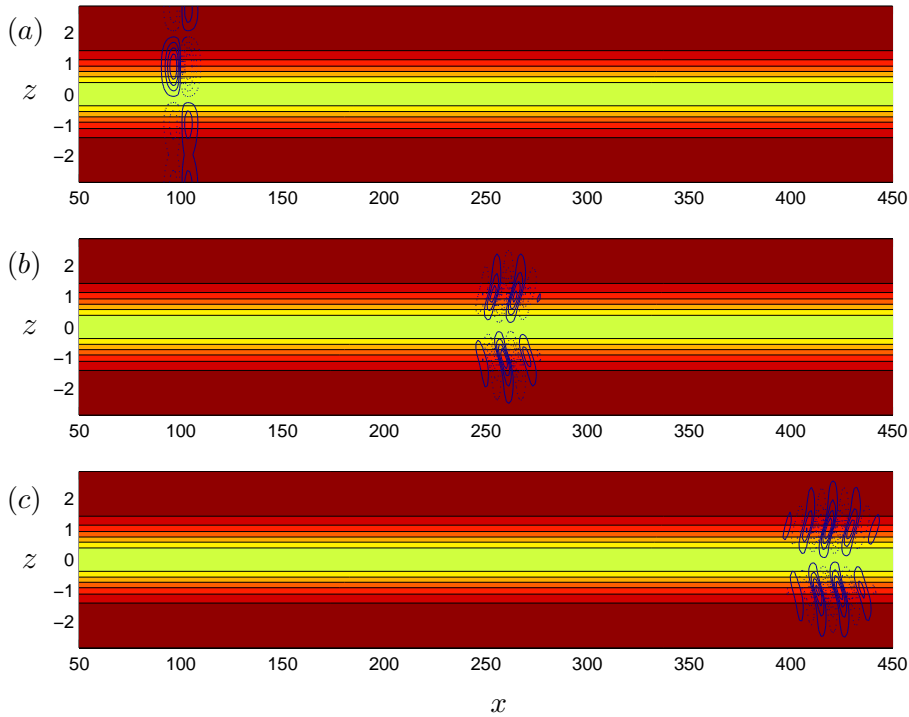


FIGURE 2. Streak impulse response of the base flow defined in figure 1 (*b*) in a plane parallel to the wall, at $y = 1.8$, for (*a*) $t = 0$; (*b*) $t = 200$ and (*c*) $t = 400$. The initial packet is centered around $z_0 = 0.85$. The background color represent the streamwise velocity of the base flow, with high to lower velocity ranging from red to yellow. The blue isolines indicate the wall-normal perturbation velocity; dotted lines denote negative values.

packet needs to be unambiguously determined. Figure 2 merely demonstrates that the crest of the wave packet is advected downstream.

3.1. Temporal instability

Temporal instability results are presented with the aim of comparing them to the inviscid analysis of Andersson *et al.* (2001) so that the present formulation may be validated. The amplitude spectrum $\tilde{e}(k_x, t)$ is extracted from the impulse response simulations by means of (4) and equation (12) is then used to retrieve the temporal growth rate ω_i for different streamwise wavenumbers. The results for the base flow depicted in figure 1 (*b*) are displayed in figure 3 for different values of the Reynolds number and they are compared with the inviscid instability results of Andersson *et al.* (2001) obtained directly from the dispersion relation. The latter calculation is reproduced as a

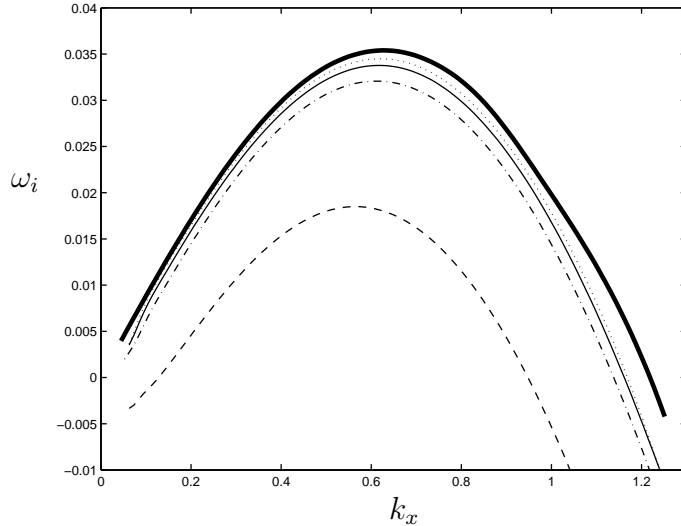


FIGURE 3. Temporal growth rate ω_i versus streamwise wavenumber k_x for the base flow of figure 1 (b). The inviscid results of Andersson *et al.* (2001) are represented by the thick solid line: —; $Re = 1047$: —; $Re = 2000$: $\cdot\cdot\cdot\cdot$; $Re = 500$: - · - ·; $Re = 100$: - - - -.

thick solid line, whereas the thin solid line represents the growth rate curve at $Re = 1047$, i.e. the local Reynolds number prevailing at the streamwise station indicated by a star in figure 1 (a). Since a streak family $U(X, y, z)$, defined by the upstream amplitude A_0 and the spanwise wavenumber β_0 , obeys the nonlinear boundary layer equations, it is independent of the Reynolds number (Schlichting 1979; Andersson *et al.* 2001). As a consequence, varying the local Reynolds number $Re(X)$ of a given profile $U(y, z)$ amounts to moving along the plate and varying the spanwise wavenumber β_0 so that the local spanwise wavenumber $\beta_0 \delta_* / \delta_{*0}$ remains constant. The impulse response corresponding to such base flows yields in figure 3 the various growth rate curves indicated by a dotted line ($Re = 2000$), a dash-dotted line ($Re = 500$) and a dashed line ($Re = 100$). As expected, we note that the viscous temporal growth rate curves approach their inviscid counterpart as the Reynolds number increases, which validates the present approach. Furthermore, the range of unstable wavenumbers shrinks as viscosity is enhanced and the most unstable wavenumber k_x^{max} decreases. Higher wavenumbers are noticeably more affected by viscosity than lower wavenumbers.

In figure 3 we have avoided to display results at very low wavenumbers since two kinds of difficulties are encountered. First, the impulse response approach is intrinsically limited to streamwise wavelengths smaller than the length of the computational domain. A further restrictive factor is related to

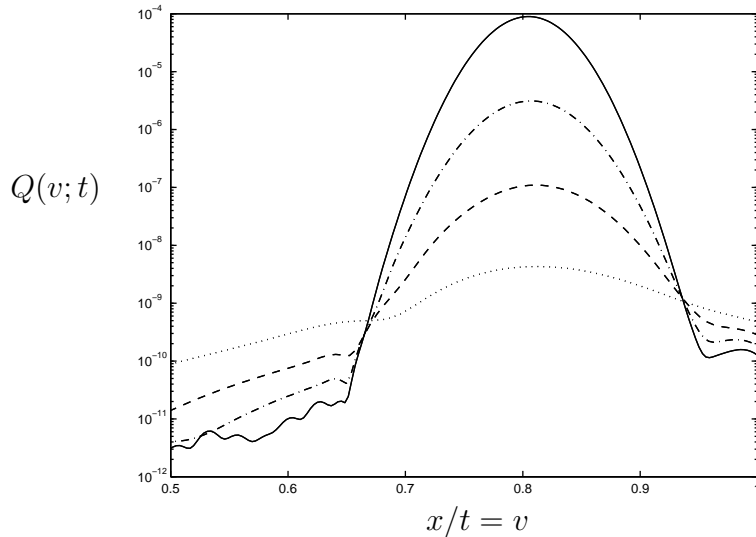


FIGURE 4. Amplitude Q of the wave packet as a function of the ray velocity $x/t = v$ for different times $t = 100$: \cdots ; $t = 200$: $---$; $t = 300$: $- \cdot - \cdot$; $t = 400$: $—$. The base flow is extracted at $X = 632$, $A = 0.36$, $Re = 1047$ as in figure 1 (*b*).

the fact that the full nonlinear Navier–Stokes equations are effectively solved in the numerical code. As a consequence, the long-lived transients at low k_x are contaminated by nonlinear interactions from higher wavenumbers before a reliable exponential growth rate becomes observable. Since the primary goal of this investigation remains the determination of the spatio-temporal behavior, curing this problem has not been pursued further. In any case, the parallel flow assumption breaks down at long wavelengths.

3.2. Spatio-temporal instability

To determine the spatio-temporal instability properties of the streaks, the wave packet velocity field is observed in physical space along rays of group velocity $x/t = v$, as outlined in section 2.2. The evolution of the amplitude $Q(x, t)$, defined by equation (8), is represented in figure 4 as a function of v at different times, again for the base flow of figure 1 (*b*). Note that the amplitude grows between two well-defined trailing and leading edge velocities v^- and v^+ . The first neutral ray $x/t = v^-$ is positive and therefore it may immediately be concluded that the instability is convective! It is also worth noticing that the amplitude of the wave packet ahead of the velocity v^+ ($v > v^+$) experiences lower decay rates than the tail of the wave packet behind the velocity v^- ($v < v^-$). Since the front part is associated to velocities of order unity, it corresponds to the contribution from the continuous spectrum of disturbances (Grosch & Salwen 1978), i.e. free-stream perturbations that are advected at

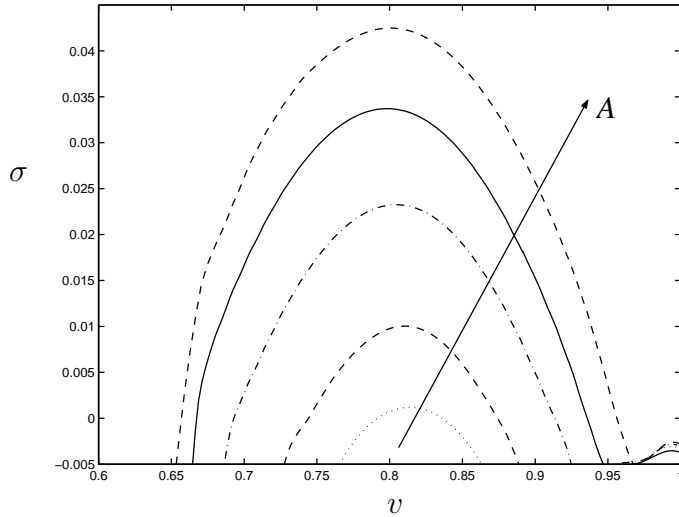


FIGURE 5. Temporal growth rate versus ray velocity $x/t = v$ for different increasing saturated streak amplitudes $A = 0.28, 0.31, 0.34, 0.36, 0.38$ at $X = 632$ and $Re = 1047$. The solid line corresponds to the base flow at $A = 0.36$ depicted in figure 1 (b) and indicated by a star in figure 1 (a). The other curves correspond to scanning the vertical line $X = 632$ of unstable streaks in figure 1 (a) for lower and higher amplitude settings.

the free-stream velocity and damped by viscous diffusion. The growth rate $\sigma(v)$ obtained from the data in figure 4 by applying equation (13) is displayed by the solid line in figure 5. The growth rate curve is close to a parabola with trailing and leading edge velocities $v^- = 0.66$ and $v^+ = 0.935$. The maximum growth rate is $\sigma^{max} = 0.0338$ and it is attained along the ray $v^{max} = 0.80$. The maximum temporal growth rate was found to be $\omega_i^{max} = 0.0337$ (see figure 3). The agreement, within 1%, between these two numerically determined values constitutes a further validation check of the impulse response approach.

The temporal growth rate curve versus group velocity is displayed in figure 5 for other unstable streak amplitudes at streamwise position $X = 632$. Such base states correspond to lower and higher amplitudes A along the vertical line $X = 632$ in figure 1 (a). This growth rate diagram constitutes the spatio-temporal analogue of the inviscid temporal growth rates curves (figure 16 a in Andersson *et al.* 2001) for the same streak amplitude settings at the same streamwise station. Recall that, in this earlier study, the critical streak amplitude for breakdown was determined and the most dangerous type of disturbance was identified to be the sinuous mode of instability. It can be seen from figure 5 that the growth rates and the spreading rate $\Delta v \equiv v^+ - v^-$

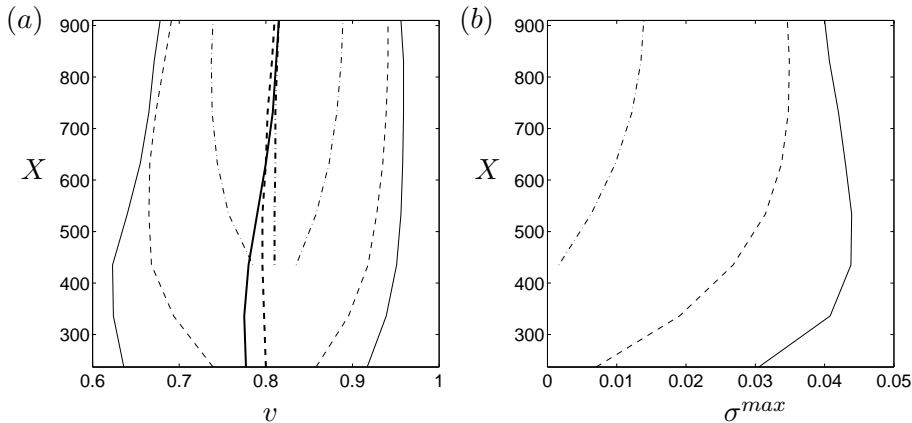


FIGURE 6. Impulse response characteristics of extracted parallel streaks as a function of streamwise distance X for three distinct upstream streak amplitudes at $X = 0$. $A = 0.28$: —; $A = 0.22$: - - - -; $A = 0.16$: · · · ·. (a) Leading-edge velocity v^+ (thin lines), trailing-edge velocity v^- (thin lines), center velocity v^{max} (thick lines). (b) Maximum temporal growth rate σ^{max} .

of the wave packet increase with streak amplitude. Moreover, the maximum growth rate σ^{max} occurs approximately at the group velocity $v^{max} = 0.8$ for all streak amplitudes. This value is quite close to the phase velocities $c_r = \omega_r/k_x$ obtained in the temporal analysis of Andersson *et al.* (2001), as displayed in figure 16(b) of that paper.

A parametric study has been carried out to fully document the main features of the impulse response for different amplitudes and streamwise positions. The results are synthesized in figure 6. The characteristic velocities v^- , v^+ and v^{max} are displayed in figure 6(a), while the maximum growth rate σ^{max} is shown in figure 6(b). The data are plotted as a function of the streamwise coordinate X for three distinct streak evolution curves corresponding to upstream amplitudes $A = 0.28, 0.22, 0.16$ at $X = 0$ in figure 1(a). These upstream settings give rise to the first, third and fifth highest streak evolution curves in figure 1(a). Note that for the lowest amplitude considered (dash-dotted lines in figure 6) the streak becomes unstable only for $X > 450$. It can first be seen that v^{max} is quite insensitive to streamwise position and streak amplitude. Furthermore, the spreading rate of the wave packet $\Delta v = v^+ - v^-$ increases together with the maximum temporal growth rate σ^{max} . For the highest amplitude streak (solid lines in figure 6) the growth rate σ^{max} reaches a maximum for small X while the wave packet center velocity is slightly lower than further downstream.

From the above parametric study, it can be concluded that the impulse response of streaks gives rise to a wave packet with a center velocity v^{max} of the order of 80% of the free-stream velocity U_∞ . The wave packet spreading rate varies with the streak amplitude and the position X between approximately 10% and 30% of U_∞ : the leading edge moves at a velocity v^+ which is around 90% of U_∞ while the trailing edge moves at a velocity v^- which is around 70% of U_∞ . According to figure 6, the latter estimates are quite sensitive to streak amplitude. In any case, one may unambiguously state that the secondary instability of optimal streaks is highly convective for a wide range of amplitudes and streamwise stations.

4. Discussion

A surprising feature of the above results is that the secondary streak instability is “even more convective” than the primary Tollmien-Schlichting instability of the Blasius velocity profile. According to Gaster (1975) and Gaster & Grant (1975), the leading-edge and trailing-edge velocities of a Tollmien-Schlichting wave packet in the absence of streaks are respectively $v^+ = 0.5$ and $v^- = 0.36$ at $Re = 1000$. In the presence of streaks, the trailing edge velocity is $v^- \sim 0.7$. Thus, unstable perturbations travel much faster on the streaky base flow. Surely, these two situations correspond to radically distinct instability mechanisms: while the Tollmien-Schlichting instability is driven by viscosity, the streak instability is essentially inviscid in nature and driven by the presence of inflection points in the velocity profile. In order to further examine this behavior it is useful to evaluate, for both instances, the distribution of the kinetic energy production terms in the cross-stream (y, z) plane.

Consider the perturbation kinetic energy equation averaged over the streamwise length L_x of the box

$$\begin{aligned} \frac{d}{dt} \left[\int_0^{y_{max}} \int_0^{\lambda_z} \frac{1}{2} (\overline{u^2} + \overline{v^2} + \overline{w^2}) dy dz \right] = & - \int_0^{y_{max}} \int_0^{\lambda_z} \frac{\partial U}{\partial y} \overline{uv} dy dz + \\ & - \int_0^{y_{max}} \int_0^{\lambda_z} \frac{\partial U}{\partial z} \overline{uw} dy dz - \frac{1}{Re} \int_0^{y_{max}} \int_0^{\lambda_z} \overline{\boldsymbol{\omega} \cdot \boldsymbol{\omega}} dy dz, \end{aligned} \quad (14)$$

where a bar denotes the streamwise average

$$\overline{(\cdot)} = \frac{1}{L_x} \int_0^{L_x} (\cdot) dx,$$

and $\boldsymbol{\omega}$ the perturbation vorticity vector. This balance equation is derived in a straightforward manner from the Navier–Stokes equations linearized around the base flow $U(y, z)$. The first production term of density $-\frac{\partial U}{\partial y} \overline{uv}$ represents the work of the Reynolds stress $\tau_{xy} = -\overline{uv}$ on the wall-normal basic shear $\frac{\partial U}{\partial y}$, while the second production term of density $-\frac{\partial U}{\partial z} \overline{uw}$ is associated with the work of the Reynolds stress $\tau_{xz} = -\overline{uw}$ on the spanwise basic shear $\frac{\partial U}{\partial z}$. The last term represents viscous dissipation. Contour levels of the total production

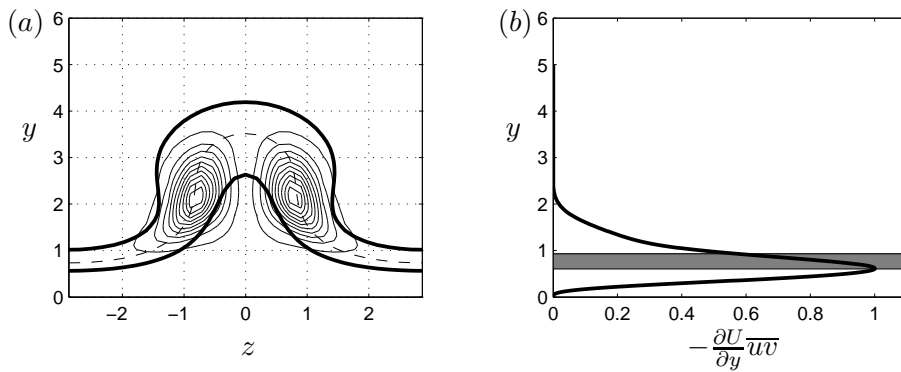


FIGURE 7. Production of perturbation kinetic energy and wave packet characteristic velocities. (a) Contour levels (thin solid lines) of the total production density $-\frac{\partial U}{\partial y}\overline{uv} - \frac{\partial U}{\partial z}\overline{uw}$ in a cross-stream (y, z) plane for the impulse response of the streaky base flow of figure 1 (b). The outer contour is 5% of the maximum and contour spacing is 10% of the maximum. The thick solid lines represent the base flow velocity contours $U(y, z) = v^+$ and $U(y, z) = v^-$ with $v^+ = 0.935$ and $v^- = 0.66$. The dashed line represents the base flow velocity contour $U(y, z) = v^{max}$ with $v^{max} = 0.80$. (b) Wall-normal profile (thick solid line) of the production density $-\frac{\partial U}{\partial y}\overline{uv}$ for the impulse response of the Blasius base flow. The grey horizontal strip delineates the region of base flow velocities $v^- < U_B(y) < v^+$ with $v^+ = 0.5$ and $v^- = 0.36$.

density $-\frac{\partial U}{\partial y}\overline{uv} - \frac{\partial U}{\partial z}\overline{uw}$ are displayed in figure 7 (a) for the streaky base flow of figure 1 (a), at time $t = 300$, together with the contours $U(y, z) = v^+$, $U(y, z) = v^-$ and $U(y, z) = v^{max}$ pertaining to the wave packet. For comparison, we have displayed in figure 7 (b) the wall-normal profile of the production density term $-\frac{\partial U}{\partial y}\overline{uv}$ corresponding to the two-dimensional impulse response of the primary Tollmien-Schlichting instability in the Blasius boundary layer at the same Reynolds number $Re = 1047$. In this case there is no spanwise-shear production term since there are no spanwise variations. The grey horizontal strip delineates the region $v^- < U_B(y) < v^+$. The results of Gaster (1975) are recovered for the leading- and trailing-edge velocities.

In the case of streaks (figure 7 a), the wall-normal shear production term $-\frac{\partial U}{\partial y}\overline{uv}$ is found to be negative and one order of magnitude smaller than the spanwise shear production term $-\frac{\partial U}{\partial z}\overline{uw}$. The streak instability is of inviscid inflectional type and primarily triggered by the regions of high spanwise shear on the flanks of the low-speed region. The areas of strongest production lie slightly above the position of maximum shear at $y = 1.5$ in figure 7 (a).

The regions of largest energy production density are well correlated not only with the areas of high spanwise shear but also with the regions of streamwise velocity fluctuations (see Bottaro & Klingmann 1996). This finding is in qualitative agreement with earlier investigations of streamwise vortices: according to Swearingen & Blackwelder (1987), the experimentally observed sinuous instability of Görtler vortices is primarily associated with the spanwise shear of the streaky flow. Park & Huerre (1995) later established theoretically that the sinuous instability was indeed driven by the spanwise shear production term. According to figure 7(a), the basic streamwise velocity prevailing at the point of maximum production is seen to coincide with the center velocity v^{max} of the wave packet. In the same way, the regions of significant production are seen to be approximately confined in a domain where the basic streamwise velocity is such that $v^- < U(y, z) < v^+$. These features reveal the strong correlation between the basic velocities in the production area and the characteristic velocities of the wave packet.

In the case of the Blasius boundary layer (figure 7b), the wall-normal shear production term is confined in a region closer to the wall, where the basic velocities are smaller. The correlation between production location and the band $v^- < U_B(y) < v^+$ is not as obvious quantitatively. Nonetheless, the fact that v^- and v^+ are smaller than in the case of streaks is qualitatively consistent with the location of production closer to the wall.¹

It should be emphasized again that the impulse response properties are very much dictated by the nature of the instability mechanisms. In the case of the Blasius layer, the mechanism is viscous and active in low basic velocity areas close to the wall, while in the case of streaks, it is inviscid in nature and active in higher basic velocity areas further away from the wall. As a result the impulse response wave packet of streaks travels faster downstream than its counterpart for the Blasius profile. These features account for the fact that the presence of streaks makes the flow even more convectively unstable than the Blasius layer.

It might be argued that the Tollmien-Schlichting instability is still active when streaks are present, even if the associated growth rates are much smaller than those of the inviscid sinuous instability. Cossu & Brandt (2002) have recently demonstrated that Tollmien-Schlichting waves do remain unstable for streak amplitudes that are smaller than any of those considered here. However, Tollmien-Schlichting waves are quenched above a certain streak amplitude level which is Reynolds-number dependent. In the range of Reynolds numbers considered here, this level is about 17% of U_∞ and lower than the threshold for the onset of the streak instability, which is 26% of U_∞ .

The sinuous streak instability is induced by the mean spanwise shear on the sides of the region of defect velocity as in classical two-dimensional wakes past a bluff body. It is therefore instructive to compare the instability properties of

¹In general, there is no reason to expect that the border of the production region should coincide with the contours $U(y, z) = v^+$ and $U(y, z) = v^-$.

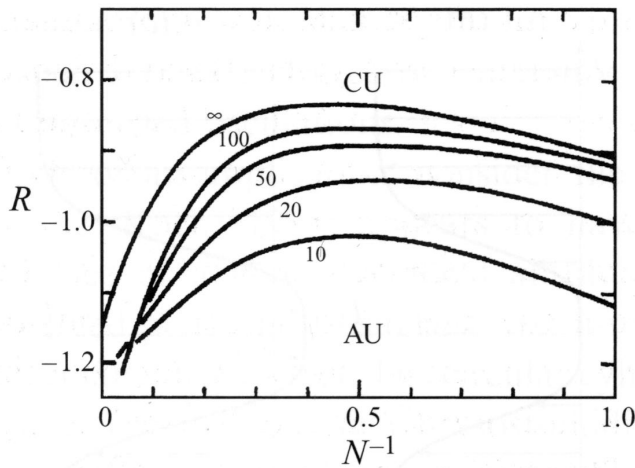


FIGURE 8. Absolute/convective instability boundary in the (N^{-1}, R) plane at various wake Reynolds numbers indicated near the curves for the wake profile family (15). AU and CU denotes the domain of absolute and convective instability respectively. After Monkewitz (1988).

the streaky base flows with those of two-dimensional wakes (LeCunff & Bottaro 1993). At this point one may note that for the bluff body, the wake and the resulting instability are isolated in the spanwise direction, whereas the streak instability arises on a spanwise periodic basic flow. However, the production density spatial distribution represented in figure 7(a) indicates that the streak instability is triggered locally by the basic spanwise shear. This is further confirmed by the complete Floquet analysis in Andersson *et al.* (2001) which demonstrates that the instability features are quite insensitive to variations in the Floquet spanwise detuning parameter.

To carry out the comparison, let us consider the symmetric wake profiles introduced by Monkewitz (1988) and defined by the two-parameter family

$$U_w(z_w; R, N) = 1 - R + 2RF(z_w; N), \quad (15)$$

where

$$R \equiv \frac{U_c - U_{max}}{U_c + U_{max}},$$

and

$$F(z_w; N) \equiv \frac{1}{1 + \sinh^{2N}[z_w \sinh^{-1}(1)]}.$$

In the above relations, the length scale is the half-width of the wake and the velocity scale is the average velocity $(U_c + U_{max})/2$, where U_c is the minimum

velocity on the center line and U_{max} the maximum velocity in the high-speed regions. The velocity ratio R controls the depth of the wake. The shape factor N , which controls the steepness of the shear layers, varies between one, corresponding to the fully developed $\text{sech}^2 z$ wake, to infinity, a top-hat wake bounded by two vortex sheets. The curves representing the absolute instability boundary in the $R - N^{-1}$ plane for different Reynolds numbers are reproduced from Monkewitz (1988) in figure 8. In order to match our streak base state $U(y, z)$ with the family of wakes $U_w(z_w)$, one must select a spanwise profile at a specific wall-normal distance and extend it for all y so as to obtain a corresponding y -invariant wake. Let us choose the spanwise streak profile at the wall-normal distance $y = 2.1$ displayed as a solid line in figure 9 and associated with the Reynolds stress production peak in figure 7 (a). Note that this profile is typical of fully developed streaks induced by free stream turbulence. It may differ in detail from those produced by well-controlled artificial disturbances close to the excitation station. For instance (Asai *et al.* 2002) observe velocity overshoots on both sides of the wake profile which are smoothed out further downstream of the source region.

The best fit to the chosen profile with Monkewitz' family, indicated by a dotted line in figure 9, is obtained for $N = 1$ and $R = -0.25$, provided that $z_w = 0.8z$. Such a scale factor applied to the spanwise variable effectively means that the streak half-width is 80% of the local boundary layer displacement thickness. The wake Reynolds number defined with respect to its half-width and the average velocity $(U_c + U_{max})/2$ is then found to be 960, instead of 1047 in boundary layer variables. According to Monkewitz (1988), inviscid results are applicable as soon as the wake Reynolds number exceeds 200: the relevant absolute/convective instability transition curve in figure 8 therefore pertains to $Re = \infty$. The fitted wake $N = 1$, $R = -0.25$ is seen to lie above the range of R -values in figure 8 on the convectively unstable side. It is clearly well above the absolute/convective instability transition curve at $Re = \infty$. If this fitting procedure is repeated at other wall-normal distances in the region of significant spanwise shear, one finds the velocity ratio to vary within the range $-0.35 < R < -0.2$, which is again too high for absolute instability to occur.

The above procedure may be further validated by inferring from Monkewitz' results the trailing-edge velocity v^- of the streak impulse response. By definition the trailing-edge velocity is such that, in the co-moving frame, the instability is marginally convective/absolute at the velocity ratio R_{cr} . In other words, v^- is given by

$$\frac{(U_c - v^-) - (U_{max} - v^-)}{(U_c - v^-) + (U_{max} - v^-)} = R_{cr}.$$

For the profile in figure 9, $U_{max} = 0.997$, $U_c = 0.594$ and according to figure 8, $R_{cr} = -0.9$ in the inviscid limit. The resulting value of the trailing-edge velocity is then $v^- = 0.58$ to be compared with $v^- = 0.66$ obtained from the detailed analysis of the streak impulse response in section 3. Thus, the extraction of a two-dimensional wake at the wall-normal distance of maximum Reynolds

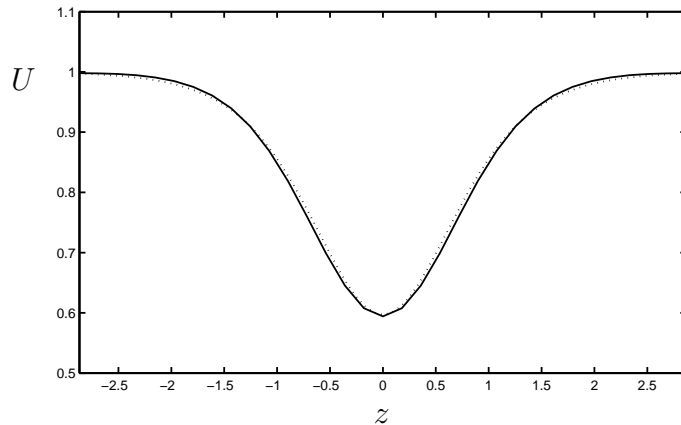


FIGURE 9. Wake-like velocity profile in the spanwise direction z . —: base flow of figure 1 (*b*) at the maximum production elevation $y = 2.1$. \cdots : Monkewitz (1988) model of two dimensional wakes with $N = 1$, $R = -0.25$, and $z_w = 0.8z$.

stress production is seen to lead to reasonable estimates of the trailing-edge velocity v^- , which confirms the dominant effect of the spanwise shear over its wall-normal counterpart in the triggering of the sinuous instability.

5. Conclusions

The main results of the present investigation may be summarized as follows: the instability of saturated optimal streaks in the flat-plate boundary layer is clearly convective. More surprisingly it is even more convective than the Blasius boundary layer in the absence of streaks. Whereas the trailing-edge velocity of a Tollmien-Schlichting wave packet in the Blasius boundary layer is 35% of the free-stream velocity, the trailing-edge velocity of a wave packet riding on saturated optimal streaks is around 70% of the free-stream velocity. This feature is due to the fact that the instability of the Blasius boundary layer and of the streaks are driven by distinct physical mechanisms: the Tollmien-Schlichting instability is viscous in character and its production is located in a low-velocity region close to the wall; the streak instability is inviscid in character, it is primarily induced by the spanwise shear and its production is located further away from the wall in a higher velocity region. All the optimal streaks considered in this study are stable with respect to Tollmien-Schlichting waves, as demonstrated by Cossu & Brandt (2002). The streak impulse response consists of the sinuous mode of instability triggered by the spanwise wake-like profile. This feature has been further confirmed by comparing the numerical results with the absolute/convective instability properties of the family of two-dimensional wakes constructed by Monkewitz (1988). The streak profile $U(y, z)$ may be very approximately modeled as a two-dimensional spanwise wake flow $U(z)$ which is

independent of the wall-normal coordinate, provided one selects a plane parallel to the wall corresponding to the peak of Reynolds stress production.

The results have been obtained under the assumption of zero-detuning ($\delta k_z = 0$), the flow being excited in the fundamental mode by a spanwise periodic array of localized initial perturbations with the same spanwise wavelength as the underlying streaks. A similar analysis can be conducted for the subharmonic mode ($\delta k_z = \pi/\lambda_z$), in which case the flow is excited by a periodic array with twice the streak spanwise wavelength. Preliminary simulations indicate similar features: the subharmonic mode is also convectively unstable, with characteristic wave packet velocities that are close to those of the fundamental mode. Note that the temporal instability characteristics were also found by Andersson *et al.* (2001) to be quite insensitive to the value of the detuning parameter δk_z .

This study was initially motivated by the conjecture that the streak instability being essentially wake-like in the spanwise direction, it could give rise to an absolute instability for sufficiently deep profiles, as in classical wakes. Our conclusions do not confirm this conjecture: the streak instability is produced sufficiently high above the wall, in regions where local streamwise velocities are large so that perturbations are advected away. The convective nature of the secondary streak instability implies that the type of by-pass transition studied here is essentially noise-driven: streaks behave as flow amplifiers in terms of the classification introduced by Huerre & Monkewitz (1990). Intrinsic transition criteria similar to those suggested by Lingwood (1995, 1996) in rotating disk boundary layers are therefore not likely to exist. The criteria are bound to be external-noise dependent, since both the streaks and the secondary instability are noise-driven. As concerns transition in boundary layers subject to high levels of free-stream turbulence, it is important to note that the relation of the modal secondary instability to streak breakdown has not been definitely proven. Flow visualizations (Matsubara & Alfredsson 2001) show that some streaks develop a streamwise waviness of relatively short wavelength, which these authors attribute to a secondary instability.

The present results concerning the convective nature of the instability of streaks in two-dimensional flat-plate boundary layers are in qualitative agreement with those of Koch (2002) regarding the secondary instability of secondary cross-flow vortices in three-dimensional swept-wing boundary layers. In the latter case, the impulse response wave packet pertaining to the fundamental mode (zero detuning, i.e. same periodicity as the underlying basic flow) propagates along the axis of the primary cross-flow vortices. The dominant part of the wave packet travels at around 80% of the boundary layer edge velocity, as in the present investigation.

The near-wall dynamics of fully turbulent boundary layers is known to give rise to a self-sustaining process consisting of streamwise vortices which transfer momentum to generate streaks. In turn, the streaks are unstable and regenerate vortices (Waleffe 1995, 1997; Jeong, Hussain, Schoppa & Kim 1997; Kawahara,

Jiménez, Uhlmann & Pinelli 1998; Jiménez & Pinelli 1999; Schoppa & Hussain 2002). The instability properties of the streaky structures in wall-bounded turbulent flows are qualitatively similar to those of transitional streaks: the dominant mode is sinuous in character. In this situation, we speculate that the characteristic wave packet velocities of the regenerated vortices will be determined by the peak of the Reynolds stress production term. A more detailed investigation remains to be carried out.

The family of two-dimensional wake profiles introduced by Monkewitz (1988) has proven to be helpful in determining the local absolute/convective instability properties of classical wakes behind bluff bodies. The present results suggest that the analysis of a corresponding three-dimensional model $U(y, z)$ for an isolated streak would shed light on the instability characteristics of the various streaky structures encountered in transitional or fully turbulent wall-bounded flows.

The work was performed during the first author's visit at the Hydrodynamics Laboratory (LadHyX) and supported by École Polytechnique and TFR (Teknikvetenskapliga forskningsrådet). Computer time was provided by the Institut du Développement et des Ressources en Informatique Scientifique (IDRIS).

References

- ANDERSSON, P., BERGGREN, M. & HENNINGSON, D. S. 1999 Optimal disturbances and bypass transition in boundary layers. *Phys. Fluids* **11**, 134–150.
- ANDERSSON, P., BRANDT, L., BOTTARO, A. & HENNINGSON, D. S. 2001 On the breakdown of boundary layers streaks. *J. Fluid Mech.* **428**, 29–60.
- ASAI, M., MINAGAWA, M. & NISHIOKA, M. 2002 The instability and breakdown of a near-wall low-speed streak. *J. Fluid Mech.* **455**, 289–314.
- BECH, K. H., HENNINGSON, D. S. & HENKES, R. A. W. M. 1998 Linear and nonlinear development of localized disturbances in zero and adverse pressure gradient boundary layers. *Phys. Fluids* **10**, 1405–1418.
- BERS, A. 1983 Space-time evolution of plasma instabilities – absolute and convective. In *Handbook of Plasma Physics* (ed. M. N. Rosenbluth & R. Z. Sagdeev), , vol. 1, pp. 451–517. North-Holland.
- BOTTARO, A. & KLINGMANN, B. G. B. 1996 On the linear breakdown of Görtler vortices. *Eur. J. Mech. B/Fluids* **15**, 301–330.
- BRANCHER, P. & CHOMAZ, J. M. 1997 Absolute and convective secondary instabilities in spatially periodic shear flows. *Phys. Rev. Lett.* **78**, 658–661.
- BREUER, K. S. & HARITONIDIS, J. H. 1990 The evolution of a localized disturbance in a laminar boundary layer. Part 1. Weak disturbances. *J. Fluid Mech.* **220**, 569–594.
- BREVDO, L. & BRIDGES, T. 1996 Absolute and convective instability of spatially periodic flows. *Phil. Trans. R. Soc. London A* **354**, 1027–1064.

- BUTLER, K. M. & FARRELL, B. F. 1992 Three-dimensional optimal perturbations in viscous shear flow. *Phys. Fluids A* **4**, 1637–1650.
- CHOMAZ, J. M., COUAIRO, A. & JULIEN, S. 1999 Absolute and convective nature of the Eckhaus and zigzag instability with throughflow. *Phys. Fluids* **11**, 3369–3373.
- CHOMAZ, J. M., HUERRE, P. & REDEKOPP, L. G. 1991 A frequency selection criterion in spatially developing flows. *Stud. Appl. Math.* **84**, 119–144.
- COSSU, C. & BRANDT, L. 2002 Stabilization of Tollmien-Schlichting waves by finite amplitude optimal streaks in the Blasius boundary layer. *Phys. Fluids* **14**, L57–L60.
- DELBENDE, I. & CHOMAZ, J.-M. 1998 Nonlinear convective/absolute instabilities of parallel two-dimensional wakes. *Phys. Fluids* **10**, 2724–2736.
- DELBENDE, I., CHOMAZ, J.-M. & HUERRE, P. 1998 Absolute and convective instabilities in the Batchelor vortex: a numerical study of the linear impulse response. *J. of Fluid Mech.* **355**, 229–254.
- GASTER, M. 1975 A theoretical model of a wave packet in a boundary layer over a flat plate. *Proc. R. Soc. London, Ser. A* **347**, 271–289.
- GASTER, M. & GRANT, I. 1975 An experimental investigation of the formation and development of a wave packet in a laminar boundary layer. *Proc. R. Soc. London, Ser. A* **347**, 253–269.
- GROSCHE, C. E. & SALWEN, H. 1978 The continuous spectrum of the Orr-Sommerfeld equation. Part 1. The spectrum and the eigenfunctions. *J. Fluid Mech.* **87**, 33–54.
- HALL, P. & HORSEMAN, N. J. 1991 The linear inviscid secondary instability of longitudinal vortex structures in boundary-layers. *J. Fluid Mech.* **232**, 357–375.
- HENNINGSON, D. S., LUNDBLADH, A. & JOHANSSON, A. V. 1993 A mechanism for bypass transition from localized disturbances in wall-bounded shear flows. *J. Fluid Mech.* **250**, 169–207.
- HUERRE, P. 1988 On the absolute/convective nature of primary and secondary instabilities. In *Propagation in Systems Far from Equilibrium* (ed. J. E. Wesfreid, H. R. Brand, P. Manneville, G. Albinet & N. Boccara), pp. 340–353. Springer.
- HUERRE, P. 2000 Open shear flow instabilities. In *Perspectives in Fluid Dynamics* (ed. G. K. Batchelor, H. K. Moffatt & M. G. Worster), pp. 159–229. Cambridge University Press.
- HUERRE, P. & MONKEWITZ, P. A. 1990 Local and global instabilities in spatially developing flows. *Annu. Rev. Fluid Mech.* **22**, 473–537.
- HUERRE, P. & ROSSI, M. 1998 Hydrodynamic instabilities in open flows. In *Hydrodynamic and Nonlinear Instabilities* (ed. C. Godrèche & P. Manneville), pp. 81–294. Cambridge University Press.
- JEONG, J., HUSSAIN, F., SCHOPPA, W. & KIM, J. 1997 Coherent structures near the wall in a turbulent channel flow. *J. Fluid Mech.* **332**, 185–214.
- JIMÉNEZ, J. & PINELLI, A. 1999 The autonomous cycle of near wall turbulence. *J. Fluid Mech.* **389**, 335–359.
- KAWAHARA, G., JIMÉNEZ, J., UHLMANN, M. & PINELLI, A. 1998 The instability of streaks in near-wall turbulence. *Tech. Rep.*. NASA-Stanford University Center for Turbulence Research, Annual Research Briefs, pp. 155–170.
- KIM, J., MOIN, P. & MOSER, R. 1987 Turbulence statistics in fully developed channel flow. *J. Fluid Mech.* **177**, 133–166.

- KOCH, W. 2002 On the spatio-temporal stability of primary and secondary crossflow vortices in a three-dimensional boundary layer. *J. Fluid Mech.* **456**, 85–112.
- LECUNFF, C. & BOTTARO, A. 1993 Linear stability of shear profiles and relation to the secondary instability of the dean flow. *Phys. Fluids A* **5**, 2161–2171.
- LINGWOOD, R. 1995 Absolute instability of the boundary layer on a rotating disk. *J. Fluid Mech.* **299**, 17–33.
- LINGWOOD, R. 1996 An experimental study of absolute instability of the rotating-disk boundary-layer flow. *J. Fluid Mech.* **314**, 373–405.
- LUCHINI, P. 2000 Reynolds-number independent instability of the boundary layer over a flat surface. Part 2: Optimal perturbations. *J. Fluid Mech.* **404**, 289–309.
- LUNDBLADH, A., BERLIN, S., SKOTE, M., HILDINGS, C., CHOI, J., KIM, J. & HENNINGSON, D. S. 1999 An efficient spectral method for simulation of incompressible flow over a flat plate. Technical Report KTH/MEK/TR-99/11-SE. KTH, Department of Mechanics, Stockholm.
- MATSUBARA, M. & ALFREDSSON, P. H. 2001 Disturbance growth in boundary layers subjected to free stream turbulence. *J. Fluid Mech.* **430**, 149–168.
- MONKEWITZ, P. 1988 The absolute and convective nature of instability in two-dimensional wakes at low Reynolds numbers. *Phys. Fluids* **31**, 999–1006.
- MORKOVIN, M. V. & RESHOKTO, E. 1990 Dialogue on progress and issues in instability and transition research. In *Laminar-Turbulent Transition* (ed. D. Arnal & R. Michel), pp. 3–39. Springer.
- NAYFEH, A. H. & MOOK, D. T. 1979 *Nonlinear oscillations*. Wiley-Interscience.
- OLENDRARU, C., SELLIER, A., ROSSI, M. & HUERRE, P. 1999 Inviscid instability of the Batchelor vortex: Absolute-convective transition and spatial branches. *Phys. Fluids* **11**, 1805–1820.
- PARK, D. S. & HUERRE, P. 1995 Primary and secondary instabilities of the asymptotic suction boundary layer on a curved plate. *J. Fluid Mech.* **283**, 249–272.
- PIER, B. & HUERRE, P. 2001 Nonlinear self-sustained structures and fronts in spatially developing wake flows. *J. Fluid Mech.* **435**, 145–174.
- RODDIER, F. 1971 *Distributions et transformation de Fourier*. McGraw-Hill.
- SARIC, W. S., REED, H. L. & KERSCHEN, E. J. 2002 Boundary-layer receptivity to freestream disturbances. *Annu. Rev. Fluid Mech.* **34**, 291–319.
- SCHLICHTING, H. 1979 *Boundary-Layer Theory*. New York: Mc Graw-Hill.
- SCHMID, P. J. & HENNINGSON, D. S. 2001 *Stability and Transition in Shear Flows*. New York: Springer.
- SCHOPPA, W. & HUSSAIN, F. 2002 Coherent structure generation in near-wall turbulence. *J. Fluid Mech.* **453**, 57–108.
- SWEARINGEN, J. D. & BLACKWELDER, R. F. 1987 The growth and breakdown of streamwise vortices in the presence of a wall. *J. Fluid Mech.* **182**, 255–290.
- WALEFFE, F. 1995 Hydrodynamic stability and turbulence: Beyond transients to a self-sustaining process. *Stud. Appl. Math.* **95**, 319–343.
- WALEFFE, F. 1997 On a self-sustaining process in shear flows. *Phys. Fluids* **9**, 883–900.
- WU, X. & CHOUDARI, M. 2001 Linear and nonlinear instabilities of blasius boundary layer perturbed by streamwise vortices part ii: Intermittent instability induced by long-wavelength klebanoff modes. Report 2001-45. ICASE.

WU, X. & LUO, J. 2001 Instability of Blasius boundary layer in the presence of steady streaks. Annual research briefs. Center for Turbulence Research, Stanford (CA).

Paper 3

3

Transition of streamwise streaks in zero-pressure-gradient boundary layers

By Luca Brandt and Dan S. Henningson¹

Department of Mechanics, Royal Institute of Technology (KTH),
S-100 44 Stockholm, Sweden

A transition scenario initiated by streamwise low- and high-speed streaks in a flat plate boundary layer is studied. In many shear flows, the perturbations that show the highest potential for transient energy amplification consist of streamwise aligned vortices. Due to the lift-up mechanism these optimal disturbances lead to elongated streamwise streaks downstream, with significant spanwise modulation. In a previous investigation (Andersson, Brandt, Bottaro & Henningson 2001), the stability of these streaks in a zero-pressure-gradient boundary layer has been studied by means of Floquet theory and numerical simulations. The sinuous instability mode was found to be the most dangerous disturbance. We present here the first simulation of the breakdown to turbulence originating from the sinuous instability of streamwise streaks. The main structures observed during the transition process consist of elongated quasi-streamwise vortices located on the flanks of the low speed streak. Vortices of alternating sign are overlapping in the streamwise direction in a staggered pattern. The present scenario is compared with transition initiated by transition initiated by a pair of oblique waves. The relevance of this scenario to transition induced by free-stream turbulence is also discussed.

1. Introduction

1.1. *Natural transition*

Transition from laminar to turbulent flow has traditionally been studied in terms of exponentially growing eigensolutions to the linearized disturbance equations. Equations for the evolution of a disturbance, linearized around a mean velocity profile were first derived by Lord Rayleigh (1880) for an inviscid flow; later Orr (1907) and Sommerfeld (1908) included the effects of viscosity, deriving independently what we today call the Orr–Sommerfeld equation. Assuming a wave-like form of the velocity perturbation and Fourier transforming the equation, it reduces to an eigenvalue problem for exponentially

¹Also at FOI, The Swedish Defense Research Agency, Aeronautics Division, SE-17290 Stockholm, Sweden

growing or decaying disturbances. The first solutions for unstable waves, traveling in the direction of the flow (two-dimensional waves), were presented by Tollmien (1929) and Schlichting (1933). The existence of such solutions (later called Tollmien–Schlichting waves) was experimentally verified by Schubauer & Skramstad (1947) in a zero pressure gradient boundary layer.

If an amplified Tollmien–Schlichting wave grows above an amplitude in u_{rms} of about 1% of the free-stream velocity, the flow become susceptible to secondary instability. Klebanoff, Tidstrom & Sargent (1962) observed that three-dimensional perturbations, which are present in any natural flow, were strongly amplified. The three-dimensional structure of the flow was characterized by regions of enhanced and diminished perturbation velocity amplitudes alternating in the spanwise direction, denoted by them “peaks and valleys”. The spanwise scale of the new pattern was of the same order as the streamwise wavelength of the Tollmien–Schlichting (TS) waves and the velocity time signal showed the appearance of high-frequency disturbance spikes at the peak position. This transition scenario was later denoted as K-type after Klebanoff and also fundamental since the frequency of the secondary, spanwise periodic, fluctuations is the same as that of the TS-waves. In the nonlinear stages of the K-type scenario, rows of “ Λ -shaped” vortices, aligned in the streamwise directions, have been observed. Another scenario was also observed, first by Kachanov, Kozlov & Levchenko (1977). This is denoted N-type after Novosibirsk, where the experiments were carried out or H-type after Herbert, who performed a theoretical analysis of the secondary instability of TS-waves (Herbert 1983). In this scenario, the frequency of the secondary instability mode is half that of the TS-waves and, thus, this is also known as subharmonic breakdown. “ Λ -shaped” vortices are also present in this case, but they are arranged in a staggered pattern. Theoretically, this scenario is more likely to occur than the fundamental or K-type, because of its higher growth rate for TS amplitudes of the order of 1% of the free-stream velocity. The temporal calculations by Spalart & Yang (1987) also showed that this was the case. In experiments, however, K-type is often seen in many cases where H-type is theoretically favored, due to the presence of low-amplitude streamwise vorticity in the background flow (Herbert 1988). A review on the physical mechanisms involved can be found in Kachanov (1994).

Transition originating from exponentially growing eigenfunctions is usually called *classical* or *natural* transition. This is observed naturally in flows only if the background turbulence is very small. For higher values, the disturbances inside the boundary layer are large enough that other mechanisms play an important role and the natural scenario is by-passed.

1.2. *By-pass transition*

1.2.1. *Transient growth of streamwise streaks*

In 1969 Morkovin coined the expression “bypass transition”, noting that “we can bypass the TS-mechanism altogether”. In fact, experiments reveal that

many flows, including channel and boundary layer flows, may undergo transition for Reynolds numbers well below the critical ones from linear stability theory. Ellingsen & Palm (1975) proposed a growth mechanism, considering the inviscid evolution of an initial disturbance independent of the streamwise coordinate in a shear layer. These authors showed that the streamwise velocity component may grow linearly in time, producing alternating low- and high-velocity streaks. Moffat (1967) also identified such a streak growth mechanism in a model of turbulent uniform shear flow (see also the review article by Phillips 1969). Later Hultgren & Gustavsson (1981) considered the temporal evolution of a three-dimensional disturbance in a boundary layer and found that in a viscous flow the initial growth is followed by a viscous decay (*transient growth*).

Landahl (1975, 1980) extended this result to the linear evolution of localized disturbances and formalized a physical explanation for this growth. A wall normal displacement of a fluid element in a shear layer will cause a perturbation in the streamwise velocity, since the fluid particle will initially retain its horizontal momentum. It was observed that weak pairs of quasi streamwise counter rotating vortices are able to lift up fluid with low velocity from the wall and bring high-speed fluid towards the wall, and so they are the most effective in forcing streamwise oriented streaks of high and low streamwise velocity. This mechanism, denoted the *lift-up effect*, is inherently a three-dimensional phenomenon. Some insight into it may also be gained from the equation for the wall normal vorticity of the perturbation (the Squire equation), which is proportional to the streamwise velocity for streamwise independent disturbances. The equation is, in fact, forced by a term due to the interaction between the spanwise variation of the wall-normal velocity perturbation and the mean shear of the base flow.

From a mathematical point of view, it is now clear that since the linearized Navier–Stokes operator is non-normal for many flow cases (e.g. shear flows), a significant transient growth may occur before the subsequent exponential behaviour (see Butler & Farrell 1992; Reddy & Henningson 1993; Schmid & Henningson 2001). Such growth is larger for disturbances mainly periodic in the spanwise direction, i.e. with low streamwise wavenumbers in a temporal formulation or low-frequency in a spatial one; it can exist for sub-critical values of the Reynolds number and it is the underlying mechanism in bypass transition phenomena. Andersson, Berggren & Henningson (1999) and Luchini (2000) used an optimization technique to determine which disturbance present at the leading edge of a flat plate will give the maximum spatial transient growth in a non-parallel boundary layer. They also found a pair of counter rotating streamwise vortices as the most effective in streak’s generation.

One of the most interesting cases in which disturbances originating from non-modal growth are responsible for transition, is in the presence of free-stream turbulence. Inside the boundary layer the turbulence is highly damped, but low frequency oscillations, associated with long streaky structures, appear.

The effect of free-stream streamwise vorticity on a laminar boundary layer is studied in Wundrow & Goldstein (2001). As the streaks grow downstream, they break down into regions of intense randomized flow, turbulent *spots*. Experiments with flow visualizations by for example Matsubara & Alfredsson (2001) report on the presence of a high frequency "wiggle" of the streak before the subsequent breakdown into a turbulent spot. Numerical simulations of a transitional boundary layer under free-stream turbulence are presented in Jacobs & Durbin (2001).

An other case where transient growth plays an important role is in the so called *oblique transition*. In this scenario, streamwise aligned vortices are generated by nonlinear interaction between a pair of oblique waves with equal angle but opposite sign in the flow direction. These vortices, in turn, induce streamwise streaks, which may grow past a certain amplitude and become unstable, initiating the breakdown to a turbulent flow. Oblique transition has been studied in detail by Schmid & Henningson (1992) and Elofsson & Alfredsson (1998) in a channel flow and both numerically and experimentally by Berlin, Wiegel & Henningson (1999) for a boundary layer flow.

1.2.2. *Secondary instability of streaks*

If the disturbance energy of the streaks becomes sufficiently large, secondary instability can take place and provoke early breakdown and transition, overruling the theoretically predicted modal decay. Carefully controlled experiments on the breakdown of streaks in channel flow were conducted by Elofsson, Kawakami & Alfredsson (1999). They generated elongated streamwise streaky structures by applying wall suction, and triggered a secondary instability by the use of earphones. They observed that the growth rate of the secondary instability modes was unaffected by a change of the Reynolds number of their flow and that the instability appeared as spanwise (sinuous-type) oscillations of the streaks in cross-stream planes. For numerical/theoretical studies on the instability in channel flows the reader is referred to the works of Waleffe (1995, 1997) and Reddy *et al.* (1998). Flow visualizations of the instability and breakdown of a near-wall low-speed streak in a boundary layer can be found in the recent experiments by Asai, Minagawa & Nishioka (1999, 2002).

In Andersson, Brandt, Bottaro & Henningson (2001), direct numerical simulations (DNS) were used to follow the nonlinear saturation of the optimally growing streaks in a spatially evolving zero-pressure-gradient boundary layer. The complete velocity vector field from the linear results by Andersson *et al.* (1999) was used as input close to the leading edge and the downstream nonlinear development monitored for different initial amplitudes of the perturbation. Inviscid secondary instability calculations using Floquet theory were performed on the mean flows obtained and it was found that the streak critical amplitude, beyond which streamwise travelling waves are excited, is about 26% of the free-stream velocity. The sinuous instability mode (either the fundamental or the

subharmonic, depending on the streak amplitude) represents the most dangerous disturbance. Varicose waves are more stable, and are characterized by a critical amplitude of about 37%.

In the present paper we study the transition process resulting from the sinuous secondary instability using DNS. The late stages of the process are investigated and flow structures identified. This is the first numerical study which accounts in detail for the sinuous breakdown of streaks in boundary layers.

The paper is organized as follows. After an introduction in section 2, where the numerical method employed is described, the features of this novel scenario are presented in section 3. In section 4 this is compared with the other well-known transition scenarios, such as transition initiated by TS waves, pairs of oblique waves and transition due to free-stream turbulence. In addition there is a discussion regarding the relevance of the reported results in the description of the dynamics of near-wall turbulent streaks. The main conclusions of the paper are summarized in section 5.

2. Numerical method

2.1. Numerical scheme

The simulation code (see Lundbladh *et al.* 1999) employed for the present computations uses spectral methods to solve the three-dimensional, time dependent, incompressible Navier–Stokes equations. The algorithm is similar to that of Kim, Moin & Moser (1987), i.e. Fourier representation in the streamwise and spanwise directions and Chebyshev polynomials in the wall-normal direction, together with a pseudo-spectral treatment of the nonlinear terms. The time advancement used is a four-step low-storage third-order Runge–Kutta method for the nonlinear terms and a second-order Crank–Nicolson method for the linear terms. Aliasing errors from the evaluation of the nonlinear terms are removed by the $\frac{3}{2}$ -rule when the FFTs are calculated in the wall parallel plane. In wall normal direction it has been found more efficient to increase resolution rather than using dealiasing.

To correctly account for the downstream boundary layer growth a spatial technique is necessary. This requirement is combined with the periodic boundary condition in the streamwise direction by the implementation of a “fringe region”, similar to that described by Bertolotti, Herbert & Spalart (1992). In this region, at the downstream end of the computational box, the function $\lambda(x)$ in equation (1) is smoothly raised from zero and the flow is forced to a desired solution \mathbf{v} in the following manner,

$$\frac{\partial \mathbf{u}}{\partial t} = NS(\mathbf{u}) + \lambda(x)(\mathbf{v} - \mathbf{u}) + \mathbf{g}, \quad (1)$$

$$\nabla \cdot \mathbf{u} = 0, \quad (2)$$

where \mathbf{u} is the solution vector and $NS(\mathbf{u})$ the right hand side of the (unforced) momentum equations. Both \mathbf{g} , which is a disturbance forcing, and \mathbf{v} may depend on the three spatial coordinates and time. The forcing vector \mathbf{v} is smoothly changed from the laminar boundary layer profile at the beginning of the fringe region to the prescribed inflow velocity vector. This is normally a boundary layer profile, but can also contain a disturbance. A convenient form of the fringe function is as follows:

$$\lambda(x) = \lambda_{max} [S(\frac{x - x_{start}}{\Delta_{rise}}) - S(\frac{x - x_{end}}{\Delta_{fall}} + 1)], \quad (3)$$

where λ_{max} is the maximum strength of the damping, x_{start} to x_{end} the spatial extent of the region where the damping function is nonzero and Δ_{rise} and Δ_{fall} the rise and fall distance of the damping function. $S(a)$ is a smooth step function rising from zero for negative a to one for $a \geq 1$. We have used the following form for S , which has the advantage of having continuous derivatives of all orders.

$$S(a) = \begin{cases} 0 & a \leq 0 \\ 1/[1 + \exp(\frac{1}{a-1} + \frac{1}{a})] & 0 < a < 1 \\ 1 & a \geq 1 \end{cases} \quad (4)$$

This method damps disturbances flowing out of the physical region and smoothly transforms the flow to the desired inflow state, with a minimal upstream influence.

In order to set the free-stream boundary condition at some $y = y_{max}$ closer to the wall, a generalization of the boundary condition used by Malik, Zang & Hussaini (1985) is implemented. Since it is applied in Fourier space with different coefficients for each wavenumber, it is nonlocal in physical space and takes the following form,

$$\frac{\partial \hat{\mathbf{u}}}{\partial y} + |k| \hat{\mathbf{u}} = \frac{\partial \hat{\mathbf{v}}_0}{\partial y} + |k| \hat{\mathbf{v}}_0, \quad (5)$$

where k is the absolute value of the horizontal wavenumber vector and $\hat{\mathbf{u}}$ is the Fourier transforms of \mathbf{u} . Here \mathbf{v}_0 denotes the local solution of the Blasius equation and $\hat{\mathbf{v}}_0$ its Fourier transform.

2.2. Disturbance generation and parameter settings

The presented numerical implementation provides several possibilities for disturbances generation. The velocity vector field from the simulations presented in Andersson *et al.* (2001), figure 9, is used as inflow condition. In those simulations a spanwise antisymmetric harmonic volume force was added to the nonlinear streaks to trigger their sinuous secondary instability. Here the saturated streaks, \mathbf{v}_s , and the secondary instability mode, \mathbf{v}_d , obtained filtering the velocity field at the frequency ω of the forcing, are introduced in the fringe region by adding them to the Blasius solution to give the forcing vector $\mathbf{v} = \mathbf{v}_0 + \mathbf{v}_s + A \mathbf{v}_d e^{i\omega t}$ in equation (1). An amplification factor A is used for the secondary instability to give transition within the computational box,

	$x_l \times y_l \times z_l$ δ_0^*	$n_x \times n_y \times n_z$ (resolution)	$Re_{\delta_0^*}$
Box1	$380 \times 10.7 \times 6.86$	$1024 \times 97 \times 96$	875
Box2	$380 \times 10.7 \times 6.86$	$1440 \times 97 \times 72$	875
Box3	$318 \times 9 \times 5.75$	$1440 \times 97 \times 72$	1044

TABLE 1. Resolution and box dimensions for the simulations presented. The box dimensions includes the fringe region, and are made dimensionless with respect to δ_0^* , the displacement thickness at the beginning of the computational box. Note that z_l corresponds in all cases to one spanwise wavelength of the streak. The total number of Fourier modes is indicated, corresponding to $n_x/2$ or $n_z/2$ conjugate pairs.

in the present case $A = 10^3$. The analysis of the fringe region technique by Nordström, Nordin & Henningson (1999) shows that no error is introduced in the simulations if the forcing is solution to the Navier-Stokes equations. This is true in the present case since the forcing vector is the result of previous direct numerical simulations performed by means of the same numerical code.

The box sizes and resolutions used for the simulations presented in this paper are displayed in table 1. The dimensions are reported in terms of δ_0^* which denotes the Blasius boundary layer displacement thickness at the beginning of the computational box. Box1 and Box2 follow the evolution of the secondary instability mode from the same upstream station and differ only in the number of spectral modes. Box3 has a larger inlet Re and is used to provide some fully developed turbulence within the computational box with a still feasible number of modes; the inflow of Box3 corresponds to $x = 125$ in Box1 and Box2. If not stated otherwise, in the results presented the coordinates will be scaled with the displacement thickness δ_0^* of Box1 and Box2. The inflow position $x = 0$, $Re = 875$ in the present paper corresponds to $x/L = 1.03$ in figure 9 in Andersson *et al.* (2001).

A check on the resolution of the present simulations is obtained comparing the minima of the spanwise vorticity component in the transition region obtained using Box1 and Box2. The data, extracted at the same phase angle during the period of the secondary instability mode, are reported in Table 2 while the isocontours of the instantaneous spanwise vorticity are displayed in figure 1 in the $x-y$ plane located at the centre of the low-speed region ($z = 0$). The difference in the y position of the minima considered is divided by $3\delta_0^*$, the length of the structure in the wall-normal direction, while the difference in the x position is related to the streamwise wavelength of the secondary instability mode ($\lambda_x = 11.9\delta_0^*$). The maximum of the difference in the vorticity field between the two simulations is less than 6% for values of x less than 250. This is a first confirmation that the periodicity of the flow is maintained for x positions upstream of 250.

x	y	ω_z	$\Delta x/\lambda_x$	$\Delta y/3\delta_0^*$	$\Delta\omega_z/\omega_z$
205.60	1.57	-0.74	0.013	0.009	-0.013
210.51	1.2	-0.80	0.022	0.009	-0.008
215.86	0.8	-0.86	0.018	0.008	0.01
222.62	3.33	-0.66	0.00	0.043	0.0085
222.92	1.01	-1.42	0.021	0.033	0.0032
228.02	1.17	-1.45	0.034	0.053	0.0523
234.23	1.94	-0.86	0.008	0.00	0.02
238.64	2.74	-0.88	0.00	0.033	0.0054
247.39	0.93	-1.71	0.005	0.009	0.045

TABLE 2. Position of some local minima of the spanwise vorticity for the simulation with Box2 and the relative error with the same minima for the simulation with Box1. The difference in the y position is divided by $3\delta_0^*$, the length of the structure in the wall normal direction, while the difference in the x position is related to the streamwise wavelength of the secondary instability mode ($\lambda_x = 11.9\delta_0^*$).

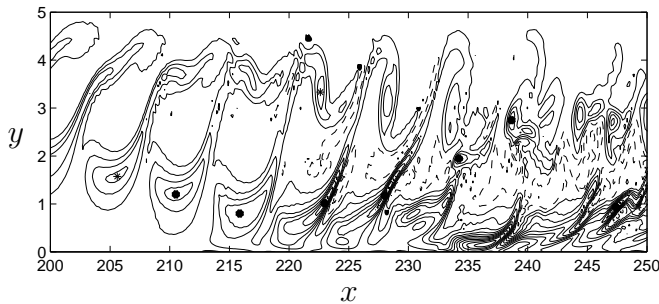


FIGURE 1. Isocontours of the instantaneous spanwise vorticity component at $z = 0$, $Re_{\delta_0^*} = 875$. Contour levels: minimum -2.1, maximum 0.7, spacing 0.2 (— negative values). The stars represent the points reported in Table 2.

The resolution of Box3 is the same as Box2 in the y and z directions, while it is slightly increased in the streamwise variable. To show that in the Box3-simulation we are following the same phenomena from a position further downstream, the energy in the different Fourier modes is compared with the that obtained using Box2 in figure 2. Sixteen velocity fields are saved during one period of the secondary instability mode. These velocity fields are then transformed in time and in the spanwise direction to Fourier space and the notation (ω, β) , where ω and β are the frequency and spanwise wavenumber, each normalized with the corresponding fundamental frequency and wavenumber, is used. The same behaviour is observed for $x \lesssim 250$; hence we can assume that

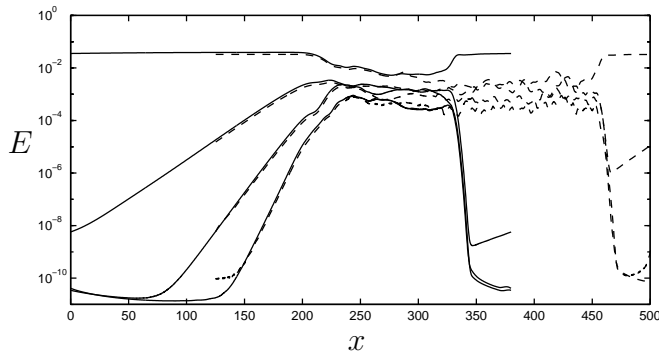


FIGURE 2. Energy in four different modes $(\omega, \beta) = (0, 1)$, $(1, 1)$, $(2, 1)$ and $(3, 1)$, from two different simulations; Box2: —, Box3 - - -. The effect of the fringe region can be seen.

the resolution is adequate also for the simulation with Box3, as confirmed by plots of the energy spectra (not reported here). The evolution of the perturbation in the fringe region can also be seen in figure 2: both in Box2 and Box3 the fringe is 60 units long, therefore one can estimate the x interval not affected by the fringe technique that extend up to $x \approx 310$ and $x \approx 445$ respectively (see Nordström *et al.* 1999, for the analysis of the upstream influence of the fringe region).

3. Results

In the first part of this section we give an overview of the full transition scenario of a streamwise streak subjected to sinuous secondary instability. Instantaneous flow structures and mechanisms responsible for the breakdown are discussed in section 3.4. In section 4 we compare this new scenario with other known transition scenarios.

3.1. Friction coefficient and predictability

The skin friction coefficient is shown in figure 3 versus the streamwise location; it is obtained by averaging in time and in the spanwise direction. Also the values for a Blasius laminar flow and a turbulent boundary layer are displayed for comparison. The C_f starts to rise at $x \approx 190$ and reaches two maxima at $x \approx 250$ and $x \approx 310$. The streamwise location of maximum skin friction may be used to define the completion of the transition process, and in fact, as will be shown in the next section, the flow starts to lose its predictability and periodicity at $x \approx 250$. Strong streaks are already present at the beginning of the simulations, therefore the value of C_f is higher than in the laminar case. The increase in wall shear stress is due to the nonlinear modification of the mean velocity profile which is positive close to the wall and becomes negative for higher y , see Figure 13 in Andersson *et al.* (2001).

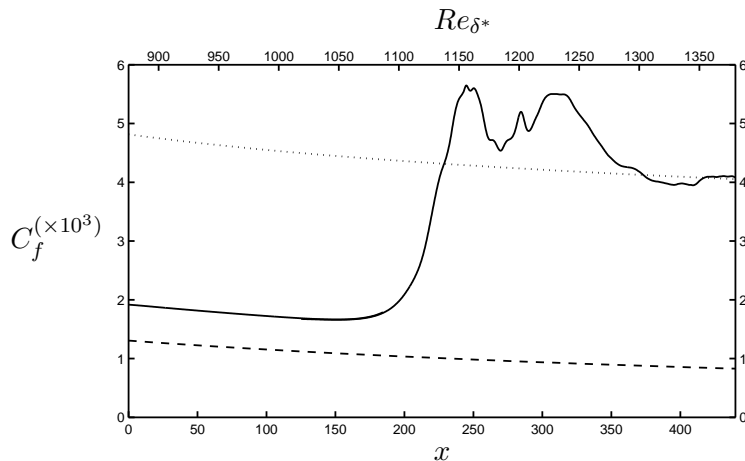


FIGURE 3. Skin friction coefficient versus the streamwise position. Both the streamwise variable x used throughout the paper and the corresponding Reynolds number based on the local Blasius displacement thickness are displayed. Present simulations: —, laminar values: - - -, turbulent coefficient according to Prandtl–Schlichting formula: · · ·.

A characteristic of turbulent flows is its unpredictability. In fact two flows initially very close, will become completely uncorrelated as time goes on. Before discussing the flow characteristics, we need to determine for which downstream positions the flow may still be considered deterministic, i.e. determined by the periodic inflow conditions and where instead it can be seen as randomized. This would give us a further indication of the transition location and help in identifying the flow structures fundamental in the transition process.

A quantitative measure of the aperiodicity and loss of predictability can be defined by a functional g , given by

$$g(f) = \log_{10} \left[\frac{1}{N} \sum (f(t) - f(t + mT))^2 \right]^{1/2}$$

where $f(t)$ and $f(t + mT)$ are the values of a quantity f at time t and after an integer number m of periods (T), and the summation is over the $N = N_y \times N_z$ points defining a $y-z$ plane. In Sandham & Kleiser (1992) the authors define a similar quantity for the case of temporal simulations of transition in a channel flow originating from secondary instability of Tollmien–Schlichting waves. In that case the loss of symmetry between the two halves of the channel is considered as time evolves. In our spatial simulations the loss of time periodicity at the different x positions is studied as the disturbance travels downstream.

The values of g obtained from the streamwise velocity component are shown in figure 4. Expressing the growth of the aperiodicity as $e^{\sigma x}$, we can interpolate the data to obtain a value of $\sigma = 0.016$ for $x < 240$, which is comparable with

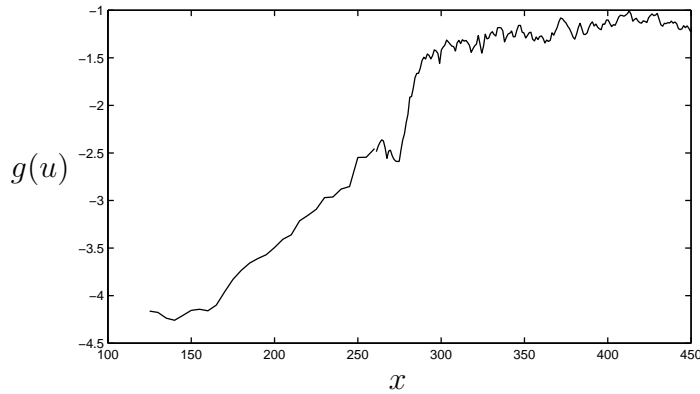


FIGURE 4. The aperiodicity measure g for the streamwise velocity component u , showing the loss of predictability during the transition process.

the growth of the energy $\sigma_e = 2\sigma_u = 0.033$ of the secondary instability mode obtained from the data shown in figure 2. In this region the flow is governed by the growth of the secondary instability modes, so if a difference is present in two initial conditions it will grow as the secondary instability itself. The loss of predictability occurs very late in the transition process, noticed by the sharp change of slope at $x \approx 250$. This result is consistent with the location of maximum skin friction. At this location the Reynolds numbers based on the friction velocity u_τ and the momentum loss thickness or the boundary layer thickness δ_{99} are respectively $Re_{\tau,\theta} \approx 35$ and $Re_{\tau,\delta_{99}} \approx 240$. For $x \approx 300$ the decorrelation becomes larger and then stays constant with the downstream position.

3.2. Spectral analysis and eigenmode structure

3.2.1. Development of Fourier components

The energy in some time and spanwise Fourier modes is displayed in figure 5, where the zero frequency mode represents the streak. The secondary instability mode ($\omega = 1$) is present at the beginning of the computation, while the higher harmonics are excited as the flow evolves downstream (compare figure 2). The energy growth is exponential for a long streamwise distance and the growth rate of the first harmonic ($\omega = 2$) is twice that of the fundamental secondary instability and similarly for higher frequencies, the growth rate is proportional to the harmonic order. This is a consequence of the fact that the first harmonic is forced by nonlinear interactions of the fundamental mode and so its exponential behaviour is given by the sum of those of the interacting modes. In the same way the mode with $\omega = 3$ is induced by the interaction of $\omega = 1$ and $\omega = 2$ modes and it is characterized by a growth rate that is about $3\sigma_e$. It is interesting to note that the energy content is of the same order for modes

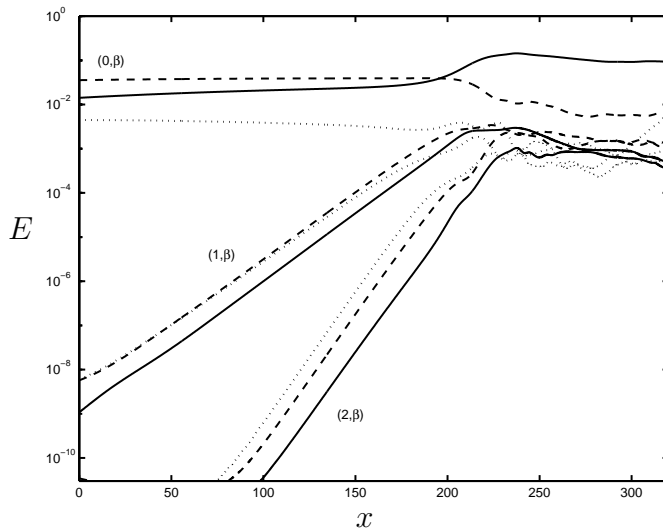


FIGURE 5. Energy in different Fourier modes (ω, β) versus the streamwise position. Frequencies: zero (streaks), one (secondary instability), two (higher harmonic). —, $\beta = 0$; - - -, $\beta = 1$; \cdots , $\beta = 2$.

with different spanwise wavenumbers but with the same frequency. This result is different from the one obtained when the same analysis is applied to a case of transition initiated by two oblique waves (see Berlin *et al.* 1999) or by Tollmien–Schlichting waves (see Laurien & Kleiser 1989; Rist & Fasel 1995, for example). In these cases nonlinear interactions are important to select the modes dominating the transition process, namely the streamwise independent ones, while here streaks are induced from the start and they develop to a highly nonlinear stage before they become unstable to time dependent disturbances; thus the harmonics in the spanwise direction are generated during the streak growth and are responsible for the large spanwise shear of the flow. The instability of such a flow is then characterized by modes strongly localized in the spanwise direction so that a number of wavenumbers β is needed to correctly capture them (see Andersson *et al.* 2001).

The growth in the different harmonics starts to saturate around position $x = 200$ and soon the energy becomes of the same order for the different ω values. From this point ($x \approx 220$) the Fourier transform in time of the whole velocity fields is no longer accurate since not enough frequencies are resolved. In fact higher and higher harmonics are excited until the energy spectra fill out with increasing values in a large low-frequency band, due to the now strong nonlinear interactions. Analysis of the time signal of the streamwise velocity fluctuations at different locations reveals thus some interesting features of the flow. In fact at positions further downstream of the transition point and in

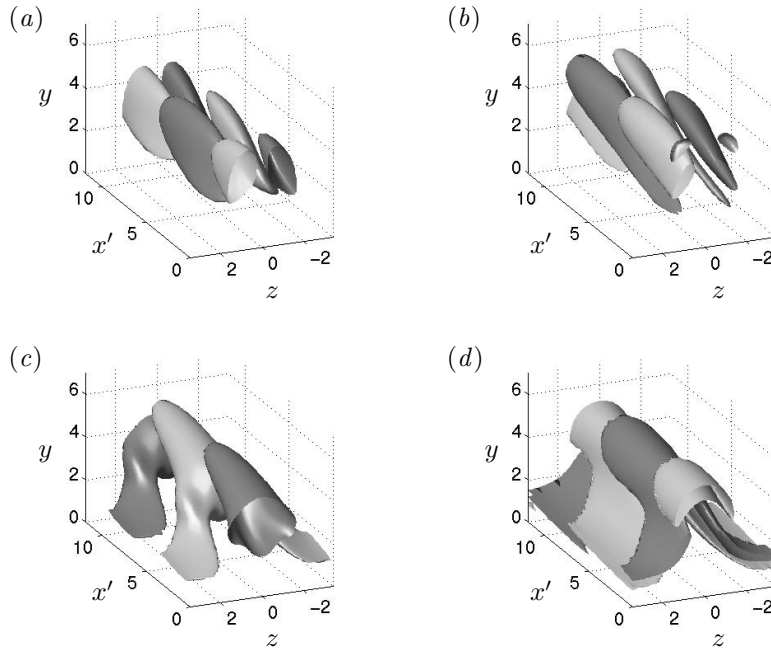


FIGURE 6. Isosurface of positive and negative values of the secondary instability eigenmode. (a) streamwise velocity component; (b) wall normal velocity component; (c) spanwise velocity component; (d) streamwise vorticity component. The streamwise coordinate $x' = x - 125$ reflects the local view of the figure.

the outer part of the boundary layer the flow still maintains the dominating periodicity of the inflow perturbation, while close to the wall the time traces look random and completely uncorrelated to the secondary instability mode. A similar behaviour is observed in the natural transition scenario by Meyer *et al.* (1999). They noted in fact, that the growth of some non-periodic random perturbation occurs in the near-wall region below the deterministic evolution of stable ring-like structures. Finally, some features of the mean flow can be assessed by looking at the different components of the stationary disturbance in figure 5, i. e. $(0, \beta)$ modes, recalling that the $(0, 1)$ and $(0, 2)$ modes represent the spanwise modulation of the flow and the $(0, 0)$ is the distortion from the Blasius profile. The energy in the first two decreases by a factor of ten as soon as the late stages of the transition process are reached, indicating that the mean flow is losing its modulation, while the latter mode is growing since the mean laminar velocity profile is approaching its turbulent counterpart.

3.2.2. Eigenmode structure and streamwise vorticity generation

As observed in a number of experiments and numerical studies, see Swearingen & Blackwelder (1987); LeCunff & Bottaro (1993) for example, the sinusoidal instability can be related to the spanwise inflectional points of the mean flow. Andersson *et al.* (2001) have shown that the streamwise velocity of the secondary instability modes is concentrated around the critical layer, i.e. the layer of constant value of the mean field velocity corresponding to the phase speed of the disturbance which is $u = 0.81U_\infty$ in the present case, thus confirming the inviscid nature of the instability considered. In this work we extend the previous analysis to consider the complete three-dimensional structure of the eigenfunction in order to investigate the instability mechanism leading to the formation of streamwise vorticity.

A three-dimensional plot of the secondary instability mode is displayed in figure 6. This is obtained from the Fourier transformed velocity fields discussed in section 3.2.1, filtering at the fundamental frequency. The mode is characterized by a streamwise wavelength $\lambda_x = 11.9$ and a frequency $\omega = 0.43$; only one wavelength λ_x is shown in the plots around position $x = 125$. Isosurfaces of positive and negative streamwise and wall-normal velocity are plotted in figure 6 (a) and (b) and show the odd symmetry of this kind of instability. The fluctuations are stronger around $z = 0$, i.e. in the low-speed region. The result is the spanwise oscillation of the low-speed streak. The spanwise velocity, seen in figure 6 (c), is in fact characterized by alternating positive and negative values, with a symmetric distribution of the disturbance with respect to the streak. All the perturbation velocity components appear tilted towards the streamwise direction.

In figure 6 (d) the streamwise disturbance vorticity is also shown. This is symmetric with respect to the streak; structures of the same sign appear above the low- and high-speed streak, connected by legs situated along the flanks of the low-speed region. In a similar manner to Kawahara *et al.* (1998) we analyse the production of streamwise vorticity for the unstable sinusoidal eigenfunction. Since the structures observed at the late stages of transition consist of elongated quasi-streamwise vortices, we focus our study on the streamwise component only. The streamwise vorticity of the base flow is initially very low so that its production is almost entirely related to the instability features. Analysis of the wall-normal and spanwise vorticity showed in fact that vorticity fluctuations are mainly induced by the periodic advection of the strong shear layers of the streaky base flow by the velocity fluctuations.

To derive an equation for the streamwise vorticity perturbation, we consider a parallel base flow, consisting at leading order only of the streamwise velocity component, i.e. $\vec{U} = (U(y, z), 0, 0)$. This is shown in Andersson *et al.* (2001) to describe correctly the streak's instability. This yields

$$\left(\frac{\partial}{\partial t} + U \frac{\partial}{\partial x}\right) \omega_x = \frac{\partial U}{\partial z} \frac{\partial v}{\partial x} - \frac{\partial U}{\partial y} \frac{\partial w}{\partial x} + \frac{1}{Re} \nabla^2 \omega_x \quad (6)$$

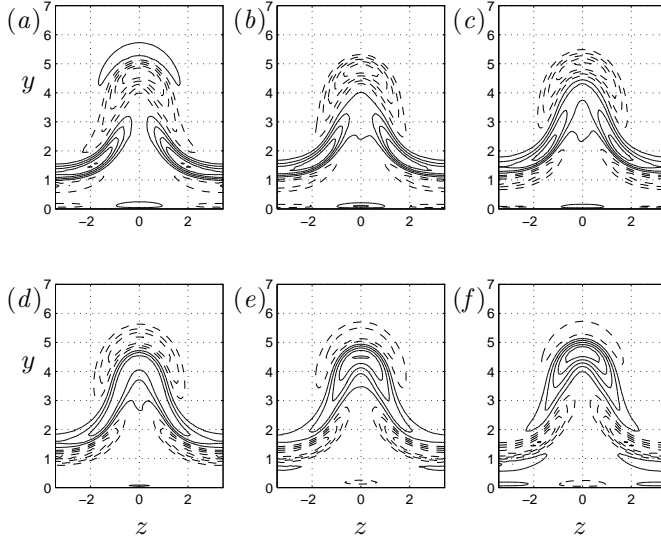


FIGURE 7. Streamwise vorticity of the secondary instability mode during half a period of the disturbance evolution at $x = 125$. From time $t = 1T/10$ to $t = 6T/10$ for (a) to (f). Contour levels: min 0.019, max 0.019, spacing 4×10^{-3} .

where the first two terms on the right hand side represent vorticity production by vortex tilting and the third represents viscous dissipation, which we will neglect. The first of the two production terms is due to the tilting of the spanwise disturbance vorticity ($\frac{\partial v}{\partial x}$) by the spanwise shear ($\frac{\partial U}{\partial z}$), while the second represents the tilting of the wall-normal vorticity perturbation ($\frac{\partial w}{\partial x}$) by the mean wall normal shear ($\frac{\partial U}{\partial y}$). In figures 7, 8, 9 we display contour levels of the streamwise vorticity ω_x and of the two production terms at position $x = 125$ during half a period of the disturbance evolution, in such a way that the plot in the lower right-hand corner is the exact opposite of the one in the upper left-hand corner (or they have a phase difference of π). The wall normal shear is larger than the spanwise shear; the former is largest in the regions above the high-speed streak while the latter is largest on the flanks on the low-speed streak. Moreover the w velocity fluctuations are larger than those of v , thus the $-\frac{\partial U}{\partial y} \frac{\partial w}{\partial x}$ term is the largest one and attains its maximum in the high-speed regions. In fact, one can note that the production of ω_x driven by $\frac{\partial U}{\partial y}$ (figure 9) is located in the regions on top of the low- and high-velocity streak, while the tilting of ω_z by $\frac{\partial U}{\partial z}$ (figure 8) is responsible for the 'legs' of the ω_x structures observed in figure 6 (d).

The physical mechanism responsible for streamwise vorticity generation can be explained by considering the eigenmode of the wall-normal and spanwise velocity, which are both inclined towards the streamwise direction by the mean

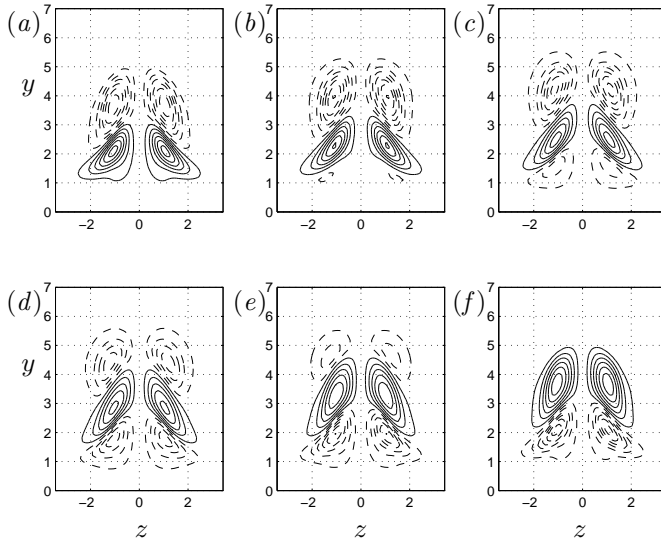


FIGURE 8. Production of streamwise vorticity of the secondary instability mode due to spanwise shear $\frac{\partial U}{\partial z} \frac{\partial v}{\partial x}$, during half a period of the disturbance evolution at $x = 125$. From time $t = 1T/10$ to $t = 6T/10$ for (a) to (f). Contour levels: min -6.5×10^{-4} , max 5.5×10^{-4} , spacing 1×10^{-4} .

shear of the base flow. For the first production term in equation (6) the inclined v structures directly induce streamwise and spanwise vorticity. This is in turn tilted in the streamwise direction by the mean spanwise shear, leading to the production of new streamwise vorticity. The induced vorticity increases the oscillation of the streak and therefore the wall-normal velocity fluctuations. Thus, the process is self-inducing with increasing values of the perturbation as it travels downstream. Similarly for the second term on the right hand side of equation (6), the induced streamwise vorticity, creates new spanwise velocity and the amplification can continue.

We finally note that the production of the perturbation kinetic energy in the linear stages of the secondary instability is only due to the spanwise shear-driven term, $-(\frac{\partial U}{\partial z}) \overline{uv}$.

3.2.3. Weakly nonlinear stages of transition

In figure 10 the velocity fluctuations intensities of the fundamental mode and its first two harmonics are shown in a cross-stream plane at position $x = 175$. At this point nonlinear interaction has begun to be relevant and the higher harmonics are clearly distinguished in frequency spectra. In the case of sinusoidal instability the fundamental mode is characterized by fluctuations in the wall-normal and streamwise velocities which are antisymmetric with respect to the line of symmetry of the background streak, while the spanwise velocity

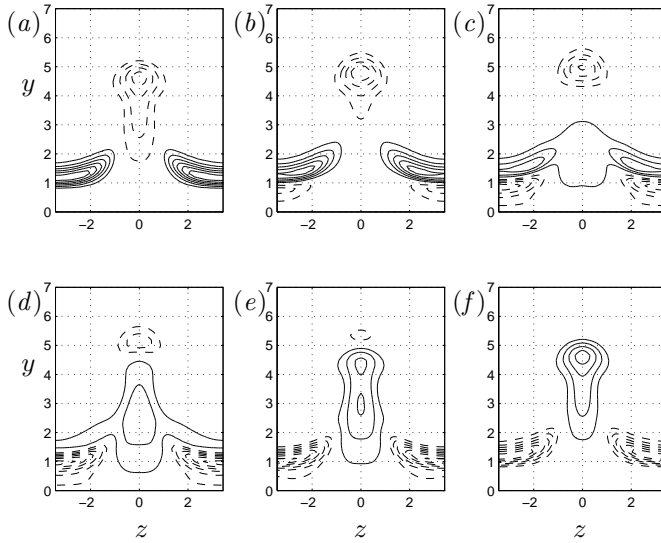


FIGURE 9. Production of streamwise vorticity of the secondary instability mode due to wall normal shear $-\frac{\partial U}{\partial y} \frac{\partial w}{\partial x}$, during half a period of the disturbance evolution at $x = 125$. From time $t = 1T/10$ to $t = 6T/10$ for (a) to (f). Contour levels: min -1.2×10^{-3} , max 1.2×10^{-3} , spacing 2×10^{-4} .

is even. Considering that the harmonics are forced by quadratic interactions, it is possible to show that the modes with frequencies 3ω , 5ω , etc. have the same symmetry as the fundamental mode, while for 2ω , 4ω , 6ω , etc. the u, v fluctuations are symmetric and the spanwise antisymmetric. One can also note that the v, w velocity fluctuations are stronger further from the wall than the u component.

3.3. Time-averaged properties

We present here the results obtained by averaging the velocity over time, during 50 periods of the fundamental streak instability, and in the spanwise direction. We first show in figure 11 the development of the boundary layer displacement (δ^*) and momentum thickness (θ), together with the theoretical values for a Blasius laminar flow. In the region $200 \lesssim x \lesssim 250$, δ^* decreases, whereas θ is still increasing. The latter is related to the fact that the average skin friction increases. A similar behaviour of the boundary layer thickness and of the momentum-loss has been observed by Matsubara & Alfredsson (2001) in a boundary layer subjected to free-stream turbulence. Note also that, at the beginning of the computations, θ is already larger than the laminar value due to the presence of a strong streak.

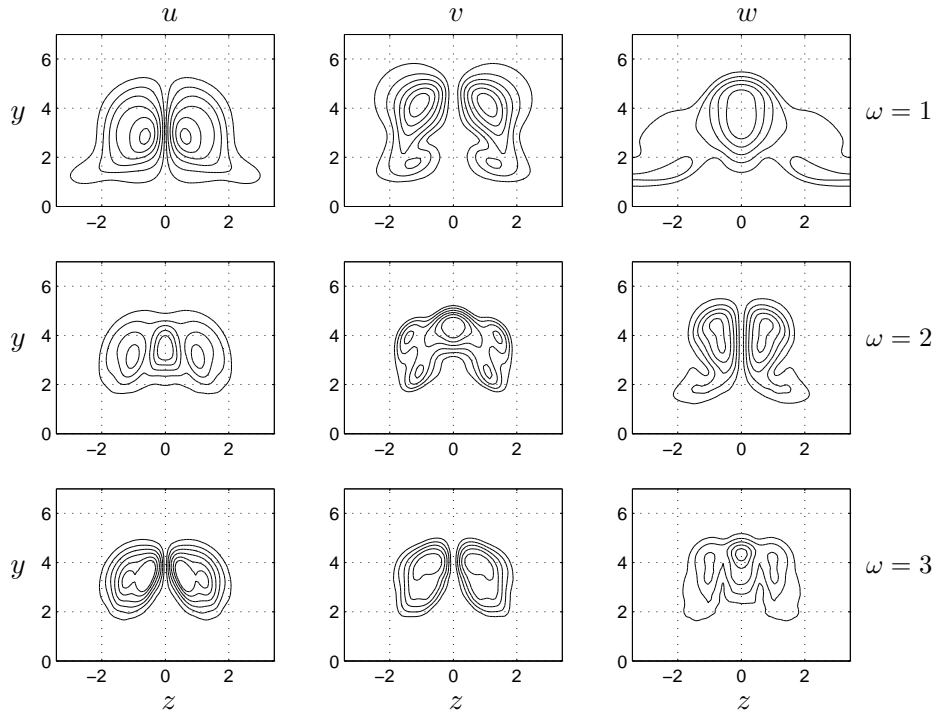


FIGURE 10. Root-mean-square values of the three velocity components in cross-stream plane at position $x = 175$ at the frequency of the secondary instability mode and its first two harmonics. Contour levels: $u(\omega = 1)$ min 2×10^{-3} , max 5.2×10^{-2} , spacing 1×10^{-2} ; $v(\omega = 1)$ min 3×10^{-3} , max 1.3×10^{-2} , spacing 2×10^{-3} ; $w(\omega = 1)$ min 8×10^{-3} , max 2.4×10^{-2} , spacing 4×10^{-3} ; $u(\omega = 2)$ min 2×10^{-3} , max 1.4×10^{-2} , spacing 3×10^{-3} ; $v(\omega = 2)$ min 1.8×10^{-3} , max 4.3×10^{-3} , spacing 5×10^{-4} ; $w(\omega = 2)$ min 7×10^{-4} , max 3.9×10^{-3} , spacing 8×10^{-4} ; $u(\omega = 3)$ min 7×10^{-4} , max 4.5×10^{-3} , spacing 8×10^{-4} ; $v(\omega = 3)$ min 5×10^{-5} , max 1.7×10^{-4} , spacing 3×10^{-5} ; $w(\omega = 3)$ min 3×10^{-5} , max 1.5×10^{-4} , spacing 3×10^{-5} .

3.3.1. Transitional flow

Mean velocity profiles at various locations in the transitional zone are displayed in figure 12, where the wall normal coordinate is made non dimensional with the local displacement thickness δ^* . The evolution from the laminar flow to a turbulent one can be seen. At position $x = 215$ a strong inflectional mean profile is present during the large growth of the skin friction coefficient, see figure 3. In the outer part of the boundary layer one can see an over-shoot of the velocity before approaching the final value. The same behaviour of the

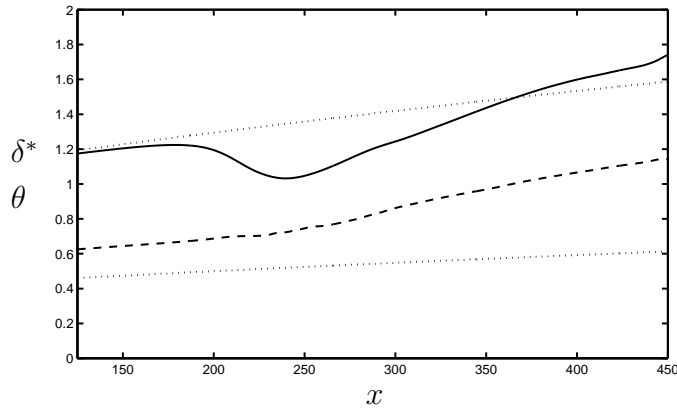


FIGURE 11. Integral boundary layer parameters: —, displacement thickness δ^* ; ---, momentum thickness θ ; \cdots , theoretical values for laminar Blasius profile.

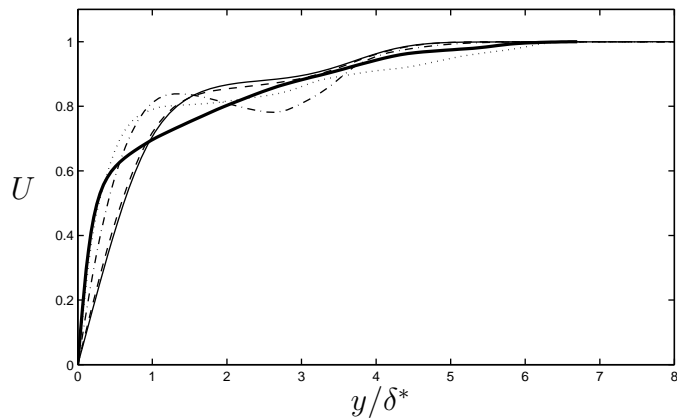


FIGURE 12. Average streamwise velocity in outer coordinates at different streamwise positions; $x = 126$: — (thin line), $x = 185$: ---, $x = 215$: - · - ·, $x = 268$: \cdots , $x = 399$: — (thick line).

mean flow was observed by Wu *et al.* (1999) in their simulations of transition induced by free-stream turbulence.

At the early stages of transition, the averaging of the streamwise velocity provides information on the evolution of the streak during the process, since the spanwise modulation dominates in the r.m.s. values. These are displayed in figure 13 together with the other two velocity components. In the experiments of Matsubara & Alfredsson (2001) on transition induced by upstream-generated grid turbulence the u_{rms} value attained by the streaky

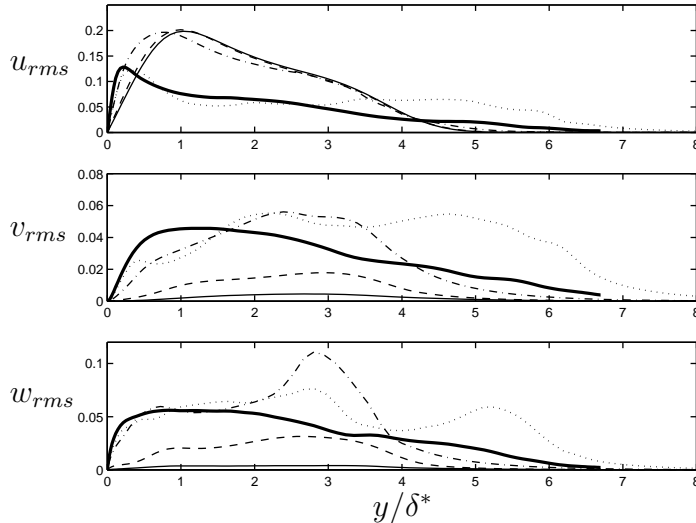


FIGURE 13. Root-mean-square values of the three velocity components in outer coordinates at different streamwise positions; $x = 126$: — (thin line), $x = 185$: - - -, $x = 215$: - · - ·, $x = 268$: ···, $x = 399$: — (thick line).

structure before the breakdown is about 11 – 12%. In our case, instead, the streak amplitude at the beginning of transition is about 19%, but, as observed in Wundrow & Goldstein (2001), the averaged values usually reported in the experiments are likely to mask the stronger localized distortions which induce the breakdown. However, the same qualitative behaviour of the u_{rms} is observed as in the experiments, i.e. the peak is sharpening, moving closer to the wall and reaching values of approximately 12 – 13%.

As the flow develops downstream, the r.m.s. values of the wall normal and spanwise velocity components increase especially in the outer part of the boundary layer, around $y \approx 3$. This corresponds to the wall normal region where the secondary instability is localized, see figure 10. One can also note that the spanwise velocity fluctuations are larger than the wall normal ones, and a considerable value of $w_{rms} \approx 11\%$ is attained at $x = 215$. This result is not unexpected since the kind of instability studied is characterized until its late stages by a strong spanwise oscillations of the low-speed streak. It is also interesting to notice that at $x = 268$ the mean velocity profile, figure 12, and the u_{rms} are very close to the turbulent ones, especially close to the wall, but the v_{rms} and w_{rms} are characterized by large values in the upper part of the boundary layer. As we will see in a later section, these oscillations represent structures, formed in the transition region which survive downstream while the shear stress at the wall increases and the near wall flow may be considered turbulent.

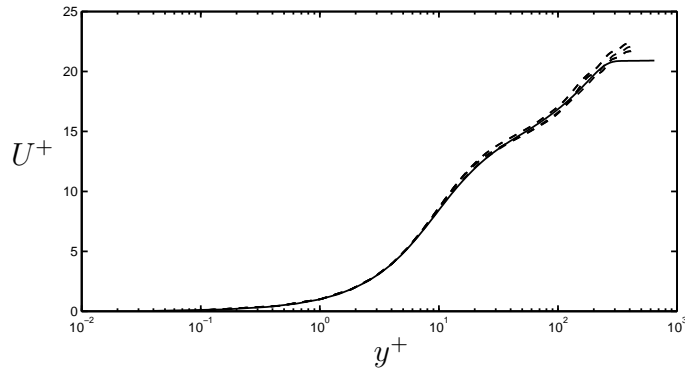


FIGURE 14. Mean streamwise velocity profiles in inner scaling. - - -: present simulations at $Re_\theta = 845$ ($x = 360$), $Re_\theta = 875$ ($x = 375$) and $Re_\theta = 910$ ($x = 400$); —: Skote(2001) simulations at $Re_\theta = 685$.

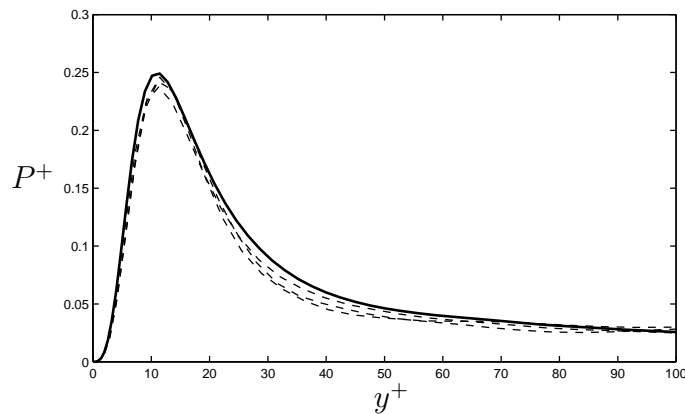


FIGURE 15. Time averaged non-dimensional turbulence kinetic energy production, $P^+ = -\overline{uv}^+ \frac{\partial U^+}{\partial y^+}$, near the wall. - - -: present simulations at $Re_\theta = 845$ ($x = 360$), $Re_\theta = 875$ ($x = 375$) and $Re_\theta = 910$ ($x = 400$); —: Skote(2001) simulations at $Re_\theta = 685$

3.3.2. Quasi turbulent flow

In this section we discuss the results of the statistics obtained towards the downstream end of the simulations, where the flow becomes uncorrelated to the inflow conditions and the skin friction coefficient approaches turbulent values, see figures 3 and 4.

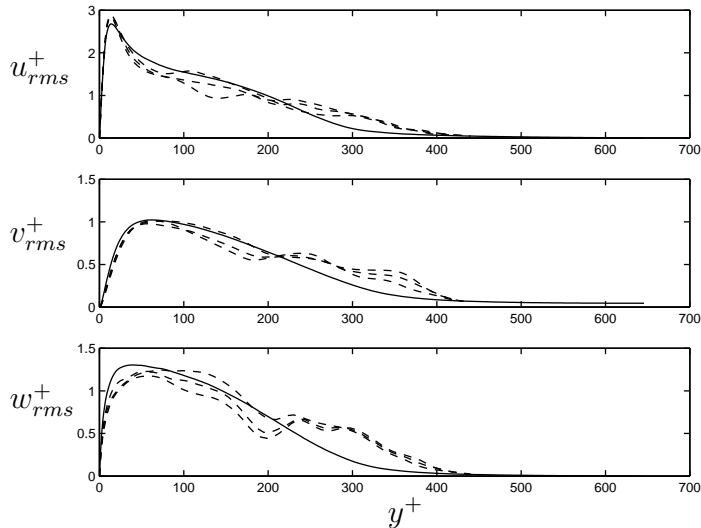


FIGURE 16. Root-mean-square values of the three velocity components in inner coordinates. - - -: present simulations at $Re_\theta = 845$ ($x = 360$), $Re_\theta = 875$ ($x = 375$) and $Re_\theta = 910$ ($x = 400$); —: Skote(2001) simulations at $Re_\theta = 685$.

The mean velocity profiles are displayed in inner coordinates in figure 14 at three different downstream positions, together with the results from the spatial simulations of a fully turbulent boundary layer with zero pressure gradient by Skote (2001) are shown for comparison, although for a lower value of the momentum thickness Reynolds number Re_θ . Profiles of the time-averaged turbulence kinetic energy production normalized with wall parameters are shown in figure 15 at the same three streamwise stations and compared again with the DNS data of Skote (2001). Note that all profiles show a maximum of $P^+ = 0.25$ at $y^+ = 12$, showing self-similarity.

The r.m.s. values for the three velocity components are displayed in figure 16. The results show large differences compared to a fully turbulent flow in the outer part of the boundary layer, where periodic flow structure are still present, as shown earlier. Thus, analysis of the results indicates that the averaged quantities reproduce well close to the wall the features of a turbulent flow.

3.4. Flow structures

3.4.1. Overall features

Before discussing in detail the instantaneous flow structures we give a first general idea of the transition scenario by showing snapshots of the flow. In figure 17 the instantaneous streamwise velocity component of the perturbation

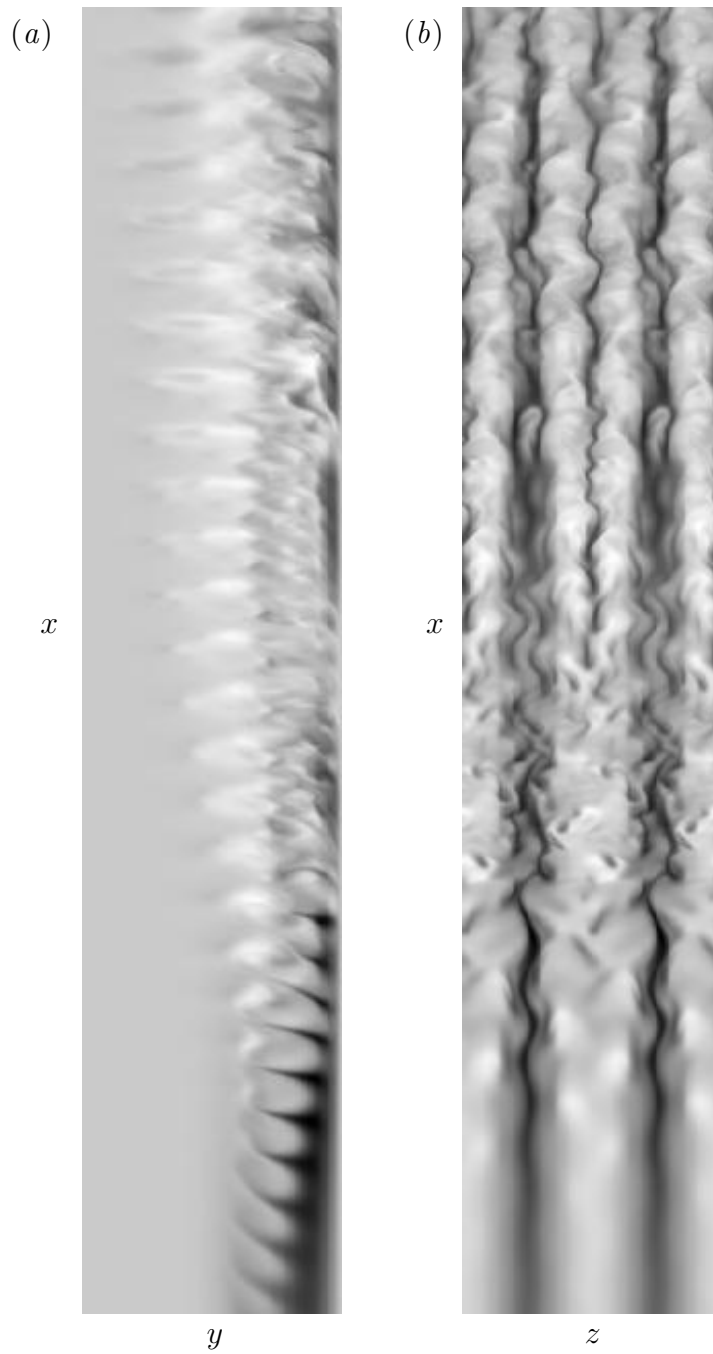


FIGURE 17. Visualization of streak breakdown using streamwise velocity component of the perturbation in (a) a wall normal x - y plane at $z = 0$ and (b) a wall parallel x - z plane at $y = 0.45$. $x \in [185, 360]$. Grey scale from dark to light corresponding to negative to positive values. The flow is from bottom to top. In (b) two spanwise streaks are displayed.

is shown in a longitudinal plane perpendicular to the wall for $z = 0$, corresponding to the center of the undisturbed low-speed streak and in a plane parallel to the wall, at $y = 0.47$. The perturbation velocity field is defined as the difference between the solution velocity field and the mean value in the spanwise direction for each value of x and y . It can be clearly seen that the sinuous instability consists of harmonic antisymmetric streamwise oscillations of the low-speed region. In figure 17 (a) one can note that the perturbation is first seen in the outer part of the boundary layer. The disturbance then moves towards the wall until the wall-shear is considerably increased. At the end of the computational box some periodicity can still be seen in the disturbance in the outer part of the boundary layer, as discussed previously, while close to the wall the flow is now turbulent. In figure 17 (b) two streaks can be seen within one computational domain at the end of the transition process; note that the spanwise dimension of the box for $x > 350$ is less than 275 in wall units.

A three-dimensional picture of the flow field from the laminar to the turbulent region is shown in figure 18. The lighter grey isosurface represents the low-speed streaks, while the dark grey represents regions of low pressure. These correspond to strong rotational fluid motions and are used to identify vortices. Also, visualizations using negative values of the second largest eigenvalue of the Hessian of the pressure (see Jeong *et al.* 1997) are performed and no relevant differences are observed. The main structures observed during the transition process consist of elongated quasi-streamwise vortices located on the flanks of the low-speed streak. Vortices of alternating sign are overlapping in the streamwise direction in a staggered pattern and they are symmetric counterparts, both inclined away from the wall and tilted in the downstream direction towards the middle of the undisturbed low-speed region. The strength and extent of these vortices and the spanwise motion of the low-speed streak increase downstream before the breakdown. Note also that the downstream end of the streamwise vortices, located in the outer part of the boundary layer, is tilted and propagates in the spanwise direction to form arch vortices. Towards the end of the box the flow has a more turbulent nature and more complicated low-pressure structures occur. It also seems that there is no connection between the laminar and turbulent-region low-speed streaks, since the streak is disrupted at transition and those which appear downstream are not a continuation from upstream.

3.4.2. Late stages of transition

To study in detail the late stages of the streak breakdown, we plot in figure 19 the instantaneous flow in vertical planes at different streamwise positions, covering a distance corresponding to about one half of the secondary instability wavelength. The velocity vectors show the spanwise and wall-normal velocity. The thick black isolines represent the streamwise velocity and the white line regions of low pressure. In the background, the streamwise vorticity is shown from negative values (light areas) to positive (dark areas). One can follow the

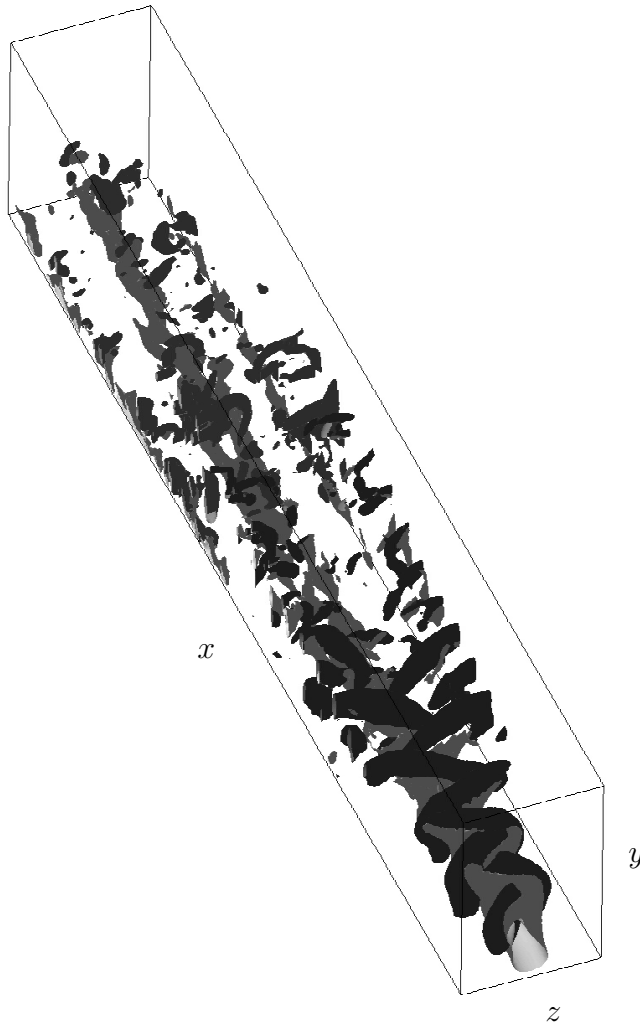


FIGURE 18. The flow field from the laminar to the turbulent region. The x -values correspond to the range $x \in [185, 360]$. The grey structures are the low-speed streaks and the darker ones are regions with low pressure. Contour levels are -0.14 for the streamwise velocity fluctuations and -0.014 for the pressure for $x < 268$ and -0.0065 further downstream. The streamwise scale is one third of the cross-stream scale.

evolution of one of the two quasi-streamwise vortices observed in figure 18, namely the one characterized by negative vorticity, located on the flank of the low-speed streak denoted by negative z . In figure 19 (*a*), one can note that the vortex with $\omega_x > 0$ is still visible in the upper part of the boundary layer,

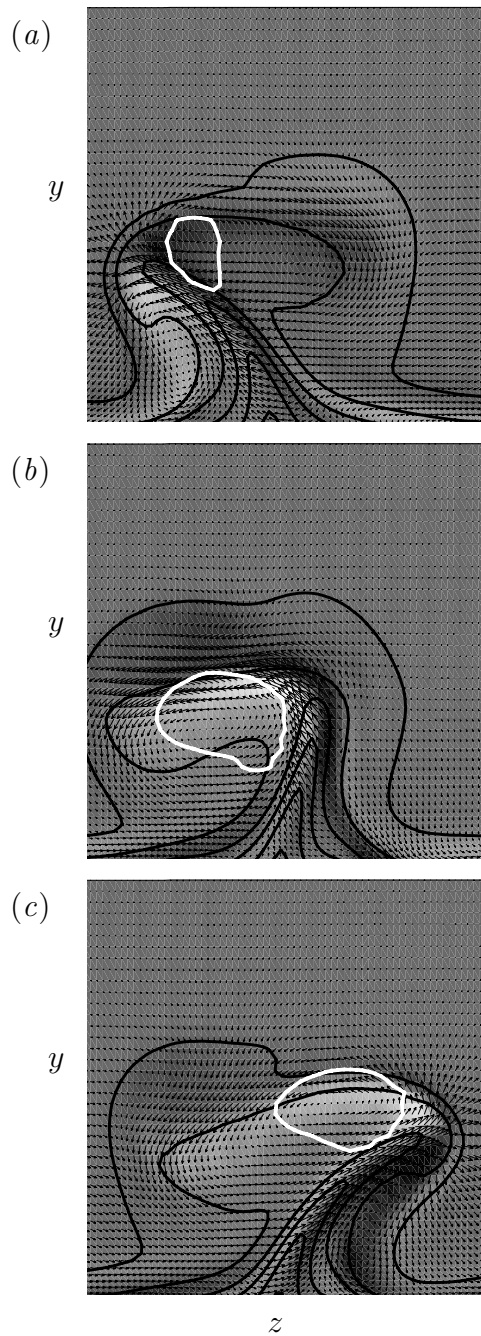


FIGURE 19. Vertical cross-stream planes at position (a) $x = 208$, (b) $x = 211$, (c) $x = 213$. The velocity vectors represent spanwise and wall-normal velocity. Thick black isolines represent the streamwise velocity and the white line regions of low pressure. The background shows values of streamwise vorticity from negative values (light areas) to positive (dark areas).

where the pressure attains its minimum value. However a negative vortex, i.e. with rotation in the counter-clockwise sense, is already formed below this and is moving in the positive z -direction and towards the upper part of the boundary layer. Regions of strong negative streamwise vorticity are associated with vortices; positive values of ω_x indicate instead regions of strong spanwise gradient of the wall-normal velocity on the positive flank of the low-speed streak and region of wall-normal gradient of the spanwise velocity in the dark area above the high-speed streak. Similarly when the streak is moving in the negative z -direction, regions of positive ω_x are associated with vortices. By symmetry, in fact, the ω_x distribution half a wavelength away is obtained by reflection and sign inversion (apart from the amplification downstream). Comparing the areas of negative streamwise vorticity of the full velocity field with the isosurfaces of the same quantity displayed in figure 6 (*d*), one can note that only one of the two legs observed in the secondary instability mode, is still present as the main feature of the breakdown. We note also that the leg which is able to induce stronger streaks and then to create stronger mean shear is the one which is still amplified and survive in the late stages. Its symmetric counterpart is working to reduce the mean flow modulation and so it is reasonable to assume that this is the reason for its disappearance. Analysis of the first harmonic of the secondary instability mode shows in fact that the phase lock between the two is such that negative ω_x is increased for negative z . The odd symmetry of this mode implies that at the same time positive ω_x is balancing the negative leg located on the positive side of the low-speed streak. The first harmonic of the secondary instability mode acts also to induce negative vorticity ahead of the V structure typical of the fundamental mode, as can be observed in figure 19 (*c*) where the negative vortex has reached regions of positive z .

Following the evolution of the streamwise vorticity from the linear amplification to the late stages, we note that at the early stages, the instability growth is characterized by increasing values of the flattened ω_x structures displayed in figure 6 (*d*), with the spanwise symmetry of the eigenfunction slightly destroyed by the higher harmonic and by the mean streamwise vorticity. At downstream position $x \approx 205$ the negative and positive ω_x structures are located on the negative and positive flanks of the low-speed region and follow its oscillations (see figure 19). Note also that the low-speed streak is becoming narrower. The final stages of the breakdown are shown in figure 20, in plots similar to the ones of figure 19. In figure 20 (*a*) one can see that as the oscillation of the low-speed region is increased, the upper part of it is subjected to strong motion in the negative direction while the lower part has begun to move in the opposite direction. A similar phase delay between the top and bottom parts of the streak during the sinuous breakdown was also observed in channel flow by Elofsson *et al.* (1999). Considering the dark and light areas in figure 20 (*a*), one can note that the adjacent layers of positive and negative ω_x , located in the low-speed region, roll up to form an arc in the $y-z$ plane. As a result of this the upper part separates and continues its periodic motion in the outer part of the boundary layer. This can be seen in figure 20 (*b*) where one can also

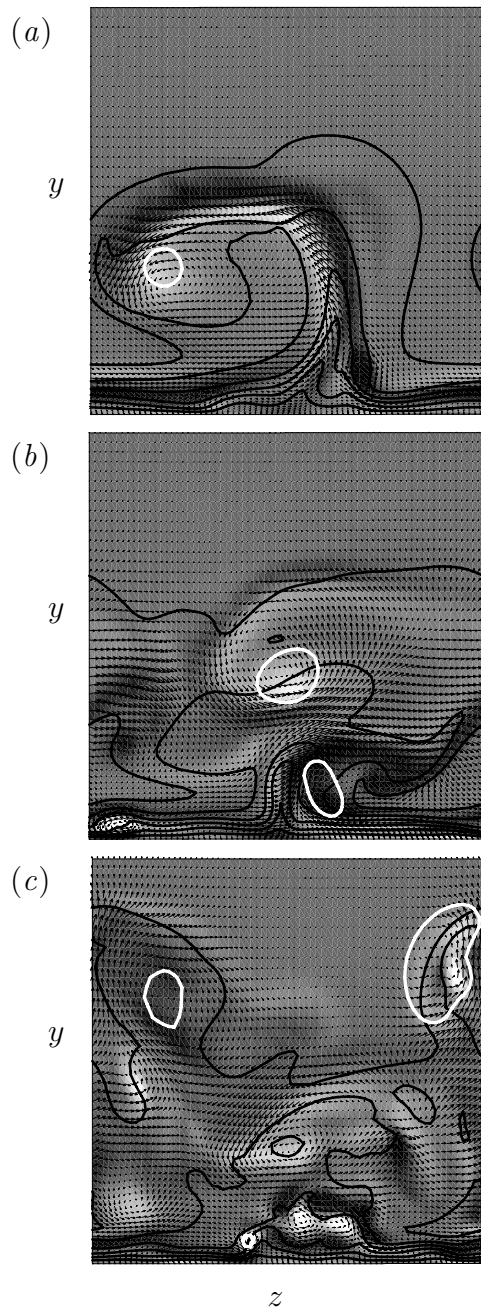


FIGURE 20. Vertical cross-stream planes at position (a) $x = 221$, (b) $x = 234$, (c) $x = 256$. The velocity vectors represent spanwise and wall normal velocity. Thick black isolines represent the streamwise velocity and the white line regions of low pressure. The background shows values of streamwise vorticity from negative values (light areas) to positive (dark areas).

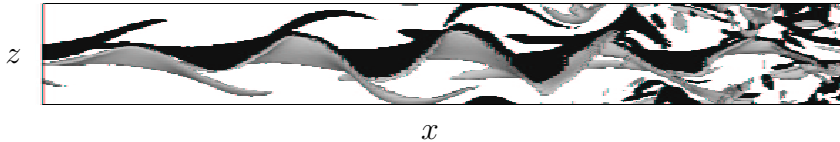


FIGURE 21. Top view of isosurfaces of positive (lighter grey) and negative (dark grey) wall normal vorticity, $\omega_y = \pm 0.53$. $x \in [190, 245]$.

note that the low-speed region is now localized closer to the wall. This lower streak is still subjected to sinuous instability and two vortices can be seen: a positive one similar to the ones observed in figure 19, located on the flank of the streak, and a negative one further away from the wall as a trace of the previous oscillation in the opposite direction. The region of large ω_x on the flank of the streak in figure 20 appear now much more localized. The breakdown of the lower streak is then similar to the process already observed. The higher and lower part are moving in opposite directions and the streak is disrupted. Finally, figure 20(c) shows an instantaneous plot of the flow downstream of the breakdown, where many and disordered structures can be observed.

In figure 21 we display at the actual scale a view from the top of isosurfaces of positive and negative wall-normal vorticity, ω_y , in the final stages of the breakdown. This quantity is almost entirely determined by the mean spanwise shear, $\frac{\partial U}{\partial z}$, so that its downstream evolution is dominated by the spanwise motion of the low-speed region. It is interesting to notice how the upper part separates and continues its motion independently (see the tongue-like structures on the sides of the central low-speed streak). We recall that structures of spanwise vorticity in a plane normal to the wall at $z = 0$ are shown in figure 1. In this case it is the mean normal shear, $\frac{\partial U}{\partial y}$, which determines the largest vorticity. The thin periodic structures represent the shear induced by the motion of the low-speed streak. From this, we can conclude that, except for the arch vortices displaced in the outer part of the boundary layer, the structures of ω_y and ω_z are determined by the motion of the low-speed streak and its associated strong shear layers.

Finally we analyse in detail the main structures detected at the late stages of the transition process. In figure 22 we display a top and side view, at the actual scale, of the low-pressure structures shown before. The region of instantaneous negative streamwise velocity perturbation is also shown for reference. From the top view one can note how the vortices form arches in the spanwise direction invading the whole domain. The side view shows quasi-streamwise structures, tilted away from the wall, which look similar to the leg of the Λ -vortex observed in transition initiated by TS waves, see Rist & Fasel (1995) for example. However, the top view clearly reveals the staggered pattern of these structures. Figure 23 shows the flow pattern in a smaller region, of streamwise extent equal to about one wavelength of the secondary instability mode, just

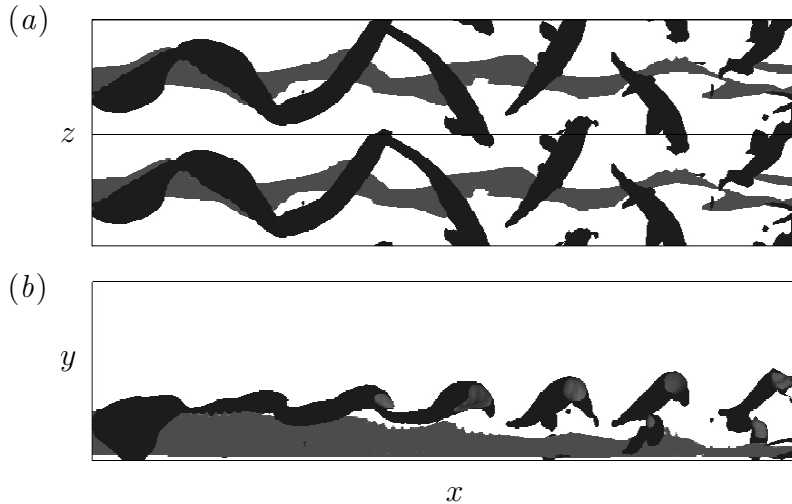


FIGURE 22. (a) Top and (b) side view of the structures at the late stages of transition. $x \in [203, 245]$. Lighter grey represents negative streamwise velocity perturbation and dark grey regions of low pressure. In (a) two spanwise streaks are displayed.

before the final breakdown. The low-speed region is now lower than the original laminar unstable streak. It is still oscillating in the spanwise direction and there are quasi-streamwise vortices located on its flanks in a staggered pattern. In the outer part of the boundary layer, the arch vortices formed before, can be seen. They are now uncorrelated to the streak oscillation underneath.

3.4.3. Visualization by timelines

In experimental investigations of boundary layer transition flow structures are typically investigated through flow visualizations using either hydrogen bubbles or smoke. Here we perform a numerical visualization following the evolution of massless particles. Timelines are generated by releasing particles along lines parallel to the spanwise direction at different times during one period of the secondary instability mode. The instantaneous evolution of these particles is determined by the instantaneous velocity field. In figure 24 we display the evolution of a single material line released at position $x = 150$ and $y = 3$. Two streamwise vortical structures can be seen on the sides of the low-speed region; one is growing and moving away from the wall while the other is approaching the wall. The structures observed from the evolution of a line released half a period later would present the opposite behaviour. Since the particles followed are located in the outer part of the boundary layer, a regular pattern can also be seen downstream of the transition point, $x \approx 250$. Note that the smoke visualizations by Asai *et al.* (1999) in a cross-stream plane also show

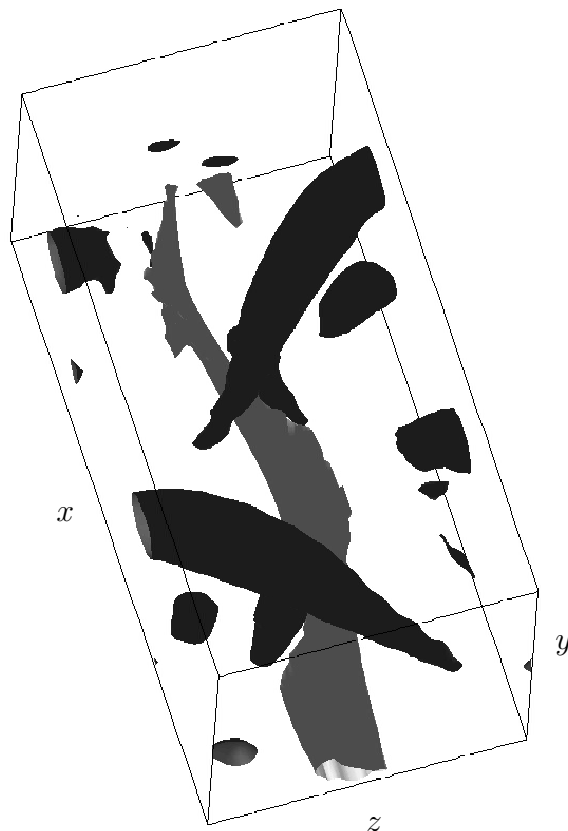


FIGURE 23. Structures at the late stages of transition, shown for one wavelength of the secondary instability. $x \in [227, 239]$. Grey represents negative streamwise velocity perturbation and dark grey regions of low pressure. The flow is from the bottom to the top.

the presence of vortical structures on the flanks of the low-speed streak. The evolution of a material line normal to the wall released at the centre of the low-speed streak has also been studied. The motion of the particles consists of spanwise oscillations of different amplitude and phase at different distances from the wall.

4. Discussion

4.1. Relation to transition induced by free-stream turbulence

Experiments on boundary layers subject to free-stream turbulence show that transition is characterized by the occurrence of strong streamwise streaks (Klebanoff 1971; Kendall 1985; Westin *et al.* 1994). In Andersson *et al.* (2001)

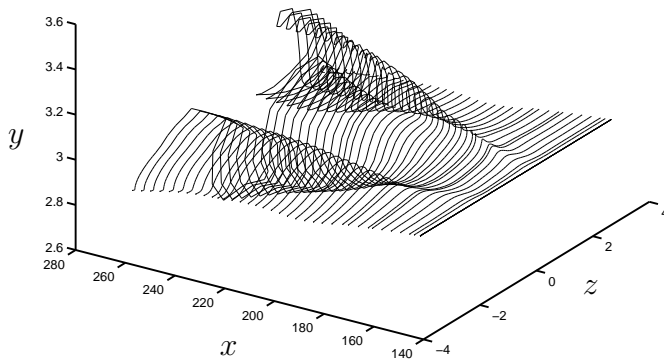


FIGURE 24. Evolution of a spanwise material line released at position $x = 150$ and $y = 3$.

and Matsubara & Alfredsson (2001) it was also shown that the wall-normal mode shape of the optimal disturbance found in the theoretical works of Andersson *et al.* (1999) and Luchini (2000) are remarkably similar to the u_{rms} values measured in boundary layers with free-stream turbulence. A nonlinear mechanism for boundary layer receptivity to free-stream disturbance has been proposed by Berlin & Henningson (1999) and Brandt, Henningson & Ponziani (2002); this is responsible for the generation of streamwise vortices, which in turn, induce the growth of similar streaks. It is now understood that the growth of streaks can be explained successfully by the theory of non-modal growth. However, there is still uncertainty in the way turbulent spots are formed in the boundary layer, once strong streaks are present. In fact, controlled experiments are impossible in a boundary layer under free-stream turbulence and no definitive proof is given of a secondary instability. Flow visualizations (Matsubara & Alfredsson 2001) show that some streaks develop a streamwise waviness of relatively short wavelength, before the formation of spots. These authors attribute this wavy type of motion to a secondary instability, leading to laminar-turbulent transition analogously to what has been observed in channel flows (Reddy *et al.* 1998; Elofsson *et al.* 1999) and in boundary layer flows under controlled conditions (Bakchinov *et al.* 1995; Asai *et al.* 1999). In the theoretical work of Wundrow & Goldstein (2001) it is shown how initially linear, but of broadband nature, perturbations of the upstream flow ultimately lead to strong shear layers in certain localized spanwise regions. These highly inflectional shear layers can then support rapidly growing inviscid instabilities. Jacobs & Durbin (2001) write that no evidence of sinuous, or other prefatory streak instability, is observed in their simulations of a boundary layer under

free-stream turbulence. Jacobs & Durbin (2001) conjecture that streaks become a receptivity site for smaller-scale free-stream turbulence which initiates an instability near the top of the boundary layer.

In the present work we use a simpler flow configuration (steady streak) and show that sinuous instability can lead directly to a turbulent flow and that some of the basic averaged flow data present interesting similarities with experiments and/or simulations of by-pass transition under free-stream turbulence. An important similarity is observed in the development of the boundary layer thickness. The peculiar decrease of this parameter during the late stages of transition seems to be a common feature of our simulation and the experimental results of Matsubara & Alfredsson (2001), which was not observed in other transition scenarios. Future experiments and numerical simulations may be compared with the present results in order to assess a firmer connection between the proposed transition scenario and the streak breakdown in boundary layers subjected to free-stream turbulence. For this purpose it is important to re-emphasize that in order to isolate and observe the features of the streak transition scenario we have simulated the spatial evolution of an instability mode which is induced by a continuous harmonic forcing at the upstream inlet. In a boundary layer subject to free-stream turbulence the secondary instability would, rather, be triggered by localized perturbations, more likely the ones present in the free stream. Therefore the instability would then develop as a localized wavepacket.

4.2. Comparison to O-type, K-type and H-type transition

In this section, we compare the late stages of transition initiated by sinuous instability of streamwise streaks with three different scenarios, observed and studied in flat-plate boundary layers. We consider transition initiated by a pair of oblique waves (O-type), and K- and H-type transition, resulting from the secondary instability of TS-waves. The reader is referred to the experimental study of Bake, Fernholz & Kachanov (2000) for a recent thorough investigation of the resemblance of K- and H-regimes.

Berlin *et al.* (1999) noticed that the structures they identified in the late stages of oblique transition have many similarities with those previous investigations have found in the K- and H-type transition. In fact, they observed that before the flow has reached a fully turbulent state, Λ -shaped structures, consisting of pairs of streamwise counter-rotating vortices are formed. They also noted that inside the Λ -structures there is an upward motion. The lift-up of low streamwise velocity causes strong wall-normal gradients, located on top of the Λ -vortices, again in close similarity to the shear layers observed by Williams, Fasel & Hama (1984) and Rist & Fasel (1995) for example, in K-type transition. Measurements using hot-wire probes revealed that the positions of the Λ -shaped vortices coincided with the appearance of u_{rms} peaks and high-frequency oscillations (spikes). Further, the Λ -vortices observed in O-type transition are associated with inflectional profiles in both the normal and

spanwise directions. Berlin *et al.* (1999) explained the similarities between the O-, K-, and H-regimes by considering the common features of all three transition scenarios, namely oblique waves and streamwise streaks. They speculated that the pattern of Λ -vortices appearing in these three transition scenarios is independent of the presence of Tollmien-Schlichting waves. Using a criterion of positive interference of the normal velocity between the streamwise vortices and the oblique waves, they were able to predict the appearance of the Λ -vortices.

In the present case, streamwise streaks and oblique waves are also the fundamental features at the breakdown and the structures observed present similarities and differences. Similarly to the other transition scenarios, we have found counter-rotating streamwise vortices located on opposite flanks of the low-speed region; the vortex with $\omega_x > 0$ being on the positive side. The structures are inclined away from the wall and tilted in the downstream direction towards the middle of the undisturbed low-speed region. However, the streamwise vortices appear in a staggered pattern, alternating in the streamwise direction. Comparing the present case with oblique transition, we note that the different alignment of the streamwise vortices is due to the symmetry of the fundamental perturbation growing on the streaks. Analysis of the results presented in Berlin *et al.* (1999), shows in fact that the strong streaks induced by nonlinear interactions are perturbed by periodic disturbances, given by the oblique waves themselves, which are symmetric with respect to the streak. Looking also at the symmetry of the late stages of the breakdown, we can relate oblique transition to varicose instability of the streaks.

The different symmetry of the streamwise vorticity perturbation can be used to explain similarities and differences observed in the two scenarios. In the present work, we have followed the evolution of the streamwise vorticity and noted that the initially symmetric distribution is disrupted towards the breakdown. Of the two symmetric 'legs' of positive and negative ω_x alternating in the streamwise direction which can be seen in an instantaneous configuration, only one is amplified downstream, specifically the leg which is able to induce stronger shear layers on the mean flow. Thus, we recover the staggered pattern of quasi-streamwise vortices observed at the final stages of the breakdown. In Berlin *et al.* (1999), isosurfaces of positive and negative instantaneous streamwise vorticity are also shown. One can note that the distribution of ω_x is now antisymmetric. The downstream evolution of ω_x is also characterized by the growth of structures with positive sign on the positive side of the low-speed streak and with negative sign on the negative flank. In this case, however, the structures are not staggered in the streamwise direction and they appear with the typical Λ -shape. The same ideas apply in K- and H-type transition, where the oblique modes of the perturbation are also symmetric with respect to the streamwise vortices. We also note that the same interference criterion introduced in Berlin *et al.* (1999) can be used in the present transition scenario. Interference of positive wall-normal velocity of the secondary instability mode

and of the mean flow can lead to the appearance of a single streamwise vortex on a side of the low-speed region.

The four transition scenarios considered show different behaviours at the downstream tip of the quasi-streamwise vortices. In transition induced by TS-wave instability, a spanwise vortex connecting the legs of the Λ -vortex is observed. This is due to the fact that strong spanwise vorticity is already present as it characterizes the primary instability. Two-dimensional Tollmien-Schlichting waves consist in fact of rolls of spanwise vorticity concentrated around the critical layer. The secondary instability induces a three-dimensional flow and hence streamwise vorticity, by bending the ω_z structures (see Herbert 1988). In oblique transition instead, the legs of the Λ -structures develop independently and are then drawn towards each other. The same evolution of the streamwise vortices is observed in the present case; however the lack of a symmetric counterpart on the other side of the low-speed streak allows the vortex to tilt, cross the low-speed region and generate the observed arches.

4.3. Comparison to transition in vortex-dominated flows

The secondary instability mechanisms considered here show similarities with transition in flows with curvature or in rotating channels, where the dominating instability results in streamwise vortices which, in turn, create streaks (see Swearingen & Blackwelder 1987; Li & Malik 1995, for the case of Görtler vortices). Further, three-dimensional vortical structure detected in the simulations of transition to turbulence in Görtler flow performed by Liu & Domaradzki (1993) show interesting analogies with transition in Blasius flow. In fact, they observed that close to the transition point vorticity structures are associated with a series of connected hairpin vortices in the outer part of the boundary layer. However, these vortices play a smaller role in the transition process than the streamwise vortical structure which is observed to develop close to the wall in the low-speed region between the vortices. They note, in fact, that the turbulent kinetic energy production is related to regions of large spanwise shear. This high-vorticity structure is associated with the sinuous mode of the secondary instability. Park & Huerre (1995) studied the secondary instability of Görtler vortices and found that the sinuous mode completely dominates close to the wall, while the varicose mode is strong near the head of the low-speed region. They indicate, in agreement with Liu & Domaradzki (1993), that the sinuous mode is dominant in the transition and that the horseshoe vortices observed can be interpreted as arising from the nonlinear evolution of the varicose mode (also unstable but with lower growth rates). We recall here that the streaks considered in the present study are unstable only to antisymmetric disturbances and therefore a simpler scenario is expected as the disturbance reaches such high levels that it disrupts any type of flow symmetry. It is interesting to note also that Liu & Domaradzki (1993) documented the formation in the turbulent regime of two low-speed streaks located close to the wall in the region of the original low- and high-speed streaks; this is very similar to what

we observed in the present simulation towards the end of the computational box.

4.4. Comparison to streak instabilities in the near-wall region of turbulent flows

Streamwise vortices and streaks are also fundamental structures in the near-wall region of turbulent boundary layers and the vortices seem to be related to streak instabilities. In fact, the structures we identified show a close resemblance to the ones detected in turbulent wall flows (see Schoppa & Hussain 1997; Jiménez & Simens 2001). Kim, Kline & Reynolds (1971) were the first to show the importance of local intermittent inflectional instability in the bursting events, which are associated with periods of strong turbulent production. They observed three oscillatory types of motion of the streaks: a growing streamwise vortex, a transverse vortex and a wavy motion in the spanwise and wall-normal direction. Later, Swearingen & Blackwelder (1987) compared and related the latter two modes observed in Kim *et al.* (1971) to the secondary varicose and sinuous instability of streamwise vortices measured during transition on a concave wall. In the same way as Swearingen & Blackwelder (1987), we can speculate that the first type of oscillatory motion observed by Kim *et al.* (1971), i.e. growth of a streamwise vortex, which is by far the most often observed in their experiments, is related to the growth of either of the two streamwise vortices observed on the flank of the low-speed streak. This is a common feature of sinuous and varicose instability, see the discussion in the previous section, and therefore it is the most likely to be visualized if the hydrogen bubbles are released slightly off-centre of the low-speed streak. Recent studies on the instability of a base flow generated by the superposition of a turbulent mean flow and the streaky structures (Waleffe 1997; Schoppa & Hussain 1997; Kawahara *et al.* 1998) have found that the dominating instability is sinuous. In fact, the evolution of the streamwise vorticity observed in the present simulations of transitional flow is similar to that observed by Schoppa & Hussain (1997) in their analysis of the streak instability in the near wall region of a turbulent flow. Schoppa & Hussain (1997) attribute the formation (collapse) of regions of strong vorticity with compact cross-section, similar to the one observed in figure 20 (*b*) to the local vortex stretching due to positive $\frac{\partial u}{\partial x}$. The strong spanwise shear of the flow is responsible for the generation of $\frac{\partial u}{\partial x}$ as the oscillation of the low-speed region reaches considerable amplitudes. Regions of positive $\frac{\partial u}{\partial x}$ are located downstream of the streak crests, causing direct stretching of the local ω_x . Note also that the behaviour of the region close to the wall from the final stages of the transition is similar to that observed by Jiménez & Pinelli (1999) and Jiménez & Simens (2001) in limiting conditions for the streak cycle to be self-sustained (see as example the structures close to the wall in figure 23).

On the other hand, in the experiments by Acarlar & Smith (1987) a low-speed streak was generated in an otherwise laminar boundary layer by blowing through a slot in the wall. The streak became unstable and horseshoe vortices

were formed. In the simulations by Skote, Haritonidis & Henningson (2002) the Acarlar & Smith (1987) experiment was numerically reproduced and the process of horseshoe vortex generation further investigated. Skote *et al.* (2002) show that the appearance of an unstable wall-normal velocity profile is a precursor to the appearance of horseshoe vortices, and thus associated to varicose instability of the turbulent streaks. We note that both streamwise vortices staggered on the flanks of the low-speed streak and hairpin vortices have been observed in turbulent boundary layers. We, therefore, believe that both types of streak instability are present in turbulent boundary layers and that the mechanisms and scenarios observed in the transition of streaky structure are closely related to the near-wall events in turbulent flows, in spite of the different time and space scales involved.

5. Summary and conclusions

We have performed the first numerical simulation of a by-pass transition scenario initiated by the sinuous instability of a streamwise streak in an incompressible flat-plate boundary layer flow. Andersson *et al.* (1999) and Luchini (2000) showed that the perturbations at the leading edge of a flat plate that show the highest potential for transient energy amplification consist of a pair of streamwise vortices. Due to the lift-up mechanism these optimal disturbances lead to elongated streamwise streaks downstream. If the streak amplitude reaches a threshold value, secondary instability can occur and provoke transition. The most dangerous type of secondary instability has been found by Andersson *et al.* (2001) to be the sinuous one, consisting of spanwise oscillation of the low-speed region. Here, we have studied in detail the late stages of transition originating from this scenario and compared them with other transition scenarios and flows where streak instability is also present. The following points summarize the main findings.

The main structures observed during the transition process consist of elongated quasi-streamwise vortices located on the flanks of the low-speed streak. Vortices of alternating sign are overlapping in the streamwise direction in a staggered pattern, both inclined away from the wall and tilted in the downstream direction towards the middle of the undisturbed low-speed region.

We have followed the evolution of the streamwise vorticity of the perturbation. The streamwise vorticity of the secondary instability mode is symmetric with respect to the streak; structures of the same sign appear above the low- and high-speed streak, connected by legs situated along the flanks of the low-speed region. Positive and negative structures alternate in the streamwise direction. At the late stages of the breakdown only one of the two legs is still present and amplified. This is the leg which is able to induce stronger streaks and in turn to create stronger mean shear. The observed staggered pattern is a result of this process.

At the late stages, we observe an increasing phase difference between the lower and upper parts of the low-speed streak, which are then moving in opposite directions. Thus the streak is disrupted. The periodic motion of the upper part continues far downstream in the outer part of the boundary layer, while closer to the wall streaks of turbulent nature are observed.

In other transition scenarios (see Rist & Fasel 1995; Berlin *et al.* 1999, for numerical studies on the late stages), positive and negative streamwise vortices are also present on the side of the low-speed region but they are not staggered in the streamwise direction. Instead the left and the right streamwise vortices join at the centre of the streak and form the typical Λ -structures seen in K and H-type transition. The difference is found in the symmetry of the streamwise vorticity of the fundamental secondary instability. In the present case the vorticity disturbance is symmetric, while in oblique transition and K- and H-type of transition the streamwise vorticity is antisymmetric. A common feature of the scenarios considered, we note that the vortex which is amplified at the late stages is the one which is inducing a stronger mean shear.

The structures and their evolution observed in the present simulation of a transitional boundary layer show important similarities with the sinuous streak instability observed in the near-wall region of a turbulent boundary layer (see Jeong *et al.* 1997; Schoppa & Hussain 1997; Jiménez & Pinelli 1999).

This research was supported by TFR (Teknikvetenskapliga forskningsrådet). Computer time was provided by the Center for Parallel Computers (PDC) at the Royal Institute of Technology (KTH) and by the National Supercomputer Center in Sweden (NSC).

References

- ACARLAR, M. S. & SMITH, C. R. 1987 A study of hairpin vortices in a laminar boundary layer. Part 2. Hairpin vortices generated by fluid injection. *J. Fluid Mech.* **175**, 43–68.
- ANDERSSON, P., BERGGREN, M. & HENNINGSON, D. S. 1999 Optimal disturbances and bypass transition in boundary layers. *Phys. Fluids* **11** (1), 134–150.
- ANDERSSON, P., BRANDT, L., BOTTARO, A. & HENNINGSON, D. S. 2001 On the breakdown of boundary layers streaks. *J. Fluid Mech.* **428**, 29–60.
- ASAI, M., MINAGAWA, M. & NISHIOKA, M. 1999 Instability and breakdown of three-dimensional high-shear layer associated with a near-wall low-speed streak. In *Proc. IUTAM Symp.* (ed. H. F. Fasel & W. S. Saric), pp. 269–274. Springer.
- ASAI, M., MINAGAWA, M. & NISHIOKA, M. 2002 The instability and breakdown of near-wall low-speed streaks. *J. Fluid Mech.* **455**, 289–314.
- BAKCHINOV, A. A., GREK, G. R., KLINGMANN, B. G. B. & KOZLOV, V. V. 1995 Transition experiments in a boundary layer with embedded streamwise vortices. *Phys. Fluids* **7**, 820–832.

- BAKE, S., FERNHOLZ, H. H. & KACHANOV, Y. S. 2000 Resemblance of K- and N-regimes of boundary-layer transition at late stages. *Eur. J. Mech. B/Fluids* **19**, 1–22.
- BERLIN, S. & HENNINGSON, D. S. 1999 A nonlinear mechanism for receptivity of free-stream disturbances. *Phys. Fluids* **11** (12), 3749–3760.
- BERLIN, S., WIEGEL, M. & HENNINGSON, D. S. 1999 Numerical and experimental investigations of oblique boundary layer transition. *J. Fluid Mech.* **393**, 23–57.
- BERTOLOTTI, F. P., HERBERT, T. & SPALART, P. R. 1992 Linear and nonlinear stability of the Blasius boundary layer. *J. Fluid Mech.* **242**, 441–474.
- BRANDT, L., HENNINGSON, D. S. & PONZIANI, D. 2002 Weakly non-linear analysis of boundary layer receptivity to free-stream disturbances. *Phys. Fluids* **14** (4), 1426–1441.
- BUTLER, K. M. & FARRELL, B. F. 1992 Three-dimensional optimal perturbations in viscous shear flow. *Phys. Fluids A* **4**, 1637–1650.
- ELLINGSEN, T. & PALM, E. 1975 Stability of linear flow. *Phys. Fluids* **18**, 487.
- ELOFSSON, P. A. & ALFREDSSON, P. H. 1998 An experimental study of oblique transition in plane Poiseuille flow. *J. Fluid Mech.* **358**, 177–202.
- ELOFSSON, P. A., KAWAKAMI, M. & ALFREDSSON, P. H. 1999 Experiments on the stability of streamwise streaks in plane Poiseuille flow. *Phys. Fluids* **11**, 915–930.
- HERBERT, T. 1983 Secondary instability of plane channel flow to subharmonic three-dimensional disturbances. *Phys. Fluids* **26**, 871–874.
- HERBERT, T. 1988 Secondary instability of boundary-layers. *Annu. Rev. Fluid Mech.* **20**, 487–526.
- HULTGREN, L. S. & GUSTAVSSON, L. H. 1981 Algebraic growth of disturbances in a laminar boundary layer. *Phys. Fluids* **24** (6), 1000–1004.
- JACOBS, R. J. & DURBIN, P. A. 2001 Simulations of bypass transition. *J. Fluid Mech.* **428**, 185–212.
- JEONG, J., HUSSAIN, F., SCHOPPA, W. & KIM, J. 1997 Coherent structures near the wall in a turbulent channel flow. *J. Fluid Mech.* **332**, 185–214.
- JIMÉNEZ, J. & PINELLI, A. 1999 The autonomous cycle of near wall turbulence. *J. Fluid Mech.* **389**, 335–359.
- JIMÉNEZ, J. & SIMENS, M. P. 2001 Low dimensional dynamics of a turbulent wall flow. *J. Fluid Mech.* **435**, 81–91.
- KACHANOV, Y. S. 1994 Physical mechanism of laminar boundary-layer transition. *Annu. Rev. Fluid Mech.* (26), 411–82.
- KACHANOV, Y. S., KOZLOV, V. V. & LEVCHENKO, V. Y. 1977 Nonlinear development of a wave in a boundary layer. *Izv. Akad. Nauk SSSR Mekh. Zhid. Gaza* **3**, 49–58, in Russian.
- KAWAHARA, G., JIMÉNEZ, J., UHLMANN, M. & PINELLI, A. 1998 The instability of streaks in near-wall turbulence. *Tech. Rep.*. NASA-Stanford University Center for Turbulence Research, Annual Research Briefs, pp. 155–170.
- KENDALL, J. M. 1985 Experimental study of disturbances produced in a pre-transitional laminar boundary layer by weak free-stream turbulence. *AIAA Paper* **85**, 1695.
- KIM, H. T., KLINE, S. J. & REYNOLDS, W. C. 1971 The production of turbulence near a smooth wall in a turbulent boundary layer. *J. Fluid Mech.* **50**, 133–160.

- KIM, J., MOIN, P. & MOSER, R. 1987 Turbulence statistics in fully developed channel flow. *J. Fluid Mech.* **177**, 133–166.
- KLEBANOFF, P. S. 1971 Effect of free-stream turbulence on the laminar boundary layer. *Bull. Am. Phys. Soc.* **10**, 1323.
- KLEBANOFF, P. S., TIDSTROM, K. D. & SARGENT, L. M. 1962 The three-dimensional nature of boundary layer instability. *J. Fluid Mech.* **12**, 1–34.
- LANDAHL, M. T. 1975 Wave breakdown and turbulence. *SIAM J. Appl. Maths* **28**, 735.
- LANDAHL, M. T. 1980 A note on an algebraic instability of inviscid parallel shear flows. *J. Fluid Mech.* **98**, 243–251.
- LAURIEN, E. & KLEISER, L. 1989 Numerical simulation of boundary-layer transition and transition control. *J. Fluid Mech.* **199**, 403–440.
- LECUNFF, C. & BOTTARO, A. 1993 Linear stability of shear profiles and relation to the secondary instability of the Dean flow. *Phys. Fluids A* **5**, 2161–2171.
- LI, F. & MALIK, M. R. 1995 Fundamental and subharmonic secondary instabilities of Görtler vortices. *J. Fluid Mech.* **297**, 77–100.
- LIU, W. & DOMARADZKI, A. J. 1993 Direct numerical simulation of transition to turbulence in Görtler flows. *J. Fluid Mech.* **246**, 267–299.
- LUCHINI, P. 2000 Reynolds-number independent instability of the boundary layer over a flat surface. Part 2: Optimal perturbations. *J. Fluid Mech.* **404**, 289–309.
- LUNDBLADH, A., BERLIN, S., SKOTE, M., HILDINGS, C., CHOI, J., KIM, J. & HENNINGSON, D. S. 1999 An efficient spectral method for simulation of incompressible flow over a flat plate. Technical Report KTH/MEK/TR-99/11-SE. KTH, Department of Mechanics, Stockholm.
- MALIK, M. R., ZANG, T. A. & HUSSAINI, M. Y. 1985 A spectral collocation method for the Navier-Stokes equations. *J. Comp. Phys.* **61**, 64–88.
- MATSUBARA, M. & ALFREDSSON, P. H. 2001 Disturbance growth in boundary layers subjected to free stream turbulence. *J. Fluid. Mech.* **430**, 149–168.
- MEYER, D. G. W., RIST, U., BORODULIN, V. I., GAPONENKO, V. R., KACHANOV, Y. S., LIAN, Q. X. & LEE, C. B. 1999 Late-stage transitional boundary-layer structures. Direct numerical simulation and experiment. In *Proc. IUTAM Symp.* (ed. H. F. Fasel & W. S. Saric), pp. 167–172. Springer.
- MOFFAT, H. K. 1967 In *Proceedings international colloquium on atmospheric turbulence and radio wave propagation* (ed. A. M. Yaglom & V. I. Tatarsky), pp. 166–188. Nauka, Moscow.
- NORDSTRÖM, J., NORDIN, N. & HENNINGSON, D. S. 1999 The fringe region technique and the Fourier method used in the direct numerical simulation of spatially evolving viscous flows. *SIAM J. Sci. Comp.* **20**, 1365–1393.
- ORR, W. M. F. 1907 The stability or instability of the steady motions of a perfect liquid and of a viscous liquid. Part I: A perfect liquid. Part II: A viscous liquid. *Proc. R. Irish Acad. A* **27**, 9–138.
- PARK, D. S. & HUERRE, P. 1995 Primary and secondary instabilities of the asymptotic suction boundary layer on a curved plate. *J. Fluid Mech.* **283**, 249–272.
- PHILLIPS, O. M. 1969 Shear-flow turbulence. *Annu. Rev. Fluid Mech.* **1**, 245–264.
- RAYLEIGH, L. 1880 On the stability of certain fluid motions. *Proc. Math. Soc. Lond.* **11**, 57–70.

- REDDY, S. C. & HENNINGSON, D. S. 1993 Energy growth in viscous channel flows. *J. Fluid Mech.* **252**, 209–238.
- REDDY, S. C., SCHMID, P. J., BAGGETT, J. S. & HENNINGSON, D. S. 1998 On the stability of streamwise streaks and transition thresholds in plane channel flows. *J. Fluid Mech.* **365**, 269–303.
- RIST, U. & FASEL, H. 1995 Direct numerical simulation of controlled transition in a flat-plate boundary layer. *J. Fluid Mech.* **298**, 211–248.
- SANDHAM, N. D. & KLEISER, L. 1992 The late stages of transition to turbulence in channel flow. *J. Fluid Mech.* **245**, 319–348.
- SCHLICHTING, H. 1933 Berechnung der anfängung kleiner störungen bei der plattenströmung. *ZAMM* **13**, 171–174.
- SCHMID, P. & HENNINGSON, D. S. 1992 A new mechanism for rapid transition involving a pair of oblique waves. *Phys. Fluids A* **4**, 1986–1989.
- SCHMID, P. J. & HENNINGSON, D. S. 2001 *Stability and Transition in Shear Flows*. New York: Springer.
- SCHOPPA, W. & HUSSAIN, F. 1997 Genesis and dynamics of coherent structures in near-wall turbulence: a new look. In *Self-Sustaining Mechanisms of Wall Turbulence* (ed. R. L. Panton), chap. 7, pp. 385–422. Computational Mechanics Publications, Southampton.
- SCHUBAUER, G. B. & SKRAMSTAD, H. F. 1947 Laminar boundary layer oscillations and the stability of laminar flow. *J. Aero. Sci.* **14**, 69–78.
- SKOTE, M. 2001 Studies of turbulent boundary layer flow through direct numerical simulation. PhD thesis, Royal Institute of Technology, Stockholm, Sweden.
- SKOTE, M., HARITONIDIS, J. H. & HENNINGSON, D. S. 2001 Varicose instabilities in turbulent boundary layers. *Phys. Fluids* (to appear).
- SOMMERFELD, A. 1908 Ein beitrag zur hydrodynamischen erklärang der turbulenten flüssigkeitbewegungen. In *Atti. del 4. Congr. Internat. dei Mat. III, Roma*, pp. 116–124.
- SPALART, P. R. & YANG, K. 1987 Numerical study of ribbon induced transition in Blasius flow. *J. Fluid Mech.* **178**, 345–365.
- SWEARINGEN, J. D. & BLACKWELDER, R. F. 1987 The growth and breakdown of streamwise vortices in the presence of a wall. *J. Fluid Mech.* **182**, 255–290.
- TOLLMIEEN, W. 1929 Über die entstehung der turbulenz. *Nachr. Ges. Wiss. Göttingen* *21-24*, English translation NACA TM 609, 1931.
- WALEFFE, F. 1995 Hydrodynamic stability and turbulence: Beyond transients to a self-sustaining process. *Stud. Appl. Math.* **95**, 319–343.
- WALEFFE, F. 1997 On a self-sustaining process in shear flows. *Phys. Fluids A*, **9**, 883–900.
- WESTIN, K. J. A., BOIKO, A. V., KLINGMANN, B. G. B., KOZLOV, V. V. & ALFREDSSON, P. H. 1994 Experiments in a boundary layer subject to free-stream turbulence. Part 1: Boundary layer structure and receptivity. *J. Fluid Mech.* **281**, 193–218.
- WILLIAMS, D. R., FASEL, H. & HAMA, F. R. 1984 Experimental determination of the three-dimensional vorticity field in the boundary-layer transition process. *J. Fluid Mech.* **149**, 179–203.
- WU, X., JACOBS, R. G., HUNT, J. C. R. & DURBIN, P. A. 1999 Simulation of

- boundary layer transition induced by periodically passing wakes. *J. Fluid Mech.* **398**, 109–153.
- WUNDROW, D. W. & GOLDSTEIN, M. E. 2001 Effect on a laminar boundary layer of small-amplitude streamwise vorticity in the upstream flow. *J. Fluid Mech.* **426**, 229–262.

Paper 4

4

Stabilization of Tollmien-Schlichting waves by finite amplitude optimal streaks in the Blasius boundary layer

By Carlo Cossu[†] and Luca Brandt^{*}

[†]LadHyX, CNRS-École Polytechnique, F-91128 Palaiseau Cedex, France

^{*}Department of Mechanics, Royal Institute of Technology,
S-10044 Stockholm, Sweden

In this Letter we show by numerical simulation that streamwise streaks of sufficiently large amplitude are able to stabilize Tollmien-Schlichting waves in zero pressure gradient boundary layers at least up to $Re = 1000$. This stabilization is due to the spanwise averaged part of the nonlinear basic flow distortion induced by the streaks and occurs for streak amplitudes lower than the critical threshold beyond which secondary inflectional instability is observed. A new control strategy is implemented using optimal perturbations in order to generate the streaks.

In boundary layer flows with low levels of background disturbances, transition is initiated by the exponential amplification of the unstable Tollmien-Schlichting (TS) waves followed by secondary instabilities and breakdown to turbulence as soon as the u_{rms} amplitude of the primary instability is of the order of 1% of the freestream velocity (Herbert 1988). In the presence of free stream turbulence (FST), narrow elongated regions of alternated low and high streamwise velocity called “streamwise streaks” slowly oscillate in the boundary layer (Klebanoff 1971). For sufficiently large values of FST “bypass transition” is observed. For intermediate levels of FST it was however surprisingly found by Boiko *et al.* (1994) that the spatial amplification rate of small amplitude TS-waves was *lower* than in the quiet case. This effect was mainly attributed (Boiko *et al.* 1994) to the 2D mean distortion of the velocity profile observed in the presence of the FST (Westin *et al.* 1994), which is produced by the nonlinear saturation of the streaks (Andersson *et al.* 2001). In this Letter we investigate by direct numerical simulation whether artificially induced streaks are able to completely stabilize TS-waves. This could be an effective alternative way to control primary instabilities in boundary layers with low levels of ambient noise.

Numerical method

The incompressible 3D Navier-Stokes equations are integrated using a pseudo-spectral code described in Lundbladh *et al.* (1999). The code uses Fourier

expansions in the streamwise and spanwise directions and Chebyshev polynomials in the wall-normal direction. The time stepping scheme is a low storage third-order Runge–Kutta method for the nonlinear terms and a second-order Crank–Nicolson method for the linear terms. Dealiasing is used in the streamwise and spanwise directions. Two types of simulations are performed in the present study: in the case of “spatial simulations”, i.e. simulations of non-parallel basic flows, a fringe region is employed to enforce inflow and outflow boundary conditions in a periodic domain; in the case of “temporal” simulations a volume force is used to keep the basic flow parallel.

Case	Inlet A_s	Maximum A_s	A_s at Re=1047
A	0.0000	0.0000	0.0000
B	0.0618	0.1400	0.1396
C	0.0927	0.2018	0.2017
D	0.1235	0.2558	0.2558
E	0.1695	0.3199	0.3174

TABLE 1. Streak amplitude for the computed basic flows.

Basic flow

The basic flows we consider are zero pressure gradient boundary layers with steady, nonlinearly saturated, spanwise periodic streaks of different amplitudes. We use optimal perturbations (Schmid & Henningson 2001) in order to generate the streaks with minimum input energy. These optimal perturbations consist of vortices aligned in the streamwise direction which, owing to the “lift-up” effect (Landahl 1980), have the highest potentiality for spatial transient growth (Andersson *et al.* 1999; Luchini 2000). As in Andersson *et al.* (2001), the optimal perturbation computed by Andersson *et al.* (1999) is used as inflow condition close to the leading edge and its downstream evolution is followed until nonlinear saturation for different initial amplitudes. For the computation of the basic flows we use a box with inlet at $\text{Re} = 468.5$ and dimensions of $1128 \delta_{*0} \times 20 \delta_{*0} \times 12.83 \delta_{*0}$, in the streamwise, wall-normal and spanwise directions, respectively, where $576 \times 65 \times 32$ collocation points are used. We denote by δ_{*0} the boundary layer thickness at the inlet. The spanwise extension of the domain corresponds to one wavelength of the optimally growing streaks. Denoting by x , y , and z the streamwise, wall-normal, and spanwise coordinates, respectively, we use the following definition of the streak amplitude (see Andersson *et al.* 2001):

$$A_s(x) = \left[\max_{y,z} (U - U_B) - \min_{y,z} (U - U_B) \right] / 2U_\infty,$$

where U_∞ is the free stream velocity, $U_B(x, y)$ is the Blasius solution, and $U(x, y, z)$ is the streamwise velocity of the streak. We list in table 1 the five different cases considered. Case A is nothing but the Blasius boundary layer without streaks. In figure 1 we display the evolution of the amplitude of the streaks B,C,D,E versus the Reynolds number $Re = U_\infty \delta_* / \nu$ based on local boundary layer thickness δ_* . It has recently been shown by Andersson *et al.* (2001) that optimal streaks with amplitude $A_s > 0.26$ are subject to secondary inflectional instabilities. Streak E is therefore secondarily unstable.

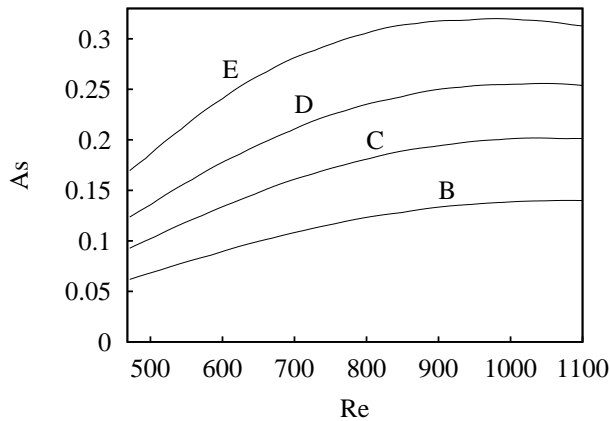


FIGURE 1. Streamwise spatial evolution of the amplitude of streaks B,C,D and E.

Spatial stability

In the same spirit as Boiko *et al.* (1994), we first test the spatial stability of the computed basic flows to two-dimensional harmonic perturbations of dimensionless frequency $F = 2\pi f\nu/U_\infty^2$. The same computational parameters adopted in the evaluation of the basic flows are used in this type of simulation. The perturbation is induced by a two-dimensional time periodic volume force localized at the inlet position, extending up to $Re \sim 480$, of amplitude small enough to ensure a linear evolution of the perturbations. The computations were carried on for sufficiently large times to achieve converged time periodic solutions in all the computational domain. In figure 2 we show the downstream development of the amplitude, based on the norm

$$\left[\int_0^\infty (u'^2 + v'^2 + w'^2) dy \right]^{1/2} / 2U_\infty,$$

of two-dimensional waves at the frequency $F = 1.316 \cdot 10^{-4}$ of the forcing. In the Blasius boundary layer (case A) the perturbations decay until they reach branch I of the linear neutral stability curve situated at $Re = 635$ in the parallel

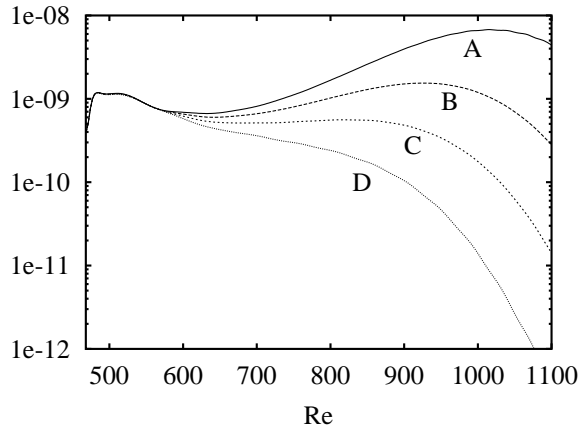


FIGURE 2. Spatial evolution of the amplitude of 2D perturbations in the Blasius boundary layer without streaks (case A) and with streaks of increasing amplitude (cases B to D).

flow approximation. After, they begin to grow until branch II is reached at $Re = 1000$. When the basic flow contains a low amplitude streak (case B) an unstable domain still exists but the growth of the TS waves is attenuated in a way similar to that observed in the presence of free stream turbulence (Boiko *et al.* 1994). Case C presents a region of marginal stability around $Re = 750$, where the streak amplitude is about 0.17. In the case of largest amplitude streaks (case D), the forced TS-waves are stable. Similar results apply to forcing frequencies $F = 1.6 \cdot 10^{-4}$ and $F = 2.0 \cdot 10^{-4}$.

Temporal stability

In the spatial simulations we considered only some frequencies F and we forced only 2D perturbations. To verify the behavior of more general 3D perturbations of any frequency, we decided to investigate the temporal stability of the parallel basic flows $(U(y, z), 0, 0)$ obtained by extracting the streak velocity profiles at the streamwise station corresponding to $Re = 1047$. As shown in figure 1, at that streamwise station the streak amplitude is very slowly varying in the streamwise direction. For this type of simulations, the computational domain measures $1200 \delta_* \times 9 \delta_* \times 5.74 \delta_*$ in the streamwise, wall-normal and spanwise direction, respectively, where $1024 \times 97 \times 32$ collocation points are used. In order to consider all the wavenumbers and frequencies at once, we study the flow response to an impulse-like initial condition. This initial condition, already used in other studies (Breuer & Haritonidis 1990; Henningson *et al.* 1993; Bech *et al.* 1998), is given by

$$(u_0, v_0, w_0) = (U, \partial\psi_0/\partial z, -\partial\psi_0/\partial y)$$

with

$$\psi_0 = P_0 \bar{x} \bar{y}^3 \bar{z} e^{-(\bar{x}^2 + \bar{y}^2 + \bar{z}^2)},$$

where $\bar{x} = (x - x_0)/p_x$, $\bar{y} = y/p_y$ and $\bar{z} = (z - z_0)/p_z$. We use an initial disturbance amplitude P_0 sufficiently small to ensure a linear development of the perturbations and length scales $p_x = 5\delta_*$, $p_y = 2\delta_*$ and $p_z = 1.5\delta_*$ small enough to reproduce a localized impulse within the limits of a good resolution in the truncated spectral space of our numerical simulations. In order to avoid any particular spanwise symmetry of the solution, the initial disturbance is centered off-axis, around $z_0 = -2\delta_*$. The temporal evolution of the *rms* perturbation kinetic energy E , integrated over the whole computational domain, is shown in figure 3. Since all the modes are excited by the initial condition, any unstable mode would emerge after an initial transient. The Blasius boundary layer (case A) is linearly unstable at $\text{Re} = 1047$ and TS-waves emerge clearly at times $t > 600$; the perturbation growth is exponential, with values in agreement with the results of the linear Orr-Sommerfeld analysis. The low amplitude streak (case B) is also unstable but with a lower amplification rate. Streaks with larger amplitude (case C and D) are stable and, after the initial transient, perturbations decay for large times. A too large amplitude of the streaks (case E), however, leads to inflectional instability (cf. Andersson *et al.* 2001).

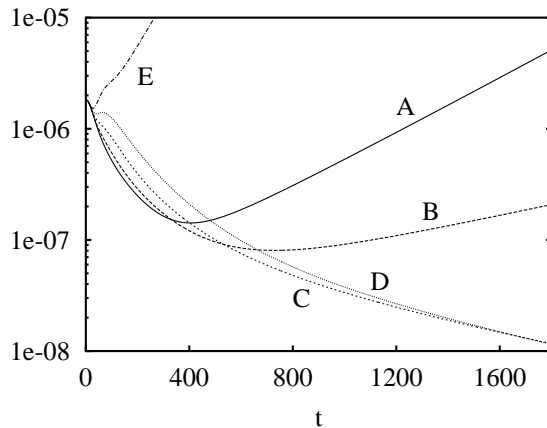


FIGURE 3. Temporal evolution of the *rms* perturbation energy at $\text{Re} = 1047$ for the Blasius boundary layer without streaks (case A), and with streaks of increasing amplitude (cases B,C,D and E).

Interpretation

We now try to isolate the mechanism responsible for the observed stabilization of the Blasius boundary layer. The basic flow distortion $\Delta U(y, z) = U(y, z) - U_B(y)$ can be separated into its spanwise averaged part $\overline{\Delta U}(y)$ and its spanwise varying part $\widehat{\Delta U}(y, z) = \Delta U(y, z) - \overline{\Delta U}(y)$. Note that nonlinear effects are essential to generate $\overline{\Delta U}(y)$. In figure 4a and 4b we reproduce the spanwise averaged velocity $\overline{U}(y) = U_B(y) + \overline{\Delta U}(y)$ of the basic solutions at

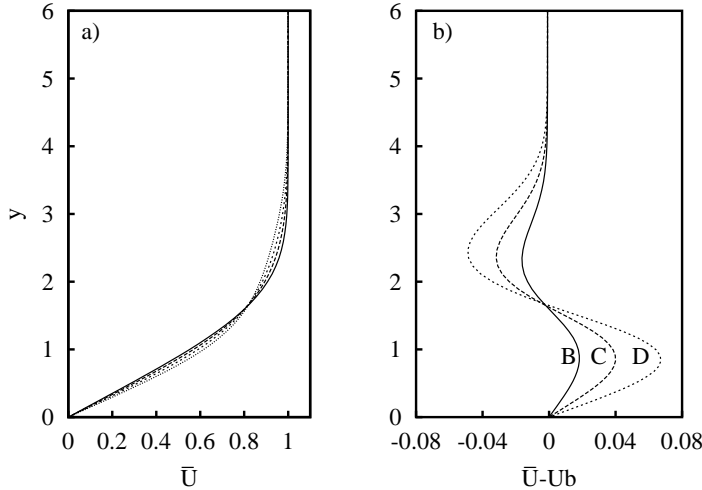


FIGURE 4. (a) Spanwise averaged streamwise velocity profiles $\bar{U}(y)$, at $Re = 1047$, of the Blasius boundary layer (solid line) and of the streaky boundary layers B, C and D. (b) Corresponding spanwise averaged basic flow distortions $\bar{\Delta U}(y) = \bar{U}(y) - U_B(y)$.

$Re = 1047$ and the corresponding $\bar{\Delta U}(y)$. It can be seen how the increase of the streak amplitude leads to fuller \bar{U} -profiles and should thus have a stabilizing effect on the TS-waves (Boiko *et al.* 1994). On the other hand, the term $\bar{\Delta U}(y, z)$, leads to velocity profiles which, based on a 2D local stability analysis (Wundrow & Goldstein 2001), are more unstable, at some spanwise stations z , than the Blasius profile. The results of the complete 3D stability analysis, displayed in figure 3, may interpreted as follows: without streaks (case A), the Blasius profile is unstable to TS waves due to a viscous instability. Low amplitude streaks (case B) are neither able to stabilize the viscous instability with $\bar{\Delta U}(y)$, nor to create, with $\bar{\Delta U}(y, z)$, shears strong enough to support fully 3D inflectional instabilities. For moderate streak amplitudes (cases C and D), $\bar{\Delta U}(y)$ is able to completely stabilize the flow but, for too large amplitudes (case E) the term $\bar{\Delta U}(y, z)$ supports inflectional instabilities and the basic flow becomes unstable again. To confirm this interpretation we performed 3D temporal simulations for the artificial basic flows \bar{D} and \bar{D} obtained by considering only the spanwise varying or the spanwise uniform part of the basic flow distortion, i.e. $U_{\bar{D}} = U_B + \bar{\Delta U}$ and $U_{\bar{D}} = U_B + \bar{\Delta U}$. The temporal evolutions of the *rms* perturbation energies pertaining to these basic flows and to the complete streak D are displayed in figure 5; the figure reveals both the destabilizing role of $\bar{\Delta U}(y, z)$ and, more importantly, the dominating stabilizing action of

$\overline{\Delta U}(y)$, to which the global stabilization of TS-waves can finally be attributed. The same result applies to case C.

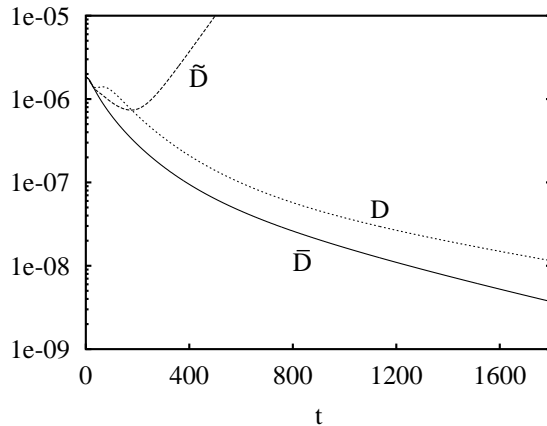


FIGURE 5. Temporal evolution of the *rms* perturbation energy at $Re = 1047$ for the complete streak \bar{D} and for the artificial basic flows \tilde{D} and \bar{D} .

Boundary layer control

We have shown that it is possible to modify an unstable Blasius boundary layer into a stable streaky flow introducing streamwise vortices near the leading edge. The “actuator” input energy is minimized by the choice of an optimal forcing and is of $O(1/Re)$ when compared to the streak energy (see Andersson *et al.* 1999; Luchini 2000). Moreover, it was recently observed by Andersson *et al.* (2001) that the steady saturated streaks induced by the optimal vortices maintain an almost constant amplitude for a large distance downstream. The stabilization is obtained, in open-loop, through a modification of the basic flow induced by actuators situated upstream of the unstable domain. The local skin friction coefficient of the streaky flow is increased, at worst, by less than 20%, compared to the Blasius boundary layer. We tested this control strategy for Reynolds numbers up to 1047 for a fixed spanwise periodicity of the streaks. For larger Reynolds number probably larger streak amplitudes would be necessary to achieve stabilization. The maximum allowed amplitude is however limited by the appearance of secondary instabilities on the streaks. We are therefore currently identifying stabilizing streak amplitude thresholds for a wider range of Reynolds numbers and of spanwise wavelength.

The authors kindly thank P. Huerre for his comments on this Letter. The computational facilities were provided by CNRS/IDRIS. L.B. acknowledges financial support by École Polytechnique (EGIDE) and VR (Vetenskapsrådet) during his stay at LadHyX, where this work was performed.

References

- ANDERSSON, P., BERGGREN, M. & HENNINGSON, D. 1999. Optimal disturbances and bypass transition in boundary layers. *Phys. Fluids*. **11** (1), 134–150.
- ANDERSSON, P., BRANDT, L., BOTTARO, A. & HENNINGSON, D. S. 2001. On the breakdown of boundary layers streaks. *J. Fluid Mech.* **428**, 29–60.
- K. H. Bech, D. S. Henningson, and R. A. W. M. Henkes, 1998. Linear and nonlinear development of localized disturbances in zero and adverse pressure gradient boundary layers. *Phys. Fluids* **10** (6), 1405–1418.
- BOIKO, A. V., WESTIN, K. J. A., KLINGMANN, B. G. B., KOZLOV, V. V. & ALFREDSSON, P. H. 1994. Experiments in a boundary layer subjected to free stream turbulence. Part 2. The role of TS-waves in the transition process. *J. Fluid Mech.* **281**, 219–245.
- BREUER, K. S. and Haritonidis, J. H. 1990. The evolution of a localized disturbance in a laminar boundary layer. Part 1. Weak disturbances. *J. Fluid Mech.*, **220**, 569–594.
- HENNINGSON, D.S., LUNDBLADH, A., JOHANSSON, A.V. 1993. A mechanism for bypass transition from localized disturbances in wall-bounded shear flows *J. Fluid Mech.*, **250**, 169-207 .
- HERBERT, T. 1988 Secondary Instability of boundary layers. *Ann. Rev. Fluid Mech.* **20**, 487–526.
- KLEBANOFF, P. S. 1971. Effect of free-stream turbulence on the laminar boundary layer. *Bull. Am. Phys. Soc.* **10**, 1323.
- LANDAHL, M. T. 1980 A note on an algebraic instability of inviscid parallel shear flows. *J. Fluid Mech.* **98**, 243–251.
- LUCHINI, P. 2000. Reynolds number independent instability of the boundary layer over a flat surface: optimal perturbations. *J. Fluid Mech.*, **404**, 289–309.
- LUNDBLADH, A., BERLIN, S., SKOTE, M., HILDINGS, C., CHOI, J., KIM, J., HENNINGSON, D. S. 1999. An efficient Spectral Method for Simulation of Incompressible Flow over a Flat Plate TRITA-MEK, Technical Report 1999.11, Royal Institute of Technology, Stockholm,1999.
- SCHMID, P. J. & HENNINGSON, D.S. 2001. Stability and Transition in Shear Flows. *Springer*.
- WESTIN, K. J. A., BOIKO, A. V., KLINGMANN, B. G. B., KOZLOV, V. V. & ALFREDSSON, P. H. 1994. Experiments in a boundary layer subject to free-stream turbulence. Part I: Boundary layer structure and receptivity. *J. Fluid Mech.* **281**, 193–218.
- WUNDROW, D. W. & GOLDSTEIN, M. E. 2001. Effect on a laminar boundary layer of small-amplitude streamwise vorticity in the upstream flow. *J. Fluid Mech.* **426**, 229–262.

Paper 5

On the stabilizing role of boundary layer streaks on Tollmien-Schlichting waves

By Carlo Cossu[†] and Luca Brandt^{*}

[†]Laboratoire d'Hydrodynamique (LadHyX), CNRS-École Polytechnique, F-91128 Palaiseau Cedex, France

^{*}Department of Mechanics, Royal Institute of Technology, S-10044 Stockholm, Sweden

The linear stability of the boundary layer developing on a flat plate in the presence of finite amplitude streamwise streaks is investigated. The streaks are assumed steady and spanwise periodic. It is found that the streaks have a stabilizing effect on the viscous instability and that this effect increases with the streak amplitude. Neutral curves are computed for a set of streaky boundary layers. As the amplitude of the streaks is increased, the most unstable viscous waves evolve from the 'classical' two-dimensional Tollmien-Schlichting waves into three-dimensional varicose fundamental modes. For these modes, the viscous instability is fed by the work of the uw -Reynolds stress against the wall normal shear $\partial U/\partial y$, just as in the two-dimensional boundary layer. However, the work of the uw -Reynolds stress against the spanwise shear $\partial U/\partial z$ is stabilizing and, together with the viscous dissipation, is able to quench the viscous instability for sufficiently large streak amplitudes. Varicose subharmonic modes may also be unstable but have growth rates which typically are an order of magnitude lower than those of fundamental modes and become unstable for larger Reynolds numbers. Sinuous modes appear to be always stable to viscous instabilities but, as already known, a limit amplitude exists above which they are destabilized by an inviscid instability of inflectional nature; therefore, only streaks of intermediate amplitude, stable to inflectional instabilities, are considered in the present article. The possible relevance of the streak stabilizing role for applications in boundary layer transition delay is discussed. The efficiency of the streak generation, which exploits the 'lift-up' mechanism, the fact that the actuators do not need to cover all the unstable domain, and the large reductions in the induced temporal growth rates are seen as very promising factors.

1. Introduction

1.1. *Streaky boundary layers*

In the absence of external perturbations or wall imperfections, the boundary layer developing on a flat plate is spanwise uniform (2D) and is well described

by the Blasius similarity solution (see e.g. Schlichting 1979). In the 2D boundary layer, however, small amounts of streamwise vorticity are very effective in pushing low momentum fluid away from the wall and high momentum fluid towards the wall eventually leading to large elongated spanwise modulations of the streamwise velocity called streamwise streaks. This phenomenon, known as the ‘lift-up effect’ (Landahl 1980), is based on an inviscid mechanism and applies to shear flows in general (Ellingsen & Palm 1975). The effect of viscosity eventually dominates rendering the growth of the streaks only transient. However, the growth of the streaks may attain values of the order of the Reynolds number (Gustavsson 1991) before their final viscous decay. The potential of shear flows to exhibit such large transient growths is related to the non-normal nature of the linearized stability operator (for a review the reader may refer to the book by Schmid & Henningson 2001). The most dangerous perturbations, leading to the ‘optimal transient growths’, have been found to consist of streamwise vortices and have been computed for a number of shear flows. In flat plate boundary layers, the most amplified perturbations have spanwise scales of the order of the boundary layer thickness (Andersson, Berggren & Henningson 1999; Luchini 2000). Streamwise streaks are therefore expected to appear whenever a boundary layer is exposed to perturbations with streamwise vorticity.

An extensively studied case in which streamwise streaks appear is the boundary layer developing in the presence of free stream turbulence. In early observations, Dryden (1937) and Taylor (1939) reported that spanwise modulation of the boundary layer thickness are generated in the presence of free stream turbulence. These observations were confirmed and further detailed by, among others, Arnal & Juillen (1978) and Kendall (1985) who coined for the observed streaks the term of ‘Klebanoff mode’ referring to early observations by Klebanoff (1971). The streaks forced by free stream turbulence typically slowly oscillate in the boundary layer in a random way. Streamwise streaks may also be forced by streamwise vortices artificially generated in the free stream (e.g. Tani & Komoda 1962), by blowing and suction at the wall (e.g. Kachanov & Tararykin 1987) or by roughness elements placed on the wall (e.g. Bakchinov *et al.* 1995; White 2002).

1.2. *Stability of streaky boundary layers*

In the absence of streaks the (2D) Blasius boundary layer is linearly stable to inviscid perturbations. Prandtl (1921) suggested that viscosity may, contrary to intuition, lead to instability if the work of the Reynolds stress, generated by viscous modes, against the wall-normal shear is positive and exceeds the viscous dissipation. Based on approximate solutions of the Orr-Sommerfeld equation, Tollmien (1929) was then able to predict linear (viscous) instability of the Blasius boundary layer when the Reynolds number exceeds a critical value later refined by Schlichting (1933). These linear stability predictions were later confirmed by the celebrated experiments of Schubauer & Skramstad

(1947) who, by periodically vibrating a ribbon in the boundary layer, were able to observe unstable Tollmien-Schlichting (TS) waves. As TS waves grow to amplitudes of the order of 1% of the free-stream velocity, secondary instability sets in (for a review see Herbert 1988), eventually leading to breakdown and transition to turbulence. This scenario is today well understood and often referred to as the ‘classical’ transition scenario of boundary layers in a low noise environment.

In the case of streaky boundary layers, the streamwise velocity profiles develop inflection points which may support inviscid instabilities for sufficiently large streak amplitudes, thereby leading to breakdown and transition to turbulence (Brandt & Henningson 2002). It has been found (Andersson *et al.* 2001) that the critical streak amplitude for the onset of inflectional instabilities is 26% of the free-stream velocity U_∞ . In the quest for other possible transition mechanisms in streaky boundary layers, the development of the TS waves in the presence of streaks and their interaction have been studied in the past (for a review see Reed & Saric 1989). Most of the attention has been focused on possible destabilizing resonances between TS waves and streaks of the same order. In particular, the nonlinear interaction of finite amplitude TS waves with streaks received most of the attention (starting with Tani & Komoda, 1962 and Komoda, 1967 and many others thereafter). Streaks may, however, reach finite amplitude before the TS waves and therefore a preliminary step should be to consider the streaky boundary layer as a 3D basic flow in which linear 3D waves develop. Only a few investigations, essentially experimental, concerning this linear growth phase are currently available, as summarized below.

Tani & Komoda (1962) considered the development of viscous waves in a streaky boundary layer. Small wings located outside the boundary layer were used to generate steady streamwise vortices which, upon entering the boundary layer, led to the development of steady spanwise periodic modulations of its thickness, i.e. to steady streamwise streaks. A ribbon was then vibrated in the boundary layer at the frequency and Reynolds number where unstable TS waves exist in the 2D Blasius boundary layer (to which we refer from here on, as Blasius-TS waves). For small ribbon vibration amplitudes, three-dimensional waves were detected with mode shapes similar to the Blasius-TS waves but with a distinct two-peak (or M-shaped) structure in the *rms* streamwise perturbation velocity near the wall in the low speed region. Unfortunately, no explicit measure of the growth rates of such waves was provided.

Kachanov & Tararykin (1987) generated streamwise steady streaks by blowing and suction at the wall and used a vibrating ribbon to generate TS-type waves. They found 3D waves having essentially the same phase speed as the Blasius-TS waves and with essentially the same M-shaped structure observed by Tani & Komoda (1962). Surprisingly, however, these streaky-TS-waves did not amplify as they would have done in the absence of the streaks in the same parameter range.

Arnal & Juillen (1978) detected ‘natural’ (unforced) TS-type waves riding on the unsteady streaks induced by free stream turbulence. Grek *et al.* (1989) and Boiko *et al.* (1994) forced TS waves with a vibrating ribbon in a boundary layer exposed to free stream turbulence. Using refined wave detection techniques they found unstable streaky-TS-waves, which were, however, less amplified than Blasius-TS-waves. These streaky-TS-waves had a phase speed and shapes very similar to Blasius-TS waves. Boiko *et al.* (1994) attributed the growth rate defect to the stabilizing role of the 2D averaged basic flow distortion induced by the streaks; however, they also found that a mere 2D stability analysis of the average velocity profile was unable to predict a correct growth rate.

Using temporal and spatial numerical simulations, the present authors (Cossu & Brandt 2002, from now on referred as CB), found that steady streaks of sufficiently large amplitude are able to reduce the growth of TS waves up to their complete stabilization and suggested the optimal forcing of steady streaks as a possible appealing method to delay transition in boundary layers within a low noise environment. The temporal stability results in CB were however limited to fundamental modes, to a single streamwise station along the streak and a single Reynolds number.

1.3. Scope of the present study

The scope of the present investigation is to extend the results of CB to a wider range of streamwise stations and Reynolds numbers, thus providing a complete picture of the stability of the whole streaky boundary layer, and to gain insight into the physical mechanism leading to viscous stability or instability of the streaky-TS-waves, by computing the associated Reynolds stresses and induced production and dissipation terms.

The direct temporal numerical simulations used by CB are ill-suited for the computation of neutral curves because large computation times are required when the perturbation growth rate is very small. We therefore apply to the same 3D basic flows considered in CB, a linear temporal viscous stability analysis based on the extension of the classical Orr-Sommerfeld and Squire equations to basic flows which are non-uniform in the spanwise direction. The same kind of 3D stability analysis, summarized by Schmid & Henningson (2001), has already been applied to analyse the secondary, inflectional type, instability of streaks induced by Görtler vortices (Yu & Liu 1991, 1994), and of finite amplitude streaks developing in Couette (Waleffe 1995) and Poiseuille (Reddy *et al.* 1998) flows. We consider both sinuous and varicose symmetries of the perturbations for low and large amplitude streaks. Sinuous modes, however, have been found unstable only to inflectional type instabilities for large amplitude streaks with eigenfunctions and growth rates closely matching those computed in the inviscid approximation by Andersson *et al.* (2001). We therefore present

only the results concerning streaks of intermediate amplitude, stable to inflectional instabilities, and discuss only the varicose modes, the sinuous modes being stable for the streaks under consideration.

The article is organized as follows. In section 2 we describe the streaky basic flows. In section 3 we introduce the equations and the parameters governing the temporal stability of the 3D basic flows to viscous perturbations and briefly recall the definition of the perturbation kinetic energy production and dissipation. The numerical results are presented in section 4. In particular, the effect of the streak amplitude and of the Reynolds number on the stability and energy production and dissipation are described. In the same section we then discuss the stability of the whole streaky boundary layers and the implications for transition delay. We finally summarize the results in section 5.

2. Basic flows

Following the standard boundary layer approach, we define the reference length \bar{L} and the corresponding Reynolds number $Re_L = \bar{L}\bar{U}_\infty/\bar{\nu}$, where $\bar{\nu}$ is the fluid kinematic viscosity, \bar{U}_∞ is the freestream velocity and dimensional quantities are denoted by $\bar{\cdot}$. The boundary layer reference scale is defined as $\bar{\delta}_L = (\bar{L}\bar{\nu}/\bar{U}_\infty)^{1/2}$. At the streamwise station \bar{X} , a local Reynolds number $Re_X = \bar{X}\bar{U}_\infty/\bar{\nu}$ and characteristic boundary layer reference scale $\bar{\delta}_X = (\bar{X}\bar{\nu}/\bar{U}_\infty)^{1/2}$ are also defined. The streamwise, wall-normal and spanwise variables are denoted $(\bar{X}, \bar{y}, \bar{z})$, with corresponding velocities $(\bar{U}, \bar{V}, \bar{W})$. The streamwise coordinate and velocity component are respectively made dimensionless with \bar{L} and \bar{U}_∞ , while (\bar{y}, \bar{z}) and (\bar{V}, \bar{W}) are respectively made dimensionless with $\bar{\delta}_X$ and $\bar{U}_\infty Re_X^{-1/2}$.

In the framework of the linearized boundary layer equations Andersson *et al.* (1999) and Luchini (2000) computed the optimal perturbations that, applied at the flat plate leading edge, lead to the maximum perturbation energy at the reference downstream distance \bar{L} . The task was not straightforward due to the nonparallel nature of the boundary layer equations and to their singularity at the leading edge. In the large Re_L limit, the optimal perturbations consisted in streamwise vortices and the most amplified disturbances in streamwise streaks. In both studies steadiness and spanwise periodicity were assumed; the optimal spanwise wavenumber, scaled on $\bar{\delta}_L$, was found to be $\beta_{opt} = 0.45$. Due to the large growth of the streaks, however, nonlinear terms soon come into play even for very small amplitudes of the streamwise optimal vortices. The effect of nonlinear terms is essentially to saturate the streamwise energy growth and to move slightly upstream the location of maximum streak amplitude.

Closely following Andersson *et al.* (2001) and CB, we consider as basic flows zero pressure gradient boundary layers on a flat plate with steady, nonlinear, spanwise periodic streaks generated by forcing ‘linearly-optimal’ perturbations of different amplitudes at the leading edge. The assumed spanwise wavenumber is the optimal one $\beta_{opt} = 0.45$. A set of nonlinear streaks is computed

following the procedure of Andersson *et al.* (2001) in which the linear optimal velocity field, obtained in Andersson *et al.* (1999), is given as inflow at $X = 0.4$ and its nonlinear development is computed up to $X = 6$ by integrating the Navier-Stokes equations with the pseudospectral code described in Lundbladh *et al.* (1999). The code uses Fourier expansions in the streamwise and spanwise directions and Chebyshev polynomials in the wall-normal direction. The time stepping scheme is a low storage third-order Runge-Kutta method for the nonlinear terms and a second-order Crank-Nicolson method for the linear terms. Dealiasing is performed in the streamwise and spanwise directions. For the computation of the basic flows we set $Re_L = 185185$ and used two computational boxes. The first box has an inlet at $X = 0.4$, corresponding to $Re_X = 74193$, and dimensions of $1228 \delta_L \times 21.77 \delta_L \times 13.97 \delta_L$, in the streamwise, wall-normal and spanwise directions respectively where $576 \times 65 \times 32$ collocation points are respectively used. The spanwise extension of the domain corresponds to one wavelength of the optimally growing streaks. This first domain allows us to follow the perturbation up to $X = 3$. To further extend the computations and follow the streak viscous decay, a second computational box is used. Its inflow is at $X = 2.63$, corresponding to $Re_X = 486750$ and it uses as inflow condition the nonlinear saturated field from the first box simulations. The dimensions of this second domain are $2509 \delta_L \times 42.38 \delta_L \times 13.97 \delta_L$ and $576 \times 97 \times 32$ collocation points are used.

Different indicators may be introduced to measure the streak amplitude. Tani & Komoda (1962) defined the relative spanwise variation of the local displacement thickness

$$T(X) = \frac{\max_z \delta^*(X, z) - \min_z \delta^*(X, z)}{\min_z \delta^*(X, z)}, \quad (1)$$

with

$$\delta^*(X, z) = \int_0^\infty [1 - U(X, y, z)] dy. \quad (2)$$

Andersson *et al.* (2001) used an indicator based on a local maximum of the streamwise velocity deviation $\Delta U(X, y, z) = U(X, y, z) - U_B(X, y)$ from the Blasius profile $U_B(X, y)$:

$$A_s(X) = \frac{1}{2} \left[\max_{y,z} \Delta U(X, y, z) - \min_{y,z} \Delta U(X, y, z) \right], \quad (3)$$

to which they correlated the appearance of inflectional instabilities. The threshold amplitude was found to be $A_s = 0.26$. We therefore only consider streaks with $A_s < 0.26$ in all the domain. Another indicator of the intensity of the streaks, used to optimize their linear growth in the large Reynolds number limit (Luchini 2000), is given by the local integral of the streamwise velocity deviation:

$$E_U(X) = \left[\frac{1}{\lambda_z} \int_0^{\lambda_z} \int_0^\infty (\Delta U(X, y, z))^2 dy dz \right]^{1/2}. \quad (4)$$

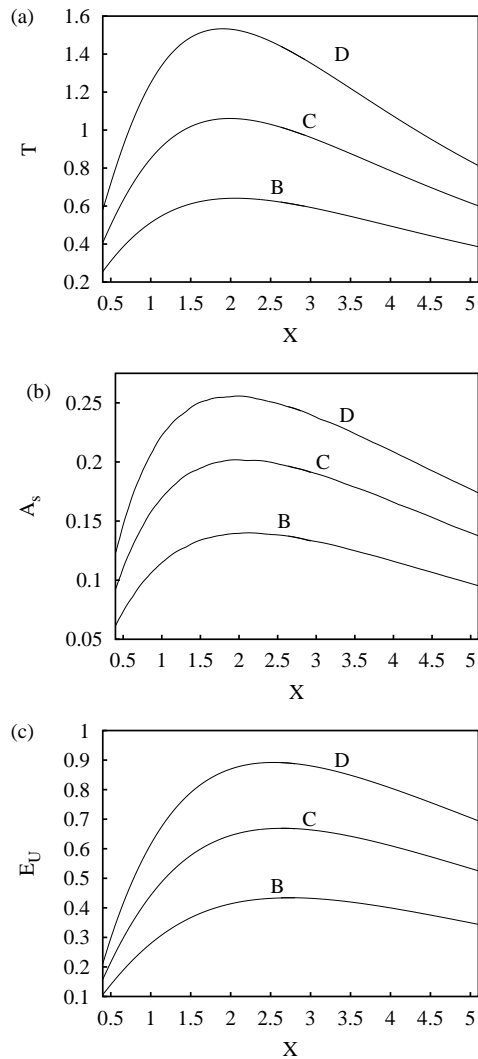


FIGURE 1. Streamwise evolution of the different indicators used to define the amplitude of streaks in the computed basic flows: (a) $T(X)$, (b) $A_s(X)$ and (c) $E_U(X)$.

We computed four basic flows, listed in table 1, denoted by A, B, C and D, corresponding to four increasing amplitudes of the upstream forcing. Case A is nothing but the Blasius boundary layer without streaks, while case D roughly represent the limit case before secondary inflectional instability. The streamwise evolution of streak amplitudes $T(X)$, $A_s(X)$ and $E_U(X)$ of the computed streaks is displayed in figure 1. The $T(X)$ and $A_s(X)$ measures are

Case	Inlet A_s	Maximum A_s	A_s at $X=2$
A	0.0000	0.0000	0.0000
B	0.0618	0.1400	0.1396
C	0.0927	0.2018	0.2017
D	0.1235	0.2558	0.2558

TABLE 1. Streak amplitude A_s for the computed basic flows. Case A corresponds to the Blasius boundary layer. Cases B, C and D are obtained increasing the amplitude of the upstream forcing.

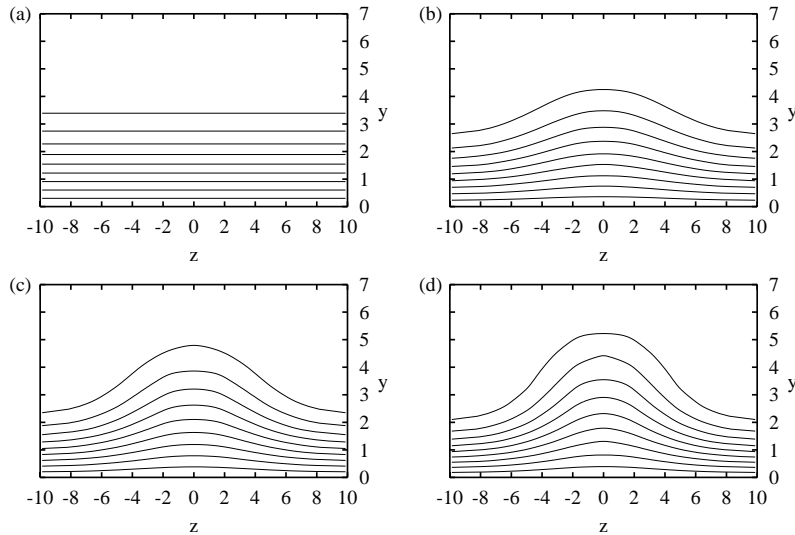


FIGURE 2. Contour plot of the streamwise velocity profile $U(y, z)$ at $X = 2$ for (a) the Blasius boundary layer (case A), and for the streaky flows of increasing amplitude B, C, and D (respectively b,c,d). The contours levels 0.1, 0.2, ..., 0.9 are the same in all the plots. The y - and z - coordinates are expressed in $\bar{\delta}_X$ units.

very similar and give essentially the same information. The maximum of the streak amplitude, for both indicators $T(X)$ and $A_s(X)$ is reached at roughly $X = 2$. The $E_U(X)$ measure is more sensitive to the boundary layer growth and gives a maximum of the streak amplitude around $X = 2.7$, which is the station where the maximum energy of the linear optimal streaks is attained (Andersson *et al.* 1999). In figure 2 we represent the $U(y, z)$ streamwise velocity isolines corresponding to the Blasius boundary layer (case A) and to the increasing amplitude streaks B, C and D prevailing at $X = 2$. The streaks are symmetric about the $z = 0$ axis, which is situated in the low speed region. One clearly

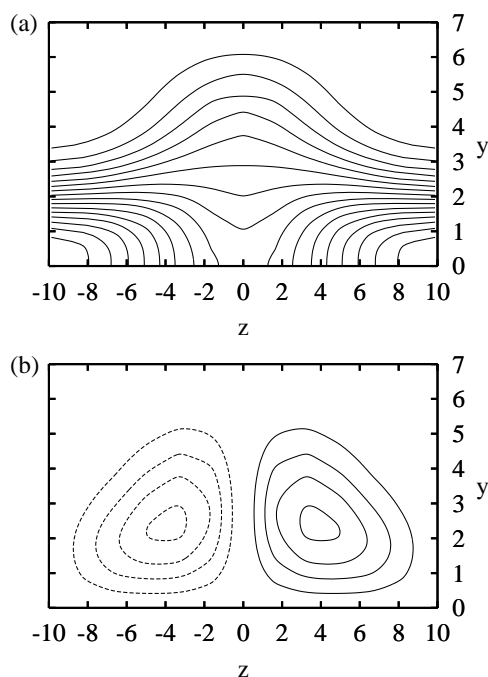


FIGURE 3. Contour plot of (a) the wall-normal shear $\partial U/\partial y$ and (b) the spanwise shear $\partial U/\partial z$ at $X = 2$ for the streaky flow C. The contour spacing is 0.05 in both plots. The y - and z -coordinates are expressed in $\bar{\delta}_X$ units.

observes how the increase of the streak amplitude expands the low velocity and compresses the high velocity regions. In figure 3 the cross-plane profiles of the wall-normal $\partial U/\partial y$ and spanwise $\partial U/\partial z$ streamwise velocity gradients are reported for streak C at $X = 2$ (cf. figure 2c). The maximum of the wall-normal shear is found in the near-wall high speed region of the streak, while the maximum spanwise velocity gradient is located in the middle of the boundary layer, in the flanks of the low-speed region.

Andersson *et al.* (2001) verified that the computed basic flows are effectively boundary layer solutions, i.e. that the basic velocity field is independent of Re_L , when expressed in boundary layer variables. However, even if the streaky basic flows are boundary layer solutions, they are not self-similar in the streamwise direction, i.e. it is not possible to rescale them into a single profile $U(y, z)$ as for the Blasius profile $U_B(y)$ and it will therefore be necessary to analyse the stability of the profiles at each X .

3. Formulation of the stability analysis

3.1. Governing equations

The stability analysis of the streaky basic flows is performed under a set of standard simplifying assumptions. The streaky flows satisfy the boundary layer approximation according to which variations of the streamwise velocity \bar{U} with \bar{X} are very slow, and the (dimensional) wall-normal and spanwise velocity components \bar{V} and \bar{W} are very small (of order $Re_X^{-1/2}$), compared to \bar{U} . It is therefore justified to analyse the local stability of the streaks by considering, at each streamwise station \bar{X} , the parallel flow obtained by ‘freezing’ the local streamwise velocity profile $\bar{U}(\bar{X}, \bar{y}, \bar{z})$ and neglecting the \bar{V} and \bar{W} velocity components. Exactly the same assumptions are made to analyse the viscous instability of the 2D Blasius flow in the so called ‘parallel flow approximation’ (see e.g. Drazin & Reid 1981), the inviscid instability of streaky basic flows (Andersson *et al.* 2001) and the viscous instability of Görtler vortices (Yu & Liu 1991, 1994). We therefore proceed to linearize the Navier-Stokes equations about the parallel basic flow $(U(X; y, z), 0, 0)$. In this context, X must be considered as a parameter and not as the current streamwise coordinate, which we call instead x . The linearized equations for the perturbation velocity components u', v', w' and pressure p' read:

$$\begin{aligned} u'_x + v'_y + w'_z &= 0, \\ u'_t + Uu'_x + U_y v' + U_z w' &= -p'_x + (1/R) \nabla^2 u', \\ v'_t + Uv'_x &= -p'_y + (1/R) \nabla^2 v', \\ w'_t + Uw'_x &= -p'_z + (1/R) \nabla^2 w', \end{aligned} \tag{5}$$

where all the velocities have been rescaled with \bar{U}_∞ and all the lengths with the local boundary layer thickness $\bar{\delta}_X$. The local Reynolds number based on $\bar{\delta}_X$ is defined by $R = \bar{U}_\infty \bar{\delta}_X / \bar{\nu} = Re_X^{1/2}$. To allow easy comparisons of the results, we also introduce the Reynolds number based on the local displacement thickness of the Blasius boundary layer in the absence of streaks $R_{\delta^*} = 1.72 R$. Homogeneous Dirichlet boundary conditions on u', v' and w' are enforced at the wall and in the freestream. The linearized Navier-Stokes equations (5) may be reduced in a straightforward way (Waleffe 1995; Schmid & Henningson 2001) to a system for the wall-normal perturbation velocity v' and the wall-normal perturbation vorticity $\eta' = u'_z - w'_x$:

$$\begin{aligned} \nabla^2 v'_t + (U\nabla^2 + U_{zz} - U_{yy}) v'_x + 2U_z v'_{xz} - (1/R) \nabla^4 v' + \\ -2U_z w'_{xy} - 2U_{yz} w'_x &= 0, \\ \eta'_t + U\eta'_x - (1/R) \nabla^2 \eta' - U_z v'_y + U_{yz} v' + U_y v'_z + U_{zz} w' &= 0, \end{aligned} \tag{6}$$

where w' may be eliminated by using the equation

$$w'_{xx} + w'_{zz} = -\eta'_x - v'_{yz}. \tag{7}$$

Homogeneous boundary conditions hold at the wall and in the freestream for v', v'_x, η' and w' . Solutions to the system (6) are sought in the form of normal modes

$$[v', \eta', w'] = [\widehat{v}(y, z), \widehat{\eta}(y, z), \widehat{w}(y, z)] e^{i(\alpha x - \omega t)} + c.c. \quad (8)$$

where α is the streamwise wavenumber, ω the circular frequency, $i = \sqrt{-1}$ and *c.c.* stands for 'complex conjugate'. The complex phase speed is defined by $c = \omega/\alpha$; the wave phase speed is given by the real part of c . The following system, which extends the usual Orr-Sommerfeld-Squire formulation to parallel spanwise non-uniform basic flows, is thus obtained:

$$\begin{aligned} & \left[-i\omega \widehat{\nabla}^2 + i\alpha (U \widehat{\nabla}^2 + U_{zz} - U_{yy}) + 2i\alpha U_z D_z - (1/R) \widehat{\nabla}^4 \right] \widehat{v} + \\ & -2i\alpha (U_z D_y + U_{yz}) \widehat{w} = 0, \\ & \left[-i\omega + i\alpha U - (1/R) \widehat{\nabla}^2 \right] \widehat{\eta} + (U_{yz} - U_z D_y) \widehat{v} + (U_y D_z + U_{zz}) \widehat{w} = 0, \end{aligned} \quad (9)$$

with the additional identity

$$(D_{zz} - \alpha^2) \widehat{w} = -i\alpha \widehat{\eta} - D_y D_z \widehat{v}, \quad (10)$$

where $D_y = \partial/\partial y$, $D_z = \partial/\partial z$ and $\widehat{\nabla}^2 = D_{yy} + D_{zz} - \alpha^2$. Homogeneous boundary conditions hold at the wall and in the freestream for \widehat{v} , \widehat{v}_x , $\widehat{\eta}$ and \widehat{w} . Equation (10) can be used to eliminate \widehat{w} from the system (9) which can then be recast in a standard generalized eigenvalue problem.

Due to the spanwise periodicity of the basic flow, the following Floquet expansion may be applied to the normal modes (see e.g. Schmid & Henningson 2001):

$$\widehat{v}(y, z) = e^{i\gamma\beta_0 z} \sum_{k=-\infty}^{\infty} \tilde{v}_k(y) e^{ik\beta_0 z}; \quad \widehat{\eta}(y, z) = e^{i\gamma\beta_0 z} \sum_{k=-\infty}^{\infty} \tilde{\eta}_k(y) e^{ik\beta_0 z}, \quad (11)$$

where β_0 is the spanwise wavenumber corresponding to the basic flow periodicity and γ is the detuning parameter, assumed real, which ranges from 0 to 1/2. The modes corresponding to the special values $\gamma = 0$ and $\gamma = 1/2$ are respectively called fundamental and subharmonic. As the basic flow is symmetric about $z = 0$, the modes can be further divided into separate classes according to their odd or even symmetry with respect to the basic flow. In particular, the fundamental modes with an odd symmetry, usually called varicose with reference to their streamline patterns in the (x, z) plane, admit the following expansion:

$$\widehat{v}(y, z) = \sum_{k=0}^{\infty} \tilde{v}_k(y) \cos k\beta_0 z; \quad \widehat{\eta}(y, z) = \sum_{k=1}^{\infty} \tilde{\eta}_k(y) \sin k\beta_0 z \quad (12)$$

The fundamental modes with an even symmetry, usually called sinuous, are of the form

$$\widehat{v}(y, z) = \sum_{k=1}^{\infty} \tilde{v}_k(y) \sin k\beta_0 z; \quad \widehat{\eta}(y, z) = \sum_{k=0}^{\infty} \tilde{\eta}_k(y) \cos k\beta_0 z. \quad (13)$$

For subharmonic modes, the same considerations hold, except that the spanwise periodicity of the disturbances is twice that of the basic flow. In this case the odd modes that, by extension, we still call varicose, admit the expansion

$$\widehat{v}(y, z) = \sum_{k=0}^{\infty} \tilde{v}_k(y) \cos\left(\frac{k+1}{2}\right) \beta_0 z ; \quad \widehat{\eta}(y, z) = \sum_{k=1}^{\infty} \tilde{\eta}_k(y) \sin\left(\frac{k+1}{2}\right) \beta_0 z \quad (14)$$

while the even modes, called sinuous, are expanded according to

$$\widehat{v}(y, z) = \sum_{k=1}^{\infty} \tilde{v}_k(y) \sin\left(\frac{k+1}{2}\right) \beta_0 z ; \quad \widehat{\eta}(y, z) = \sum_{k=0}^{\infty} \tilde{\eta}_k(y) \cos\left(\frac{k+1}{2}\right) \beta_0 z. \quad (15)$$

Note that spanwise uniform perturbations are considered to be ‘fundamental’ and are therefore not considered among subharmonic modes. Note also that the ‘varicose’ (‘sinuous’) label attributed to the subharmonic odd (even) mode is somehow arbitrary because this mode is varicose (sinuous) with respect to the $z = 0$ axis which we arbitrarily choose in the low speed region of the streak; it would be sinuous (varicose) with respect to the high speed region of the streak.

3.2. Numerical procedure

In order to solve the temporal eigenvalue problem, system (9) and the auxiliary equation (10), are discretized according to the expansions (12)-(13) or (14)-(15) truncated to N_z terms and Chebyshev expansions truncated to N_y terms are assumed for $\tilde{v}_k(y)$, $\tilde{\eta}_k(y)$ and $\tilde{w}_k(y)$. The semi-infinite y domain is mapped to $(0, L_y)$ through an algebraic transform and the velocity and vorticity fields are evaluated at the Gauss-Lobatto collocation points (see e.g. Canuto *et al.* 1988). The results presented in the following have been obtained with $N_y + 1 = 65$ collocation points in the wall normal direction and $N_z = 32$ points in the spanwise direction. Convergence tests were performed on a few selected cases using 97 points in y and 48 in z . For a set of real streamwise wavenumbers α at a given Reynolds number R , the complex eigenvalue ω with the largest imaginary part was sought using an implicitly restarted Arnoldi method (Lehoucq *et al.* 1998). The results are considered converged when a relative error below 10^{-9} is attained on the eigenvalues. The used numerical technique is similar to that implemented by Reddy *et al.* (1998), except that the products on the right-hand-side of equations (9a, b) are evaluated in physical space and not by convolution in the spanwise spectral space and a different technique is used to sort the leading eigenvalue. The numerical code has been carefully validated in the case of sinuous modes by comparing the results obtained for large amplitude streaks (not discussed in this article) with the inviscid results of Andersson *et al.* (2001) and with those obtained by Reddy *et al.* (1998) for the same basic flow. In the case of varicose modes, the validation was obtained by recovering standard results for the 2D Blasius profile. We also checked that we obtained the same growth rates as in the direct numerical simulations of the impulse response of the same streaky basic flows performed in CB.

3.3. Production and dissipation of the perturbation kinetic energy

Prandtl (1921) used the perturbation kinetic energy equation to gain a physical understanding of the viscous instability mechanism responsible for the destabilization of TS waves in Blasius profile $U_B(y)$. His rationale was later extended to $U(y, z)$ profiles in the context of the inflectional secondary instability of Görtler vortices (see e.g. Yu & Liu 1994; Park & Huerre 1995). The basic idea is to derive in the usual way the evolution equation for the perturbation kinetic energy density $e' = (u'^2 + v'^2 + w'^2)/2$ from the linearized Navier-Stokes equations (5). Upon integration over a wavelength in the streamwise and spanwise directions and from the wall to infinity in the wall-normal direction, the divergence terms in the evolution equation give a zero global contribution to the energy balance and one is left with

$$\frac{\partial E}{\partial t} = T_y + T_z - D \quad (16)$$

where the following definitions hold:

$$E = \frac{1}{\lambda_x \lambda_z} \int_0^{\lambda_z} \int_0^{\infty} \int_0^{\lambda_x} e' dx dy dz, \quad (17)$$

$$D = \frac{1}{\lambda_x \lambda_z} \frac{1}{R} \int_0^{\lambda_z} \int_0^{\infty} \int_0^{\lambda_x} (\xi'^2 + \eta'^2 + \zeta'^2) dx dy dz, \quad (18)$$

$$T_y = \frac{1}{\lambda_x \lambda_z} \int_0^{\lambda_z} \int_0^{\infty} \int_0^{\lambda_x} (-u'v') \frac{\partial U}{\partial y} dx dy dz, \quad (19)$$

$$T_z = \frac{1}{\lambda_x \lambda_z} \int_0^{\lambda_z} \int_0^{\infty} \int_0^{\lambda_x} (-u'w') \frac{\partial U}{\partial z} dx dy dz. \quad (20)$$

The quantity E is the total perturbation kinetic energy, D is the viscous dissipation term given by the square of the norm of the perturbation vorticity vector (ξ', η', ζ') . T_y and T_z are the perturbation kinetic energy production terms associated with the work of the Reynolds stresses against, respectively, the wall-normal shear $\partial U/\partial y$ and spanwise shear $\partial U/\partial z$. Assuming the normal mode expansion (8) for the perturbations, and upon integration in the streamwise direction, the terms in the energy balance equation are easily seen to be in the form $(E, D, T_y, T_z) = (\widehat{E}, \widehat{D}, \widehat{T}_y, \widehat{T}_z)e^{2\omega_i t}$ with

$$\widehat{E} = \frac{1}{\lambda_z} \int_0^{\lambda_z} \int_0^{\infty} \widehat{e} dy dz, \quad \widehat{D} = \frac{1}{\lambda_z} \int_0^{\lambda_z} \int_0^{\infty} \widehat{d} dy dz, \quad (21)$$

$$\widehat{T}_y = \frac{1}{\lambda_z} \int_0^{\lambda_z} \int_0^{\infty} \widehat{\tau}_{uv} \frac{\partial U}{\partial y} dy dz, \quad \widehat{T}_z = \frac{1}{\lambda_z} \int_0^{\lambda_z} \int_0^{\infty} \widehat{\tau}_{uw} \frac{\partial U}{\partial z} dy dz, \quad (22)$$

and

$$\begin{aligned} \widehat{e} &= (\widehat{u}\widehat{u}^* + \widehat{v}\widehat{v}^* + \widehat{w}\widehat{w}^*), \quad \widehat{d} = 2 \left(\widehat{\xi}\widehat{\xi}^* + \widehat{\eta}\widehat{\eta}^* + \widehat{\zeta}\widehat{\zeta}^* \right) / R, \\ \widehat{\tau}_{uv} &= -(\widehat{u}\widehat{v}^* + \widehat{u}^*\widehat{v}), \quad \widehat{\tau}_{uw} = -(\widehat{u}\widehat{w}^* + \widehat{u}^*\widehat{w}). \end{aligned}$$

The following identity is immediately derived from equation (16):

$$\omega_i = \frac{\widehat{T}_y}{2\widehat{E}} + \frac{\widehat{T}_z}{2\widehat{E}} - \frac{\widehat{D}}{2\widehat{E}}. \quad (23)$$

In order to evaluate the different terms entering equation (23) one has to know the eigenmode and eigenvalue corresponding to the selected velocity profile $U(y, z)$, Reynolds number R and streamwise wavenumber α . In the absence of errors in the computation, the left-hand side, coming from the eigenvalue computation, and the right-hand side derived from the corresponding mode shape, should match. However, equation (23) is more than an a-posteriori consistency check of the eigenvalue problem solution, it provides an insight into the viscous instability mechanism by separating the three terms which contribute to the temporal growth rate ω_i . A viscous instability is seen to appear when the work of the Reynolds stresses against the basic shears is able to overcome viscous dissipation. In the following, equation (23) will therefore be used to analyse the magnitude of the different physical contributions leading to a given growth rate.

4. Results

4.1. Role of the streak amplitude at a fixed streamwise station and Reynolds number

We begin by investigating the effect of an increasing streak amplitude on the boundary layer stability, keeping fixed the streamwise station X and the reference Reynolds number Re_L (and therefore the local Reynolds number R). For a set of wavenumbers α we compute the eigenvalues having the largest imaginary part ω_i pertaining to the streamwise velocity profiles of the Blasius boundary layer (A) and of the streaks B, C and D prevailing at $X = 2$. We select $Re_L = 750\,000$ which gives, at $X = 2$, $Re_X = 1\,500\,000$, $R = 1224$ and $R_{\delta^*} = 2107$. All the streaks under consideration are stable to sinuous perturbations. In figure 4 we display the temporal growth rate curves $\omega_i(\alpha)$ (on the top row) and the corresponding phase speeds $c_r = \omega_r/\alpha$ (on the bottom row) of varicose perturbations of respectively fundamental (on the left column) and subharmonic type (on the right column). At the Reynolds number under consideration the Blasius boundary layer is unstable. The effect of streaks of increasing amplitude is to reduce the growth rates of fundamental modes (streaks B, C) up to their complete stabilization for case D. The fundamental modes phase speeds are roughly unchanged with respect to the Blasius-TS waves; they are only slightly reduced as the amplitude and/or wavenumber is increased. The fundamental varicose mode therefore appears to be a sort of ‘continuation’ of the 2D Blasius-TS waves into 3D streaky-TS waves.

Subharmonic modes exhibit growth rates which are an order of magnitude smaller than their fundamental counterparts except for streak D which is stable to fundamental perturbations but is slightly unstable to subharmonic perturbations (this is however a very special case, as will be seen in the following).

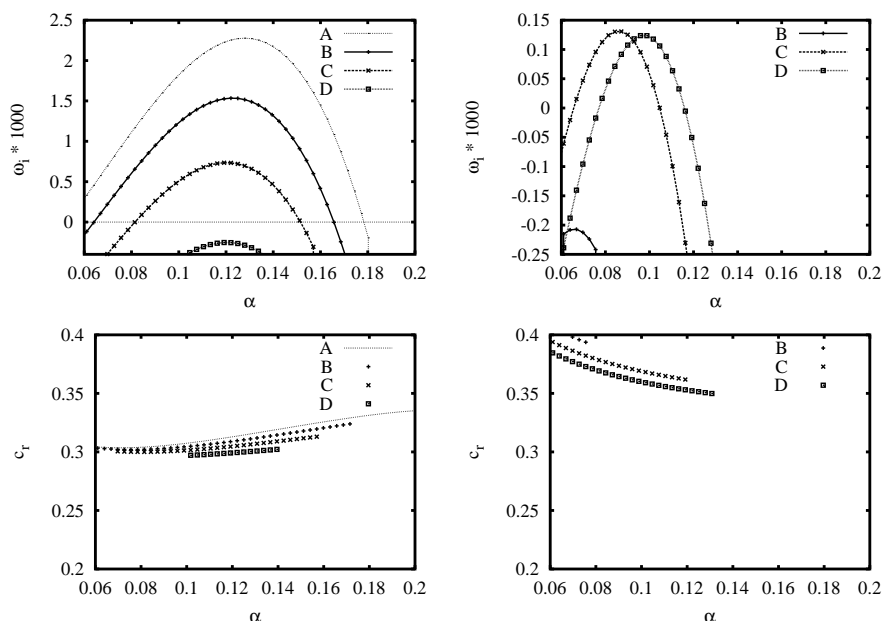


FIGURE 4. Growth rate ω_i (top row) and corresponding real phase speed c_r (bottom row) versus streamwise wavenumber α of fundamental (left column) and subharmonic (right column) modes for the Blasius boundary layer A and the streaky flows B, C and D at $X = 2$ for $R = 1224$.

The subharmonic-mode phase speeds may differ up to 25% from the Blasius-TS phase speeds and they follow an opposite trend since they decrease with increasing wavenumbers. The effect of increasing amplitude is not monotone; the low amplitude streak B is stable while streaks C and D are unstable, but streak D is less unstable than streak C.

In figure 5 we display the *rms* velocity amplitudes $|\hat{u}(y, z)|$, $|\hat{v}(y, z)|$ and $|\hat{w}(y, z)|$ of the most unstable varicose fundamental and subharmonic modes of streak C. The contours of the basic flow velocity $U(y, z) = c_r$, corresponding to the phase speed of the mode, and $U(y, z) = 0.99U_\infty$, denoting the boundary layer thickness have also been included for reference. Fundamental and subharmonic modes have quite different structures, but for both, most of the energy is in the streamwise component \hat{u} . The fundamental mode displays a $|\hat{u}|$ double-peaked structure concentrated in the low-speed and near the high-speed region: The wall normal profile in the low speed region has the M-shaped structure observed by Tani & Komoda (1962) and Kachanov & Tararykin (1987). The component $|\hat{w}|$ is mainly localized in the two regions below the position of maximum spanwise shear $|\partial U/\partial z|$ (see figure 3) and attains its maximum amplitude on the line where $U(y, z) = c_r$. The component $|\hat{v}|$ attains its largest

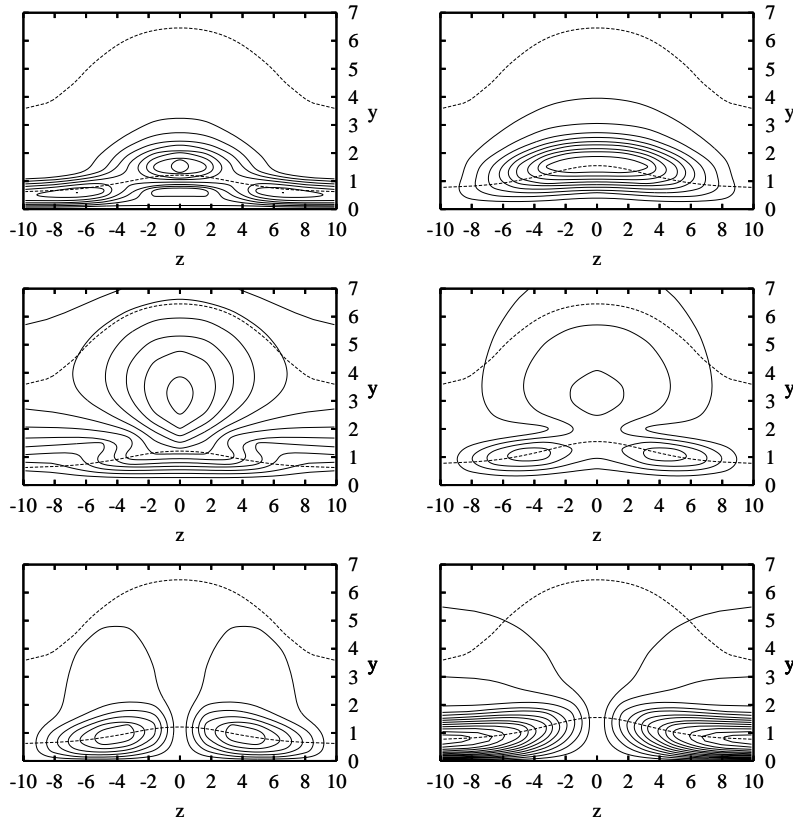


FIGURE 5. *rms* amplitudes of the $\hat{u}(y, z)$ (top), $\hat{v}(y, z)$ (middle) and $\hat{w}(y, z)$ (bottom) components of the most unstable varicose fundamental (left) and subharmonic (right) modes for the streak C profile extracted at $X = 2$ with $R = 1224$. The whole mode has been normalized with \hat{u}_{max} and the contour levels are spaced by $0.1\hat{u}_{max}$ for \hat{u} , $0.01\hat{u}_{max}$ for \hat{v} and $0.02\hat{u}_{max}$ for \hat{w} . The contours $U = c_r$ and $U = 0.99U_\infty$ represented by dashed lines of the corresponding basic flows have also been included.

values in the low-speed region, it is smaller than $|\hat{u}|$ and $|\hat{w}|$, and it protrudes further away from the wall, as for Blasius-TS waves. The subharmonic mode displays a $|\hat{u}|$ single-peaked structure concentrated in the low-speed region, while $|\hat{w}|$ is localized in the high-speed region. $|\hat{v}|$ is smaller than $|\hat{u}|$ and $|\hat{w}|$, it protrudes further away from the wall and has two peaks situated in the same regions as the $|\hat{w}|$ -maxima of the fundamental mode. All the components of the mode reach their maximum amplitude on the $U(y, z) = c_r$ line.

Case	$\ \tilde{u}_0\ $	$\ \tilde{u}_1\ $	$\ \tilde{u}_2\ $
A	1.000	0.000	0.000
B	1.000	0.399	0.156
C	1.000	0.540	0.303
D	1.000	0.641	0.449

TABLE 2. Norms of the first spanwise harmonics $\tilde{u}_0(y)$, $\tilde{u}_1(y)$, $\tilde{u}_2(y)$ of the $\hat{u}(y, z)$ most unstable varicose fundamental modes of streaks A,B,C and D with the same parameters as in figures 4 and 5.

Case	$\omega_{i,max} * 10^3$	$\widehat{T}_y/2\widehat{E} * 10^3$	$\widehat{T}_z/2\widehat{E} * 10^3$	$\widehat{D}/2\widehat{E} * 10^3$
A	3.91668463	6.3942359	0.	2.47534592
B	2.63927744	9.7013363	-2.82568584	4.23475597
C	1.26350209	12.0851384	-4.88611863	5.94099013
D	-0.498663542	13.6826327	-6.28768442	7.89361186

TABLE 3. Maximum growth rates and normalized kinetic energy production and dissipation components pertaining to the varicose fundamental modes for the streaks considered in figure 4.

To give an idea of the level of three-dimensionality of the streaky-TS fundamental modes, we document in table 2 the norms $\|\tilde{u}_k\| = [\int_0^\infty |\tilde{u}_k|^2 dy]^{1/2}$, ($k = 0, 1, 2$) of the spanwise uniform part \tilde{u}_0 of the mode and of the first two spanwise harmonics \tilde{u}_1 and \tilde{u}_2 . The most unstable mode of the Blasius profile (case A) is 2D, and therefore there is no energy in the first two spanwise harmonics. For the streaky basic flows, however, the modes are truly 3D: For increasing streak amplitudes, the sum of the energies contained in \tilde{u}_1 and \tilde{u}_2 may exceed the energy contained in \tilde{u}_0 . With this in mind we can now analyse the shapes of $|\tilde{u}_0(y)|$, $|\tilde{u}_1(y)|$ and $|\tilde{u}_2(y)|$, plotted in figure 6. The spanwise oscillating parts $|\tilde{u}_1(y)|$ and $|\tilde{u}_2(y)|$ keep a fairly constant shape even if their amplitude increases with streak amplitude, as documented above. On the contrary, the spanwise uniform part $|\tilde{u}_0(y)|$ changes its shape. A local ‘minimum’ appears at the position of maximum amplitude of $|\tilde{u}_1(y)|$ and $|\tilde{u}_2(y)|$. This minimum deepens as the streak amplitude increases.

To get further insight into the physical mechanisms responsible for the observed reduction in the fundamental mode growth rates, we report in table 3 the different terms entering equation (23). These are evaluated for the wavenumbers leading to the maximum growth, i.e. at the peak of the $\omega_i(\alpha)$ curves in the top left of figure 4. The relative difference between the imaginary part of the computed eigenvalue, on the left-hand side, and the sum of the terms on the right-hand side of (23) was found to be below 4%. The instability of the Blasius boundary layer (case A) must be ascribed, as already well known, to the excess of kinetic energy production T_y , over the viscous dissipation D .

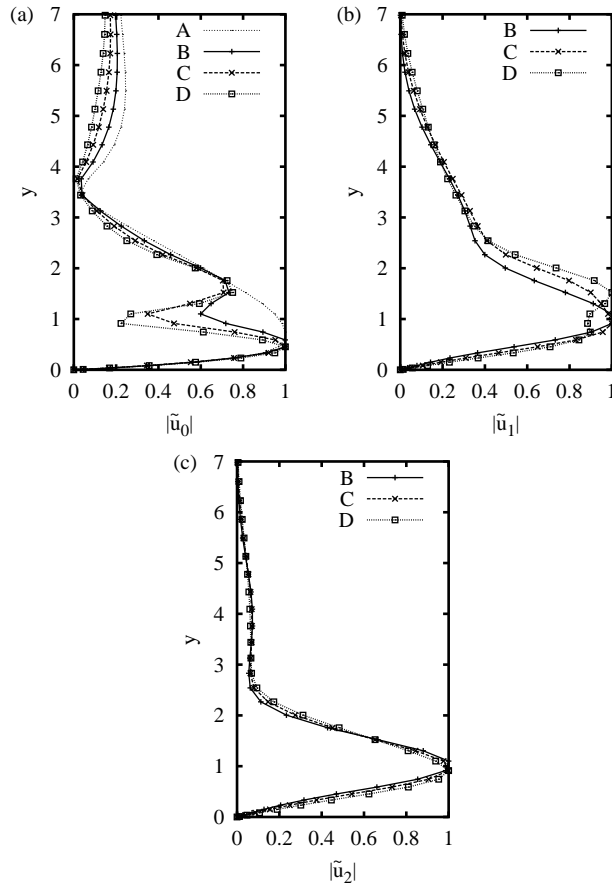


FIGURE 6. Wall-normal distribution of: (a) the spanwise independent, (b) the first and (c) the second harmonics of the \hat{u} -component for the fundamental mode displayed in figure 5. The y coordinate is expressed in $\bar{\delta}_X$ units.

As the Blasius profile is 2D, the spanwise shear $\partial U/\partial z$ is zero and therefore there is no contribution from T_z . For streaky flow profiles, however, the term T_z comes into play and it is stabilizing. The absolute value of the normalized production and dissipation terms is seen to increase with streak amplitude but the stabilizing contribution $(\hat{T}_z - \hat{D})/2\hat{E}$ grows more than the destabilizing contribution $\hat{T}_y/2\hat{E}$, thereby ultimately leading to stability. The negative production term $\hat{T}_z/2\hat{E}$ is of the same order of magnitude as the dissipation term $\hat{D}/2\hat{E}$ and therefore it plays an essential role in the stabilization process. A sample distribution of Reynolds stresses is given in figure 7 for the most unstable fundamental mode of streak C. The $\hat{\tau}_{uv}$ term (figure 7a) is concentrated

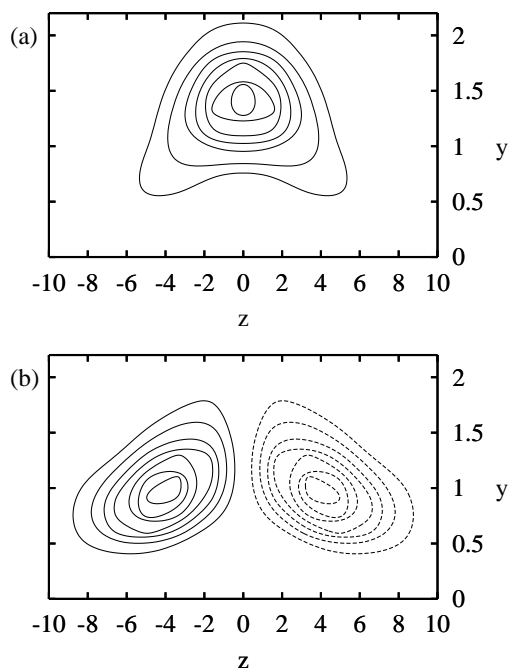


FIGURE 7. Normalized Reynolds stresses (a) $\hat{\tau}_{uv}(y, z)/2\hat{E}$ and (b) $\hat{\tau}_{uv}(y, z)/2\hat{E}$ pertaining to streak C at $X = 2$, $R = 1224$, for $\alpha = 0.119$. The contour spacing is $0.002\hat{u}_{max}$. Dashed lines indicate negative values.

in the low-speed region of the underlying streak and it is positive, while $\hat{\tau}_{uv}$ (figure 7b) is localized on the flanks of the low-speed region and it is antisymmetric with respect to the $z = 0$ axis. The distribution of the corresponding induced production terms and of the viscous dissipation term are displayed in figure 8. The Reynolds stress $\hat{\tau}_{uv}$ and the wall-normal shear $\partial U/\partial y$ having the same symmetry and the same sign almost everywhere (see figure 3), their product gives a dominating positive contribution to T_y (figure 8a). The kinetic energy production is localized in the low-speed region, as one would also expect from quasi-2D local analysis. On the other hand, the Reynolds stress $\hat{\tau}_{uv}$ and the spanwise shear $\partial U/\partial z$ have the same symmetry but opposite sign therefore leading to the negative production distribution in figure 8(b), and to the stabilizing contribution of T_z . The kinetic energy negative production is localized on the flanks of the low-speed region and may not be accounted for by quasi-2D local (in z) analyses. The viscous dissipation, represented in figure 8(c), is essentially concentrated very near the wall in the region of highest wall-normal shear. A local maximum of lower-intensity can be observed in the low-speed region, in the area of highest positive production.

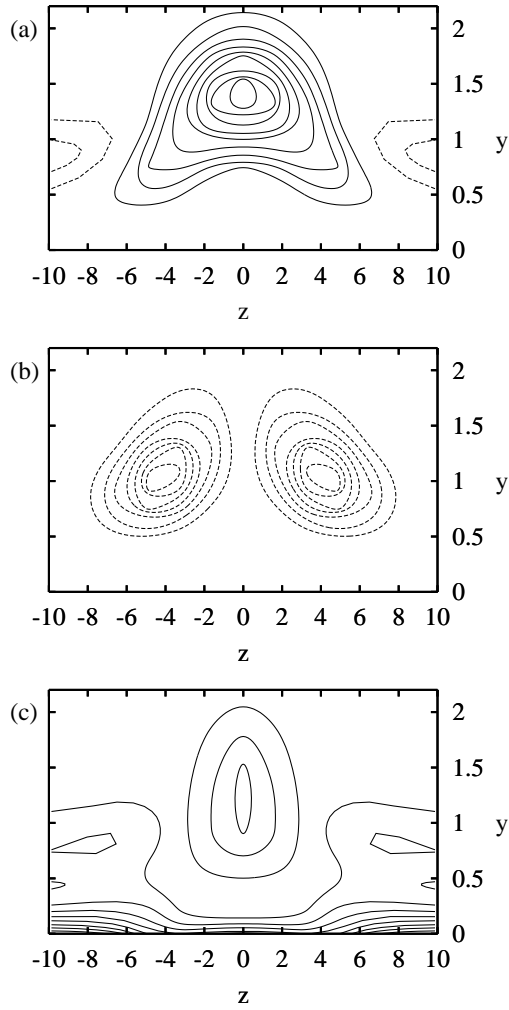


FIGURE 8. Normalized production of perturbation kinetic energy: (a) $\hat{\tau}_{uv}(\partial U/\partial y)/|\hat{T}_y|$, (b) $\hat{\tau}_{uw}(\partial U/\partial z)/|\hat{T}_z|$, and (c) dissipation $\hat{d}/|\hat{D}|$ pertaining to most unstable fundamental mode of streak C at $X = 2$, $R = 1224$, $\alpha = 0.119$. The contour spacing is 0.05. Dashed lines indicate negative values.

4.2. Influence of viscosity on the streak temporal stability at fixed streak amplitude and streamwise station

In order to analyse the influence of viscosity on the temporal stability of the streaky boundary layer profiles, we now consider the effect of varying the reference Reynolds number Re_L , and therefore the local Reynolds number R , for

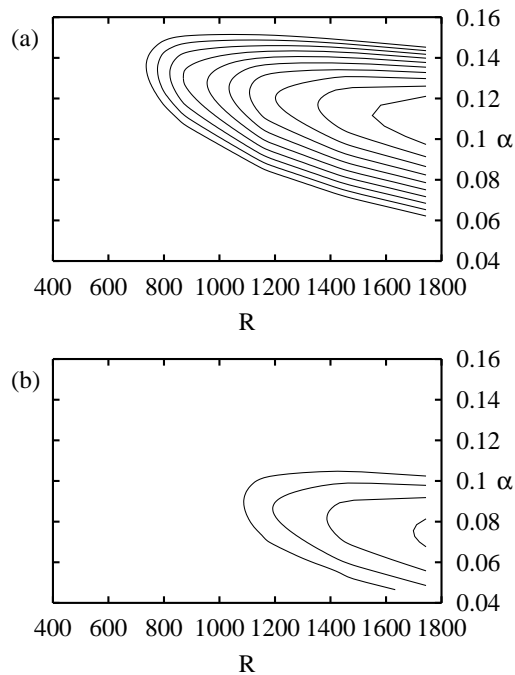


FIGURE 9. Growth rate ω_i of the varicose fundamental (a) and subharmonic (b) modes in the streamwise wavenumber α and local Reynolds number R plane for the C streak profile at $X = 2$. Contours start from the neutral curve and proceed, outer to inner, with a spacing of 10^{-4} .

a fixed streak amplitude (streak C) at a fixed streamwise station ($X = 2$). Sinuous modes are stable for this profile. The results concerning the varicose modes are presented in figure 9, where the curves $\omega_i(\alpha, R)$ of the fundamental (figure 9a) and subharmonic (figure 9b) modes are displayed. For the profile under consideration the critical Reynolds number is found to be $R = 734$, i.e. more than twice the critical Reynolds number of the Blasius boundary layer in the absence of streaks ($R = 304$). The critical mode is the fundamental. Except for a very small region in the parameter plane (roughly $\alpha < 0.07$ and $R > 1100$), the subharmonic varicose modes become unstable at larger Reynolds numbers and their growth rates are smaller than those of the fundamental modes.

To compare the combined effects of viscosity and streak amplitude at fixed X , we repeated the calculations for the other streak profiles at $X = 2$. In figures 10(a) and 10(b) we display, respectively, the varicose fundamental and subharmonic neutral curves pertaining to each streak. The effect of increasing

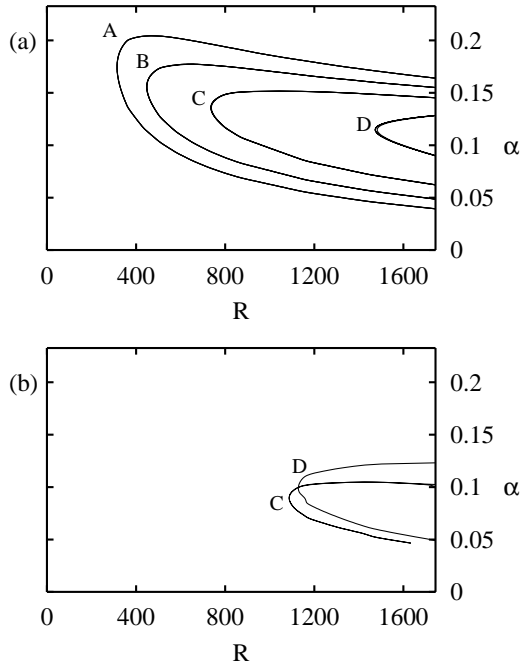


FIGURE 10. Neutral stability curves of (a) the fundamental varicose and (b) subharmonic varicose modes as a function of the streamwise wavenumber α and the local Reynolds number R for the Blasius profile (case A) and streaks B, C, and D (outermost to inner curves) extracted at $X = 2$. Subharmonic modes of streak B profiles are stable in the considered Reynolds number range.

streak amplitude is to delay the instability of the fundamental modes, as expected from the results in the previous section (see figure 4). The outermost neutral curve shown on the left of figure 10 is the well known neutral curve of the Blasius boundary layer (case A, with a critical Reynolds number $R = 304$). The neutral curves corresponding to streaks of increasing amplitude B, C and D are regularly ordered from outer to inner. The largest amplitude profile, the one corresponding to streak D, is able to delay the instability up to $R = 1467$. The amplitude effect on subharmonic modes, as also seen in the previous section, is not monotone; the C and D profiles exhibit essentially the same critical Reynolds number, $R \approx 1100$.

It is important to note that the neutral curves presented in figure 10 are *local* neutral curves corresponding to the velocity profiles prevailing at $X = 2$ i.e., the variation of $R = Re_X^{1/2} = (X Re_L)^{1/2}$ has been obtained through a variation of Re_L at fixed X . Two different stations X will in general exhibit

different stability properties even at the same R because, contrary to the Blasius boundary layer, the streaky boundary layers are not self-similar.

4.3. Stability along the streaky boundary layer

We now consider the stability of a streaky boundary layer by examining the properties of its profiles at different streamwise stations X . For the selected X and a range of local Reynolds number R , we compute the growth rates $\omega_i(\alpha; R, X)$ and then retrieve the maximum growth rate $\omega_{i,max}(R, X)$ by maximizing ω_i over α at constant R and X . The results pertaining to the varicose modes of streak D, which is the one of largest allowed amplitude before the onset of sinuous inflectional instabilities, are documented in figure 11. From the previous sections we know that, for the Reynolds numbers under consideration, the effect of increasing R is destabilizing. This is confirmed by the analysis of figure 11, where it is seen that, for a constant X , an increase in R leads to instability and then to an increase of the maximum growth rate in the unstable region (i.e. $(\partial\omega_{i,max}/\partial R)_X > 0$) for both fundamental and subharmonic modes. The role of X is related to the local streak amplitude. Concerning the fundamental modes, we know from the results above that the role of an increasing streak amplitude is stabilizing. The maximum amplitude of streak D is attained roughly at $X = 2$ when T or A_s are used as measures of the streak amplitude and roughly at $X = 2.5$, when E_U is used (see figure 1). The former measure seems to better account for the effects of the streak amplitude on the stability; in fact, upstream of the peak amplitude ($X < 2.5$), we observe that increasing X at constant R is stabilizing (i.e. $(\partial\omega_{i,max}/\partial X)_R < 0$) because as X increases the streak amplitude also increases. Downstream of the peak amplitude ($X > 2.5$), when X increases the streak amplitude decreases therefore leading to an increase of the growth rates with X at constant R (i.e. $(\partial\omega_{i,max}/\partial X)_R > 0$). Subharmonic modes exhibit growth rates generally lower than those of the fundamental modes, except in a narrow region (roughly $2 < X < 2.5$ and $1000 < R < 1400$) where they become unstable slightly before the fundamental modes.

A streaky boundary layer obtained in an experiment or in a numerical simulation sees the same viscosity and freestream velocity at each streamwise station \bar{X} . Physically realizable streaks are therefore obtained at fixed reference Reynolds number Re_L . Along a ‘physical streak’ the local Reynolds number is given by $R = (Re_L X)^{1/2}$, where Re_L is a constant. To visualize the stability properties of physically realizable streaks, dashed lines corresponding to streaks at $Re_L = 200\,000, 400\,000, \dots, 1\,000\,000$ are introduced on figure 11. As X increases, the local Reynolds number R also increases so that the effects of varying X and R on the stability are coupled. In particular, in the part of the streak which is upstream of its maximum amplitude, the destabilizing role of increasing R and the stabilizing role of increasing X are in competition. Assuming, for instance, $Re_L = 200\,000$, streak D is stable up to $X = 4.2$, corresponding to $R \approx 880$, to both varicose and subharmonic modes. For

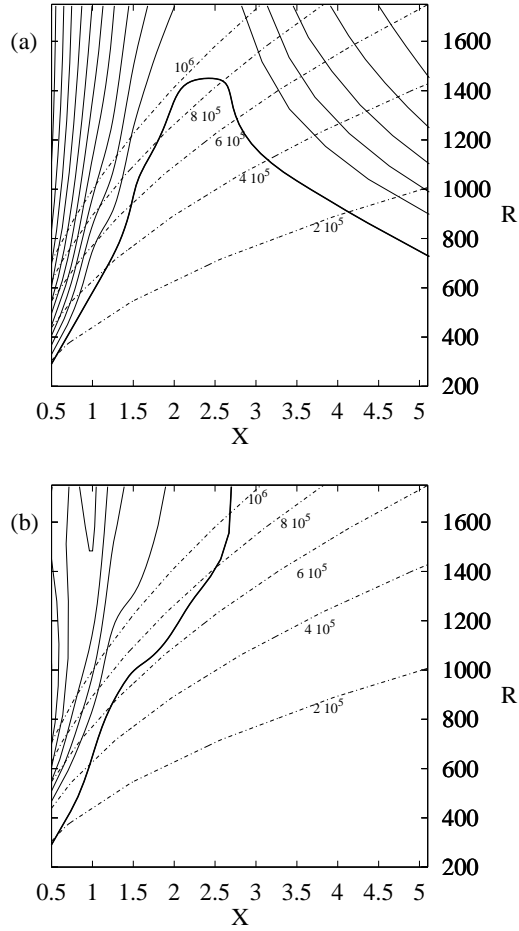


FIGURE 11. Maximum growth rate $\omega_{i,max}$ of (a) varicose fundamental and (b) subharmonic modes pertaining to streak D as a function of streamwise station X and local Reynolds number R . Contour levels are 0 (thick line), $2 \cdot 10^{-4}$, $4 \cdot 10^{-4}$, $6 \cdot 10^{-4}$, ... The dashed lines represent physically realizable streaks at $Re_L = 2 \cdot 10^5, 4 \cdot 10^5, \dots, 10^6$.

$Re_L = 600\,000$ a pocket of instability to both varicose and subharmonic modes appears in the upstream part of the streak (roughly $X < 1.5$) where the streak amplitude is not large enough to counterbalance the destabilizing effect of the Reynolds number R . In the range $1.5 < X < 2.7$ the stabilizing effect of the streak amplitude dominates, but eventually, for $X > 2.7$, at roughly $R = 1300$, fundamental modes become unstable again.

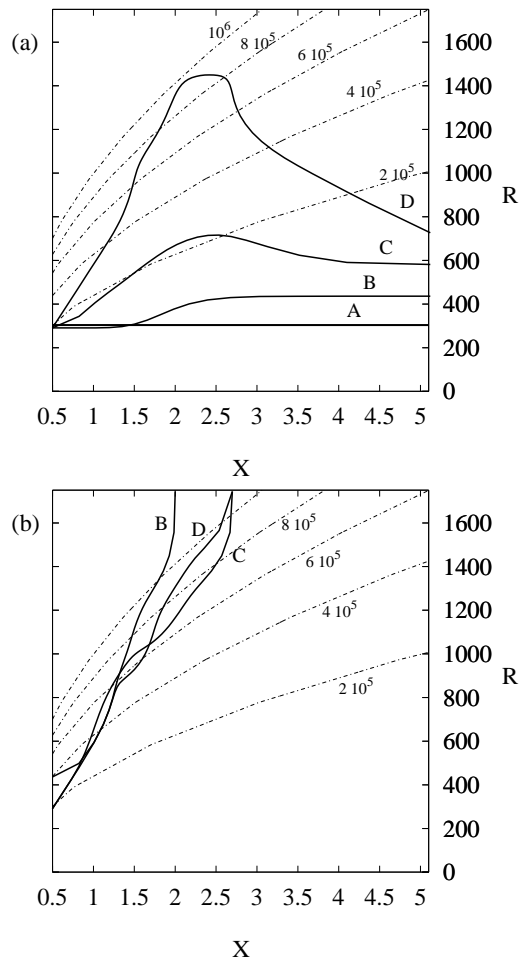


FIGURE 12. Neutral stability curves for (a) fundamental varicose and (b) subharmonic varicose modes for the Blasius boundary layer A and the streaks B, C and D as a function of streamwise station X and local Reynolds number R . The dashed lines represent physically realizable streaks at $Re_L = 2 \cdot 10^5, 4 \cdot 10^5, \dots, 10^6$.

The computations have been repeated for the others streaky basic flows; the corresponding neutral curves are displayed in figure 12. As expected, streak D is the most effective in delaying the instability. The fundamental-mode neutral curve for the lowest amplitude streak is very close to the neutral curve of the Blasius boundary layer, which becomes unstable at $R = 304$ for all X . It can be seen that for all the streaks under consideration the maximum amplitude profile, prevailing at $X \approx 2.5$, may be stable for quite large values of R (e.g.

$R = 1450$ for streak D). However, the stability of a physically realizable streak, obtained following one of the dashed lines in the plot, may be obtained only up to lower R values (e.g. $R = 880$ for streak D) because in the upstream part of the streak the amplitude is not large enough to counterbalance the destabilizing increase of R . This effect is particularly strong for the streaks we consider here because, as their growth is optimized, they have, upstream of their peak value, amplitudes that are generally lower than for other possible non-optimal streaks.

4.4. Implications for transition delay

In low noise environments, the path to boundary layer transition consists of a receptivity phase, in which external disturbances enter the boundary layer, followed by the amplification of these low amplitude disturbances, which is well described by linear stability theory; secondary instability and breakdown follows, once unstable waves reach large enough amplitudes. Most of ‘open-loop’ transition delay methods rely on the suppression or reduction of the exponential growth of the unstable waves in the linear regime, obtained for instance by enforcing favourable pressure gradients, through wall suction, fluid heating or cooling, etc. The forcing of steady streaks in a flat plate boundary layer might be as effective as other methods in delaying transition. A clear advantage of this scheme is the fact that the ‘actuators’ modifying the basic flow stability behavior would be placed upstream of the unstable region and presumably require little energy because the streak extracts its energy from the basic flow itself through the ‘lift-up’ effect. In the previous section we have shown that for streak D it is possible to delay the onset of instability up to R above 850 (corresponding to R_{δ^*} above 1450 and Re_X above 720000) by choosing $Re_L = 200000$. For largest Re_L a pocket of instability appears in the upstream part of the streak, which is however followed by a large region of stable flow. It is therefore interesting to compare, in the unstable domain, the maximum growth rates $\omega_{i,max}^D(R, X)$ in the case of streak D to the maximum growth rates $\omega_{i,max}^A(R)$ that would have been experienced in the absence of streaks (case A) at the same Reynolds number R . In figure 13 we display the relative reduction of the maximum growth rate defined as: $[\omega_{i,max}^A(R) - \omega_{i,max}^D(R, X)]/\omega_{i,max}^A(R)$. In the region where the streak is stable the reduction is, by definition, 100%. Considering fundamental modes, very large growth rate reductions, typically of the order of 60% to 90% are observed in the unstable region downstream of the streak amplitude peak ($X > 2.5$), for $R < 1500$ (i.e. $R_{\delta^*} < 2580$, $Re_X < 2250000$). In the unstable upstream region, appearing for $Re_L > 200000$, the relative reduction is less important. However, in this region the growth rates are smaller in absolute value and they are not experienced for a very long streamwise region in a physically realizable streak. The growth rates of subharmonic modes are so weak that they do not exceed 0.3% of the Blasius-TS waves growth rates.

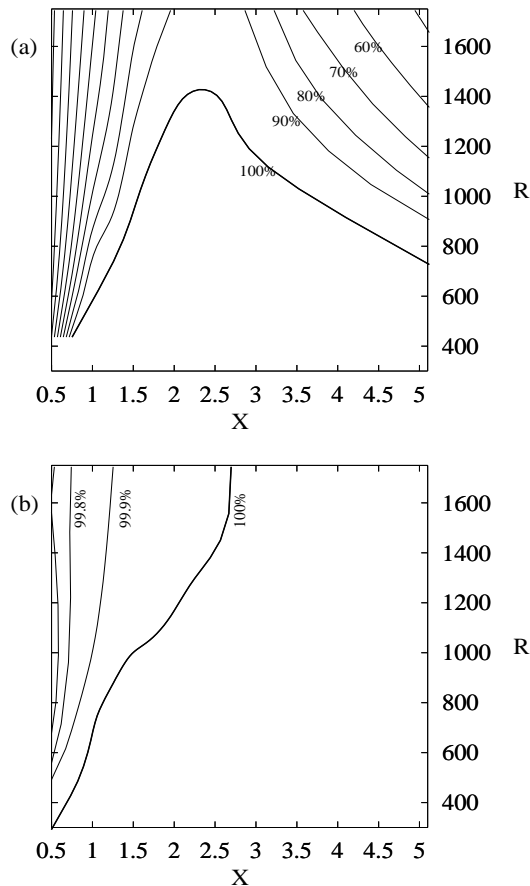


FIGURE 13. Relative reduction of the Blasius 2D maximum temporal growth rate in the presence of streak D. Contours levels are at 100% (thick line), 90%, 80%,... inner to outer for the fundamental case (a) and 100% (thick line), 99.9%, 99.8%,... outer to inner for the subharmonic case (b).

To allow a quantitative comparison with other transition delay methods, the computation of spatial growth rates would be necessary to estimate the total growths at fixed real frequency (the so called n -factors used in the celebrated e^N method), but this is beyond the scope of the present article. We just remark that if Gaster's formula is used to convert temporal growth rates to spatial growth rates with the group velocity as a conversion factor, the results presented in figure 13 would not be qualitatively different because the Blasius-TS-waves and the streaky-TS waves have very similar group velocities at the same Reynolds number. To evaluate the performance of the proposed control

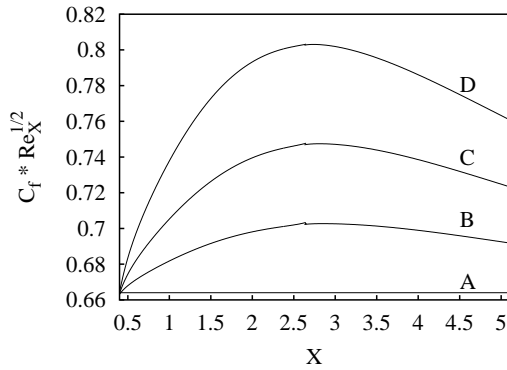


FIGURE 14. Streamwise evolution of normalized skin friction coefficient $C_f Re_X^{1/2}$ for the Blasius boundary layer A and for streaky boundary layers B, C and D.

strategy one must also evaluate the energy used in the generation of the streaks and the energy loss due to the presence of the streaks in the boundary layer. The energy used to generate the streaks is negligible because the ‘lift-up’ effect act as an amplifier of the actuator energy. Typically the lift-up gain is of order Re_X in the linear approximation. On the other hand, the skin friction coefficient C_f pertaining to the B, C and D basic flows is larger than that of the Blasius 2D boundary layer. The C_f increase is due to the spanwise uniform part of the basic flow distortion induced by streaks through nonlinear effects. These lead to ‘fuller’ velocity profiles (see CB) and to larger shear at the wall. On figure 14 we display the streamwise evolution of normalized skin friction coefficient $C_f Re_X^{1/2}$ for the Blasius boundary layer A and the streaks under consideration. The skin friction coefficient increases at worst by less than 20% when compared to the Blasius case.

It is, finally, worth remarking that the results we present in this study concern a very particular family of streaks. Even if it is known that the streak profiles themselves are not very sensitive to their ‘upstream history’, their amplitude evolution along X is sensitive to both the shape and the amplitude of upstream forcing. It should be observed that if the upstream vortices are induced using wall roughness elements or blowing-suction slots, their amplitude evolution would not be the same as for the optimal perturbations used here (see e.g. White 2002). In this study, we did not try to optimize the streak generation in order to maximize the delay in instability onset or the transition Reynolds numbers, but we think that this optimization could increase the performance of a possible streak-based transition delay protocol.

5. Conclusions

In this article we have analysed the linear viscous stability of the boundary layer on a flat plate in the presence of nonlinear streamwise streaks assumed steady and spanwise periodic. It was already known that inflectional sinuous instabilities set in when the streak amplitude is large. However, little was known about the viscous stability of streaks of lower but finite amplitude. For the family of intermediate-amplitude streaks considered in the present study, the main results may be summarized as follows:

- The streaks have a stabilizing effect on the viscous instability of the flat plate boundary layer. This stabilizing effect increases with the streak amplitude.
- The most unstable waves prevailing at a given streamwise station are modified by streaks of increasing amplitude. They evolve from the ‘classical’ 2D TS waves into 3D varicose fundamental modes with essentially the same phase speed but with lower growth rates and a characteristic M-shaped structure of their *rms* streamwise velocity amplitude.
- The viscous instability is, in the presence of the streaks, fed by the work of the uv -Reynolds stress against the wall normal shear $\partial U/\partial y$, just as in the 2D boundary layer. However, the work of the uv -Reynolds stresses against the spanwise shear $\partial U/\partial z$ is stabilizing. This stabilizing contribution and the viscous dissipation increase with the streak amplitude, thereby reducing the growth rate and eventually leading to stability.
- Varicose subharmonic modes may also be unstable but have growth rates which typically are an order of magnitude lower than those of fundamental modes. Sinuous modes appear always stable to viscous instabilities.
- As the streaks are not self-similar, their stability depends both on the Reynolds number and on the streamwise evolution of their amplitude.
- For the particular streaks considered in this study, it is found that for low reference Reynolds numbers Re_L , the streak is characterized by an upstream region of stable flow followed by a region of unstable flow. For large enough Re_L , a pocket of instability appears in the upstream stable region. However, the growth rates in the unstable domains are always lower than the growth rates that would have been observed in the absence of the streaks.

These results confirm and extend those obtained by the present authors (Cossu & Brandt 2002) and are in agreement with early experimental investigations of linear viscous modes in streaky boundary layers. In particular, we retrieve the M-shaped structure of the streaky 3D viscous modes found by Tani & Komoda (1962) and Kachanov & Tararykin (1987). We also find that the TS growth rates are reduced by the streaks and that their phase velocity is only slightly changed, as reported by Kachanov & Tararykin (1987). Unfortunately, differences in the basic flows prevent quantitative comparison with experiments.

The approach taken in the present study is a direct extension of the ‘classical’ 2D boundary layer transition analysis. The streaky boundary layers are considered as 3D basic flows and the streaky 3D TS waves arise as the most unstable linear modes. The present article only deals with this linear analysis but, in the present context, nonlinear effects would naturally arise as soon as 3D streaky-TS waves reach finite amplitudes. In the 2D boundary layer, the 2D TS waves are unstable to 3D secondary perturbations for amplitudes of the order of 1% U_∞ and it is not clear, at the moment, if and how 3D streaky TS waves experience such a kind of secondary instability.

The possible relevance of streak stabilization for applications in boundary layer transition delay has also been discussed. Further investigation is needed on the issue of a ‘practical’ streak generation scheme and on the computation of total spatial growth (n-factor) reductions in the presence of streaks. However, the efficiency of the generation of the streaks, which exploits the ‘lift-up’ mechanism, the fact that the actuators do not need to cover all the unstable domain, and the large induced temporal growth rates reductions are seen as very promising trends. In a different physical context, a similar control paradigm, based on roughness element-induced streak generation, was put forward to delay cross-flow instability (Saric, Carrillo Jr. & Reibert 1998; Wassermann & Kloker 2002).

Our results may probably be related also to the observed average reduction of the growth of small amplitude TS waves developing in a boundary layer exposed to free stream turbulence (Boiko *et al.* 1994; Bakchinov *et al.* 1995; Fasel 2002). In this case however, streaks of different spanwise scales coexist in the boundary layer and, furthermore, they are unsteady, so that further investigation seems necessary to assess the importance of these two additional factors.

We kindly acknowledge P. Huerre and D.S. Henningson for their useful remarks on the manuscript and S. Reddy for providing the stability code which was used to validate our numerical method. Part of the computational facilities were provided by CNRS/IDRIS. LB acknowledges financial support by VR (Vetenskapsrådet) and by École Polytechnique during his stay at LadHyX.

References

- ANDERSSON, P., BERGGREN, M. & HENNINGSON, D. 1999 Optimal disturbances and bypass transition in boundary layers. *Phys. Fluids* **11** (1), 134–150.
- ANDERSSON, P., BRANDT, L., BOTTARO, A. & HENNINGSON, D. 2001 On the breakdown of boundary layers streaks. *J. Fluid Mech.* **428**, 29–60.
- ARNAL, D. & JUILLEN, J. C. 1978 Contribution expérimentale à l’étude de la reptivité d’une couche limite laminaire à la turbulence de l’écoulement général. Rapport Technique 1/5018. ONERA.
- BAKCHINOV, A. A., GREK, G. R., KLINGMANN, B. G. B. & KOZLOV, V. V. 1995

- Transition experiments in a boundary layer with embedded streamwise vortices. *Phys. Fluids* **7**, 820.
- BOIKO, A. V., WESTIN, K. J. A., KLINGMANN, B. G. B., KOZLOV, V. V. & ALFREDSSON, P. H. 1994 Experiments in a boundary layer subjected to free stream turbulence. part 2. the role of TS-waves in the transition process. *J. Fluid Mech.* **281**, 219–245.
- BRANDT, L. & HENNINGSON, D. S. 2002 Transition of streamwise streaks in zero-pressure-gradient boundary layers. *J. Fluid Mech.* **472**, 229–262.
- CANUTO, C., HUSSAINI, Y. M., QUARTERONI, A. & ZANG, T. A. 1988 *Spectral Methods in Fluid Dynamics*. New York: Springer.
- COSSU, C. & BRANDT, L. 2002 Stabilization of Tollmien-Schlichting waves by finite amplitude optimal streaks in the Blasius boundary layer. *Phys. Fluids* **14**, L57–L60.
- DRAZIN, P. & REID, W. 1981 *Hydrodynamic Stability*. Cambridge Univ. Press.
- DRYDEN, H. L. 1936 Air flow in the boundary layer near plate. Report 562. NACA.
- ELLINGSEN, T. & PALM, E. 1975 Stability of linear flow. *Phys. Fluids* **18**, 487.
- FASEL, H. 2002 Numerical investigation of the interaction of the Klebanoff-mode with a Tollmien-Schlichting wave. *J. Fluid Mech.* **450**, 1–33.
- GREK, H. R., KOSLOV, V. V. & RAMAZANOV, M. P. 1989 Investigation of boundary layer stability in the presence of high degree of free-stream turbulence. In *Proc. of Intl Seminar of Problems of Wind Tunnel Modeling*, , vol. 1. Novosibirsk (in Russian).
- GUSTAVSSON, L. H. 1991 Energy growth of three-dimensional disturbances in plane Poiseuille flow. *J. Fluid Mech.* **224**, 241–260.
- HERBERT, T. 1988 Secondary instability of boundary-layers. *Annu. Rev. Fluid Mech.* (20), 487–526.
- KACHANOV, Y. S. & TARARYKIN, O. I. 1987 Experimental investigation of a relaxing boundary layer. *Izv. SO AN SSSR, Ser. Tech. Nauk* **18**.
- KENDALL, J. M. 1985 Experimental study of disturbances produced in a pre-transitional laminar boundary layer by weak free-stream turbulence. *AIAA Paper* **85**, 1695.
- KLEBANOFF, P. S. 1971 Effect of free-stream turbulence on the laminar boundary layer. *Bull. Am. Phys. Soc.* **10**, 1323.
- KOMODA, H. 1967 Nonlinear development of disturbance in a laminar boundary layer. *Phys. Fluids Suppl.* **10**, S87.
- LANDAHL, M. T. 1980 A note on an algebraic instability of inviscid parallel shear flows. *J. Fluid Mech.* **98**, 243.
- LEHOUCQ, R. B., SORENSEN, D. C. & YANG, C. 1998 *ARPACK user guide: Solution of Large-Scale Eigenvalue Problems with Implicitly Restarted Arnoldi Methods*. Philadelphia: SIAM.
- LUCHINI, P. 2000 Reynolds-number independent instability of the boundary layer over a flat surface. part 2: Optimal perturbations. *J. Fluid Mech.* **404**, 289–309.
- LUNDBLADH, A., BERLIN, S., SKOTE, M., HILDINGS, C., CHOI, J., KIM, J. & HENNINGSON, D. S. 1999 An efficient spectral method for simulation of incompressible flow over a flat plate. Technical Report KTH/MEK/TR-99/11-SE. KTH, Department of Mechanics, Stockholm.

- PARK, D. S. & HUERRE, P. 1995 Primary and secondary instabilities of the asymptotic suction boundary layer on a curved plate. *J. Fluid Mech.* **283**, 249–272.
- PRANDTL, L. 1921 Bemerkungen über die Entstehung der Turbulenz. *ZAMM* **1**, 431–436.
- REDDY, S. C., SCHMID, P. J., BAGGETT, J. S. & HENNINGSON, D. S. 1998 On the stability of streamwise streaks and transition thresholds in plane channel flows. *J. Fluid Mech.* **365**, 269.
- REED, H. L. & SARIC, W. S. 1989 Stability of three-dimensional boundary layers. *Annu. Rev. Fluid Mech.* **21**, 235–284.
- SARIC, W. S., CARRILLO JR., R. B. & REIBERT, M. S. 1998 Leading-edge roughness as a transition control mechanism. *AIAA Paper-98-0781*.
- SCHLICHTING, H. 1933 Berechnung der anfängung kleiner störungen bei der plattenströmung. *ZAMM* **13**, 171–174.
- SCHLICHTING, H. 1979 *Boundary-Layer Theory*. New York: Mc Graw-Hill.
- SCHMID, P. J. & HENNINGSON, D. S. 2001 *Stability and Transition in Shear Flows*. New York: Springer.
- SCHUBAUER, G. B. & SKRAMSTAD, H. K. 1947 Laminar boundary layer oscillations and transitions on a flat plate. *J. Aero. Sci.* **14**, 69–76.
- TANI, I. & KOMODA, H. 1962 Boundary layer transition in the presence of streamwise vortices. *J. Aerospace Sci.* **29**, 440.
- TAYLOR, G. I. 1939 Some recent developments in the study of turbulence. In *Proc. 5th Intl. Congr. Appl. Mech.* (ed. J. Hartog & H. Peters), pp. 294–310. Wiley.
- TOLLMIE, W. 1929 Über die entstehung der turbulenz. *Nachr. Ges. Wiss. Göttingen* *21-24*, English translation NACA TM 609, 1931.
- WALEFFE, F. 1995 Hydrodynamic stability and turbulence: Beyond transients to a self-sustaining process. *Stud. Appl. Math.* **95**, 319–343.
- WASSERMANN, P. & KLOKER, M. 2002 Mechanisms and passive control of crossflow-vortex-induced transition in a three-dimensional boundary layer. *J. Fluid Mech.* **456**, 49–84.
- WHITE, E. B. 2002 Transient growth of stationary disturbances in a flat plate boundary layer. *Phys. Fluids* **14**, 4429–4439.
- YU, X. & LIU, J. 1991 On the secondary instability in Goertler flow. *Phys. Fluids A* **3**, 1845.
- YU, X. & LIU, J. 1994 On the mechanism of sinuous and varicose modes in three-dimensional viscous secondary instability of nonlinear Görtler rolls. *Phys. Fluids* **6** (2), 736–750.

Paper 6

6

Weakly nonlinear analysis of boundary layer receptivity to free-stream disturbances

By Luca Brandt[†], Dan S. Henningson[†], and Donatella Ponziani[‡]

[†]Department of Mechanics, Royal Institute of Technology (KTH), S-100 44
Stockholm, Sweden

[‡]Department of Mechanics and Aeronautics, *University of Rome "La Sapienza"*, 18
Via Eudossiana, 00184 Rome, Italy

The intent of the present paper is to study the receptivity of a zero pressure gradient boundary layer to free-stream disturbances with the aim to isolate the essential features involved in the generation of streamwise streaks. A weakly nonlinear formulation based on a perturbation expansion in the amplitude of the disturbance truncated at second order is used. It is shown that the perturbation model provide an efficient tool able to disentangle the sequence of events in the receptivity process. Two types of solutions are investigated: the first case amounts to the receptivity to oblique waves generated by a wave-like external forcing term oscillating in the free-stream, the second the receptivity to free-stream turbulence-like disturbances, represented as a superposition of modes of the continuous spectrum of the Orr–Sommerfeld and Squire operators. A scaling property of the governing equations with the Reynolds number is also shown to be valid. The relation between this nonlinear receptivity process and previously investigated linear ones is also discussed.

1. Introduction

The objective of the present work is the study of the stability and receptivity of the boundary layer subjected to free-stream disturbances. From a theoretical point of view, boundary layer stability has traditionally been analyzed in terms of the eigensolutions of the Orr–Sommerfeld, Squire equations that reduces the study to exponentially growing disturbances. Experimental findings show that transition due to turbulence in the free-stream is mainly characterized by the occurrence of streamwise elongated structures which are very different from the exponentially growing perturbations. These streamwise structures (or streaks) were first identified by Klebanoff (1971) in terms of low frequency oscillations in hot wire signals caused by low spanwise oscillations of the streaks (Kendall 1985; Westin *et al.* 1994) and are commonly referred to as Klebanoff-modes.

Further analysis of the Orr–Sommerfeld, Squire equations (Gustavsson 1991; Butler & Farrel 1992; Reddy & Henningson 1993; Trefethen *et al.*

1993) have confirmed that disturbances other than exponentially growing perturbations may lead to disturbance growth. From a mathematical point of view this is due to the non-normality of the Orr-Sommerfeld, Squire operator. The physical mechanism behind this linear mechanism is the lift-up induced by streamwise vortices that interact with the boundary layer shear thus generating streaks in the streamwise velocity component. Transition due to these types of disturbances is generally called by-pass transition.

The understanding and prediction of transition require the knowledge of how a disturbance can enter and interact with the boundary layer, commonly referred to as receptivity of the boundary layer. The disturbances are often characterized as either acoustic or vortical disturbances convected by the free-stream. Both types of disturbances have been investigated by asymptotic methods and a summary of the results can be found in the reviews by Goldstein & Hultgren (1989) and Kerschen (1990). Bertolotti (1997) has assumed as initial disturbances vortical modes, solutions of the linearized Navier-Stokes equations in the free-stream, which are waves periodic in the spanwise direction and decaying in the streamwise and has studied the boundary layer receptivity in a “linear region” excluding the leading edge. He has found receptivity to modes with zero streamwise wavenumber and has shown that the growth is most likely connected to the theories of non-modal growth. To answer the question of which disturbance present at the leading edge gives the largest disturbance in the boundary layer at a certain downstream position, Andersson *et al.* (1999) and Luchini (2000) have used an optimization technique adapted from optimal-control theory. The disturbances they found were also streamwise vortices that caused the growth of streaks, and both the wall normal disturbance shape and growth rates agreed well with the findings of Bertolotti (1997) and to experimental results. Wundrow & Goldstein (2001) used asymptotic expansions to study the effects of a small amplitude steady streamwise vorticity field on the flow over a flat plate. Their results show how an initially linear perturbation of the upstream flow leads to strong nonlinear shear layers far downstream of the leading edge.

Berlin & Henningson (1999) have carried out numerical experiments on how simple vortical free-stream disturbances interact with a laminar boundary layer, and have identified a linear and a new nonlinear receptivity mechanism. The nonlinear one was found to force streaks inside the boundary layer similar to those found in experiments on free-stream turbulence and it worked equally well for streamwise and oblique free-stream disturbances. The boundary layer response caused by the nonlinear mechanism was, depending on the initial disturbance energy, comparable to that of the linear mechanism, which was only efficient for streamwise disturbances.

In the present work we develop a theoretical analysis with the aim to isolate the features involved in the generation of streamwise streaks in flows subjected to free-stream turbulence. We consider a weakly nonlinear model based on

a perturbation expansion in terms of the amplitude of the disturbance, truncated at second order. The model, originally developed in a previous work for Poiseuille flow (Ponziani 2000; Ponziani *et al.* 2000), is here extended to boundary layer flows. This implies the inclusion of the continuous spectrum eigenfunctions in the representation of the first and the second order solutions. To validate the model we first investigate a receptivity mechanisms in a boundary layer imposing a localized disturbance both in the boundary layer and in the free-stream. In particular, we study the long time response of the system to a couple of oblique modes oscillating with a given frequency ω . For this case the linearized stability equations are driven at first order by the external disturbance and at second order by the quadratic interactions between first order terms. For the type of disturbance considered, the presence of oblique waves generates streamwise vortices which, in turn, induce the formation of streaks inside the boundary layer. The oblique modes are associated to $(\alpha, \pm\beta)$ wave numbers and their quadratic interactions produce $(0, 2\beta)$ wave numbers that correspond, in physical terms, to an elongated vortical structure, i.e. streamwise counter-rotating vortices. The results show that the generation of streamwise vorticity, which is a nonlinear mechanism, and its subsequent lift-up can indeed be recovered through the weakly nonlinear formulation. The theory is validated through comparison of the results obtained in this case with direct numerical simulations.

The model is then applied to investigate the response of the boundary layer to continuous spectrum modes. The latter are fundamental for the understanding of the interaction between free-stream vortical eddies and the boundary layer since they reduce to simple sines and cosines in the free-stream and can easily be used to represent a free-stream turbulence spectrum. By using continuous modes, which are solutions of the linear problem, the model reduces to solve a second order equation where the forcing is given by the weakly nonlinear interactions between continuous modes. An extensive parametric study is carried out to analyze the interaction between Orr-Sommerfeld as well as Squire modes, in particular considering the effect of the disturbance wave numbers. A scaling property of the resolvent of the Orr-Sommerfeld and Squire problem with the Reynolds number is shown to be valid for the results obtained.

2. The perturbation model

In the following we define the streamwise, wall normal and spanwise directions as x , y and z , respectively, with velocity perturbation $\underline{u} = (u, v, w)$. All variables are made dimensionless with respect to the constant displacement thickness δ_0^* and the free-stream velocity U_∞ (time is made non dimensional with respect to δ_0^*/U_∞). The perturbation equations are derived directly from the Navier-Stokes equations where we have superimposed a perturbation field to the base flow, namely the Blasius profile. We consider no-slip boundary conditions at the wall, solenoidal initial conditions and in order to impose periodic boundary conditions in the directions parallel to the wall we assume a parallel base flow. Although the parallel flow assumption is questionable in the limit

of low streamwise wave numbers ($\alpha \rightarrow 0$), its use is supported by the works of Berlin & Henningson (1999) and Tumin & Reshokto (2001), among others. They show in fact, that the generation of streamwise streaks is due to the same physical mechanism and that the transient growth of streamwise independent optimal disturbances is similar for the parallel and non-parallel case.

We study the evolution of a disturbance in a boundary layer over a flat plate via perturbation theory by expanding the relevant variables in terms of the amplitude of the disturbance ϵ

$$\begin{aligned}\underline{u} &= \underline{u}^{(0)} + \epsilon \underline{u}^{(1)} + \epsilon^2 \underline{u}^{(2)} + \dots \\ p &= p^{(0)} + \epsilon p^{(1)} + \epsilon^2 p^{(2)} + \dots\end{aligned}\quad (1)$$

where $\underline{u}^{(0)}, p^{(0)}$ is the given base flow, while remaining terms are unknowns to be determined by the perturbation analysis. We consider a general case in which the perturbation equations are forced by an external forcing

$$F(x, y, z, t) = \epsilon F^{(1)}(x, y, z, t),$$

with a given initial condition.

Substituting the expansion (1), truncated at second order, into the Navier-Stokes equations and collecting terms of like powers in ϵ , one obtains the governing equations for the first and the second order. These equations, can be rewritten in the normal velocity $v^{(j)}$, normal vorticity $\eta^{(j)}$ ($j = 1, 2$) formulation, thus obtaining the following Orr-Sommerfeld, Squire system

$$\left[\left(\frac{\partial}{\partial t} + u^{(0)} \frac{\partial}{\partial x} \right) \Delta - D^2 u^{(0)} \frac{\partial}{\partial x} - \frac{1}{Re} \Delta^2 \right] v^{(j)} = N_v^{(j)} + F_v^{(j)} \quad (2)$$

$$\left[\frac{\partial}{\partial t} + u^{(0)} \frac{\partial}{\partial x} - \frac{1}{Re} \Delta \right] \eta^{(j)} + D u^{(0)} \frac{\partial v^{(j)}}{\partial z} = N_\eta^{(j)} + F_\eta^{(j)} \quad (3)$$

where

$$N_v^{(j)} = - \left[\left(\frac{\partial^2}{\partial x^2} + \frac{\partial^2}{\partial z^2} \right) S_2^{(j)} - \frac{\partial^2}{\partial x \partial y} S_1^{(j)} - \frac{\partial^2}{\partial y \partial z} S_3^{(j)} \right] \quad (4)$$

$$N_\eta^{(j)} = - \left(\frac{\partial}{\partial z} S_1^{(j)} - \frac{\partial}{\partial x} S_3^{(j)} \right) \quad (5)$$

with

$$S_1^{(j)} = \frac{\partial}{\partial x} u^{(j-1)} u^{(j-1)} + \frac{\partial}{\partial y} u^{(j-1)} v^{(j-1)} + \frac{\partial}{\partial z} u^{(j-1)} w^{(j-1)} \quad (6)$$

$$S_2^{(j)} = \frac{\partial}{\partial x} u^{(j-1)} v^{(j-1)} + \frac{\partial}{\partial y} v^{(j-1)} v^{(j-1)} + \frac{\partial}{\partial z} v^{(j-1)} w^{(j-1)} \quad (7)$$

$$S_3^{(j)} = \frac{\partial}{\partial x} u^{(j-1)} w^{(j-1)} + \frac{\partial}{\partial y} v^{(j-1)} w^{(j-1)} + \frac{\partial}{\partial z} w^{(j-1)} w^{(j-1)} \quad (8)$$

The first and second order equations have constant coefficients with respect to the streamwise and spanwise directions, hence we consider the Fourier transform in the (x, z) plane by making the following form assumption for the solution $q^{(j)} = (v^{(j)}, \eta^{(j)})^T$

$$q^{(j)}(x, y, z, t) = \sum_m \sum_n \hat{q}_{mn}^{(j)}(y, t) e^{i(\alpha_m x + \beta_n z)}$$

and likewise for the external forcing. The wave numbers are defined as follows

$$\alpha_m = m 2\pi/L_x \quad (9)$$

$$\beta_n = n 2\pi/L_z \quad (10)$$

$$k_{mn}^2 = \alpha_m^2 + \beta_n^2 \quad (11)$$

where L_x and L_z are, respectively, the streamwise and spanwise lengths of the periodic domain. Hereafter, for reading convenience, the subscript m and n are omitted and we refer to the equations for the individual wave number (α_m, β_n) as (α, β) . The resulting equations in matrix form read

$$\left(\frac{\partial}{\partial t} \hat{M} - \hat{L}\right) \hat{q}^{(1)} = \hat{P} \hat{F}, \quad (12)$$

$$\left(\frac{\partial}{\partial t} \hat{M} - \hat{L}\right) \hat{q}^{(2)} = \hat{P} \sum_{k+p=m} \sum_{l+q=n} [\hat{N}(\hat{u}_{kl}^{(1)} \hat{u}_{pq}^{(1)T})]^T \quad (13)$$

where

$$\hat{L} = \begin{pmatrix} \mathcal{L}_{OS} & 0 \\ \mathcal{C} & \mathcal{L}_{SQ} \end{pmatrix}, \quad \hat{M} = \begin{pmatrix} k^2 - D^2 & 0 \\ 0 & 1 \end{pmatrix},$$

$$\hat{N} = \begin{pmatrix} i\alpha \\ D \\ i\beta \end{pmatrix}, \quad \hat{P} = \begin{pmatrix} -i\alpha D & k^2 & -i\beta D \\ -i\beta & 0 & i\alpha \end{pmatrix}.$$

\hat{L} is the linear operator that defines the classical Orr-Sommerfeld, Squire problem

$$\begin{aligned} \mathcal{L}_{OS} &= i\alpha u^{(0)}(D^2 - k^2) - i\alpha D^2 u^{(0)} - \frac{1}{Re}(D^2 - k^2)^2 \\ \mathcal{C} &= -i\beta D u^{(0)} \\ \mathcal{L}_{SQ} &= -i\alpha u^{(0)} + \frac{1}{Re}(D^2 - k^2). \end{aligned} \quad (14)$$

We introduce the inner product and the corresponding energy norm associated to the kinetic energy of the disturbance velocity according to

$$E = \int_0^\infty \hat{q}^H \hat{M} \hat{q} dy = (\hat{M} \hat{q}, \hat{q}) = \|\hat{q}\|_E. \quad (15)$$

In this investigation we consider two different types of solutions. In the first case the system of equations at first order is forced by an external force that we assume pulsating with a given frequency ω

$$\hat{F}^{(1)} = \hat{f}(y) e^{i\omega t} + \hat{f}^*(y) e^{-i\omega t},$$

where the $*$ indicates the complex conjugate. At second order, the problem is forced by the nonlinear interactions of first order terms

$$\hat{T} = \hat{P} \sum_{k+p=\bar{n}} \sum_{l+q=\bar{n}} [N(\hat{\mathbf{u}}_{kl}^{(1)} \hat{\mathbf{u}}_{pq}^{(1)})]^T. \quad (16)$$

In the second case, we assume that the solution for the first order is given by a continuous spectrum mode representation, and we solve only the second order problem.

The initial conditions are

$$\hat{q}^{(j)}(t=0) = \hat{q}_0, \quad j = 1, 2. \quad (17)$$

With regard to the boundary conditions we enforce no-slip conditions

$$\hat{v}^{(j)} = D\hat{v}^{(j)} = \hat{\eta}^{(j)} = 0 \quad (18)$$

while we assume boundedness in the free-stream. The remaining velocities are recovered by

$$\hat{u}^{(j)} = \frac{i}{k^2} (\alpha D\hat{v}^{(j)} - \beta \hat{\eta}^{(j)}) \quad (19)$$

$$\hat{w}^{(j)} = \frac{i}{k^2} (\beta D\hat{v}^{(j)} + \alpha \hat{\eta}^{(j)}) \quad (20)$$

2.1. The solution to the forced problem

We consider here the harmonically forced problem described by the system of Eqs. (12), (13) whose solution can be split into two parts (see Ponziani *et al.* 2000): one representing the long time asymptotic solution $\hat{q}^{(j)L}$ and the other describing the initial transient behavior $\hat{q}^{(j)T}$,

$$\hat{q}^{(j)} = \hat{q}^{(j)T} + \hat{q}^{(j)L}, \quad j = 1, 2. \quad (21)$$

First we consider the equations for the long time behavior at first order

$$\begin{aligned} (\pm i\omega \hat{M} - \hat{L}) \hat{q}^{(1)L} &= \hat{P} \hat{F}, \\ \hat{v}^{(1)L} = D\hat{v}^{(1)L} &= \hat{\eta}^{(1)L} = 0, \quad y = 0, \quad y = y_\infty \end{aligned} \quad (22)$$

whose long time response to the harmonic forcing is given by

$$\hat{q}_{\pm\omega}^{(1)L} = (\pm i\omega \hat{M} - \hat{L})^{-1} \hat{P} \hat{f}(y) e^{\pm i\omega t}. \quad (23)$$

The equations that describe the transient at first order are given by

$$\begin{aligned} \frac{\partial}{\partial t} \hat{M} \hat{q}^{(1)T} &= \hat{L} \hat{q}^{(1)T} \\ \hat{q}^{(1)T} &= -\hat{q}^{(1)L}, \quad t = 0 \\ \hat{v}^{(1)T} = D \hat{v}^{(1)T} &= \eta^{(1)T} = 0, \quad y = 0, \quad y = y_\infty, \end{aligned} \quad (24)$$

where we have assumed zero initial conditions, $\hat{q}_0 = 0$. Equations (22) and (24) provide a complete description of the harmonic forced linear problem; the solution of Eq. (24) is obtained as described in a later section.

With regard to the second order solution, the structure of the quadratic interaction term implies that several frequency components are excited at second order. As for the first order problem we can split the governing equations into two parts that describe the long time and the transient behavior. With regard to the former, we point out that at first order the asymptotic solution in time is characterized by given frequencies $\pm\omega$, which implies that only the zero and 2ω frequency components are excited at second order. However, as demonstrated by Trefethen *et al.* (1993), the maximum response of a system occurs for $\alpha = 0$ and $\omega = 0$; hence we reduce our analysis to the most effective part, that is the one associated to zero frequency and zero streamwise wavenumber

$$-\hat{L} \hat{q}_0^{(2)L} = \hat{T}_0^L \quad (25)$$

with solution given by

$$\hat{q}_0^{(2)L} = (-\hat{L})^{-1} \hat{T}_0^L \quad (26)$$

Here the terms \hat{T}_0^L represent the convolution sum in (16) where only the contribution with zero frequency is considered. Observe that this procedure can also be applied to the solution corresponding to the continuous spectrum modes. Indeed, if a first order solution is represented as a continuous spectrum mode, it is still characterized by a given frequency that corresponds to the real part of the associated eigenvalue.

The equations that describe the transient behavior at second order accounts for different forcing terms that arise from the self interactions between first order transient solutions and the quadratic interactions between the transient solution and the long time solutions.

2.2. Scaling of forced solution

It is possible to show a Reynolds number dependence for the norm of the resolvent of the forced problems defined by Eqs. (23) and (26). Let us introduce a new set of variables to rescale the Orr-Sommerfeld, Squire problem as Gustavsson (1991), Reddy & Henningson (1993) and Kreiss *et al.* (1994)

$$t^* = t/Re, \quad i\omega^* = i\omega Re, \quad \hat{v}^* = \hat{v}/\beta Re, \quad \hat{\eta}^* = \hat{\eta}; \quad (27)$$

with the new scaling we can rewrite (14) as

$$\begin{aligned}\mathcal{L}_{OS}^* &= i\alpha Re u^{(0)}(D^2 - k^2) - i\alpha Re D^2 u^{(0)} - (D^2 - k^2)^2 \\ \mathcal{C}^* &= -iDu^{(0)} \\ \mathcal{L}_{SQ}^* &= -i\alpha Re u^{(0)} + (D^2 - k^2).\end{aligned}\tag{28}$$

The scaled equations exhibit a dependency only on the two parameters, αRe and k^2 , rather than α , β , Re as in the original Orr-Sommerfeld, Squire equations. In the new variables the resolvent can be written as

$$\|(i\omega\hat{M} - \hat{L})^{-1}\|_E = Re\|(i\omega^*\hat{M} - \hat{L}^*)^{-1}\|_{E^*}\tag{29}$$

where E is the energy norm with respect to the original variables and E^* is the energy norm with respect to the scaled ones. It is possible to show, see Kreiss *et al.* (1994), that for $\alpha Re = 0$ (that corresponds to the maximum response of the system) the norm of the resolvent $\|(i\omega^*\hat{M} - \hat{L}^*)^{-1}\|_{E^*}$ scales as the Reynolds number as $Re \rightarrow \infty$. Hence, Eq. (29) implies that the norm of the original resolvent $\|(i\omega\hat{M} - \hat{L})^{-1}\|_E$ scales as the square of the Reynolds number.

Further, it is possible to show (see e.g. Kreiss *et al.* 1994) that if we consider Reynolds number independent forcing the amplitude of the response in the original unscaled problem is given at leading order, $O(Re^2)$, by the wall normal vorticity η . In fact, for streamwise independent modes the norm of the resolvent of the individual Orr-Sommerfeld and Squire operators is $O(Re)$. The factor Re^2 is then due to the response of the Squire operator forced by the $O(Re)$ wall normal velocity v , via the coupling term of the system. This implies that the induced streamwise vorticity, given by the solution of the Orr-Sommerfeld equation, is $O(Re)$, while the streamwise velocity, obtained from the Squire equation, is $O(Re^2)$.

2.3. The initial value problem

In accounting for the transient solution it is worth making some observations. Since the eigenfunctions of the eigenvalue problem associated to the Orr-Sommerfeld, Squire system form a complete set, see DiPrima (1969) and Salwen & Grosch (1981), we can expand the perturbation solution $\hat{q}^{(i)T}$ ($i = 1, 2$) as a superposition of modes. For Blasius boundary layer flow, the domain is semi-bounded and the spectrum has a continuous and a discrete part, see Grosch & Salwen (1978). These authors have shown that in this case the solution can be expanded in a sum over the discrete modes and in an integration over the continuous spectrum. This analysis can be simplified using a discrete representation of the continuous spectrum by cutting the upper unbounded domain at a given y_∞ . Although the eigenvalues differ from the exact representation of the continuous spectrum, particularly as the decay rate increases (see Fig. 2), their sum has been found to describe correctly the solution to the initial value problem, see Butler & Farrel (1992). Observe that formally, it is possible to expand the solution using integrals over the continuous spectrum.

However, the added computational complexity, without any significant gain in accuracy, justifies the use of the present simpler formulation.

With regard to the selection of a set of functions that are orthogonal to the set of Orr-Sommerfeld, Squire eigenfunctions, we exploit the orthogonality relation between the eigenfunctions of the Orr-Sommerfeld, Squire system (\tilde{q}) and those of the adjoint Orr-Sommerfeld, Squire problem (\tilde{q}^+). From the definition of adjoint, it is easy to show that the eigenvalues of the adjoint are the complex conjugate to the eigenvalue of the Orr-Sommerfeld, Squire system. This leads to the orthogonality condition

$$(\hat{M} \tilde{q}_j, \tilde{q}_k^+) = C \delta_{jk} \quad (30)$$

where δ_{jk} is the Kronecker symbol and C a constant that normalizes the eigenfunctions and that needs to be determined. Hence, for the initial value problem, we can exploit the completeness of the Orr-Sommerfeld, Squire eigenmodes for bounded flows to recover $\hat{q}^{(i)T}$

$$\begin{pmatrix} \hat{v}^{(i)T} \\ \hat{\eta}^{(i)T} \end{pmatrix} = \sum_l K_l \begin{pmatrix} \tilde{v}_l \\ \tilde{\eta}_l^P \end{pmatrix} e^{-i\lambda_l^{OS} t} + \sum_j B_j \begin{pmatrix} 0 \\ \tilde{\eta}_j \end{pmatrix} e^{-i\lambda_j^{SQ} t} \quad (31)$$

where $(\lambda_l^{OS}, \tilde{v}_l)$ and $(\lambda_j^{SQ}, \tilde{\eta}_j)$, respectively, are the eigenvalues and eigenvectors of the non-normal \mathcal{L}_{OS} operator, and the homogeneous \mathcal{L}_{SQ} operator and $\tilde{\eta}_l^P$ is the solution of the Squire problem forced by the Orr-Sommerfeld eigenfunctions. The coefficient K_l and B_j are determined from a given initial condition $(\hat{v}_0, \hat{\eta}_0)$ according to (30)

$$K_l = \frac{1}{2k^2} \int_0^{y_\infty} \begin{pmatrix} \tilde{\xi}_l \\ 0 \end{pmatrix}^H \begin{pmatrix} k^2 - D^2 & 0 \\ 0 & 1 \end{pmatrix} \begin{pmatrix} \hat{v}_0 \\ \hat{\eta}_0 \end{pmatrix} dy \quad (32)$$

$$B_j = \frac{1}{2k^2} \int_0^{y_\infty} \begin{pmatrix} \tilde{\xi}_j^P \\ \tilde{\zeta}_j \end{pmatrix}^H \begin{pmatrix} k^2 - D^2 & 0 \\ 0 & 1 \end{pmatrix} \begin{pmatrix} \hat{v}_0 \\ \hat{\eta}_0 \end{pmatrix} dy \quad (33)$$

where

$$\begin{pmatrix} \tilde{\xi} \\ 0 \end{pmatrix}, \quad \begin{pmatrix} \tilde{\xi}^P \\ \tilde{\zeta} \end{pmatrix}. \quad (34)$$

are the modes of the adjoint system, see Schmid & Henningson (2001).

2.4. Continuous spectrum modes

The Orr-Sommerfeld eigenvalue problem in a semi-bounded domain is characterized by a continuous and a discrete spectrum. The discrete modes decay exponentially with the distance from the wall, while the modes of the continuous spectrum are nearly sinusoidal, whereby the free-stream disturbances can

be expanded as a superposition of continuous modes. Since they are associated to stable eigenvalues, they are not relevant for the classical linear stability analysis; however they are fundamental for the understanding of the interaction between free-stream vortical eddies and the boundary layer. In order to determine the eigenfunctions of the continuous spectrum we consider first the Orr-Sommerfeld equations for a small three-dimensional disturbance with no-slip boundary conditions at the wall $\tilde{v}(0) = D\tilde{v}(0) = 0$ and boundedness at $y \rightarrow \infty$. In particular in the free-stream the mean flow is constant (i.e. $u^{(0)} = 1$ as $y/\delta^* > 3$) and the Orr-Sommerfeld equation reduces to

$$(D^2 - k^2)^2 \tilde{v} - i \alpha Re \{(1 - c)(D^2 - k^2)\} \tilde{v} = 0 \quad (35)$$

where c is the phase velocity. The above equation admits the following solution, see Grosch & Salwen (1978),

$$\tilde{v} = A e^{i\gamma y} + B e^{-i\gamma y} + C e^{-ky}, \quad y \rightarrow \infty \quad (36)$$

where

$$k^2 + \gamma^2 + i \alpha Re(1 - c) = 0.$$

From this, an analytical expression for the eigenvalues is derived

$$c = 1 - i \left(1 + \frac{\gamma^2}{k^2}\right) \frac{k^2}{\alpha Re} \quad (37)$$

where γ represents the wave number in the wall-normal direction and assumes any positive real value.

From a numerical point of view the crucial point is to enforce the boundedness of the eigenfunctions at $y \rightarrow \infty$. We follow the method introduced by Jacobs & Durbin (1998) to recover the correct behavior of the solution in the free-stream solving the equation as a two-point boundary value problem using the spectral collocation method based on Chebyshev polynomial.

We need a total of four boundary conditions: the first two are the no slip at the wall. The arbitrary normalization is $\tilde{v}(y_\infty) = 1$, where y_∞ is the maximum value of y in the wall-normal direction. The condition of boundedness as $y \rightarrow \infty$ is converted to a numerical condition at two specific values of y . In fact Eq. (36) implies

$$D^2 \tilde{v} + \gamma^2 \tilde{v} = C(k^2 + \gamma^2)e^{-ky} \quad (38)$$

in the free-stream. The missing boundary condition is derived evaluating relation (38) at two different point in the free-stream y_1, y_2

$$\frac{(D^2 \tilde{v} + \gamma^2 \tilde{v})_{y_1}}{(D^2 \tilde{v} + \gamma^2 \tilde{v})_{y_2}} = e^{k(y_2 - y_1)}. \quad (39)$$

A similar procedure is used to determine the continuous modes of the Squire equation. However in this case the free-stream behavior of the solution is given only by the two complex exponentials. Hence, from a numerical point of view it suffices to enforce the arbitrary normalization condition $\tilde{\eta}(y_\infty) = 1$.

2.5. The numerical method

The temporal eigenvalue systems and the forced problems derived in the preceding sections are solved numerically using a spectral collocation method based on Chebychev polynomials. In particular, we consider the truncated Chebychev expansion

$$\phi(\eta) = \sum_{n=0}^N \bar{\phi}^n T_n(\eta),$$

where

$$T_n(\eta) = \cos(n \arccos(\eta)) \quad (40)$$

is the Chebychev polynomial of degree n defined in the interval $-1 \leq \eta \leq 1$, and the discretization points are the Gauss–Lobatto collocation points,

$$\eta_j = \cos \frac{\pi j}{N}, \quad j = 0, 1, \dots, N,$$

that is, the extrema of the N th-order Chebyshev polynomial T_N plus the endpoints of the interval. The calculations are performed using at least 301 Chebyshev collocation points in y . The wall-normal domain varies in the range $(0, y_\infty)$, with y_∞ well outside the boundary layer (typically $y_\infty = 50$). The Chebyshev interval $-1 \leq \eta \leq 1$ is transformed into the computational domain $0 \leq y \leq y_\infty$ by the use of the mapping

$$y = y_\infty \frac{1 - \eta}{2}. \quad (41)$$

The unknown functions $\hat{q} = \hat{q}(y)$ are then approximated by

$$\hat{q}^N(y) = \sum_{n=0}^N \bar{q}^n T_n(\eta),$$

The Chebyshev coefficients \bar{q}^n , $n = 0, \dots, N$ are determined by requiring the different equations derived from (12),(13) to hold for \hat{q}^N at the collocation points y_j , $j = p, \dots, N - p$, with $p = 2$ for the fourth order Orr–Sommerfeld equation and $p = 1$ for the second order Squire equation. The boundary conditions are enforced by adding the equations

$$\sum_{n=0}^N \bar{q}^n T_n(0) = \sum_{n=0}^N \bar{q}^n T_n(y_\infty) = 0,$$

and the two additional conditions for the Orr–Sommerfeld problem

$$\sum_{n=0}^N \bar{q}^n DT_n(0) = \sum_{n=0}^N \bar{q}^n DT_n(y_\infty) = 0,$$

where DT_n denotes the y -derivative of the n -th Chebyshev polynomial.

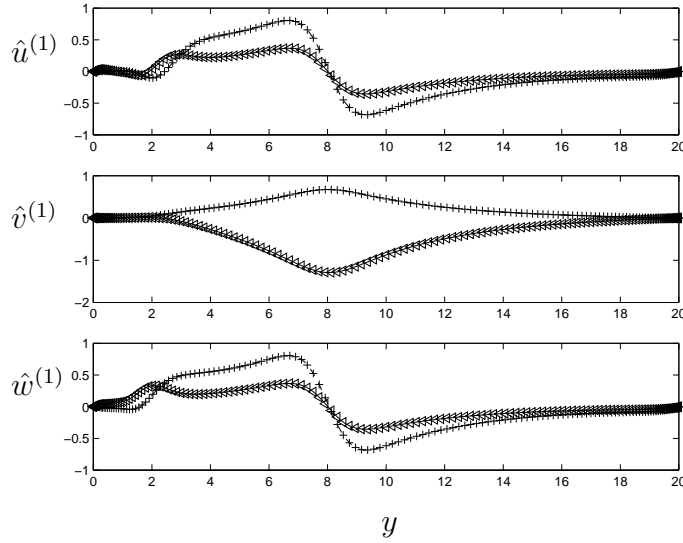


FIGURE 1. Velocity components of the linear perturbation velocity for the oblique wave with $(\alpha, \beta) = (0.2, 0.2)$. Forced problem for $Re = 400$, $y_\infty = 20$, $y_0 = 8$, $\sigma = 0.5$, $\omega = 0.2$ and $t = 100$. DNS result: + real part, < imaginary part. Perturbation model: - - -, real part; —, imaginary part .

3. Receptivity to localized forcing

3.1. Disturbance generation and parameter settings

To validate the model, we test the analytical results versus direct numerical simulations of the type presented by Berlin & Henningson (1999). In order to trigger the formation of streamwise streaks in the boundary layer we consider the response of the system to a couple of oblique waves. This is similar to the investigations reported in Berlin & Henningson (1999), although here we are able to understand the mechanism in more detail since we use an analytical formulation. The oblique waves are generated by an harmonic localized wall-normal volume force given by

$$\underline{F} = f(y) \cos(\alpha x) \cos(\beta z) e^{i\omega t} \quad (42)$$

with

$$f(y) = \frac{1}{\sqrt{2\pi\sigma}} e^{-\frac{(y-y_0)^2}{2\sigma^2}}$$

In our computations we chose $Re = 400$, and $(\alpha, \pm\beta) = (0.2, \pm 0.2)$. We analyze two cases: for the first one the forcing is in the boundary layer ($y_0 = 2.2$), for the second the forcing is in the free-stream ($y_0 = 8$). The results presented here correspond to the latter case with $\sigma = 0.5$.

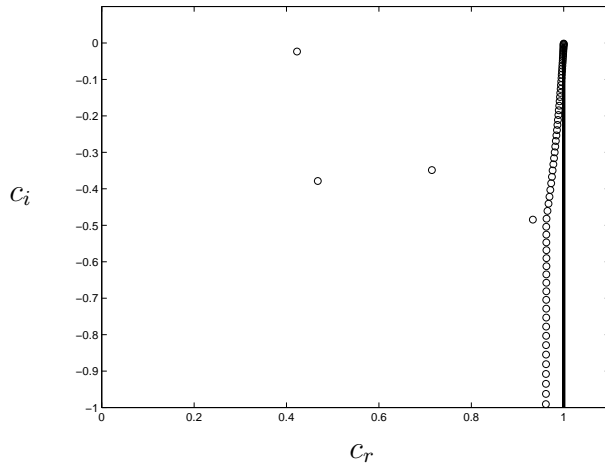


FIGURE 2. Numerically obtained Orr-Sommerfeld spectrum: $N = 301$ Chebychev modes, $Re = 400$, $(\alpha, \beta) = (0.2, 0.2)$ and $y_{max} = 20$. The solid line displays the exact continuous spectrum.

The formation of streamwise streaks in the boundary layer is initiated by two oblique waves characterized by wave numbers $(\alpha, \pm\beta) = (0.2, \pm 0.2)$. In the linear long time response of the system to the external forcing, there is no evidence of streaks generation. However, if one accounts for the second order interactions [in particular those that force the wave number $(0, 2\beta)$] it is easy to observe that the second order correction corresponds to a system of strong streamwise longitudinal vortices in the boundary layer. These results are in agreement with the work of Berlin & Henningson (1999) where the generation of streaks in the boundary layer is triggered by the nonlinear evolution of two oblique waves.

3.2. Comparison to DNS data: linear and nonlinear case

In order to validate the perturbation model and its capability to select the most effective interactions as a second order correction, we compare our results with direct numerical simulations of the forced evolution problem and an initial value problem. The DNS code, reported in Lundbladh *et al.* (1999), is used to solve the temporal problem for a parallel Blasius base flow. For a quantitative comparison we analyze the DNS results in terms of an amplitude expansion, so as to isolate the linear, quadratic and cubic part of the solution, see Henningson *et al.* (1993). We in fact run the same case with three different small amplitude disturbances. Different Fourier modes are then extracted and compared with the results obtained using the perturbation model.

We first consider the velocity field at early times, where the problem is governed by Eq. (24) and the initial value problem is solved as a superposition

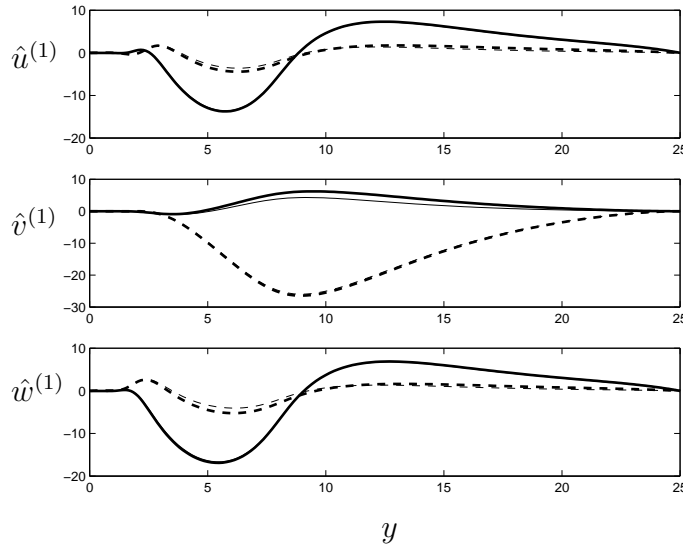


FIGURE 3. Velocity components of the linear perturbation velocity for the oblique wave with $(\alpha, \beta) = (0.2, 0.2)$. Forced problem for $Re = 400$, $y_\infty = 25$, $y_0 = 8$, $\sigma = 0.5$, $\omega = 0.2$ and $t = 50000$. DNS result: - - -, real part; —, imaginary part (thick lines). Perturbation model: - - - real part; —, imaginary part (thin lines).

of the discretized eigenmodes. Comparisons of the three velocity component for the Fourier mode $(\alpha, \beta) = (0.2, 0.2)$ are shown in Fig. 1 at time $t = 100$. The good agreement confirms the validity of the discrete representation of the continuous spectrum. An eigenvalue map for the Orr-Sommerfeld operator, obtained using $N = 301$ Chebychev polynomials, is shown in Fig. 2 together with the exact analytical solution of Eq. (37). The 150 least damped eigenfunctions are taken into account in the expansion presented in Fig. 1. We re-emphasize here that this approximation is able to correctly describe the evolution of disturbances localized in the free-stream.

With regards to the asymptotic time behavior, the numerical simulations are run to time $t = 50000$ and the response is compared with the perturbation results. Figure 3 depicts the velocity components associated to the mode $(\alpha, \beta) = (0.2, 0.2)$. The small differences observed in the figures are probably due to the accumulation of truncation errors in the DNS after such a long time integration. For the same problem, the second order correction with $(0, 2\beta)$ and $\omega = 0$ is displayed in Fig. 4. The formation of streamwise streaks in the longitudinal component is clearly seen. A similar result (not reported) is observed in the case of localized forcing inside the boundary layer ($y_0 = 2.2$, $\sigma = 0.4$). However, in the latter case, the streaks exhibit an amplitude smaller than the previous case (about one-third).

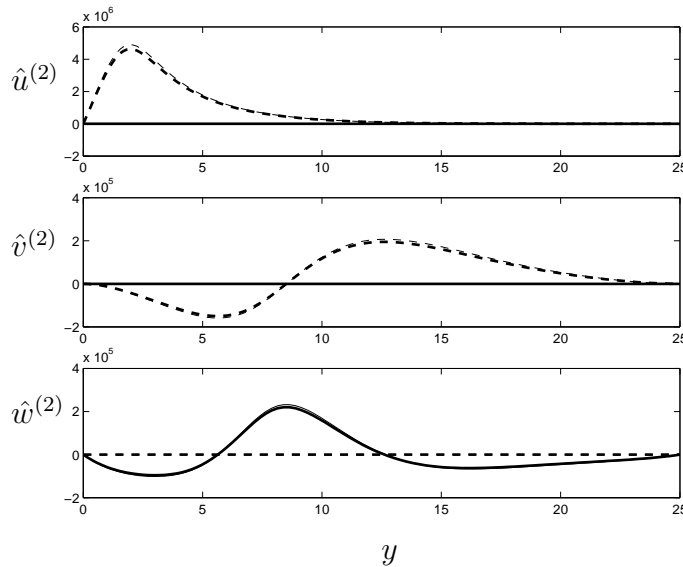


FIGURE 4. Velocity components of the second order perturbation velocity for $(\alpha, \beta) = (0, 0.4)$. Forced problem for $Re = 400$, $y_\infty = 25$, $y_0 = 8$, $\sigma = 0.5$ and $t = 50000$. DNS result: - - -, real part; —, imaginary part (thick lines). Perturbation model: - - -, real part; —, imaginary part (thin lines).

Let us consider the transient part of the solution. The time evolution of the energy of the response of the forced problems corresponding to two different wave numbers $[(0.2, 0.2), (1., 1.)]$ and for the same values of y_0 and σ ($y_0 = 8$, $\sigma = 0.5$) is shown in Fig. 5. The figure shows that the energy of the high wave number disturbances attains its asymptotic value on a scale that is one order of magnitude less than the one associated to the short wave number (both for the first and the second order corrections).

4. Role of Continuous Spectra in the Receptivity Mechanism

4.1. Reynolds number scaling

As shown in section 2.2, it is possible to prove that the resolvent, which governs the solution to the forced Orr-Sommerfeld, Squire system, is $O(Re^2)$. For the second problem we address, the forcing is given by nonlinear interactions between continuous spectrum modes, and we analyze the forced solution at different values of the Reynolds number. In Fig. 6 we compare the continuous spectrum modes of the Orr-Sommerfeld operator for $\alpha = 1$, $\beta = 0.2$ and $\gamma = 0.628$ at two different Reynolds numbers ($Re = 300$ and $Re = 500$). We observe that the modes differ only at the edge of the boundary layer and these

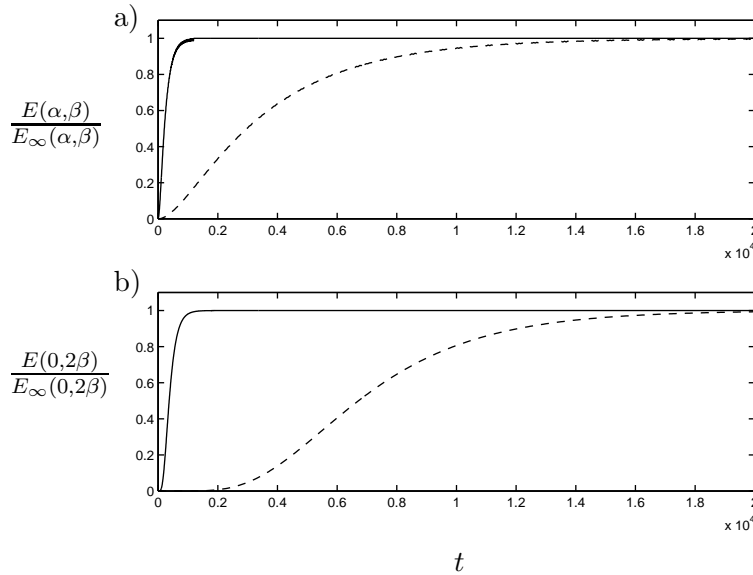


FIGURE 5. Time evolution of the energy normalized with respect to its asymptotic value. a) first order correction; b), second order correction; —, $(\alpha, \beta) = (1, 1)$; - - -, $(\alpha, \beta) = (0.2, 0.2)$.

differences are small. Hence, we assume that the forcing term is Re independent. This assumption is confirmed for large Reynolds number by the findings of Jacobs & Durbin (1998), who have shown that the penetration depth of the modes is proportional to $(\alpha Re)^{-0.13}$ which implies that for large values of Re this depth becomes smaller and smaller.

In Fig. 7 we report the plot of the maximum of the streamwise second order velocity (normalized by the first order energy and by the square of Re) as a function of the streamwise and spanwise wave numbers for a given value of γ , note that the second order distribution is displayed with reference to the (α, β) values of the corresponding first order terms. The figure clearly confirms the scaling in the energy norm found in section 2.2. The results show that the maximum amplitude is obtained for $\alpha \approx 2$ and $\beta \approx 0.15$. Further computations (not reported) verify the validity of the scaling down to $Re \approx 100$. However, for lower values of the Reynolds number the maximum response is obtained for values of β less than the one associated to $Re > 100$. Thus, it suffices to investigate the forced results only at one Reynolds number, since they can be subsequently scaled to arbitrary $Re > 100$.

4.2. Nonlinear interaction and linear forcing

In a previous work it has been demonstrated that nonlinearities play a fundamental role in boundary layer receptivity, see Berlin & Henningson (1999).

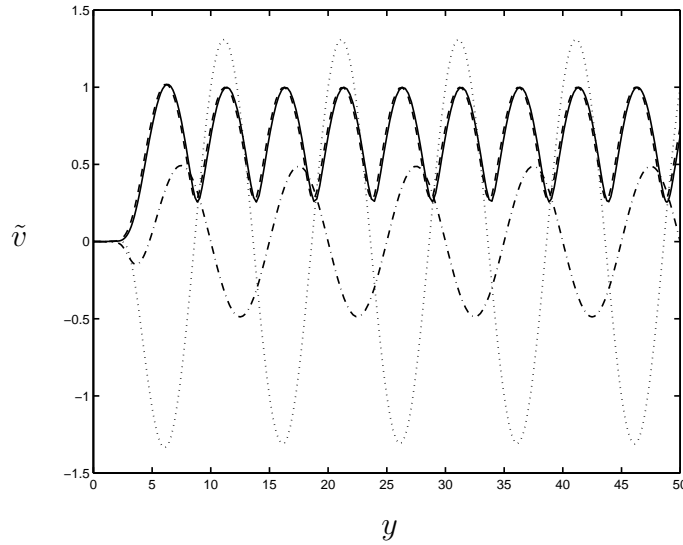


FIGURE 6. Distribution of the Orr-Sommerfeld eigenfunction $vs y$ for $\alpha = 1$, $\beta = 0.2$: —, $\|\tilde{v}\|$ for $Re = 500$; - - -, $\|\tilde{v}\|$ for $Re = 300$; \cdots , $Re(\tilde{v})$ for $Re = 300$; $\cdot - \cdot$, $Im(\tilde{v})$ for $Re = 300$.

In the present work we use a model based on a perturbation expansion in the amplitude of the disturbance truncated at second order to single out the mechanisms at work during the generation of streamwise streaks in flat plate boundary layers subject to free-stream turbulence.

Since it is possible to rather well represent free-stream turbulence as a superposition of modes associated to the continuous spectrum, see for example Jacobs & Durbin (2000), we simplify the problem analyzing the weakly nonlinear response of the system to a single pair of oblique continuous spectrum modes.

First we analyze the problem associated to the Orr-Sommerfeld continuous spectrum modes. The first order solution corresponds to two eigenmodes of the continuous spectrum with wave numbers (α, β, γ) and $(\alpha, -\beta, \gamma)$ whose damping rate is set to zero. At second order we account for the quadratic interactions between the two continuous spectrum modes and we focus our attention on the $(0, 2\beta)$ contribution. The transient part of the solution is neglected and the asymptotic time response is analyzed. We observe that the second order forcing to the $(0, 2\beta)$ modes induces strong streamwise vorticity, that in turn forces the formation of streaks inside the boundary layer by the linear lift-up mechanism. This two-step process, first the nonlinear generation of streamwise vortices and then the linear forcing of the streamwise streaks, is completely captured by the weakly nonlinear model. Figure 8 shows that the nonlinear forcing of the Orr-Sommerfeld, Squire system $[T_0^L]$, shown in Fig. 8(a)]

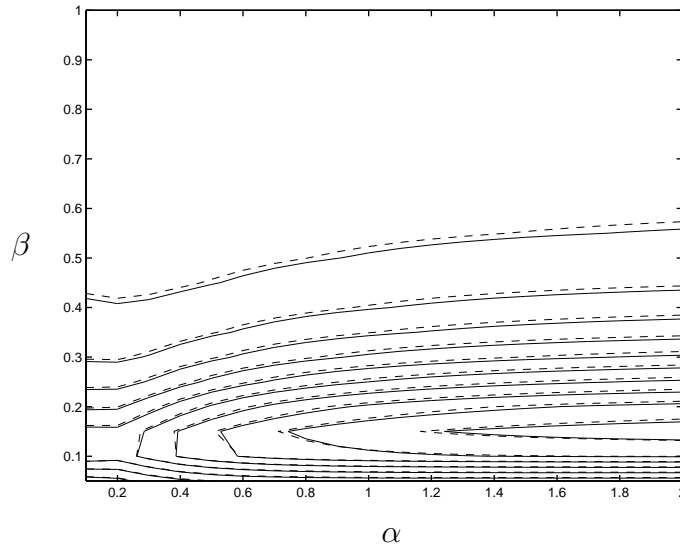


FIGURE 7. Forcing induced by Orr-Sommerfeld continuous spectrum modes for $\gamma = 0.27$. Contour levels of the maximum of the streamwise second order velocity (normalized by the first order energy and Re^2). Note that the second order distribution is displayed with reference to the (α, β) values of the corresponding first order terms. Maximum value 0.1056, contour spacing 0.011.

induces second order spanwise and normal to wall velocities [see Fig. 8(b)]. As a consequence, streamwise vorticity is produced which then creates streamwise streaks [see Fig. 8(c)] through the forcing of the Squire equation due to the coupling term [which is approximately ten times larger than the corresponding second order forcing, compare Figs. 8(a) and (d)]. Further, Fig. 8(b) shows that the second order correction in $\hat{v}^{(2)}, \hat{w}^{(2)}$ is $O(Re)$ ($|\hat{v}^{(2)}|, |\hat{w}^{(2)}| \approx 600$), while Fig. 8(c) that the streamwise velocity is $O(Re^2)$ ($|\hat{u}^{(2)}| \approx 17000$), confirming the scaling property of the resolvent of the Orr-Sommerfeld and Squire problems discussed at the end of section 2.2.

The same analysis has been carried out also considering the second order forcing induced by Squire continuous spectrum modes. The results show that the same physical mechanism is induced and the amplitude of the generated streaks is comparable for the two different classes of modes.

4.3. Parametric study

In order to find the most effective interactions between continuous spectrum modes we carried out a parametric study varying the wave numbers in the range $0.1 < \alpha < 2$, $0.05 < \beta < 1$ and $0.25 < \gamma < 20.9$ at a given Reynolds number.

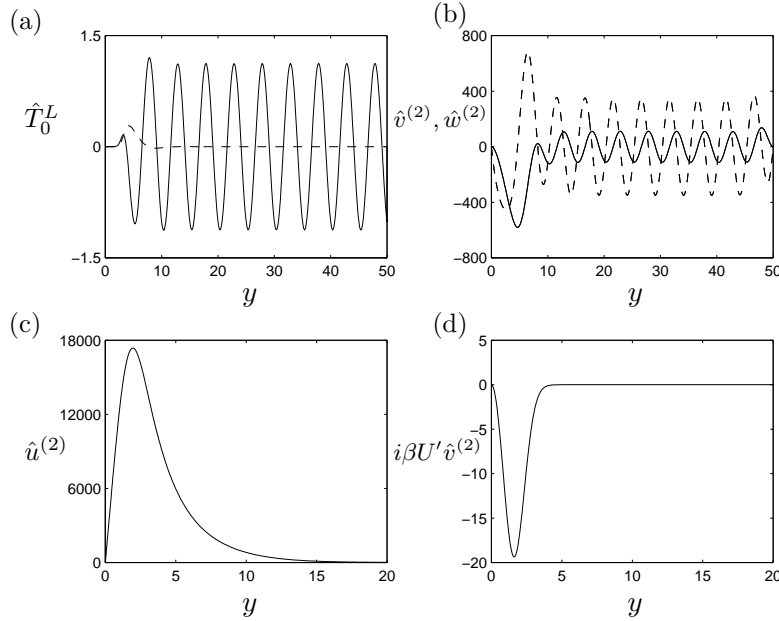


FIGURE 8. Second order solution corresponding to the nonlinear interactions of a couple of oblique Orr-Sommerfeld modes associated to the wave numbers $(0.5, \pm 0.2, 0.628)$, at $Re = 500$: (a) forcing to the Orr-Sommerfeld equation (—) and to the Squire equation (- - -); (b) normal to wall (—) and spanwise component of velocity (- - -); (c) streamwise component of velocity ; (d) forcing to the Squire equation associated to the coupling term $-i\beta U' v^{(2)}$.

In Figs. 9 and 10 we report, respectively, the results corresponding to forcing induced by Orr-Sommerfeld and Squire continuous spectrum modes. The figures depict the maximum amplifications of the streamwise velocity component normalized with respect to the energy density E of the nonlinearly interacting modes. In particular, we plot

$$A(\alpha, \beta) = \max_{\gamma} \frac{u^{(2)}(\alpha, \beta, \gamma)}{E},$$

$$B(\alpha, \gamma) = \max_{\beta} \frac{u^{(2)}(\alpha, \beta, \gamma)}{E},$$

$$C(\beta, \gamma) = \max_{\alpha} \frac{u^{(2)}(\alpha, \beta, \gamma)}{E}.$$

The results show that the maximum amplification is attained for $\alpha \approx 2$ and $\beta \approx 0.15$ (thus implying that the streaks are associated to spanwise wave number $\beta \approx 0.3$) independently of the type of forcing modes. The results also indicate that the maximum response is associated to low values of γ ($\gamma \approx 0.25$),

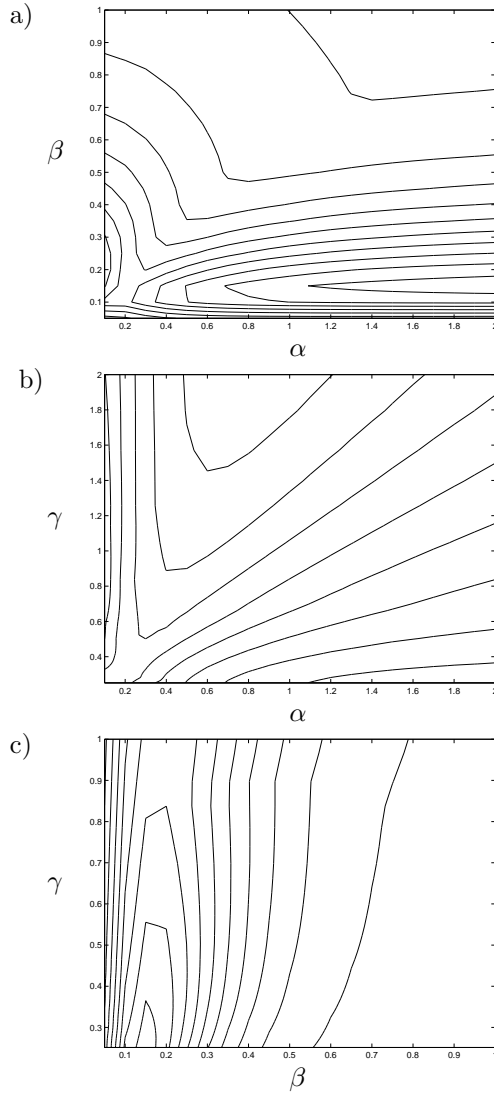


FIGURE 9. Boundary layer response to forcing induced by nonlinear interactions of Orr-Sommerfeld modes. Contour levels of the maximum amplification of the streamwise component of velocity at $Re = 300$, $y_\infty = 50$: a) $A(\alpha, \beta)$ for $0.25 < \gamma < 20.9$; b) $B(\alpha, \gamma)$ for $0.05 < \beta < 1$; c) $C(\beta, \gamma)$ for $0.1 < \alpha < 2$. The maximum is 10145 and occurs at $\alpha = 2.$, $\beta = 0.15$, $\gamma = 0.25$. Maximum contour level is 9500 and contour spacing 1000.

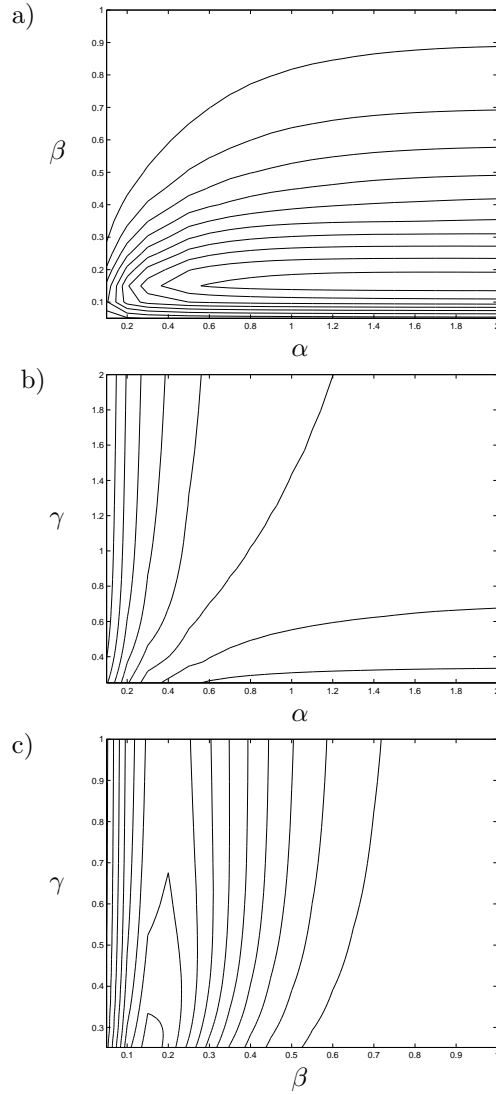


FIGURE 10. Boundary layer response to forcing induced by nonlinear interactions of Squire modes. Contour levels of the maximum amplification of the streamwise component of velocity at $Re = 300$, $y_\infty = 50$: a) $A(\alpha, \beta)$ for $0.25 < \gamma < 20.9$; b) $B(\alpha, \gamma)$ for $0.05 < \beta < 1$; c) $C(\beta, \gamma)$ for $0.1 < \alpha < 2$. The maximum is 10586 and occurs at $\alpha = 2.$, $\beta = 0.15$, $\gamma = 0.25$. Maximum contour level is 10000 and contour spacing 1000.

i.e. structures of large wall normal extent. We observe that in the case the

forcing is given by the Orr–Sommerfeld modes we find a lower maximum for $\alpha \approx 0.1$, $\beta \approx 0.2$ and $\gamma \approx 1.25$.

One should also note that these figures tend to bias high wave numbers, since they are in practice more damped than low ones. Recall in fact that for simplicity we have put the damping rate of the continuous spectrum modes to zero. This implies, for example, that the increasing amplification for higher values of α in Figs. 9 a), b) and 10 a), b) would be damped for sufficiently high values of the streamwise wavenumber. However this does not present a problem in applying the results to a real free-stream turbulence case since realistic free-stream turbulence spectra have little energy content in these higher wave numbers. This will be discussed in the next section.

4.4. Filtering with turbulent energy spectrum and streak spacing

In the results presented so far we assumed unit energy in each Fourier component of the free-stream disturbance. In order to predict which length scales may be important in a real transition initiated by free-stream turbulence, we associate each mode with a coefficient proportional to the energy spectrum of typical homogeneous and isotropic turbulence. We use here the von Kármán spectrum, which is proportional to κ^4 for large scales and matches the Kolmogorov-(5/3)-law for small scales. It has the form

$$\tilde{E}^{3D}(\alpha, \beta, \gamma) = \frac{E^{3D}(\kappa_{3D})}{4\pi\kappa_{3D}^2} = \frac{2}{3} \frac{1}{4\pi\kappa_{3D}^2} \frac{1.606(\kappa_{3D}L)^4}{(1.35 + (\kappa_{3D}L)^2)^{17/6}} Lq \quad (43)$$

where $\kappa_{3D} = \alpha^2 + \beta^2 + \gamma^2$, L is an integral length scale and q is the total turbulent kinetic energy, defined as the integral over all κ 's of the spectrum. It is possible to show that the integral length scale $L_{11} \approx 0.65L$ and that the length scale of the eddies with the maximum energy is $L_{max} \approx 3.5L$. We note that this spectrum, given in Tennekes & Lumley (1972) is a good approximation to homogeneous turbulence. The filtered results are reported in Figs. 11 and 12 for $L = 3$, $q = 1$; the figures show that the filtering moves the more effective α 's and γ 's to smaller values, while the β 's are less affected. The maximum amplification is attained for $\alpha \approx 0.3$, $\beta \approx 0.1$ for the case the forcing is given by the Orr-Sommerfeld modes and $\alpha \approx 0.3$, $\beta \approx 0.15$ for the Squire case; the corresponding values of γ is 0.25 independently of the type of the forcing modes. We note also that in the case the forcing is given by the Orr-Sommerfeld modes, a lower local maximum is still present at $\alpha \approx 0.1$, $\beta \approx 0.15$ and $\gamma \approx 0.33$. Similar results were obtained for different choices of the integral length scale L .

One of the objectives of the present work is to find the wave numbers associated to free-stream disturbances which are most effective in the generations of streamwise vortices. Matsubara & Alfredsson (2001) in their experimental work observed that the spanwise distance to the first minimum of two point velocity correlations, which closely corresponds to half the streak spacing, stays almost constant in the downstream direction. This suggests that the boundary

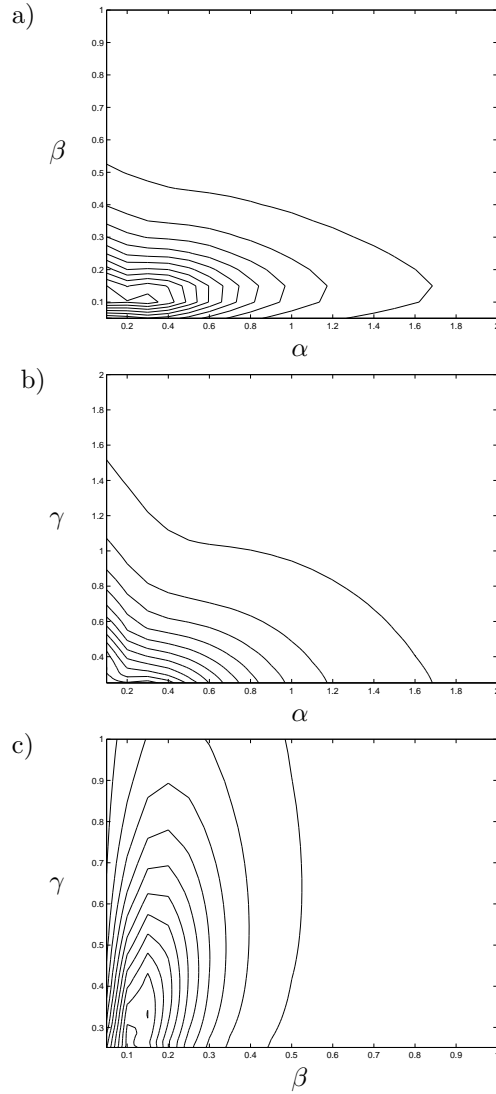


FIGURE 11. Boundary layer response to forcing induced by nonlinear interactions of Orr-Sommerfeld modes filtered by turbulent kinetic energy spectrum. Contour levels of the maximum amplification of the streamwise component of velocity at $Re = 300$, $y_\infty = 50$: a) $A(\alpha, \beta)$ for $0.25 < \gamma < 20.9$; b) $B(\alpha, \gamma)$ for $0.05 < \beta < 1$; c) $C(\beta, \gamma)$ for $0.1 < \alpha < 2$. The maximum is 1106 and occurs at $\alpha = 0.3$, $\beta = 0.1$, $\gamma = 0.25$. Maximum contour level is 1050 and contour spacing 100.

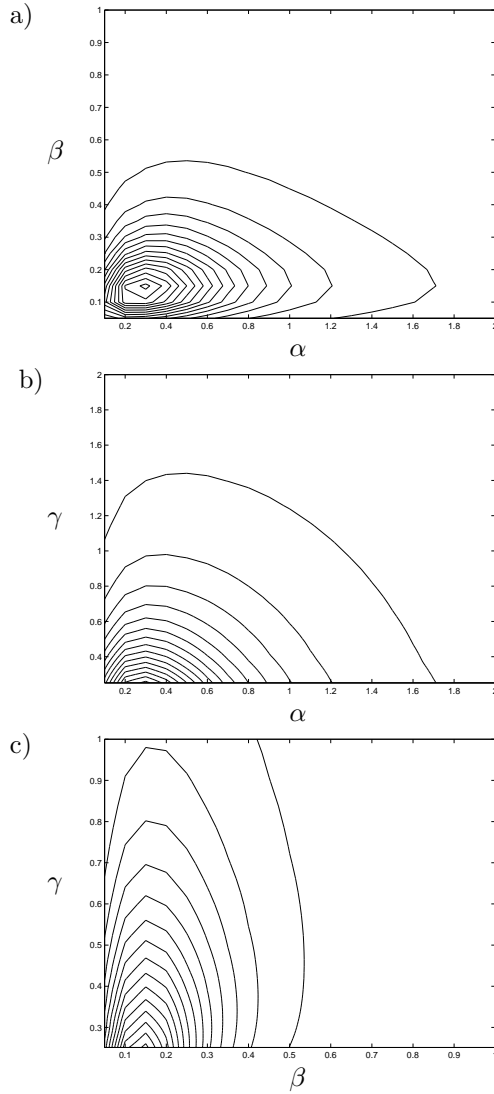


FIGURE 12. Boundary layer response to forcing induced by nonlinear interactions of Squire modes filtered by turbulent kinetic energy spectrum. Contour levels of the maximum amplification of the streamwise component of velocity at $Re = 300$, $y_\infty = 50$: a) $A(\alpha, \beta)$ for $0.25 < \gamma < 20.9$; b) $B(\alpha, \gamma)$ for $0.05 < \beta < 1$; c) $C(\beta, \gamma)$ for $0.1 < \alpha < 2$. The maximum is 1485 and occurs at $\alpha = 0.3$, $\beta = 0.15$, $\gamma = 0.25$. Maximum contour level is 1450 and contour spacing 100.

layer growth does not affect the streak development. When scaling these results with the local displacement thickness the characteristic length scale close to the leading edge is approximately $20\delta^* \pm 10\delta^*$, i.e. centered around a spanwise wavenumber $\beta \approx 0.3$. This is close to the β 's for which our simplified temporal model predicts the largest response. In the experiments of Matsubara & Alfredsson (2001) the growth of the boundary layer implies a variation of the spanwise scale with the respect to the local displacement thickness. In our model, we do not account for the growth of the boundary layer, but we are still able to predict the first step of the receptivity process, i.e. the formation of streamwise vortices.

4.5. Linear vs. Nonlinear Receptivity

A linear mechanism for streak generation caused by the diffusion of a free-stream streamwise vortex into the boundary layer has been studied by Andersson *et al.* (1999) and Luchini (2000), using the boundary layer equations and by Wundrow & Goldstein (2001) by means of asymptotic expansions. These studies assume the presence of the vortex at the leading edge. Bertolotti (1997) used a different method to calculate the initial streamwise vortices but still studied a linear mechanism. Here we propose a nonlinear model for receptivity, originating from oblique modes in the free-stream, with forcing at order ϵ^2 , and in this section we want to discuss the relevance of the proposed mechanism in comparison with the stronger direct forcing at order ϵ presented in the works cited above (Bertolotti 1997; Andersson *et al.* 1999; Luchini 2000; Wundrow & Goldstein 2001).

Our results show that modes in a wide range of wave numbers α, β, γ are almost equally effective in inducing streamwise streaks (see Figs. 9 and 10). On the other hand, for the linear mechanism to work, only streamwise or almost independent modes, with a definite spanwise modulation, can be considered. Therefore in a real case of free-stream turbulence, it is plausible to assume that larger total forcing is involved in the nonlinear process than in the linear one. To quantify, we consider the turbulent kinetic energy spectrum for homogeneous and isotropic turbulence defined by Eq. (43). Frequency spectra of the free-stream turbulence are usually reported from laboratory measurements. By Taylor hypothesis they can be related to one-dimensional spectra for the streamwise wavenumber α . Formally the one-dimensional spectrum E^{1D} is obtained from E^{3D} by

$$E^{1D}(\kappa_{1D}) = \int_{\kappa_{1D}}^{\infty} \frac{E^{3D}}{\kappa_{3D}} \left(1 - \frac{\kappa_{1D}^2}{\kappa_{3D}^2}\right) d\kappa_{3D},$$

see Hinze (1959); it represents the energy in all the Fourier components with wavenumber κ_{1D} , corresponding to α, β or γ (since the turbulence is assumed to be isotropic). The one-dimensional spectrum derived from the expression in

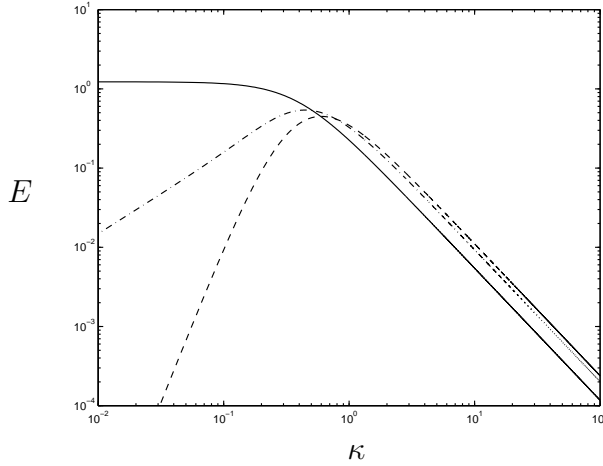


FIGURE 13. Turbulent kinetic energy spectra in homogeneous isotropic turbulence. —, $E^{1D}(\kappa_{1D})$; - · - ·, $E^{2D}(\kappa_{2D})$; - - -, $E^{3D}(\kappa_{3D})$.

Eq.(43) can be written as

$$E^{1D}(\kappa_{1D}) = \frac{18}{55} \frac{1.606}{(1.35 + (\kappa_{1D}L)^2)^{5/6}} Lq.$$

Here instead, we want to look at the energy in each plane wave characterized by wave number (α, β) . A two-dimensional energy spectrum can be defined according to

$$\tilde{E}^{2D}(\alpha, \beta) = \int_{-\infty}^{\infty} \tilde{E}^{3D} d\gamma = \frac{E^{2D}(\kappa_{2D})}{2\pi\kappa_{2D}},$$

with $\kappa_{2D}^2 = \alpha^2 + \beta^2$, which yields in our case

$$E^{2D}(\kappa_{2D}) = 2\pi\kappa_{2D} \frac{1.606L^{1/3} \left(\frac{L^2}{1.35+L^2\kappa_{2D}^2}\right)^{1/3} (4.05 + 11L^2\kappa_{2D}^2) \Gamma(1/3)}{165\sqrt{\pi} (1.35 + L^2\kappa_{2D}^2)^2 \Gamma(5/6)} Lq,$$

where Γ represents the gamma function. The three energy spectra versus the respective wave vector are displayed in Fig. 13 for $L = 3$ and the total energy $q = 1$. We can now estimate the amount of energy involved in the linear, \tilde{E}_L , and in the nonlinear mechanism, \tilde{E}_{NL} . Values of the spanwise wavenumber β of the generated streaks are assumed to be in the range $\beta \in [\beta_0, \beta_1]$. In the linear scenario, only the contribution from waves with low values of α is considered, such that

$$\tilde{E}_L = 4 \int_0^{\alpha_0} d\alpha \int_{\beta_0}^{\beta_1} \tilde{E}^{2D} d\beta$$

where α and β assume only positive values and the factor 4 in front of the integral is justified by the symmetry of the function \tilde{E}^{2D} . In the nonlinear case

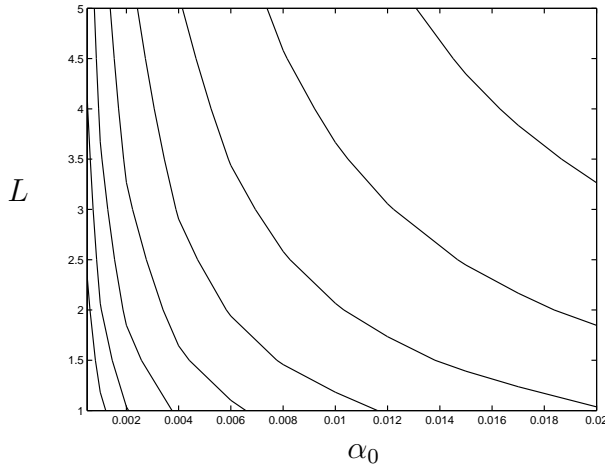


FIGURE 14. Isocontours of $\log_{10}(\frac{\tilde{E}_{NL}}{E_L})$ as function of L and α_0 . Maximum contour level is 3.5 and contour spacing 0.25. The maximum of $\frac{\tilde{E}_{NL}}{E_L}$ is 7331.21 and occurs at $L = 1$, $\alpha_0 = 0.0005$ (lower left hand corner).

oblique waves are considered: the integral is now evaluated for larger values of α and the corresponding range of β ,

$$\tilde{E}_{NL} = 4 \int_{\alpha_0}^{\alpha_1} d\alpha \int_{\beta_0/2}^{\beta_1} \tilde{E}^{2D} d\beta$$

The ratio between the two energies is then function of the integral length scale L and of the integration limits, $\frac{\tilde{E}_{NL}}{E_L} = \frac{\tilde{E}_{NL}}{E_L}(\alpha_0, \alpha_1, \beta_0, \beta_1, L)$. We can let $\beta_1, \alpha_1 \rightarrow \infty$, since the energy spectrum is decaying for large wave numbers. We also assume for simplicity $\alpha_0 = \beta_0$, such that $\frac{\tilde{E}_{NL}}{E_L} = \frac{\tilde{E}_{NL}}{E_L}(\alpha_0, L)$. Contour levels of $\log_{10}(\frac{\tilde{E}_{NL}}{E_L})$ are displayed in Fig. 14. One can note that the largest value ($\frac{\tilde{E}_{NL}}{E_L} = 7331$) is attained for the lowest values of L and α_0 considered (1 and 0.0005 respectively) and the ratio decreases for increasing values of the parameters. In Kendall's experiments (Bertolotti & Kendall 1997), with a free-stream velocity $U_\infty = 11m/s$, the u_{rms} , representing the streak's profile, was obtained by filtering at values of 4 and 6 Hz. Using Taylor hypothesis, these values can be transformed to non dimensional values of $\alpha_0 \approx 0.001, 0.0015$ for $Re_{\delta^*} = 300$. In this range, the energy in modes responsible for the linear receptivity process is about 500 times lower than the energy involved in the nonlinear process.

We have shown that the nonlinear receptivity mechanism can be seen as a two-step process: first the generation of streamwise vortices and then the formation of streaks via lift-up effect. As seen in Fig. 8(b), a strong, $O(Re)$,

amplification is associated to the generation of streamwise vortices from non-linear interaction of oblique modes. The successive formation of streaks is a linear process, present in both the linear and the nonlinear scenario, induced by streamwise vortices of order ϵ and ϵ^2 respectively. We can then assume that the strong amplification of streamwise vortices can partially compensate the order ϵ difference between the two, yielding streaks of similar amplitudes. Evidence for this can be found considering the results of the direct numerical simulations presented in Berlin & Henningson (1999), where streaks of the same order of magnitude are generated by the linear and the nonlinear mechanism for an initial energy corresponding to a v_{rms} of about 1%.

Numerical evidence of the proposed nonlinear receptivity can be found in the simulations of by-pass transition in a boundary layer subject to free-stream turbulence performed by Jacobs & Durbin (2000). They used modes of the continuous spectrum to represent homogeneous isotropic turbulence at the inflow of the computational domain ($Re_{\delta^*} = 274$). The free-stream turbulent intensity was chosen to correspond with the experiment by Roach & Brierly (1990) and ensemble-averaged numerical data are in good agreement with laboratory measurements. Jacobs & Durbin (2000) have also shown that the lowest frequency in the synthesized inlet spectrum is far higher than the dominant ones in the region of laminar streaks, i.e. zero energy initially in the zero or almost frequency modes, so that a linear receptivity mechanism can be excluded. Frequencies below those introduced at the inlet can only be generated by nonlinear interactions; hence the nonlinear receptivity mechanism is clearly capable of inducing strong streaks. On the other hand, we have to consider also the work of Bertolotti & Kendall (1997) which represents the opposite extreme, i.e. when only low frequency streamwise vortices are introduced in the free-stream. In this case, experiments under controlled conditions provided a validation of the linear model presented in Bertolotti (1997). In actual free-stream turbulence induced transition, both types of disturbances are present and it would depend on the amount of energy in low frequency disturbances whether the linear or the nonlinear mechanism dominates. The two mechanisms could interact and cooperate, with the linear one maybe dominating at the leading edge and the nonlinear forcing more active further downstream. This is still an open question and the object of future investigations.

5. Discussion and conclusion

In the present work we have investigated how free-stream disturbances affect a laminar boundary layer. In particular, we have analyzed the receptivity to oblique waves in the free-stream and to continuous spectrum modes. In both cases, we observe that the formation of streaks is the dominant feature. The underlying mechanism can be reduced to a two-step process, first the generation of streamwise vorticity and then the formation of streaks.

Previous investigators (Bertolotti 1997; Andersson *et al.* 1999; Luchini 2000; Wundrow & Goldstein 2001) have considered the influence of streamwise vortices present in the free-stream and have shown that the subsequent formation of streaks in the boundary layer can be explained in terms of linear theory by the lift-up mechanism. The most important feature of the process we have investigated is that the same streamwise vortices undergoing algebraic growth, are nonlinearly generated starting from wave-like disturbances in the free-stream. As discussed in Section 4.5, linear and nonlinear receptivity mechanisms are both capable of generation of streaks. In the first case, streamwise independent vortices of small amplitude ϵ , already present in the free-stream disturbance, are able to penetrate the boundary layer, mainly close to the leading edge. In the second, the streamwise vorticity is induced at order ϵ^2 by nonlinear interactions of free-stream disturbances also downstream of the leading edge. Which of the two is dominating in a real case, will depend on the energy content in low frequency modes of the free-stream turbulence.

The nonlinear mechanism has already been observed in the numerical experiments of Berlin & Henningson (1999). They isolated the different order interactions to show that the streamwise independent modes are the most excited. Here, we have used a perturbation expansion which has been shown to provide an efficient theoretical tool to isolate the two-step process, see also Ponziani *et al.* (2000). Formally the present model is valid for small amplitudes ϵ of the perturbation. As in all asymptotic expansions, the actual value of the small parameter ϵ that can be used, can only be determined empirically. In this case, considering the works of Berlin & Henningson (1999) and Jacobs & Durbin (2000), it seems that a turbulence level of 3% is small enough for the model to apply. Further, in Ponziani *et al.* (2000), good agreement between DNS and the nonlinear model is obtained for plane Poiseuille flow for a value of $\epsilon = 0.05$. For larger values of free-stream turbulence we expect the nonlinear scenario to become even more important, but it cannot be correctly captured by an amplitude expansion like the one we considered.

The model has been validated by comparisons with DNS data for the case the forcing is given by a couple of oblique waves. In order to apply the model to study the boundary layer receptivity to free-stream turbulence, we have exploited the fact that continuous spectrum modes can be used to represent the free-stream turbulence spectrum (Jacobs & Durbin 2000). This assumption has allowed us to further simplify the study accounting only for the response of the boundary layer to couples of continuous spectrum modes. An extensive parametric study has been carried out to isolate the most effective modes by varying the wave numbers (α , β , γ).

We have concluded that the formation of streaks is due to the second order correction induced by the coupling term in the Orr-Sommerfeld, Squire system and the receptivity is independent of the type of forcing modes. This indicates that disturbances containing normal velocity in the free-stream, are not more likely to force streamwise vorticity in the boundary layer, compared

to disturbances not containing v . On the other hand, Berlin & Henningson (1999) draw the conclusion that the normal velocity in the free-stream is more effective than other components. However, their conclusion was based on a type of disturbance which grew in size in the normal direction as the normal velocity increased. Thus their results are also consistent with the present ones which show that this increase in amplification is rather a result of increase in normal scale (or decrease in γ).

The large eddy simulations of Yang & Voke (1993) also indicated the key influence of the wall normal component of the free-stream turbulence intensity in provoking transition. Their results show in fact that the transition process begins with the production of the Reynolds stresses due to the overlapping of regions of non zero fluctuating velocity v and mean shear $\partial U/\partial y$. From our analysis we find that the components with streamwise wave number approximately zero are the ones crucial in generating disturbances inside the boundary layer, and that can be induced from nonlinear interactions of either Orr-Sommerfeld or Squire modes. The capability of modes with frequency and streamwise wavenumber approximately zero to penetrate the shear layer has been demonstrated by different authors (Hultgren & Gustavsson 1981; Westin *et al.* 1994; Jacobs & Durbin 1998; Matsubara & Alfredsson 2001), and we may thus conclude that v -components active in generating Reynolds stresses are the ones associated with nearly zero frequency and that they are the ones associated with the second order solution in our model.

The results also show that the second order forcing does not depend on the Reynolds number, thus recovering the $O(Re^2)$ scaling of the forced response described by streamwise independent disturbances governed by the Orr-Sommerfeld, Squire system. We may speculate on the implication of this scaling on the Reynolds number dependence of the forced response in the spatial problem. In a number of experiments it has been seen that the growth of the streak amplitude in boundary layers subjected to free-stream turbulence is proportional to Re , or equivalently that the energy growth is proportional to $Re_x \approx Re^2$ or downstream distance. If we assume that the Reynolds number dependence in the spatial case would be the same as in the temporal case investigated here, downstream growth of the streak amplitude predicted would be proportional to Re^2 , i.e. over predicted by a factor of Re . However, the result found here assumes a continuous deterministic forcing. Real turbulence would better be described by a stochastic forcing in a number of wave numbers. Bamieh & Dahleh (1999) have shown that a stochastic forcing reduces the scaling of the maximum response of the temporal problem from Re^2 to $Re^{3/2}$. This is still a factor $Re^{1/2}$ too large. However, the growth in a realistic free-stream turbulence case would probably further be reduced by the fact that free-stream turbulence decays with downstream distance. In our model this would correspond to a forcing which decreases with Re , thus further reducing the growth of the streak amplitude.

Acknowledgments

This research was supported by the Göran Gustavsson Foundation, TFR (Teknikvetenskapliga forskningsrådet), the C.M. Lerici Foundation and the research funding obtained by Prof. R. Piva, University of Rome "La Sapienza".

References

- ANDERSSON, P., BERGGREN, M. & HENNINGSON, D. 1999. Optimal disturbances and bypass transition in boundary layers. *Phys. Fluids*. **11** (1), 134–150.
- BAMIEH, B. & DAHLEH, M. 1999. Disturbance energy amplification in three-dimensional channel flows. In *Proceedings of the 1999 American Control Conference, IEEE, Piscataway, NJ*, pp. 4532–4537.
- BERLIN, S. & HENNINGSON, D.S. 1999. A nonlinear mechanism for receptivity of free-stream disturbances *Phys. Fluids* **11**, (12), 3749–3760.
- BERTOLOTTI, F. P. 1997. Response of the Blasius boundary layer to free-stream vorticity. *Phys. Fluids*. **9** (8), 2286–2299.
- BERTOLOTTI, F. P. & KENDALL, J. M. 1997. Response of the Blasius Boundary Layer to Controlled Free-Stream Vortices of Axial Form. *AIAA Paper Nos. 97-2018*.
- BUTLER, K. M. & FARRELL, B. F. 1992. Three-dimensional optimal perturbations in viscous shear flow. *Phys. Fluids A*. **4**, 1637–1650.
- DIPRIMA, R. C. & HABETLER, G. J. 1969. A completeness theorem for non-selfadjoint eigenvalue problems in hydrodynamic stability. *Arch. Rat. Mech. Anal.* **32**, 218–227.
- GOLDSTEIN, M. E. & HULTGREN, L. S. 1989. Boundary-layer receptivity to long-wave free-stream disturbances. *Ann. Rev. Fluid Mech.* **21**, 137–166.
- GROSCHE, C. E. & SALWEN, H. 1978. The continuous spectrum of the Orr-Sommerfeld equation. Part 1. The spectrum and the eigenfunctions. *J. Fluid Mech.* **87**, 33–54.
- GUSTAVSSON, L. H. 1991. Energy growth of three-dimensional disturbances in plane Poiseuille flow. *J. Fluid Mech.* **224**, 241–260.
- HENNINGSON, D.S., LUNDBLADH, A., JOHANSSON, A.V. 1993. A mechanism for bypass transition from localized disturbances in wall-bounded shear flows *J. Fluid Mech.*, **250**, 169–207.
- HINZE, J. O. Turbulence. *McGraw-Hill Book Company*, 1959.
- HULTGREN, L. S. & GUSTAVSSON, L. H. 1981. Algebraic growth of disturbances in a laminar boundary layer *Phys. Fluids*. **24** (6), 1000–1004.
- JACOBS, R. G. & DURBIN, P. A. 1998. Shear sheltering and continuous spectrum of the Orr-Sommerfeld equation. *Phys. Fluids*. **10** (8), 2006–2011.
- JACOBS, R. G. & DURBIN, P. A. 2000. Bypass transition phenomena studied by computer simulation. Report No. TF-77, Flow Physics and Computation Division, Department of Mechanical Engineering, Stanford University, Stanford, California 2000.
- KENDALL, J. M., 1985. Experimental study of disturbances produced in a pre-transitional laminar boundary layer by weak free-stream turbulence. *AIAA Paper* 85-1695.

- KERSCHEN, E. J. 1990. Boundary layer receptivity theory. *Appl Mech Rev.* **43** (5, Part 2), S152–157.
- KLEBANOFF, P. S. 1971. Effect of free-stream turbulence on the laminar boundary layer. *Bull. Am. Phys. Soc.* **10**, 1323.
- KREISS, G., LUNDBLADH, A., HENNINGSON, D. S. 1994. Bounds for threshold amplitudes in subcritical shear flows. *J. Fluid Mech.* **270**, 175–198.
- LUCHINI, P. 2000. Reynolds number independent instability of the boundary layer over a flat surface: optimal perturbations. *J. Fluid Mech.*, **404**, 289–309.
- LUNDBLADH, A., BERLIN, S., SKOTE, M., HILDINGS, C., CHOI, J., KIM, J., HENNINGSON, D. S. 1999. An efficient Spectral Method for Simulation of Incompressible Flow over a Flat Plate TRITA-MEK, Technical Report 1999.11, Royal Institute of Technology, Stockholm, 1999.
- MATSUBARA, M., ALFREDSSON, P.H. 2001. Disturbance growth in boundary layers subjected to free stream turbulence *J. Fluid Mech.*, (In press).
- PONZIANI, D. 2000. A weakly nonlinear analysis for transition mechanisms in Poiseuille flow *PhD Thesis*, University of Rome, La Sapienza.
- PONZIANI, D., CASCIOLA, C.M., ZIRILLI, F., PIVA, R. 2000. Weakly nonlinear analysis of a localized disturbance in Poiseuille flow *Stud. Appl. Math.*, **105**, 121–142.
- REDDY, S. C. & HENNINGSON, D. S. 1993. Energy growth in viscous channel flows. *J. Fluid Mech.* **252**, 209–238.
- ROACH, P. E. & BRIERLY, D. H. 1990. The influence of a turbulent freestream on zero pressure gradient transitional boundary layer development, Part I: test cases T3A and T3B. *ERCOTAC Workshop: Numerical Simulations of Unsteady Flows and Transition to Turbulence, Lausanne, Switzerland*, pp.319–347. Cambridge University Press.
- SALWEN, H. & GROSCH, C. E. 1981. The continuous spectrum of the Orr-Sommerfeld equation. Part 2. Eigenfunction expansions. *J. Fluid Mech.* **104**, 445–465.
- SCHMID, P. J. & HENNINGSON, D.S. 2001. *Stability and Transition in Shear Flows*. Springer.
- TENNEKES, H. & LUMLEY, J. L. 1972. *A first course in turbulence*. The MIT press.
- TREFETHEN, L. N., TREFETHEN, A. E., REDDY, S. C. & DRISCOLL, T. A. 1993. Hydrodynamic stability without eigenvalues. *Science*. **261**, 578–584.
- TUMIN, A. & RESHOKTO, E. 2001. Spatial theory of optimal disturbances in boundary layers. *Phys. Fluids*. **13** (7), 2097–2104.
- WESTIN, K. J. A., BOIKO, A. V., KLINGMANN, B. G. B., KOZLOV, V. V. & ALFREDSSON, P. H. 1994. Experiments in a boundary layer subject to free-stream turbulence. Part I: Boundary layer structure and receptivity. *J. Fluid Mech.* **281**, 193–218.
- WUNDROW, D. W. & GOLDSTEIN, M. E. 2001. Effect on a laminar boundary layer of small-amplitude streamwise vorticity in the upstream flow. *J. Fluid Mech.* **426**, 229–262.
- YANG, Z. Y. & VOKE, P. R. 1993. Large eddy simulation of transition under turbulence. *Technical report ME-FD/93.12*, University of Surrey, Dept. Mech. Eng.

Paper 7

Boundary-layer transition under free-stream turbulence

By **Luca Brandt[†]**, **Philipp Schlatter^{*}** and **Dan S. Henningson^{†‡}**

[†]Department of Mechanics, Royal Institute of Technology (KTH)
S-100 44 Stockholm, Sweden

^{*}Institute of Fluid Dynamics, Swiss Federal Institute of Technology (ETH),
CH-8092 Zürich, Switzerland

[‡]FOI, The Swedish Defense Research Agency,
Aeronautics Division, SE-17290 Stockholm, Sweden

The effect of high levels of free-stream turbulence on the transition in a Blasius boundary layer is studied by means of direct numerical simulations, where a synthetic turbulent inflow is obtained as superposition of modes of the continuous spectrum of the Orr-Sommerfeld and Squire operators. In the present bypass scenario the flow in the boundary layer develops streamwise elongated regions of high and low streamwise velocity and it is suggested that the breakdown into turbulent spots is related to local instabilities of the strong shear layers associated with these streaks. Flow structures typical of the spot precursors are presented and these show important similarities with the flow structures observed in previous studies on the secondary instability and breakdown of steady symmetric streaks.

Numerical experiments are performed by varying the energy spectrum of the incoming perturbation. It is shown that the transition location moves to lower Reynolds numbers by increasing the integral length scale of the free-stream turbulence. The receptivity to free-stream turbulence is also analysed and it is found that two distinct physical mechanisms are active depending on the energy content of the external disturbance. If low-frequency modes diffuse into the boundary layer, presumably at the leading edge, the streaks are induced by streamwise vorticity through the linear lift-up effect. If, conversely, the free-stream perturbations are mainly located above the boundary layer a nonlinear process is needed to create streamwise vortices inside the shear layer. The relevance of the two mechanisms is discussed.

1. Introduction

1.1. *Aim of the present work*

In boundary layers with free-stream turbulence intensities of 1% or more transition occurs rapidly, bypassing the classical scenario triggered by the viscous, thus slower, exponential amplification of unstable waves (the Tollmien-Schlichting waves). The former scenario, denoted bypass transition, is characterised by the appearance inside the boundary layer of streamwise elongated streaky structures of alternating high and low streamwise velocity. As the streaks grow downstream, they undergo wavy motions which precede the breakdown into regions of intense randomised flow, turbulent spots. The spots grow in size and merge until the flow is fully turbulent.

The overall picture of the transition scenario has been elucidated by flow visualisations and velocity measurements in previous experimental studies (see the review articles by Kendall 1998; Matsubara & Alfredsson 2001; Saric *et al.* 2002). However, some important points still remain unclear: These concern mainly the receptivity stage, during which perturbations enter the boundary layer, and the mechanisms of the breakdown into turbulent spots occurring on isolated streaks. To answer these questions, we present here extensive numerical simulations of transition in a Blasius boundary layer subjected to free-stream turbulence, where the turbulent inflow is generated by the superposition of modes of the continuous spectrum of the Orr-Sommerfeld and Squire operators. The simulation of a fully transitional boundary layer is a formidable task also for the modern supercomputers and therefore one cannot hope to reproduce as rich parametric studies as in experimental works. However, it is possible to correctly reproduce the main features of the transition scenario under consideration (see Jacobs & Durbin 2001) and, as a consequence, simulations can be designed to investigate specific problems, thus exploiting the advantages of a numerical study. This enabled us to identify the relevant flow structures at the breakdown, which is not possible in an experiment due to the random nature of the spot appearance. Moreover, the numerical methodology used allows to determine and manipulate the energy content of the turbulent inflow. In this way, it has been possible to investigate the receptivity mechanism and the effect of the characteristic length scale of the free-stream turbulence.

1.2. *Previous experimental and numerical work*

The occurrence of streamwise elongated structures in boundary layers subjected to free-stream turbulence was first identified by Klebanoff (1971) in terms of low-frequency oscillations in hot-wire signals caused by the slow spanwise motions of the streaks, although the first experimental results on boundary-layer disturbances under free-stream turbulence date back to Dryden (1937) and Taylor (1939). Arnal & Juillen (1978) also showed that for free-stream turbulence levels higher than 0.5–1%, the dominant disturbances inside the boundary layer are characterised by low frequencies and they are not TS-waves. Kendall (1985) observed streamwise elongated structures of narrow spanwise scales with

the maximum of the streamwise velocity fluctuations located in the middle of the boundary layer. He denoted these disturbances as Klebanoff modes.

The detailed measurements of a zero-pressure-gradient boundary layer subject to free-stream turbulence by Westin *et al.* (1994) confirmed that the amplitude of the streamwise velocity perturbation increases as the square root of the distance from the leading edge. Further, these authors compiled data from different studies and observed that different experiments with apparently similar conditions can disagree on the onset and extent of transition. In fact, a number of different parameters affect the receptivity of the boundary layer; not only the free-stream turbulence intensity, but also its spatial scales, energy spectrum and degree of isotropy and homogeneity play an important role. A complete description of disturbance growth in boundary layers disturbed by free-stream turbulence can be found in the paper by Matsubara & Alfredsson (2001), where several years of experiments performed at the Royal Institute of Technology, in Stockholm are reviewed. In the above, it is concluded that the initial growth of the streaks can be successfully explained by theories of non-modal or transient growth. These authors also show that close to the leading edge the spanwise scale of the streaks is large as compared to the boundary-layer thickness, the value which is approached further downstream, and that the streak length grows as the boundary layer thickness (see also Lundell & Alfredsson 2003).

The first direct numerical simulation (DNS) of transition in a boundary layer subjected to free-stream turbulence was attempted by Rai & Moin (1993). In that case the computational inlet was located upstream of a sharp leading edge, which imposed heavy computational requirements. Probably due to these limitations, the values of the skin-friction coefficient was found to be sensitive to grid resolution, reaching values well above those typical of turbulent boundary layers. Yang & Voke (1995) performed large-eddy simulations of a boundary layer under free-stream turbulence and indicated the key influence of the wall-normal component of the outside perturbation in provoking transition. Their results show in fact that the transition process begins with the production of the Reynolds stresses due to overlapping regions of nonzero wall-normal perturbation velocity and the mean shear of the basic flow. Wu *et al.* (1999) presented DNS of boundary layer transition beneath periodic passing wakes. In this case long streaks are precluded by the finite width of the wake; however, the breakdown into turbulent spots is still associated to low-speed regions ('backward jets') located in the upper part of the boundary layer.

Direct numerical simulations of a boundary layer disturbed by free-stream turbulence were performed by Jacobs & Durbin (2001). Implementing the methodology first proposed by Grosch & Salwen (1978), these authors constructed a turbulent inflow by expanding the free-stream turbulence as a sum of spanwise and temporal Fourier modes, times wall-normal Orr-Sommerfeld modes. The latter consisted of modes of the continuous spectrum, which can

be considered a natural basis for free-stream turbulence since they have a sinusoidal behaviour far above the boundary layer and vanish inside. Such an inflow is applied a short distance downstream of the leading edge. This methodology proved to be numerically feasible and effective since it allowed to start the computations with a finite-thickness boundary layer in a rectangular domain delimited by a wall and to avoid to compute the flow around the leading edge or the evolution of grid generated turbulence. The results obtained are in good agreement with the laboratory measurements by Roach & Brierly (1990). Jacobs & Durbin (2001) show that streaks are formed by penetration of low-frequency modes from the free-stream. The perturbation spectrum evolves from the synthetic inflow into a different spectrum dominated by low frequencies through nonlinear effects. These authors also observed that spot precursors are localised instabilities of single low-speed streaks and suggest that the breakdown of these structures is forced by the interaction between streaks and small scales in the free stream.

1.3. *Non-modal disturbance growth and receptivity*

From a theoretical point of view, a disturbance growth mechanism alternative to Tollmien-Schlichting waves is required to explain transition observed in flows at Reynolds numbers well below the critical ones from linear stability theory, as well as the different features of the structures observed. However, examining the Reynolds-Orr equation (Drazin & Reid 1981), ruling the evolution of the kinetic energy of the perturbation, a strong statement can be made on the nonlinear effects, which allows to consider simpler linear models: the nonlinear terms redistribute energy among different frequencies and scales but have no net effect on the instantaneous growth rate of the energy. This implies that there exists a linear mechanism for the energy of a disturbance of any amplitude to increase.

Ellingsen & Palm (1975) proposed a growth mechanism, considering the linear inviscid evolution of an initial disturbance independent of the streamwise coordinate in a shear layer. These authors showed that the streamwise velocity component may grow linearly in time, producing alternating low- and high-velocity streaks. Moffat also identified such a streak growth mechanism in a model of turbulent uniform shear flow (see the review article by Phillips 1969). Later Hultgren & Gustavsson (1981) considered the temporal evolution of a three-dimensional disturbance in a boundary layer and found that in a viscous flow the initial growth is followed by a viscous decay (transient growth).

Landahl (1975, 1980) studied the linear evolution of localised disturbances and formalised a physical explanation for the streak growth mechanism, which we denote the lift-up effect. Since a fluid particle in a streamwise vortex will initially retain its horizontal momentum if displaced in the wall-normal direction, such a disturbance in the wall-normal velocity will cause in a shear layer a perturbation in the streamwise velocity. It is observed that weak pairs of quasi streamwise counter rotating vortices are able to lift up fluid with low

velocity from the wall and bring high-speed fluid towards the wall, and so they are the most effective in forcing streamwise oriented streaks of high and low streamwise velocity.

It is now understood that since the linearised Navier-Stokes operator is non-normal for many flow cases, a significant transient growth may occur before the subsequent exponential behaviour (Butler & Farrell 1992; Reddy & Henningson 1993; Schmid & Henningson 2001). The class of perturbations which sustain maximum temporal growth in the linear regime takes the form of spanwise periodic streamwise vortices. Such optimal perturbations give rise to a spanwise periodic distribution of low and high-speed streaks. This growth is observed also for sub-critical values of the Reynolds number and it is the underlying mechanism triggering bypass transition phenomena. The non-normality of the governing operators is due to the coupling between the equation for the wall-normal velocity and that for the wall-normal vorticity of the perturbation, which is proportional to the streamwise velocity for streamwise independent disturbances. The latter equation is, in fact, forced by a term due to the interaction between the spanwise variation of the wall-normal velocity perturbation and the mean shear of the base flow. This is associated to the vortex-tilting phenomenon, by which normal vorticity is created by tilting the spanwise vorticity of the basic flow (see Henningson *et al.* 1993).

To answer the question of which disturbance present at the leading edge gives the largest perturbation in the boundary layer at a certain downstream position, Andersson *et al.* (1999) and Luchini (2000) have used an optimisation technique adapted from optimal-control theory. The disturbances they found were also streamwise vortices that cause the growth of streaks. These studies show that the energy growth of these optimal perturbations is proportional to the distance to the leading edge x , or alternatively that the streamwise disturbance velocity increases as the square root of x in agreement with the experimental results. Also in remarkable agreement with the experimental findings is the wall-normal shape of the streamwise velocity fluctuations, which is characterised by a maximum in the middle of the boundary layer at $y = 1.3\delta^*$, where δ^* is the local boundary-layer displacement thickness (see Matsubara & Alfredsson 2001). In the theoretical works just mentioned, the spanwise wavenumber β of the disturbance with largest growth at a given streamwise station is found to be $\beta = 0.77/\delta^*$, which corresponds to a spanwise scale approximately 40% larger than the local boundary layer thickness; a value slightly larger than that obtained by hot-wire signal correlations. Andersson *et al.* (1999) proposed also a transition prediction criterion which assumes that the Reynolds number at transition onset is inversely proportional to the square of the free-stream turbulence intensity. Although such criterion is only based on the fact that the linear growth of optimal perturbations is proportional to the square root of the local Reynolds number and it does not consider any of the nonlinear processes occurring at the late stages of the breakdown, it is able

to satisfactorily correlate data from several studies (see also Matsubara *et al.* 1999).

Wundrow & Goldstein (2001) and Goldstein & Wundrow (1998) used asymptotic expansions to study the effect of free-stream streamwise vorticity on a laminar boundary layer. Their analysis indicates that the transverse velocity components induce Klebanoff modes inside the boundary layer through a linear mechanism. These authors also show how perturbations of the upstream flow of broadband nature ultimately lead to strong shear layers in certain localised spanwise regions. These highly-inflectional shear layers can then support rapidly growing inviscid instabilities. The theoretical studies discussed so far assumed the presence of perturbations inside the boundary layer or entering it at the leading edge. Bertolotti (1997), instead, assumed as initial disturbances vortical modes in the free-stream and studied the boundary layer receptivity in a linear region excluding the leading edge. He has found receptivity to modes with zero streamwise wavenumber in good agreement with experiments. Berlin & Henningson (1999) have proposed a nonlinear receptivity mechanism by showing how oblique modes in the free stream above the boundary layer can nonlinearly interact to induce strong streaks inside the boundary layer. This nonlinear process has been further investigated in Brandt, Henningson & Ponziani (2002). The relevance of the linear receptivity scenario, assuming the presence of streamwise vortices at the leading edge, and of the nonlinear mechanism is investigated here and it will be the object of one of the sections of this article.

1.4. *Streak breakdown*

The observation that some streaks develop a streamwise waviness of relatively short wavelength has led to the hypothesis that breakdown to turbulence is caused by a secondary instability developing on the streaks (see Matsubara & Alfredsson 2001). It is known, in fact, that streaky basic flows can undergo exponential inflectional instabilities. The experiments of Swearingen & Blackwelder (1987) were the first to document the emergence of streaks with inflectional profiles due to the formation of Görtler vortices in the boundary layer over a concave wall. This investigation demonstrated that time-dependent fluctuations appear in the flow either in a spanwise symmetric (varicose) or antisymmetric (sinuous) pattern with respect to the underlying streak. The varicose perturbations are more closely related with the wall-normal inflection points while the sinuous oscillations are related with the spanwise inflectional profile and they were found to be the fastest growing. The secondary linear instability of Görtler vortices was first analysed theoretically by Hall & Horseman (1991). Park & Huerre (1995) studied the secondary instability of temporally-evolving nonlinear Görtler vortices and confirmed that the dominant sinuous mode is primarily induced by the spanwise shear while the varicose mode is triggered by the wall-normal shear. The corresponding analysis of the secondary

instability of streamwise-developing Görtler vortices was performed by Botaro & Klingmann (1996). The instability of streaks arising from the transient growth of streamwise vortices in channel flows has been studied theoretically by Waleffe (1995, 1997) and Reddy *et al.* (1998) and experimentally by Elofsson *et al.* (1999). These studies confirmed that the instability is of inflectional type and that the dominating instability appears as spanwise (sinuous) oscillations of the streaks.

Andersson *et al.* (2001) performed numerical simulations of a zero-pressure-gradient boundary layer to follow the downstream nonlinear saturation of the linear optimal perturbations obtained in Andersson *et al.* (1999). Inviscid secondary instability calculations using Floquet theory were carried out on the basic flows obtained and it was found that the streak critical amplitude, beyond which streamwise travelling waves are excited, is about 26% of the free-stream velocity. The sinuous instability mode (either the fundamental or the subharmonic, depending on the streak amplitude) represents the most dangerous disturbance. Varicose waves are more stable, and are characterised by a critical amplitude of about 37%. Brandt & Henningson (2002) studied the full transition process resulting from the sinuous secondary instability, also through direct numerical simulations. The main structures observed at the late stages of this transition scenario are found to consist of elongated quasi-streamwise vortices located on the flanks of the low-speed streaks, with vortices of alternating sign overlapping in the streamwise direction in a staggered pattern.

The widespread occurrence of streaks in various flow configurations has very recently led Asai *et al.* (2002) to examine experimentally the spatial response of a single low-speed streak in a laminar boundary layer submitted to a time-harmonic excitation of sinuous or varicose type. The growth of the sinuous mode was observed to evolve into a train of quasi-streamwise vortices with vorticity of alternate sign. By contrast, the varicose mode led to the formation of hairpin structures made up of a pair of counter-rotating vortices. To study the regeneration mechanisms and fundamental structures in a turbulent boundary layer Acarlar & Smith (1987) generated a low-speed streak in an otherwise laminar boundary layer by blowing through a slot in the wall. The streak became unstable and horseshoe vortices were formed. In the simulations by Skote *et al.* (2002) the Acarlar & Smith (1987) experiment was numerically reproduced and the process of horseshoe vortex generation further investigated. These authors show that the appearance of an unstable wall-normal velocity profile is a precursor to the appearance of horseshoe vortices, thus associated to varicose instability of streaks.

The paper is organised as follows. In section 2 the numerical method and the turbulent inflow generation procedure are introduced. The results are presented in section 3. First, the focus will be on time averaged data with particular interest on the effect of the integral scale of the outside turbulence. The boundary layer receptivity is then studied by manipulating the turbulent

inflow and by varying the free-stream turbulence intensity and the relevant receptivity mechanisms are discussed. In the last part of section 3, the turbulent spot generation is considered. Several spots are traced back in time to the location of their formation so that the relevant flow structures at the breakdown are presented. The paper ends with a summary of the main conclusions.

2. Numerical method

2.1. Numerical scheme

The simulation code (see Lundbladh *et al.* 1999) employed for the present computations uses spectral methods to solve the three-dimensional, time dependent, incompressible Navier–Stokes equations over a flat plate. Throughout the paper the streamwise, wall-normal and spanwise direction are denoted respectively by x , y and z and the corresponding velocity components by (u, v, w) . The algorithm uses Fourier representation in the streamwise and spanwise directions and Chebyshev polynomials in the wall-normal direction, together with a pseudo-spectral treatment of the nonlinear terms. The time advancement used is a four-step low-storage third-order Runge–Kutta method for the nonlinear terms and a second-order Crank–Nicolson method for the linear terms. Aliasing errors from the evaluation of the nonlinear terms are removed by the $\frac{3}{2}$ -rule when the FFTs are calculated in the wall parallel plane. In the wall-normal direction it has been found more convenient to increase resolution rather than using dealiasing.

To correctly account for the downstream boundary layer growth a spatial technique is necessary. This requirement is combined with the periodic boundary condition in the streamwise direction by the implementation of a “fringe region”, similar to that described by Bertolotti, Herbert & Spalart (1992). In this region, at the downstream end of the computational box, the function $\lambda(x)$ in equation (1) is smoothly raised from zero and the flow is forced to a desired solution \mathbf{v} in the following manner,

$$\frac{\partial \mathbf{u}}{\partial t} = NS(\mathbf{u}) + \lambda(x)(\mathbf{v} - \mathbf{u}) + \mathbf{g}, \quad (1)$$

$$\nabla \cdot \mathbf{u} = 0, \quad (2)$$

where \mathbf{u} is the solution vector and $NS(\mathbf{u})$ the right hand side of the (unforced) momentum equations. Both \mathbf{g} , which is a disturbance forcing, and \mathbf{v} may depend on the three spatial coordinates and time. The forcing vector \mathbf{v} is smoothly changed from the laminar boundary layer profile at the beginning of the fringe region to the prescribed inflow velocity vector. This is normally a boundary layer profile, but can also contain a disturbance.

2.2. Free-stream turbulence generation

The methodology adopted to induce free-stream turbulence at the inlet of the computational domain is similar to that used by Jacobs & Durbin (2001). The turbulent inflow is in fact described as a superposition of modes of the

continuous spectrum of the linearised Orr-Sommerfeld and Squire operators. These modes have been added to the forcing vector \mathbf{v} and thus introduced in the fringe region of the numerical code, as described above.

Isotropic grid turbulence can be reproduced by a sum of Fourier modes with random amplitudes (see Rogallo 1981); however in the presence of an inhomogeneous direction an alternative complete basis is required; in particular, in the present case, the new basis functions need to accommodate the wall. As pointed out in Grosch & Salwen (1978), a natural choice for the new basis is the use of the modes of the continuous spectrum. These authors showed, in fact, that the Orr-Sommerfeld and Squire eigenvalue problem for a parallel flow in a semi-bounded domain is characterised by a continuous and a discrete spectrum. The discrete modes decay exponentially with the distance from the wall, while modes of the continuous spectrum are sinusoidal in the free stream. As a consequence, by using the second type of modes, a three-dimensional wave-vector $\kappa = (\alpha, \gamma, \beta)$ can be associated to each eigenfunction of the continuous spectrum. Invoking Taylor's hypothesis, the streamwise wavenumber α is replaced by a frequency $\omega = \alpha U_\infty$ in the definition of κ and the expansion is written

$$\mathbf{u} = \sum A_N \hat{\mathbf{u}}_N(y) e^{(i\beta z + i\Re\{\alpha(\omega, \gamma, \beta)\}x - i\omega t)}, \quad (3)$$

where the spanwise wavenumber β and ω assume real values and α is a complex eigenvalue of the Orr-Sommerfeld and Squire system for a free stream (see Grosch & Salwen 1978). The streamwise wavenumber α is used in the expression above since the artificial turbulence is forced for the whole length of the fringe region. The desired wall-normal wavenumber γ enters through the eigenfunction shape $\hat{\mathbf{u}}_N(y)$ and it is defined by the specific eigenvalue α picked along the continuous spectrum so that the latter can be computed only if ω , γ and β are known. The modes of the continuous spectrum are all decaying in the streamwise direction ($\Im\{\alpha\} < 0$), with modes of largest γ being the most damped. As a consequence, to avoid forcing very large perturbation velocities at the upstream end of the fringe region we decided to consider only the real part of the eigenvalue.

In order to obtain isotropic turbulence, several wave numbers κ have to be selected in the domain $\kappa_l < \kappa < \kappa_u$, where the limiting wave numbers are determined by the chosen numerical resolution. We divide the wavenumber space (ω, γ, β) into a set of concentric spherical shells (20 in the simulations presented here). Several points are then selected on the surface of each shell and the eigenfunctions of corresponding wave numbers are included in the summation with an appropriate scaling. From a geometrical point of view, points regularly located on a sphere are defined by the vertices of a regular polyhedron. In particular, a dodecahedron (20 vertices) is considered here. To further increase the degree of isotropy and homogeneity a random three dimensional rotation is applied to the dodecahedron. By choosing an eigenfunction with wall-normal wavenumber γ , the $-\gamma$ is automatically included in the solution, and a second dodecahedron, symmetric with respect to the ω - β plane, is also

considered on each shell. In this way, of the 40 points (terms in the sum) defined on each shell, only the 10 points characterised by positive values of ω and γ need to be considered to construct a real-valued superposition.

Once the wave numbers of the eigenmodes included in the expression (3) have been obtained, the values of ω and β are directly known, while the eigenvalue α is computed from the wavenumber γ (see Grosch & Salwen 1978; Jacobs & Durbin 2001). Care has been taken to avoid $\gamma = 0$, which does not correspond to any physical eigenvalue. The numerical method used to compute the eigenfunction of the homogeneous Orr-Sommerfeld and Squire operators follows the procedure described in Jacobs & Durbin (1998) and has been employed in Brandt *et al.* (2002). Thus, for a given wave-vector both an Orr-Sommerfeld and Squire mode are calculated and the corresponding velocity components derived. An arbitrary phase shift is applied to both solutions before adding them into a velocity vector $\hat{\mathbf{u}}_N(y)$ normalised to unit energy. Note that since the individual eigenfunctions comply with continuity, their summation provides a disturbance which satisfies continuity as well. However, a numerical problem arises at the top of the computational domain. The high levels of free-stream perturbation at the top boundary limits the time step and can lead to numerical instabilities. Therefore the inflow perturbation is damped above a certain distance y_{dm} by multiplying the eigenfunctions with a smooth step function S . The following form for S , which has the advantage of having continuous derivatives of all orders, is used

$$S(y^*) = \begin{cases} 0 & y^* \leq 0 \\ 1/[1 + \exp(\frac{1}{y^*-1} + \frac{1}{y^*})] & 0 < y^* < 1 \\ 1 & y^* \geq 1 \end{cases} \quad (4)$$

where

$$y^* = 1 - \frac{y - y_{dm}}{y_{max} - y_{dm}}$$

and y_{max} indicates the coordinate of the top boundary. The distance $y_{max} - y_{dm}$ is chosen to be $20 \delta_0^*$, where δ_0^* is the boundary layer thickness at the inflow of the computational domain.

The coefficients A_N used in the sum (3) provide a random phase but the amplitude is defined so as to approximate a typical homogeneous- and isotropic-turbulence spectrum. In particular, the von Kármán spectrum is used

$$E(\kappa) \propto \frac{\kappa^4}{(C + \kappa^2)^{17/6}}. \quad (5)$$

Such a spectrum is for large scales asymptotically proportional to κ^4 , whereas it matches the Kolmogorov-(5/3)-law for small scales. Following the construction of a three-dimensional spectrum in Tennekes & Lumley (1972), an integral length scale L of the turbulence is introduced according to

$$L = \frac{1.8}{\kappa_{max}},$$

	$x_l \times y_l \times z_l$ δ_0^*	$n_x \times n_y \times n_z$ (resolution)	$Re_{\delta_0^*}$
Box1	$1000 \times 100 \times 90$	$1152 \times 201 \times 192$	300
Box2	$1000 \times 60 \times 50$	$1024 \times 121 \times 72$	300
Box3	$1000 \times 60 \times 50$	$1024 \times 121 \times 128$	300
Box4	$450 \times 100 \times 90$	$512 \times 201 \times 160$	300

TABLE 1. Resolution and box dimensions for the simulations presented. The box dimensions includes the fringe region and are made dimensionless with respect to δ_0^* , the displacement thickness at the beginning of the computational box. The length of the fringe region is 90 for all cases under consideration. The total number of Fourier modes is indicated, corresponding to $n_x/2$ or $n_z/2$ conjugate pairs.

where κ_{max} is the wavenumber of maximum energy. Denoting by q the total turbulent kinetic energy the following expression for the energy spectrum can be derived from equation (5)

$$E(\kappa) = \frac{2}{3} \frac{a (\kappa L)^4}{(b + (\kappa L)^2)^{17/6}} L q, \quad (6)$$

where $a = 1.606$ and $b = 1.350$. The length scale L_{11} defined from the longitudinal two-point correlation is related to L according to

$$L_{11} = \int_0^\infty \frac{\overline{u(x)u(x+r)}}{\overline{u^2}} dr = \frac{3\pi}{4q} \int_0^\infty \frac{E(\kappa)}{\kappa} d\kappa \approx 0.643 L. \quad (7)$$

The energy is equally distributed among all modes on the same shell and therefore the coefficient of each of the terms in equation (3) is given by

$$A_N^2(\kappa) = E(\kappa) \frac{\Delta\kappa}{n_i},$$

where $E(\kappa)$ is given in equation (6), $\Delta\kappa$ is the difference in wavenumber between two contiguous shells and n_i is the number of modes on each shell. For further details on the free-stream turbulence generation the reader is referred to Schlatter (2001).

2.3. Parameter settings

The box sizes and resolutions used for the simulations presented in this paper are displayed in table 1. The dimensions are reported in units of δ_0^* which denotes the Blasius boundary layer displacement thickness at the beginning of the computational box which is set to $Re_{\delta_0^*} = 300$ for all cases under consideration. (Note that we will denote by δ^* the local displacement thickness as computed from its definition). In all simulations performed, the length of the fringe region is chosen to be 90. The parameters used to define the free-stream turbulence and the corresponding computational domain for the cases

	Free-stream Turbulence Intensity %	Integral Length Scale L/δ_0^*	Computational Domain
Case1	4.7	5	Box1
Case2	4.7	2.5	Box1
Case3	4.7	7.5	Box1
Case4	4.7	5	Box2
Case5	4.7	5	Box3
Case6	3	7.5	Box4
Case7	1.5	7.5	Box4
Case3 α	4.7	7.5	Box4
Case6 α	3	7.5	Box4
Case7 α	1.5	7.5	Box4

TABLE 2. Parameters used to define the free-stream turbulence and the corresponding computational domain for the cases presented. In all cases under considerations 800 modes of the continuous spectrum of the Orr-Sommerfeld and Squire operators are employed. For the cases denoted by α the free-stream turbulence generation is manipulated in order to involve many modes with very low values of the streamwise wavenumber α .

presented are reported in table 2: In all cases under considerations 800 modes of the continuous spectrum of the Orr-Sommerfeld and Squire operators are employed.

Box1 is used for the averaged results in section 3.1 in which the effect of the free-stream turbulence length scales is also analysed. The analysis of the generation of the turbulent spots is performed with the results from the simulations with Box1 and, for the most of them, with the smaller Box2. The simulation labelled as Case5, using Box3, is used to check the resolution of the structures observed at the breakdown stage obtained with Box2. This proved to be more than satisfactorily. Box4 is employed for the simulations presented in section 3.2. The focus of the section is on the initial phase of the transition process, i.e. the boundary-layer receptivity to free-stream turbulence and the streak growth, therefore a shorter computational domain is sufficient. For the cases denoted by α the free-stream turbulence generation is manipulated in order to involve many modes with very low values of the streamwise wavenumber α , as described later.

3. Results

3.1. Averaged results: effect of the integral length scale of the incoming turbulence

The statistics obtained by averaging the velocity field in time and in the spanwise direction are presented in this section. Three cases, corresponding to

Case1, Case2 and Case3 in table 2, are considered. For all of them the free-stream turbulence intensity is 4.7%, whereas different integral length scales of the inflow turbulence have been used, that is $L = 2.5 \delta_0^*$, $L = 5 \delta_0^*$ and $L = 7.5 \delta_0^*$. We show that the present simulations qualitatively reproduce the main features of the transition scenario observed in the experiments of a flat-plate boundary layer subject to upstream grid-generated free-stream turbulence and focus on how the response of the boundary layer varies with the length scales of the incoming turbulence.

3.1.1. Free-stream turbulence

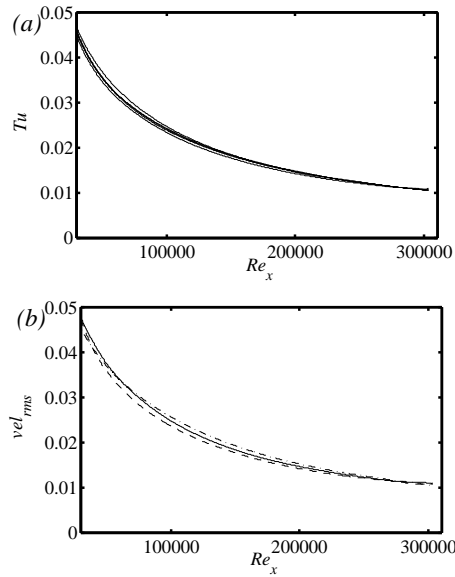


FIGURE 1. (a) Turbulence intensity versus the Reynolds number at 5 different heights above the boundary layer ($y/\delta_0^* = 30, 40, 50, 60, 70$; $L = 5\delta_0^*$). (b) rms values of the three velocity components versus the Reynolds number for $L = 5\delta_0^*$ and $y/\delta_0^* = 40$. —, u_{rms} ; - - -, v_{rms} ; - · -, w_{rms} .

We begin by documenting the free-stream turbulence induced by the methodology presented in the previous section. The objective of the implemented strategy was to force nearly isotropic and homogeneous turbulence in the free stream. In figure 1(a) the turbulence intensity $Tu = (u_{rms} + v_{rms} + w_{rms})/3$ is displayed versus the Reynolds number at 5 positions above the boundary layer to show the degree of homogeneity achieved. The difference in the level of the fluctuations among the velocity components for one selected wall-normal distance is shown in figure 1(b).

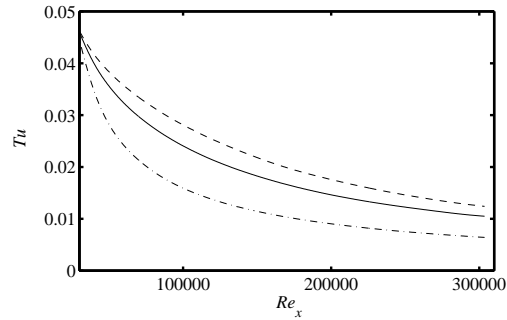


FIGURE 2. Turbulence intensity decay for the free-stream turbulence length scales considered: ---, $L = 7.5\delta_0^*$; —, $L = 5\delta_0^*$; - · -, $L = 2.5\delta_0^*$.

A comparison of the features of the artificial free-stream turbulence in the three cases under consideration is displayed in figure 2 by the downstream decay of the turbulence intensity at a position far above the boundary layer. The data in the figure have been analysed and it is possible to show that the decay obeys a power law in agreement with experimental works on isotropic homogeneous turbulence. As expected, the turbulence decay decreases for increasing length scales.

3.1.2. Effect of the integral length scale on the boundary layer transition

Before presenting the results on the effect of the free-stream turbulence in the boundary layer, it is useful to be reminded of that we are considering a scenario characterised by a high degree of intermittency. In fact, the turbulent spots occur at different positions and times. While they are convected downstream, in a still laminar boundary layer, they grow in size and merge so that only far downstream of their birth position the flow is turbulent along the full span of the considered domain.

The skin friction coefficient provides a good indication of the transition location. This is shown for the three cases considered in figure 3(a); also the values for a laminar and a turbulent boundary layer are displayed for comparison. For the case with the smallest integral length scale transition does not occur within the computational domain, while for the largest values of L a turbulent flow is observed at the end of the domain. The completion of the transition is at lower Re_x for $L = 7.5$ thus confirming the trend observed in the experimental study of Jonáš *et al.* (2000). The transition location in the present simulations is only slightly upstream than that observed in the experiments by Matsubara *et al.* (1999) and Roach & Brierly (1990) (test case T3A) with a lower free-stream turbulence level of 3%. However, the difference is not so surprising: In the experiments the turbulence affects the boundary layer from the leading edge, while in the simulations it is induced a certain distance

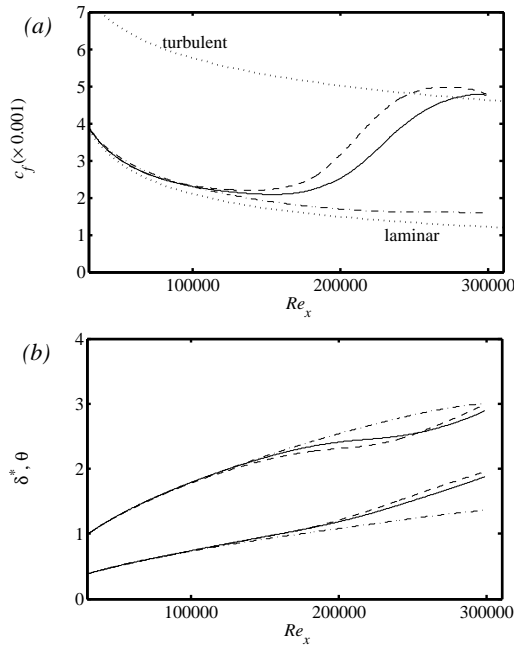


FIGURE 3. (a) Skin friction coefficient and (b) boundary-layer displacement and momentum-loss thickness for the free-stream turbulence length scales considered: - - -, $L = 7.5\delta_0^*$; —, $L = 5\delta_0^*$; - · -, $L = 2.5\delta_0^*$.

downstream. Moreover, the inlet perturbation used for the simulations in the figure has low energy content in its low-frequency components and, as will be discussed in section 3.2, this has a strong influence on the receptivity phase and, as a consequence, on the streak amplitudes. Note also that the lower decay of the free-stream turbulence in the case of Roach & Brierly (1990) lead us to believe that a larger integral length scale characterises the grid-generated turbulence.

Figure 3(b) shows the development of the boundary layer displacement and momentum-loss thicknesses δ^* and θ . The development for a laminar Blasius boundary layer is very close to that for $L = 2.5$, when transition is not observed. In close agreement to the experimental findings of Matsubara & Alfredsson (2001), the displacement thickness is seen to slightly decrease below the laminar values in the transitional region (cf. figure 3a), and then to increase faster in the quasi-turbulent flow. The momentum loss is always larger than in the laminar case owing to the fact that the skin friction increases due to the occurrence of the turbulent spots. A similar peculiar decrease of the boundary layer displacement thickness is observed in the numerical simulations of the

breakdown of a single steady streak subject to sinuous instability by Brandt & Henningson (2002).

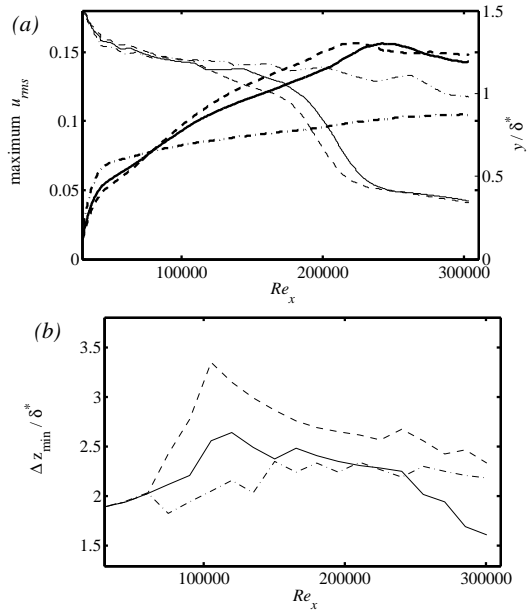


FIGURE 4. (a) maximum u_{rms} (thick lines) and its wall-normal position (thin lines), and (b) first minimum of R_{13} scaled with the local displacement thickness δ^* for the integral length scales: - - -, $L = 7.5\delta_0^*$; —, $L = 5\delta_0^*$; - · -, $L = 2.5\delta_0^*$.

Perturbations enter the boundary layer in the form of low-frequency fluctuations, mainly in the streamwise velocity component, i.e. of streamwise streaks. The maximum u_{rms} at each downstream position is displayed in figure 4(a). In all cases the energy of the streaks (u_{rms}^2) is proportional to the distance from the leading edge, as observed in the experiments (not shown here). The perturbation is initially largest in the case of $L = 2.5\delta_0^*$, indicating that the smallest scales penetrate easier into the boundary layer. However, this growth can not be sustained further downstream as in the other cases. A plausible explanation is that the free-stream turbulence decays faster for smaller L and therefore it is less effective in continuously forcing the streaks along the plate. The necessity of a continuous forcing on the streaks from the free stream was pointed out in Westin *et al.* (1998). Note also that it was shown in Brandt *et al.* (2002) that the large scales induce strongest streaks in the boundary layer but on a longer time. In figure 4(a) the wall normal position of maximum u_{rms} is also shown. The laminar streaks have a maximum at about $y = 1.3\delta^*$, while their turbulent counterparts, at the end of the domain, are located much closer to the wall.

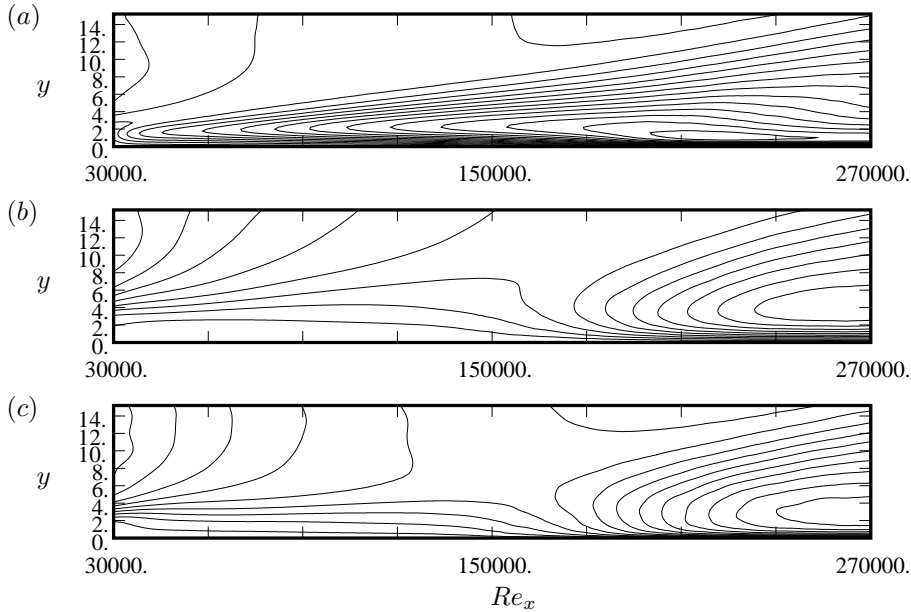


FIGURE 5. Wall-normal distribution of the *rms* values of the three velocity components versus the streamwise position for the simulation with $L = 7.5\delta_0^*$. (a), streamwise component; (b), wall-normal component; (c), spanwise component. The wall-normal coordinate is scaled by the inflow displacement thickness δ_0^* . Contour levels: u min 0.01, max 0.15, spacing 0.01; v min 0.005, max 0.05, spacing 0.005; w min 0.005, max 0.065, spacing 0.005.

In figure 4(b) we display the evolution of the first minimum of the spanwise correlation of the streamwise velocity fluctuations at the wall normal position of maximum u_{rms} ; this is a measure of half the spanwise wavelength of the streaks. It can be seen from the figure that the length scale of the perturbation inside the boundary layer is only slightly dependent on the free-stream turbulence characteristic scale. The spanwise scales observed are in agreement with the experimental results of Matsubara & Alfredsson (2001); the value obtained are lower than those pertaining to the linear optimal perturbation computed by Andersson *et al.* (1999) and Luchini (2000). It is suggested by Matsubara & Alfredsson (2001) that the difference is due to nonlinear effects, relevant for such high streak amplitudes. Note also that in the cases in which transition does occur the streak spacing decreases downstream once scaled with the local displacement thickness, indicating that the streak physical wavelength stays almost constant. On the contrary, in the case with smallest integral length scale L , the streak spacing stays constant once scaled with the local displacement thickness, indicating that the streak wavelength increases downstream.

The wall-normal distribution of the *rms* values of the three velocity components is displayed versus the streamwise position in figure 5 for the simulation with $L = 7.5\delta_0^*$. The cross-stream velocity fluctuations are weak compared to the u_{rms} and a distinct peak inside the boundary layer can be seen only at the streamwise positions where turbulent spots are observed and the streaks are of a more turbulent nature.

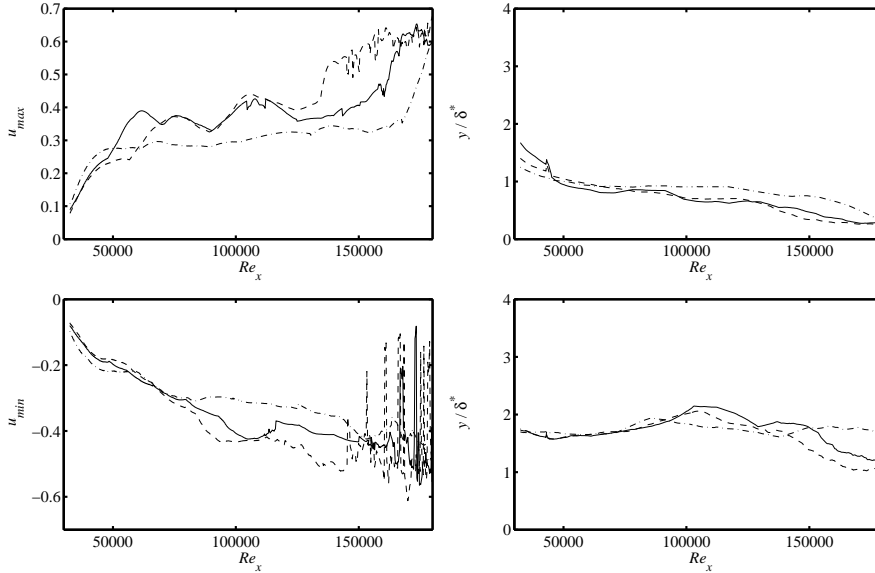


FIGURE 6. Streamwise evolution of the maximum “over time” of the streamwise velocity perturbation \hat{u}_{max} and its wall-normal position (top line). Minimum of u_{min} and its wall-normal position (bottom line). Plotted for the integral length scales: - - -, $L = 7.5\delta_0^*$; —, $L = 5\delta_0^*$; - · -, $L = 2.5\delta_0^*$.

The results presented compare well with experiments and previous simulations of a boundary layer subject to free-stream turbulence. However, before discussing in detail the instantaneous flow configurations, a new quantity is introduced to try to better follow the development of the perturbation in the laminar boundary layer. The amplitude of the streak is not averaged in time, but the maximum and minimum of the local streamwise disturbance velocity during the integration time is stored. Formally, the quantities $\hat{u}_{max}(x, y)$ and $\hat{u}_{min}(x, y)$ are defined by

$$\hat{u}_{max}(x, y) = \max_{t,z} [u(x, y, z, t) - \bar{u}(x, y, t)],$$

$$\hat{u}_{min}(x, y) = \min_{t,z} [u(x, y, z, t) - \bar{u}(x, y, t)],$$

where $\bar{u}(x, y, t)$ is the mean value of $u(x, y, z, t)$ in the spanwise direction computed over the whole width of the computational domain. The downstream

evolution of the wall-normal maximum of $\hat{u}_{max}(x, y)$ and $\hat{u}_{min}(x, y)$ is displayed in figure 6. It can be seen that the value of the maximum perturbation is not so different among the three cases considered. The highly irregular oscillations, indicating the appearance of a turbulent spot, are clearly visible at the end of the displayed domain. These oscillations continue downstream for all the cases considered. Note also that these strong oscillations are first seen in \hat{u}_{min} , confirming the fact that the breakdown is initiated on the low-speed regions. Figure 6 enables us to better explain the differences observed in the time-averaged results (cf. figure 3a and 4a). In the case of the smallest integral length scale, strong streaks and turbulent spots also occur in the boundary layer, however the fact that the time-averaged quantities are hardly affected indicates that it happens seldom. The difference appears, hence, to be related with the number and frequency of occurrence of the single events. In agreement with the *rms* values in figure 4(a), it is confirmed the fact that for the simulation with $L = 2.5\delta_0^*$ the growth rate of the perturbations decreases quite early ($Re_x \approx 80\,000$).

The values of the streak amplitudes are much larger than the corresponding *rms*. The fact that the averaged values usually reported in the experiments are likely to mask stronger localised distortions, which are able to induce the breakdown, was first suggested by Wundrow & Goldstein (2001). The streaks reach quite soon an amplitude of the order of 30% of the free-stream velocity, a sufficiently high value for the onset of a secondary instability (Andersson *et al.* 2001). The maximum positive and negative streamwise velocity perturbation exhibit a different wall-normal distribution. This can be seen in figure 6 where the y -position of the peak of the high- and low-speed streaks is also displayed. The high-speed streak is, in fact, located closer to the wall while the low-speed streak is pushed in the upper part of the boundary layer by the lift-up effect.

3.2. Streamwise streak receptivity

3.2.1. Background: proposed receptivity mechanisms

In this section we look in detail at the initial phase of the transition process, i.e. the boundary-layer receptivity to free-stream turbulence and the streak formation and following growth. The results presented refer to Case3, Case6, Case7 and Case3 α , Case6 α , Case7 α in table 2, for which a shorter computational domain is used. In the literature, two possible mechanisms for the streak generation in boundary layers subject to free-stream turbulence have been proposed: a linear and a non-linear one. A linear mechanism for streak generation caused by the diffusion and/or propagation of a free-stream streamwise vortex into the boundary layer has been studied by Andersson *et al.* (1999) and Luchini (2000) using the boundary layer equations and by Wundrow & Goldstein (2001) by means of asymptotic expansions. These studies assume the presence of streamwise vorticity at the leading edge. Bertolotti (1997) used a different method to calculate the initial streamwise vortices but still studied a linear mechanism. If a linear receptivity model is considered, the growth of

the streaks is directly induced by the streamwise vortices and it turns out to be proportional to the Reynolds number Re_{δ^*} . In Berlin & Henningson (1999) and Brandt *et al.* (2002) a nonlinear model for receptivity, originating from the interactions of oblique modes in the free-stream, has been proposed. This mechanism can be reduced to a two-step process, first the nonlinear generation of streamwise vorticity due to nonlinear interactions and then the formation of streaks due to the linear 'lift-up' effect. For this nonlinear scenario, it has been found that the streak amplitude is proportional to an amplification factor of the order $\mathcal{O}(Re_{\delta^*}^2)$ times the square of the amplitude of the outside perturbation. In contrast, the linear model assumes a stronger direct forcing proportional to the amplitude of the perturbation, but it requires the presence of streamwise vorticity inside the boundary layer.

Here, by means of DNS, we would like to compare the two mechanisms and try to identify which of the two can be considered as the most relevant in cases with known free-stream perturbation. In order to do so different levels of free-stream turbulence intensity are considered and, for the cases denoted by α , the free-stream turbulence generation is manipulated in order to involve many modes with very low values of the frequency ω and, consequently, of the streamwise wavenumber α . This is achieved by limiting the rotation of the dodecahedra used to determine the wavenumber of the modes in the inflow disturbance expansion described in section 2.2. If the rotation were completely random, the number of modes with low α would be very small; in particular only 9 ($\times 4$ for symmetry) modes with $\alpha < 0.05$ are obtained for the sequence of random coefficients used in Case3, Case6 and Case7. If we instead define the dodecahedra with 4 vertices in the (γ, β) plane and allow the rotation only around the ω -axis by multiplying the rotation angles with respect to the β and γ directions by 0.0015, 4 ($\times 4$) modes are then characterised by very low values of α and ω for each of the 20 spherical shells employed for the synthetic free-stream turbulence. In this way, the incoming disturbance is characterised by a large amount of energy in the low-frequency components. As shown by Hultgren & Gustavsson (1981) among others, modes of the continuous spectra with very low α and ω values do not feel the shear layer and they are therefore not zero inside the boundary layer. This property of the continuous spectrum modes reflect the fact that high-frequency perturbations are damped inside the boundary layer by inviscid shearing (Craik 1991), while low-frequency perturbations can diffuse into the boundary layer. It is shown in Jacobs & Durbin (1998) that the penetration depth of the continuous modes inside the shear layer is inversely proportional to the Reynolds number. Note finally that the results of this receptivity study are obtained for a fixed value of the integral length scale, $L = 7.5\delta_0^*$.

3.2.2. Results and discussion

First, the results obtained when the artificial inflow turbulence is mainly associated with disturbances outside the boundary layer are discussed; these are

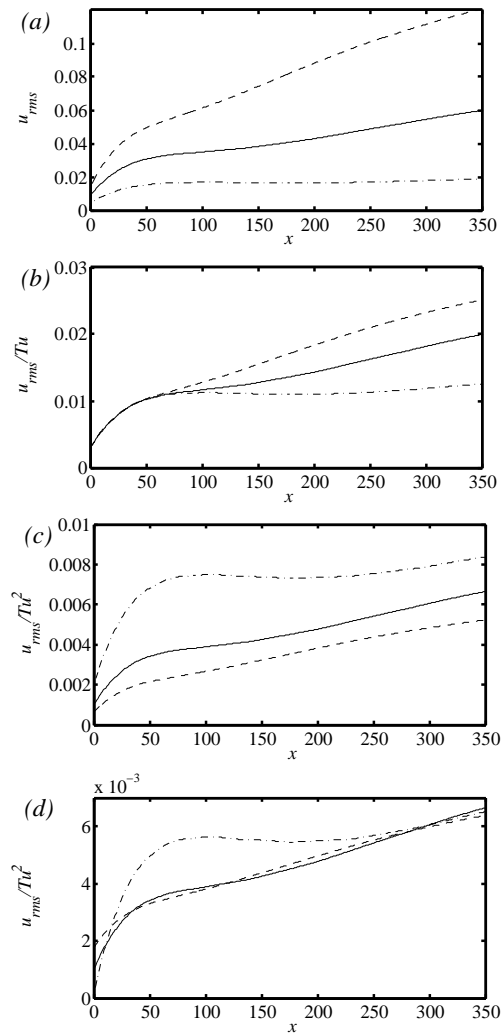


FIGURE 7. (a) Streamwise evolution of the wall-normal maximum of u_{rms} for the simulations with: - - -, $Tu = 4.7\%$; —, $Tu = 3\%$ and - · -, $Tu = 1.5\%$. The same rms -values are scaled with the free-stream turbulence intensity Tu and Tu^2 in (b) and (c) respectively. In (d) the values divided by Tu^2 are translated in order to account for the different initial phases of the development.

Case3, Case6 and Case7 in table 2. The downstream evolution of the wall-normal maximum of the streamwise velocity perturbation is reported in figure 7, where the coordinate x represents the distance from the computational

inlet made non-dimensional with δ_0^* . In figure 7(a), the amplitude attained by the streaks is shown for the three different free-stream turbulence intensities Tu under consideration. Note that the perturbation level remains quite low for the weakest amplitude of the inflow perturbation. The same rms values are divided by Tu in figure 7(b) and by Tu^2 in figure 7(c). From figure 7(b) it can be seen that the initial growth of the perturbation inside the boundary layer is linear; in the two cases of lowest Tu the growth follows the linear trend for a slightly larger downstream distance, up to $x \approx 80$. However, after this initial phase, the growth is faster for larger Tu and it can be seen in figure 7(c) that the streak amplitude follows almost parallel lines when the u_{rms} is scaled with the square of free-stream turbulence intensity. This is more evident for the two largest values of Tu . To better show that the growth of the streaks is effectively quadratic and hence governed by the non-linear mechanism, the curves in figure 7(c) are translated in order to compensate for the different initial part of the development, the linear one, and they are displayed in figure 7(d). The dashed curve, pertaining to the case with $Tu = 4.7\%$, has been vertically translated to have the same value as the solid line, pertaining to the case with $Tu = 3\%$, at $x = 40$, where the two corresponding curves begin to diverge in figure 7(b). The dash-dotted curve, Case7 with $Tu = 1.5\%$, has been moved downwards to coincide with the solid line at $x = 290$. For this case, the growth of the streak seems to scale quadratically only from this downstream station. The level of free-stream perturbations is not high enough to give a clear quadratic growth earlier; the two mechanisms considered are most likely in competition in the region between $x = 80$ and $x = 290$, being both driven by quite weak perturbations. Thus, after an initial phase in which the growth of the perturbation in the boundary layer is linear and involves the low-frequency disturbances already part of the inflow turbulence, the nonlinear mechanism discussed above takes over and becomes dominating. A certain distance (and time) is needed for the nonlinear process to take place; however this distance can be regarded as small. Note that this nonlinear receptivity process is also observed in the simulations by Jacobs & Durbin (2001). These authors show that the inflow perturbation spectrum evolves downstream into a different perturbation spectrum through the generation and successive amplification of the low-frequency components.

The results obtained for the corresponding cases denoted by α are reported in figure 8. Due to the manipulation of the modes yielding the inflow perturbation, larger values of u_{rms} are now attained inside the boundary layer already at the inlet ($x = 0$), where the perturbation consists of the low-frequency modes of the continuous spectra. It may be useful to be reminded that the statistics are obtained by averaging both in time and in the spanwise direction. For the case with $Tu = 4.7\%$, turbulent spots are observed during the integration time already within the shorter computational box used for this type of simulations. The transition location would then be moved upstream as compared to the simulation Case3 in figure 3. The sensitivity of the transition location not only to the free-stream turbulence length scales but also to its spectral components,

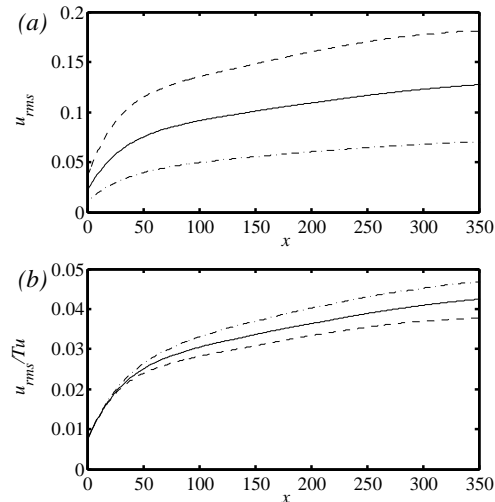


FIGURE 8. (a) Streamwise evolution of the wall-normal maximum of u_{rms} for the simulations with low-frequency modes as part of the inflow perturbation spectrum (Case3 α , Case6 α and Case7 α) and for: - - -, $Tu = 4.7\%$; —, $Tu = 3\%$ and - · -, $Tu = 1.5\%$. (b) The same rms -values are scaled with the free-stream turbulence intensity Tu .

as shown here, can further account for the difference among the numerical simulations and experimental results (Roach & Brierly 1990; Matsubara *et al.* 1999).

A fairly good collapse of the three u_{rms} curves in figure 8(a) is obtained if their values are divided by the free-stream turbulence intensity as in figure 8(b). The streak growth is slightly decreasing for increasing levels of Tu , which can be explained by the saturation occurring for the large u_{rms} observed. Thus, if significant low-frequency perturbations can impinge directly on the boundary layer, the linear mechanism becomes the dominating process responsible for the streak formation and growth.

We would like now to compare the streak growth occurring when the two different receptivity mechanism are at work with the same level of free-stream turbulence. In order to do so, the downstream evolution of the u_{rms} inside the boundary layer is normalised by its value at the inlet u_{rms}^0 . The latter is an indirect measure of the low-frequency energy of the free-stream turbulence since only modes of the continuous spectrum with low ω are not zero inside the boundary layer. The u_{rms} -values downstream indicate the level of low-frequency perturbation growing inside the boundary layer; if the linear receptivity process is active, the rms -values reflect the amplification of the low-frequency part of the free-stream turbulence spectrum. If, conversely, the nonlinear process is dominant, low-frequency perturbations are induced by

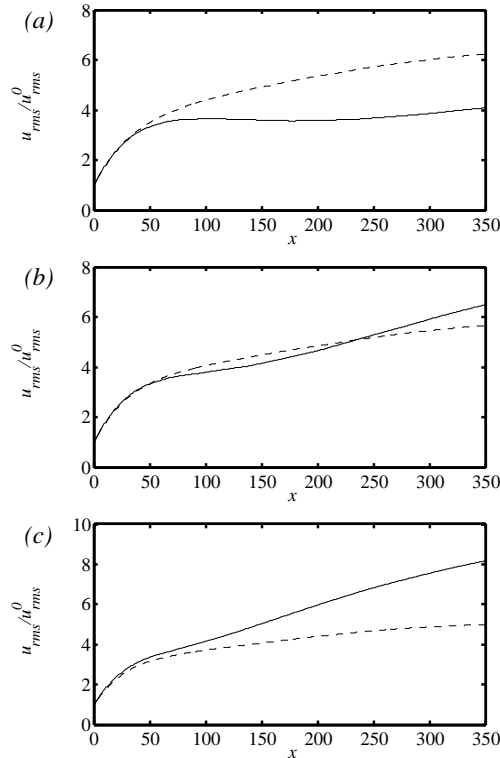


FIGURE 9. Streamwise evolution of the wall-normal maximum of u_{rms} normalised by its value at the inlet u_{rms}^0 for: (a) the simulations denoted by Case7 ($u_{rms}^0 = 0.46\%$) and Case7 α ($u_{rms}^0 = 1.13\%$), with $Tu = 1.5\%$. (b) the simulations denoted by Case6 ($u_{rms}^0 = 0.92\%$) and Case6 α ($u_{rms}^0 = 2.25\%$), with $Tu = 3\%$. (c) the simulations denoted by Case3 ($u_{rms}^0 = 1.48\%$) and Case3 α ($u_{rms}^0 = 3.64\%$), with $Tu = 4.7\%$. The dashed lines indicate the cases denoted by an α .

quadratic interactions among high-frequency modes. The normalised data are plotted in figure 9 for the three different levels of free-stream turbulence under consideration. For the lowest level $Tu = 1.5\%$ in figure 9(a), the streak growth is larger for the case in which the relevant receptivity mechanism is linear. However, for a free-stream turbulence intensity of 3%, the total amplification of the streamwise velocity perturbation inside the boundary layer is of the same order independently of which of the two mechanisms is dominating (see figure 9b). For Case6, when the nonlinear receptivity is at work, the initially slower growth becomes faster downstream of $x \approx 150$. In figure 9(c) the comparison for the two runs with $Tu = 4.7\%$ is displayed. The growth is larger

when the nonlinear receptivity mechanism is the most relevant, in spite of the fact that the actual *rms* values are larger for Case3 α .

The analysis performed here shows that two parameters may be seen as fundamental in defining the streak receptivity process: the free-stream turbulence intensity Tu and the amount of low-frequency perturbation part of the free-stream turbulence, here quantified by u_{rms}^0 . Their ratio $(u_{rms}^0/Tu)^2$ can be seen as the fraction of free-stream turbulence energy in low-frequency modes. We can conclude that the linear receptivity mechanism is the most relevant if the free-stream turbulence contains significant low-frequency disturbances, whereas the nonlinear mechanism is dominating if the free-stream turbulence is characterised by high-frequency modes. Further, considering the relative energy growth in the low-frequency components (u_{rms}/u_{rms}^0) , the nonlinear mechanism is stronger for free-stream turbulence levels larger than 3%, while the linear process is more effective for smaller values of Tu . However, if high enough energy content is initiated in low-frequency oscillations, as in the simulations denoted by an α , the linear receptivity process can overrule its nonlinear counterpart and it turns out to be the most relevant.

In many of the reference experimental studies (Roach & Brierly 1990; Matsubara & Alfredsson 2001), the turbulence is generated by a grid located upstream of the leading edge and the low-frequency perturbation components can diffuse easily into the shear layer. In those cases therefore, the linear mechanism can be considered as the most relevant. In fact, the results obtained here confirm the transition prediction model suggested by Andersson *et al.* (1999) and then supported by the experimental data in Matsubara *et al.* (1999). The proposed model is based on the assumption that the perturbation growth and thus the average breakdown location scales linearly with the free-stream turbulence level and it applies to values of Tu lower than 6%.

3.3. Turbulent spot generation

In this section we analyse the breakdown by looking at the instantaneous three-dimensional flow configurations for a number of spots, tracing back in time the location of their formation. A snapshot of the flow is shown in figure 10 where the instantaneous streamwise and spanwise velocities are plotted in a plane parallel to the wall. The overall picture of the transition scenario can be deduced from the figure. Starting from the inlet position, the perturbation in the boundary layer appears mainly in the streamwise velocity component, in the form of elongated structures. Patches of irregular motion are seen to appear further downstream; these are more evident in the spanwise component, otherwise very weak in the streaky boundary layer. For this reason, the cross-stream velocities will be used in the following to identify the perturbation riding on the streaks so that a 'natural' separation is obtained between the streaks and the growing high-frequency irregular motions observed. As they travel downstream, the spots become wider and longer. Note also that laminar streaks can be observed downstream of the spots. The turbulent region at the

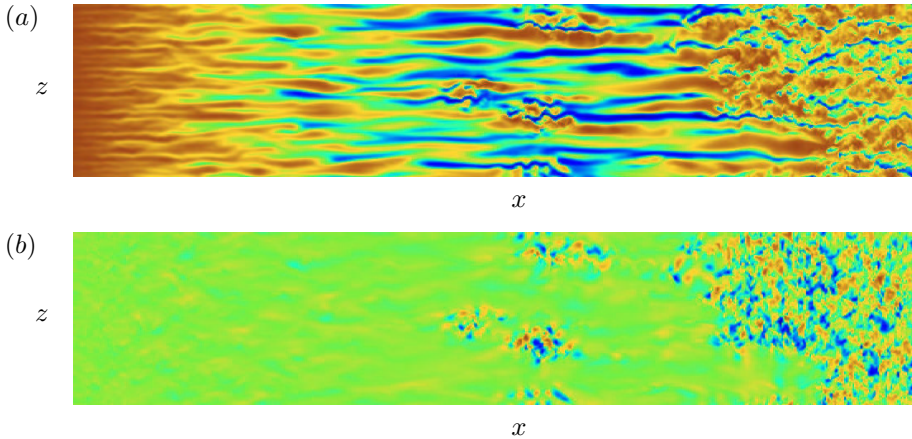


FIGURE 10. (a) Instantaneous streamwise velocity and (b) spanwise velocity in a plane parallel to the wall at $y/\delta_0^* = 2$. The plots are not at the actual scale since the domain depicted is 900 units long and 90 units wide in terms of δ_0^* . The fringe region is not shown.

end of the domain is created by the enlargement and merging of the various spots and therefore the streamwise position at which the flow is turbulent varies with time; the turbulent flow is convected downstream and it would not be seen if new spots were not formed all the time.

To follow back in time the birth of a turbulent spot, x - z planes at different wall-normal distances are saved during the numerical integration of the Navier-Stokes equations. Full three-dimensional velocity fields could then be saved at chosen times by repeating the same computation. Probably the most important feature of the spot precursors, observed in all cases considered, is the presence of regions of positive and negative wall-normal and spanwise velocity arranged in a quasi-periodic array. An example of this is shown in figure 11. It can be seen that the regular distribution of cross-stream velocities (the spanwise component only is depicted in the figure) is responsible for the associated wavy motion of the streak preceding the breakdown. Visual inspection of many velocity fields shows that it is possible to classify the type of breakdown occurring on the streaks by considering the spanwise symmetry of the wall-normal and spanwise velocities and the location relative to the underlying streak.

We show that the structures characterising the incipient spots resemble much those observed in the simplified studies on the breakdown of steady symmetric streaks, both in the sinuous case (Brandt & Henningson 2002) and in the varicose case (Asai *et al.* 2002), with the former scenario being the most frequently observed. In particular, the quasi-sinuous breakdown is observed in 16 of the 28 spots considered. This similarity with either of the two cases was observed in all the spots under consideration. Clearly, the streaks generated

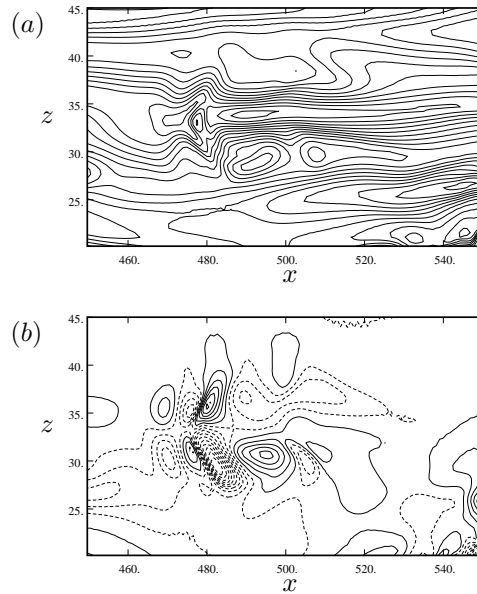


FIGURE 11. Instantaneous velocity field in the case of a varicose breakdown. (a) Streamwise velocity component. Maximum contour level 0.85, contour spacing 0.05. (b) Spanwise velocity component. Maximum contour level 0.11, contour spacing 0.02. Dashed lines indicate negative values. The coordinate are scaled with δ_0^* .

by free-stream turbulence are not symmetric and the corresponding perturbations are definitely not symmetric either; however in comparison with the model problems mentioned above the velocities conserve almost the same pattern with respect to the mean shear of the streaks. In the case of sinuous breakdown, the streaks undergo spanwise antisymmetric oscillations and the perturbation kinetic energy production is driven by the spanwise shear of the streaky flow as first observed by Swearingen & Blackwelder (1987). The strong high-frequency velocity perturbation, appearing first in the cross-stream velocity components, is located in the region between the low- and high-speed streaks. The case of the varicose or symmetric breakdown is characterised by a symmetric distribution of the high-frequency components of u and v with respect to the middle of the low-speed region, while the spanwise velocity w assumes an antisymmetric pattern; an example of this type of breakdown is shown in figure 11. In the varicose case, the wall-normal velocity shear of the basic streamwise flow is driving the instability (see Skote *et al.* 2002, among others). Note that in the sinuous scenario, conversely, the streamwise and wall-normal perturbation velocities assume an antisymmetric distribution, while the spanwise component is symmetric with respect to the low-speed streak.

3.3.1. Quasi-varicose breakdown

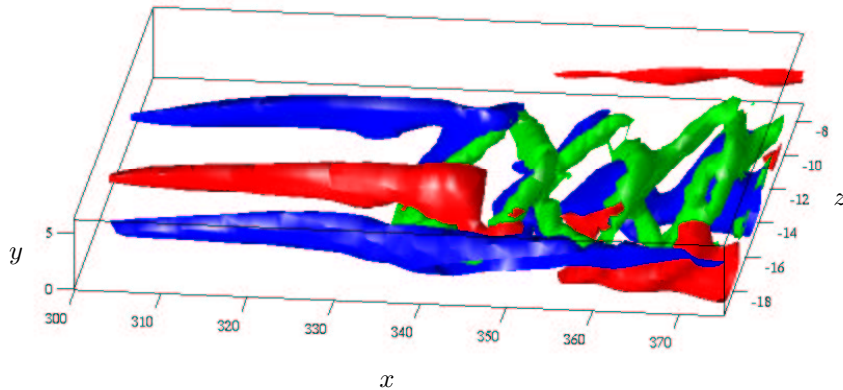


FIGURE 12. Instantaneous flow configuration at the breakdown of a streamwise streak. Red represents positive perturbation streamwise velocity ($u' = 0.13$), while blue indicates the low-speed streak ($u' = -0.13$). The green structures are regions of negative λ_2 , used to identify vortical structures.

As mentioned before, the appearance of the varicose or symmetric breakdown is essentially governed by Kelvin-Helmholtz instability of inflectional wall-normal profiles and the transition scenario is characterised by the appearance of horse-shoe or hairpin structures. An example of such vortical structures is displayed in figure 12. The green colour displays regions of negative values of the second largest eigenvalue λ_2 of the Hessian of the pressure (see Jeong *et al.* 1997), used to identify vortical structures, while the low- and high-speed streaks are shown in blue and red respectively by considering negative and positive values of the streamwise velocity u' . This is defined as the difference between the instantaneous streamwise velocity $u(x, y, z, t)$ and its spanwise average $\bar{u}(x, y, t)$. It is evident from the figure the formation of a train of hairpin vortices, with pairs of counter-rotating quasi-streamwise vortices joining in the middle of the low-speed streak. These structures point alternatively upstream and downstream and we will refer to them as V- and Λ -structures respectively. It can also be noted that they are inclined away from the wall in the downstream direction.

The full velocity field corresponding to the structures observed can be deduced from figure 13, where the cross-stream velocities are shown with velocity vectors and the streamwise component by constant levels in cross-stream $y-z$ planes cut along one wavelength of the streak varicose oscillation. The regions of strong vortical motions are also indicated by thick dashed lines. In figure 13(a) the downstream part of the head of the hairpin vortex pointing downstream (Λ -structure in figure 12) is seen to be located above the two legs of

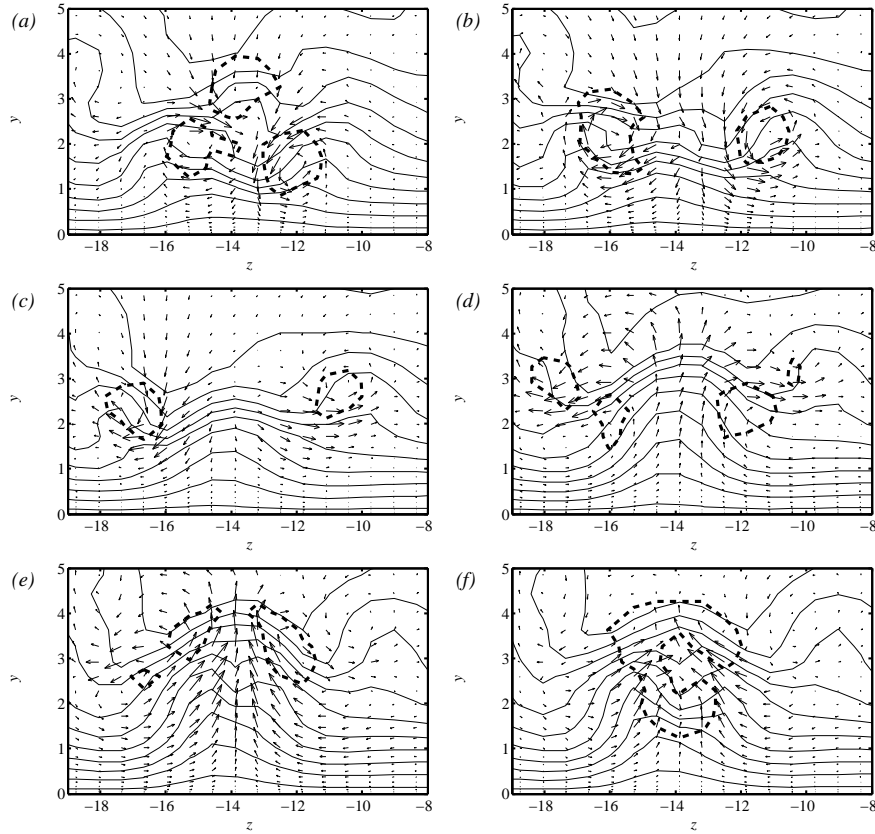


FIGURE 13. Vertical planes in the cross-stream directions. The arrows represent the spanwise and wall-normal velocities, while solid lines indicate constant streamwise velocity from 0.05 to 0.95 with spacing of 0.1. The thick dashed lines represent constant negative values of λ_2 and show the core of the vortical structures. (a) $x = 350$, (b) $x = 352$, (c) $x = 354$, (d) $x = 357$, (e) $x = 359$, (f) $x = 361$.

the V-structure pointing instead upstream. The leg of the latter correspond to quasi-streamwise vortices which slightly diverge downstream and induce negative wall-normal velocity in the middle of the low-speed streak (located at $z \approx -14$ for the particular spot precursor considered here) and positive wall-normal velocity on its sides. These streamwise vortices create two low-speed lumps in each period of the varicose oscillations (see figure 13*a,b,c*) in agreement with the streamwise velocity measurements of the varicose instability of a single steady streak in Asai *et al.* (2002). In figure 13*(d)* four vortical regions are visible: the downstream end of the V-structure and the upstream end of the Λ -structure. The legs of the latter also consist of quasi-streamwise vortices,

which instead approach each other, and induce positive wall-normal velocity in the middle of the low-speed streak. In figure 13(*f*) one can see that the two legs join above the vertex of the following V-structure as in 13(*a*). By comparing figure 13(*f*) and 13(*a*), which corresponds to what is observed just downstream of 13(*f*), one can deduce that both the head of the Λ -structure and the vertex of the V-structure are associated with negative spanwise vorticity (positive v upstream and negative v downstream).

From the analysis of flow visualisations and animations, it is further noticed how the interaction between low- and high-speed streaks plays an important role for the formation of incipient spots. It can be seen in figure 12, for example, how the interaction of the low-speed streak with a fast-moving incoming region of high streamwise velocity is the triggering cause of the instability leading to the formation of the hairpin vortices. It is observed in experiments (Lundell & Alfredsson 2003) that the streaks are tilted downstream so as the front part is located in the upper part of the boundary layer whereas the rear part is located closer to the wall. Such a structure is growing in the streamwise direction while convected downstream. As a consequence, highly inflectional wall-normal velocity profiles are induced by the high-speed region when reaching the tail of the low-speed region ahead, which thus becomes the site of a local instability.

3.3.2. Quasi-sinusoidal breakdown

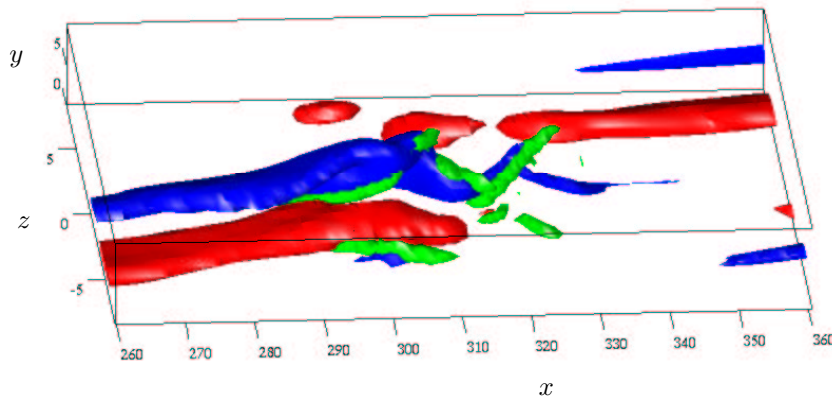


FIGURE 14. Instantaneous flow configuration at the breakdown of a streamwise streak. Red represents positive perturbation streamwise velocity ($u' = 0.14$), while blue indicates the low-speed streak ($u' = -0.14$). The green structures are regions of negative λ_2 , used to identify vortical structures.

In the case of the sinusoidal breakdown, a single low-speed streak undergoes spanwise antisymmetric oscillations, with strong high-frequency perturbation velocity located in the region of largest spanwise shear between the

low- and high-speed streaks. An instantaneous flow configuration for this type of scenario is displayed in figure 14. The characteristic vortical structures, represented in green by negative values of the eigenvalue λ_2 , consist of quasi-streamwise vortices located on the flanks of the low-speed streak (depicted in blue colour). Vortices of alternating sign are overlapping in the streamwise direction in a staggered pattern.

The instantaneous flow in vertical planes at different streamwise positions, covering a distance corresponding to about one sinuous oscillation of the low-speed streak, is displayed in figure 15. The velocity vectors show the spanwise and wall-normal velocity. The isolines represent the streamwise velocity and the thick dashed lines regions of vortical motion. The evolution of two quasi-streamwise vortices, of opposite sign, is followed in the plots. In figure 15(a) and (b) one can see the vortex characterised by negative vorticity, located on the left-hand side of the low-speed streak, following the motion of the streak in the positive z -direction. Already in figure 15(b) the vortex with positive streamwise vorticity is visible. It follows the oscillation of the low-speed streak in the negative z -direction. The flow presents remarkable similarity with the structures observed in the simulations of the sinuous breakdown of a periodic array of streaks shown in figures 18 and 19 in Brandt & Henningson (2002).

It is also important to note that for about half of the incipient spots, which have been classified as quasi-sinuous breakdown, the quasi-streamwise vortices of either positive or negative vorticity are much stronger than their counterparts. This can be ascribed to the spanwise asymmetry of the streaks generated by free-stream turbulence. An example of this 'one-side' instability is displayed in figure 16, where the evolution of one spot precursor is shown at two different times. The contour lines in the plots represent spanwise velocity component while the background shows the streamwise component with black for low velocity and white for high values. It can be seen that the spanwise oscillations of the streak are driven by alternating positive and negative spanwise velocity which is centred in the region of largest spanwise shear on one side of the low-speed streak ($z \approx -2$ in the case in the figure). The dark areas show that the spanwise oscillation of the low-speed streak is stronger in the negative z -direction. The lack of a region of significant positive streamwise velocity perturbation on the other side of the low-speed streak ($z \approx -6$) accounts for the differences with the case of the sinuous breakdown in figure 14. Note also that the high-frequency perturbation riding on the streak assumes the form of a wave packet: it travels downstream, increasing in amplitude and spreading, and can be considered the result of the instability of a spanwise velocity profile with an inflection point (and not two as in the case of symmetric streaks or wakes).

The quasi-sinuous scenario discussed in this section is also induced by the interactions between streaks; in particular, when high-speed fluid is approaching a low-speed region on a side. In this case, an inflectional profile is forming in the spanwise direction. This can be seen in figure 14 at $z \approx 0$ and

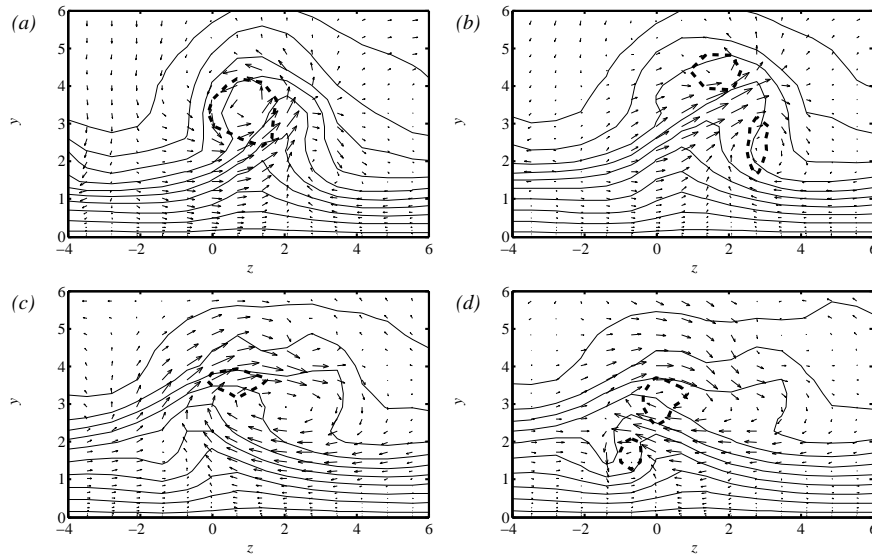


FIGURE 15. Vertical planes in the cross-stream directions. The arrows represent the spanwise and wall-normal velocities, while solid lines indicate constant streamwise velocity from 0.05 to 0.95 with spacing of 0.1. The thick dashed lines represent constant negative values of λ_2 and show the core of the vortical structures. (a) $x = 304$, (b) $x = 307$, (c) $x = 311$, (d) $x = 314$.

$300 \lesssim x \lesssim 310$, and in figure 16(a) at $z \approx -1$ and $x \approx 355$. Note also that the streaks are not perfectly aligned in the streamwise direction but they slowly oscillate in the boundary layer. Finally, it is interesting to notice that Asai *et al.* (2002) observed that wider streaks undergo more easily the varicose breakdown, while the sinuous scenario is most likely to occur with narrow streaks. The same seems to be true in the present case, as seen by comparing the width of the streaks in figures 15, 16 and 13.

4. Summary and conclusions

Numerical simulations of bypass transition in a Blasius boundary layer subjected to free-stream turbulence have been performed. The present scenario is characterised by the formation inside the boundary layer of streamwise elongated regions of high and low streamwise velocity. The free-stream turbulence is generated by the superposition of modes of the continuous spectrum of the Orr-Sommerfeld and Squire operators. The numerical methodology implemented allows to define the energy spectrum of the turbulent inflow, so that it has been possible to investigate the effect of the integral length scale of the free-stream turbulence and the receptivity process. Further, since laboratory experiments

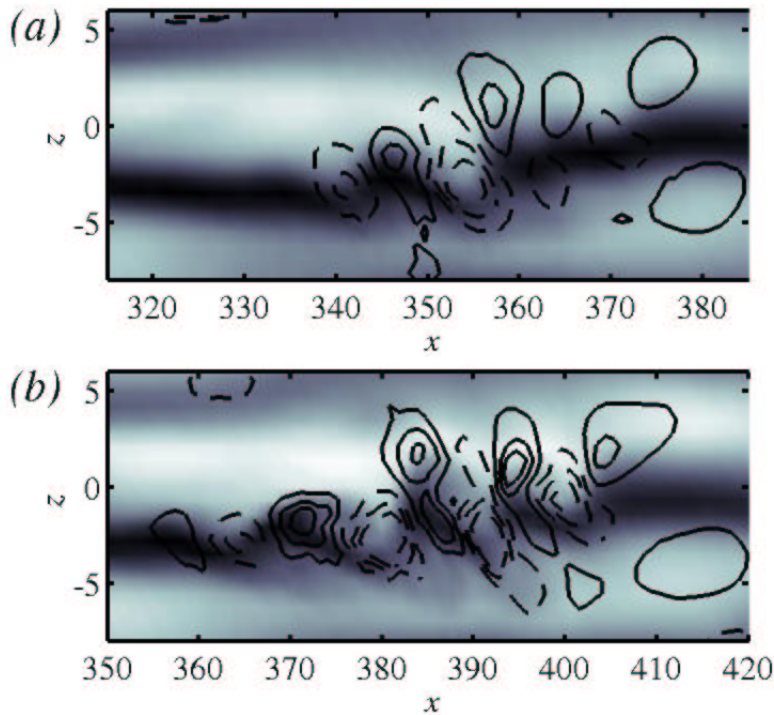


FIGURE 16. Instantaneous flow configurations at the breakdown of a streamwise streak in a plane parallel to the wall at $y = 3$. (a) $t' = 0$; (b) $t' = 41$, where t' is made non dimensional with δ_0^*/U_∞ . Lighter areas represent positive perturbation streamwise velocity, while dark areas indicate the low-speed streak. The lines represent constant spanwise velocity from -0.075 to 0.075 with spacing of 0.03 of the free-stream velocity. The dashed lines indicate negative values.

have not completely elucidated the mechanisms of formation of turbulent spots, the present study is also focused on the breakdown stage. The main findings can be summarised as follows.

Considering the same intensity of the incoming perturbation, transition occurs earlier for larger values of the integral length scale of the free-stream turbulence. It is also shown that the small scales can penetrate easier into the boundary layer and therefore induce significant streamwise velocity perturbations at lower Reynolds number. However, the growth of the perturbation is not sustained for a long distance downstream as in the cases with larger integral length scales. This is due to the fact that free-stream turbulence of small length scale decays faster and thus cannot continuously force perturbations inside the

boundary layer. Note also that the spanwise scale of the streaks is only weakly dependent on the scale of the disturbance in the free stream.

The energy spectrum of the turbulent inflow has been manipulated in order to control the amount of low-frequency disturbances present at the inlet. This enabled us to compare two possible receptivity mechanisms. A linear mechanism (Bertolotti 1997; Andersson *et al.* 1999; Luchini 2000) which requires the presence of streamwise vortices diffusing/propagating into the boundary layer at the leading edge and a nonlinear process in which the streamwise vortices are induced by the interaction of oblique waves in the free stream (Berlin & Henningson 1999; Brandt *et al.* 2002). It is found that the linear mechanism is the most relevant if the free-stream turbulence contains low-frequency disturbances, whereas the nonlinear process is active if the free-stream turbulence mainly contains high-frequency disturbances.

It is observed that the breakdown into turbulent spots occur on isolated streaks and it is associated to high-frequency motions of the low-speed streak. The characteristic structures of the spot precursors are found to be very similar to those observed in previous model studies on the secondary instability and breakdown of steady symmetric streaks, both for the sinuous symmetry, which resulted the most likely to occur, and for the varicose symmetry (see Asai *et al.* 2002, for a recent experimental investigation). From the results presented one may conclude that the breakdown is related to local instabilities driven by the strong shear layers associated with the streaks, the sinuous breakdown being driven by the spanwise shear and the varicose breakdown by the wall-normal shear. The fact that almost identical structures are observed in the case of transition induced by free-stream turbulence and in the previous model studies on streak instability leads to believe that the relevant physics has correctly been captured by these previous studies. It is observed that in some cases, due to the intrinsic asymmetry of the streaks induced by free-stream turbulence, a sinuous-like instability develops only on the side of the low-speed streak associated with the largest spanwise shear. The quasi-streamwise vortices and typical flow patterns reproduce well those observed during half a period of the sinuous oscillations of a symmetric streak.

It is also interesting to note that Schoppa & Hussain (2002) showed that steady streaks, stable to linear perturbations, can undergo a sinuous breakdown to turbulence if subjected to specific initial disturbances of sufficiently high amplitude. The breakdown is characterised by structures identical to those identified by Brandt & Henningson (2002) in the case of a linearly unstable streak. Although in the present case the background level of noise is high enough to induce such subcritical breakdown, preliminary stability calculations carried out on some instantaneous streamwise velocity profiles extracted before the appearance of an incipient spot show that these basic flows are indeed unstable. However such approach is not pursued further, since it is believed more relevant to concentrate future studies on the role of the streak motions and unsteadiness.

The direct numerical simulations have also shown the importance of the interaction between the low- and high-speed streaks, which is seen to be the main triggering mechanism of the streak instability, which is then not induced from outside the boundary layer. The relevance of such interactions was first suggested by Johansson *et al.* (1991) and Landahl (1990) for the case of near-wall turbulent streaks. Note that also Wu & Choudhari (2001) showed that the unsteadiness of the Klebanoff modes plays a crucial role. These authors found instability modes which would not have been present if streaks of the same amplitude were treated as steady.

The physical understanding of transition in boundary layers under free-stream turbulence can be used to implement future control strategies. First experimental studies show that it is possible to reduce the streak growth (Lundell 2003); however, the design of a control system, which is able to detect the presence of dangerous situations and decide when to act, needs to be improved. In the light of the observation above, a successful control strategy may aim at reducing the streak interaction and can be based on the detection of the relative position between streaks, rather than on their presence or amplitude.

It is also important to note that the similarity between the wall-layer streaks in turbulent boundary and their instability (Jiménez & Pinelli 1999; Schoppa & Hussain 2002) and the structure observed in transitional boundary layers. One can speculate that the near-wall streamwise vortices and streaks are driven by the turbulence in the outer part of the boundary layer in the same way laminar streaks are induced by the free-stream turbulence. As a consequence, the receptivity stage becomes an important ingredient of the regeneration cycle of near-wall turbulence, together with the streak formation by the linear lift-up effect and the streak breakdown, and therefore it might deserve future work.

Acknowledgments

This research was supported by VR (The Swedish Research Council). Computer time was provided by the Center for Parallel Computers (PDC) at the Royal Institute of Technology (KTH) and by the National Supercomputer Center in Sweden (NSC) at Linköping University. The authors would like to thank Prof. Henrik Alfredsson and Dr. Fredrik Lundell for the useful discussions. P.S. acknowledges financial support from the Swiss National Science Foundation and the Swiss Center of Scientific Computing (CSCS) during his visits in Stockholm.

References

- ACARLAR, M. S. & SMITH, C. R. 1987 A study of hairpin vortices in a laminar boundary layer. Part 2. Hairpin vortices generated by fluid injection. *J. Fluid Mech.* **175**, 43–68.

- ANDERSSON, P., BERGGREN, M. & HENNINGSON, D. S. 1999 Optimal disturbances and bypass transition in boundary layers. *Phys. Fluids* **11**, 134–150.
- ANDERSSON, P., BRANDT, L., BOTTARO, A. & HENNINGSON, D. S. 2001 On the breakdown of boundary layers streaks. *J. Fluid Mech.* **428**, 29–60.
- ARNAL, D. & JUILLEN, J. C. 1978 Contribution expérimentale à l'étude de la reptivité d'une couche limite laminaire à la turbulence de l'écoulement général. Rapport Technique 1/5018. ONERA.
- ASAI, M., MINAGAWA, M. & NISHIOKA, M. 2002 The instability and breakdown of a near-wall low-speed streak. *J. Fluid Mech.* **455**, 289–314.
- BERLIN, S. & HENNINGSON, D. S. 1999 A nonlinear mechanism for receptivity of free-stream disturbances. *Phys. Fluids* **11** (12), 3749–3760.
- BERTOLOTTI, F. P. 1997 Response of the blasius boundary layer to free-stream vorticity. *Phys. Fluids* **9** (8), 2286–2299.
- BERTOLOTTI, F. P., HERBERT, T. & SPALART, P. R. 1992 Linear and nonlinear stability of the Blasius boundary layer. *J. Fluid Mech.* **242**, 441–474.
- BOTTARO, A. & KLINGMANN, B. G. B. 1996 On the linear breakdown of Görtler vortices. *Eur. J. Mech. B/Fluids* **15**, 301–330.
- BRANDT, L. & HENNINGSON, D. S. 2002 Transition of streamwise streaks in zero-pressure-gradient boundary layers. *J. Fluid Mech.* **472**, 229–262.
- BRANDT, L., HENNINGSON, D. S. & PONZIANI, D. 2002 Weakly non-linear analysis of boundary layer receptivity to free-stream disturbances. *Phys. Fluids* **14** (4), 1426–1441.
- BUTLER, K. M. & FARRELL, B. F. 1992 Three-dimensional optimal perturbations in viscous shear flow. *Phys. Fluids A* **4**, 1637–1650.
- CRAIK, A. D. D. 1991 The continuous spectrum of the Orr-Sommerfeld equation: note on a paper of Grosch & Salwen. *J. Fluid Mech.* **226**, 565–571.
- DRAZIN, P. & REID, W. 1981 *Hydrodynamic Stability*. Cambridge Univ. Press.
- DRYDEN, H. L. 1937 Air ow in the boundary layer near plate. Report 562. NACA.
- ELLINGSEN, T. & PALM, E. 1975 Stability of linear flow. *Phys. Fluids* **18**, 487–488.
- ELOFSSON, P. A., KAWAKAMI, M. & ALFREDSSON, P. H. 1999 Experiments on the stability of streamwise streaks in plane Poiseuille flow. *Phys. Fluids* **11**, 915–930.
- GOLDSTEIN, M. E. & WUNDROW, D. W. 1998 On the environmental realizability of algebraically growing disturbances and their relation to klebanoff modes. *Theoret. Comput. Fluid Dynamics* **10**, 171–186.
- GROSCHE, C. E. & SALWEN, H. 1978 The continuous spectrum of the Orr-Sommerfeld equation. Part 1. The spectrum and the eigenfunctions. *J. Fluid Mech.* **87**, 33–54.
- HALL, P. & HORSEMAN, N. J. 1991 The linear inviscid secondary instability of longitudinal vortex structures in boundary-layers. *J. Fluid Mech.* **232**, 357–375.
- HENNINGSON, D. S., LUNDBLADH, A. & JOHANSSON, A. V. 1993 A mechanism for bypass transition from localized disturbances in wall-bounded shear flows. *J. Fluid Mech.* **250**, 169–207.
- HULTGREN, L. S. & GUSTAVSSON, L. H. 1981 Algebraic growth of disturbances in a laminar boundary layer. *Phys. Fluids* **24** (6), 1000–1004.
- JACOBS, R. J. & DURBIN, P. A. 1998 Shear sheltering and the continuous spectrum of the Orr-Sommerfeld equation. *Phys. Fluids* **10**, 2006–2011.
- JACOBS, R. J. & DURBIN, P. A. 2001 Simulations of bypass transition. *J. Fluid Mech.* **428**, 185–212.

- JEONG, J., HUSSAIN, F., SCHOPPA, W. & KIM, J. 1997 Coherent structures near the wall in a turbulent channel flow. *J. Fluid Mech.* **332**, 185–214.
- JIMÉNEZ, J. & PINELLI, A. 1999 The autonomous cycle of near wall turbulence. *J. Fluid Mech.* **389**, 335–359.
- JOHANSSON, A. V., ALFREDSSON, P. H. & KIM, J. 1991 Evolution and dynamics of shear-layer structures in near-wall turbulence. *J. Fluid Mech.* **224**, 579–599.
- JONÁŠ, P., MAZUR, O. & URUBA, V. 2000 On the receptivity of the by-pass transition to the length scale of the outer stream turbulence. *Eur. J. Mech. B/Fluids* **19**, 707–722.
- KENDALL, J. M. 1985 Experimental study of disturbances produced in a pre-transitional laminar boundary layer by weak free-stream turbulence. *AIAA Paper* **85**, 1695.
- KENDALL, J. M. 1998 Experiments on boundary layer receptivity to free-stream turbulence. *AIAA Paper* (98-0530).
- KLEBANOFF, P. S. 1971 Effect of free-stream turbulence on the laminar boundary layer. *Bull. Am. Phys. Soc.* **10**, 1323.
- LANDAHL, M. T. 1975 Wave breakdown and turbulence. *SIAM J. Appl. Maths* **28**, 735–756.
- LANDAHL, M. T. 1980 A note on an algebraic instability of inviscid parallel shear flows. *J. Fluid Mech.* **98**, 243–251.
- LANDAHL, M. T. 1990 On sublayer streaks. *J. Fluid Mech.* **212**, 593–614.
- LUCHINI, P. 2000 Reynolds-number independent instability of the boundary layer over a flat surface. Part 2: Optimal perturbations. *J. Fluid Mech.* **404**, 289–309.
- LUNDBLADH, A., BERLIN, S., SKOTE, M., HILDINGS, C., CHOI, J., KIM, J. & HENNINGSON, D. S. 1999 An efficient spectral method for simulation of incompressible flow over a flat plate. Technical Report KTH/MEK/TR-99/11-SE. KTH, Department of Mechanics, Stockholm.
- LUNDELL, F. 2003 Experimental studies of bypass transition and its control. PhD thesis, Royal Institute of Technology, Stockholm, Sweden.
- LUNDELL, F. & ALFREDSSON, P. H. 2003 Streamwise scaling of streaks in laminar boundary layers subjected to free-stream turbulence. *J. Fluid. Mech.* Submitted for publication.
- MATSUBARA, M. & ALFREDSSON, P. H. 2001 Disturbance growth in boundary layers subjected to free stream turbulence. *J. Fluid. Mech.* **430**, 149–168.
- MATSUBARA, M., BAKCHINOV, A. A., FRANSSON, J. H. M. & ALFREDSSON, P. H. 1999 Growth and breakdown of streaky structures in boundary layer transition induced by free stream turbulence. In *Proc. IUTAM Symp.* (ed. H. F. Fasel & W. S. Saric), pp. 371–376. Springer.
- PARK, D. S. & HUERRE, P. 1995 Primary and secondary instabilities of the asymptotic suction boundary layer on a curved plate. *J. Fluid Mech.* **283**, 249–272.
- PHILLIPS, O. M. 1969 Shear-flow turbulence. *Annu. Rev. Fluid Mech.* **1**, 245–264.
- RAI, M. M. & MOIN, P. 1993 Direct numerical simulation of transition and turbulence in a spatially evolving boundary layer. *J. Comput. Phys.* **109**, 169–192.
- REDDY, S. C. & HENNINGSON, D. S. 1993 Energy growth in viscous channel flows. *J. Fluid Mech.* **252**, 209–238.
- REDDY, S. C., SCHMID, P. J., BAGGETT, J. S. & HENNINGSON, D. S. 1998 On the

- stability of streamwise streaks and transition thresholds in plane channel flows. *J. Fluid Mech.* **365**, 269–303.
- ROACH, P. E. & BRIERLY, D. H. 1990 The influence of a turbulent freestream on zero pressure gradient transitional boundary layer development, part I: Test Cases T3A and T3B. In *Numerical simulation of unsteady flows and transition to turbulence* (ed. O. Pironneau, W. Rodi, I. L. Ryhming, A. M. Savill & T. V. Truong), pp. 319–347. Cambridge University Press.
- ROGALLO, R. S. 1981 Numerical experiments in homogeneous turbulence. *Tech. Rep.* Tech. Memo. 81315. NASA.
- SARIC, W. S., REED, H. L. & KERSCHEN, E. J. 2002 Boundary-layer receptivity to freestream disturbances. *Annu. Rev. Fluid Mech.* **34**, 291–319.
- SCHLATTER, P. 2001 Direct numerical simulation of laminar-turbulent transition in boundary layer subject to free-stream turbulence. *Tech. Rep.*. Department of Mechanics, KTH Stockholm, also Technical report, Institute of Fluid Dynamics, ETH Zürich, 2001.
- SCHMID, P. J. & HENNINGSON, D. S. 2001 *Stability and Transition in Shear Flows*. New York: Springer.
- SCHOPPA, W. & HUSSAIN, F. 2002 Coherent structure generation in near-wall turbulence. *J. Fluid Mech.* **453**, 57–108.
- SKOTE, M., HARITONIDIS, J. H. & HENNINGSON, D. S. 2002 Varicose instabilities in turbulent boundary layers. *Physics of Fluids* **14**, 2309–2323.
- SWEARINGEN, J. D. & BLACKWELDER, R. F. 1987 The growth and breakdown of streamwise vortices in the presence of a wall. *J. Fluid Mech.* **182**, 255–290.
- TAYLOR, G. I. 1939 Some recent developments in the study of turbulence. In *Proc. 5th Intl. Congr. Appl. Mech.* (ed. J. Hartog & H. Peters), pp. 294–310. Wiley.
- TENNEKES, H. & LUMLEY, J. L. 1972 *A first course in turbulence*. Cambridge MA: The MIT Press.
- WALEFFE, F. 1995 Hydrodynamic stability and turbulence: Beyond transients to a self-sustaining process. *Stud. Appl. Math.* **95**, 319–343.
- WALEFFE, F. 1997 On a self-sustaining process in shear flows. *Phys. Fluids* **9**, 883–900.
- WESTIN, K. J. A., BAKCHINOV, A. A., KOZLOV, V. V. & ALFREDSSON, P. H. 1998 Experiments on localized disturbances in a flat plate boundary layer. Part i: the receptivity and evolution of a localized free stream disturbance. *Eur. J. Mech. B/Fluids* **17**, 823–846.
- WESTIN, K. J. A., BOIKO, A. V., KLINGMANN, B. G. B., KOZLOV, V. V. & ALFREDSSON, P. H. 1994 Experiments in a boundary layer subject to free-stream turbulence. part i: Boundary layer structure and receptivity. *J. Fluid Mech.* **281**, 193–218.
- WU, X. & CHOUDHARI, M. 2001 Linear and nonlinear instabilities of Blasius boundary layer perturbed by streamwise vortices. part II: Intermittent instability induced by long-wavelength Klebanoff modes. Report 2001-45. ICASE.
- WU, X., JACOBS, R. G., HUNT, J. C. R. & DURBIN, P. A. 1999 Simulation of boundary layer transition induced by periodically passing wakes. *J. Fluid Mech.* **398**, 109–153.
- WUNDROW, D. W. & GOLDSTEIN, M. E. 2001 Effect on a laminar boundary layer of

small-amplitude streamwise vorticity in the upstream flow. *J. Fluid Mech.* **426**, 229–262.

YANG, Z. & VOKE, P. 1995 Numerical study of bypass transition. *Phys. Fluids A* **7**, 2256–2264.